Mitsuo Niinomi
Takayuki Narushima
Masaaki Nakai   *Editors*

Advances in Metallic Biomaterials

Processing and Applications

Springer

Springer Series in Biomaterials Science and Engineering

Volume 4

Series editor
Prof. Min Wang
Department of Mechanical Engineering
The University of Hong Kong
Pokfulam Road, Hong Kong
e-mail: memwang@hku.hk

Aims and scope

The Springer Series in Biomaterials Science and Engineering addresses the manufacture, structure and properties, and applications of materials that are in contact with biological systems, temporarily or permanently. It deals with many aspects of modern biomaterials, from basic science to clinical applications, as well as host responses. It covers the whole spectrum of biomaterials – polymers, metals, glasses and ceramics, and composites/hybrids – and includes both biological materials (collagen, polysaccharides, biological apatites, etc.) and synthetic materials. The materials can be in different forms: single crystals, polycrystalline materials, particles, fibers/wires, coatings, non-porous materials, porous scaffolds, etc. New and developing areas of biomaterials, such as nano-biomaterials and diagnostic and therapeutic nanodevices, are also focuses in this series. Advanced analytical techniques that are applicable in R & D and theoretical methods and analyses for biomaterials are also important topics. Frontiers in nanomedicine, regenerative medicine and other rapidly advancing areas calling for great explorations are highly relevant.

The Springer Series in Biomaterials Science and Engineering aims to provide critical reviews of important subjects in the field, publish new discoveries and significant progresses that have been made in both biomaterials development and the advancement of principles, theories and designs, and report cutting-edge research and relevant technologies. The individual volumes in the series are thematic. The goal of each volume is to give readers a comprehensive overview of an area where new knowledge has been gained and insights made. Significant topics in the area are dealt with in good depth and future directions are predicted on the basis of current developments. As a collection, the series provides authoritative works to a wide audience in academia, the research community, and industry.

Mitsuo Niinomi • Takayuki Narushima
Masaaki Nakai

Editors

Advances in Metallic Biomaterials

Processing and Applications

Springer

Editors
Mitsuo Niinomi
Institute for Materials Research
Tohoku University
Sendai, Japan

Takayuki Narushima
Department of Materials Processing
Tohoku University
Sendai, Japan

Masaaki Nakai
Institute for Materials Research
Tohoku University
Sendai, Japan

Preface

Metallic biomaterials are of great importance in the development of implant devices. They are usually used in load-bearing implants, such as artificial joints (for instance, a hip joint), spinal fixation devices, nails, bone plates and screws, and dental implants, which are designed for reconstruction of failed hard tissue. Metallic biomaterials may be employed not just as a replacement for failed hard tissue but also in the reconstruction of soft tissues such as blood vessels. Some of the representative metallic biomaterials include stainless steels, Co–Cr alloys, and titanium and its alloys. Other examples of metallic biomaterials are magnesium-based alloys, tantalum-based alloys, niobium-based alloys, and precious alloys such as gold-based alloys and silver-based alloys containing a large amount of platinum and gold. Metallic biomaterials are also employed in the fabrication of dental prostheses including crowns, dentures, inlays, and bridges.

The research and developments in metallic biomaterials are energetically being carried out, and significant new results have been achieved or currently are being achieved. According to the developments in metallic biomaterials, the latest advances in the construction of implant devices using metallic biomaterials are remarkable.

Understanding the properties of biological tissues and organs is important for the development of bio-functional metallic biomaterials, and understanding their fundamental behavior is also important. The ways in which biomaterials react with the body should also be well understood for further development of metallic biomaterials that are safe to use within the human body.

Even the safest metallic biomaterials exhibit no bio-functionality. Therefore, bioactive or bio-functional surface modifications must be performed on metallic biomaterials in order to achieve the required biological properties, for example, bone conductivity or blood compatibility.

A review of the latest advances and current fundamental knowledge concerning tissues, materials, biological reactions, and the processing and applications of metallic biomaterials is given in two volumes of books entitled *Advances in*

Metallic Biomaterials: Tissues, Materials, and Biological Reactions and *Advances in Metallic Biomaterials: Processing and Applications*.

The volume *Advances in Metallic Biomaterials: Tissues, Materials, and Biological Reactions* has the following structure: Part I Biological Tissues and Organs, Part II Metallic Biomaterials, and Part III Reaction of Metals in Human Body. Part I consists of five chapters, with each focusing on one of the following: bone tissue and biomaterials design based on the anisotropic microstructure joint and articular cartilage, metallurgy of spinal instrumentation, biomechanics of blood vessels, and tooth and tooth-supporting structures. Part II consists of six chapters, with each describing one of the following: nickel-free high-nitrogen stainless steel, Co–Cr alloys as effective metallic biomaterials, titanium alloys for biomedical applications, zirconium alloys for biomedical applications, porous tantalum for applications in orthopedic surgery, and niobium-based biomaterials. Part III consists of three chapters, with each describing one of the following: corrosion of metallic biomaterials, metal allergy to metallic biomaterials, and cytotoxicity of metallic biomaterials, respectively.

The volume *Advances in Metallic Biomaterials: Processing and Applications* has the following structure: Part I Processing Techniques, Part II Surface Modification, and Part III Applications. Part I consists of four chapters, with each focusing on one of the following techniques: additive manufacturing technology for orthopedic implants, metal injection molding (MIM) processing, smart hot forging technique in producing biomedical Co–Cr–Mo artificial implants, and electroforming as a new method for the fabrication of degradable pure iron stent. Part II consists of five chapters, with each describing one of the following: bioactive ceramic coatings, bio-functionalization of metals with polymers, adhesive strength of bioactive surface layer, surface improvement for biocompatibility of biomedical titanium alloys by dealloying in metallic melt, and functionally graded metallic biomaterials. Part III consists of three chapters, with each describing one of the following applications: metallic biomaterials in orthopedic surgery; stents: functions, characteristics, and materials; and dental metallic materials, respectively.

It is our hope that these books will be useful to readers working in a wide variety of fields that take scientific and practical interests in current and future developments in metallic biomaterials. Each chapter has been written by an international expert who works in relevant fields. We wish to express our sincere thanks to the authors named on a separate page for their excellent contributions. We also wish to express our thanks to Professor Ming Wang at the Department of Mechanical Engineering, University of Hong Kong, who is the Series Editor of Springer's books series; Springer Series in Biomaterials Science and Engineering for giving us a chance to edit these books; and Springer Beijing office for their support, especially to Ms. June Tang and Ms. Heather Feng in publishing these volumes.

Sendai, Japan   Mitsuo Niinomi
Sendai, Japan   Takayuki Narushima
Sendai, Japan   Masaaki Nakai

Contents

Part III   Applications

Contributors

Chiba Akihiko Institute for Materials Research, Tohoku University, Sendai, Japan

Hidetsugu Fukuda National Institute of Technology, Yuge College, Yuge, Kamijima-cho, Ochigun, Ehime, Japan

Tadanao Funakoshi Department of Orthopaedic Surgery, Hokkaido University Graduate School of Medicine, Sapporo, Japan

Takao Hanawa Department of Metallic Biomaterials, Institute of Biomaterials and Bioengineering, Tokyo Medical and Dental University, Chiyoda-ku, Tokyo, Japan

Masahiro Hirohashi Graduate Student, Graduate School of Engineering, Tohoku University, Sendai, Japan

Noriyuki Hisamori Department of Engineering and Applied Sciences, Faculty of Science and Technology, Sophia University, Chiyoda-ku, Tokyo, Japan

Manabu Ito Department of Spine and Spinal Cord Disorders, National Hospital Organization Hokkaido Medical Center, Sapporo, Japan

Yoshinori Itoh Hamamatsu Industrial Research Institute of Shizuoka Prefecture, Hamamatsu, Shizuoka, Japan

Toshihiro Kasuga Department of Frontier Materials, Graduate School of Engineering, Nagoya Institute of Technology, Nagoya, Aichi, Japan

Hidemi Kato Institute for Materials Research, Tohoku University, Sendai, Japan

Yunping Li Institute for Materials Research, Tohoku University, Sendai, Japan

Present Address: Materials Science and Engineering, Central South University, Changsha, China

Hirotaka Maeda Department of Frontier Materials, Graduate School of Engineering, Nagoya Institute of Technology, Nagoya, Aichi, Japan

Diego Mantovani Laboratory for Biomaterials and Bioengineering (CRC-I), Department of Mining, Metallurgy and Materials Engineering & CHU de Québec Research Center, Laval University, Québec, Canada

Hideshi Miura Department of Mechanical Engineering, Kyushu University, Nishi-ku, Fukuoka, Japan

Eri Miura-Fujiwara University of Hyogo, Himeji, Japan

Afghany Mostavan Laboratory for Biomaterials and Bioengineering (CRC-I), Department of Mining, Metallurgy and Materials Engineering & CHU de Québec Research Center, Laval University, Québec, Canada

Masaaki Nakai Institute for Materials Research, Tohoku University, Sendai, Japan

Takayuki Narushima Department of Materials Processing, Tohoku University, Sendai, Japan

Mitsuo Niinomi Institute for Materials Research, Tohoku University, Sendai, Japan

Tomohiro Onodera Department of Orthopaedic Surgery, Hokkaido University Graduate School of Medicine, Sapporo, Japan

Toshiko Osada Department of Mechanical Engineering, Kyushu University, Nishi-ku, Fukuoka, Japan

Carlo Paternoster Laboratory for Biomaterials and Bioengineering (CRC-I), Department of Mining, Metallurgy and Materials Engineering & CHU de Québec Research Center, Laval University, Québec, Canada

Agung Purnama Laboratory for Biomaterials and Bioengineering (CRC-I), Department of Mining, Metallurgy and Materials Engineering & CHU de Québec Research Center, Laval University, Québec, Canada

Hisashi Sato Nagoya Institute of Technology, Nagoya, Japan

Koichi Tsuchiya Research Center for Strategic Materials, National Institute for Materials Science, Tsukuba, Japan

Kyosuke Ueda Department of Materials Processing, Tohoku University, Sendai, Japan

Takeshi Wada Institute for Materials Research, Tohoku University, Sendai, Japan

Yoshimi Watanabe Nagoya Institute of Technology, Nagoya, Japan

Akiko Yamamoto International Center for Materials Nanoarchitectonics, National Institute for Materials Science, Tsukuba, Japan

Part I
Processing Techniques

Chapter 1
Additive Manufacturing Technology for Orthopedic Implants

Hidetsugu Fukuda

Abstract The additive manufacturing process is a method in which calculations pertaining to a thin cross-sectional shape are performed on a computer on the basis of three-dimensional computer-aided design (CAD) data. Three-dimensionally shaped objects are then created by stacking layers of the material on the basis of the calculation results. The additive manufacturing process has allowed for creating near-net shape three-dimensional structures with complex shapes, porous structures, and inclined structures, which are impossible to create with conventional machine work and casting methods; therefore, this process could potentially be a novel manufacturing method for next-generation orthopedic metallic implants. In this chapter, the principles and characteristics of the additive manufacturing technology are described, and the development of an orthopedic implant using the additive manufacturing technology is presented.

Keywords Additive manufacturing • Selective laser melting • Electron beam melting • Low modulus • Porous metallic biomaterials

1.1 Introduction

Currently, most orthopedic implants use metallic materials with high mechanical reliability against damage. They are particularly used in artificial joints sustaining heavy loads, for trauma devices, and for spinal instrumentation. Table 1.1 shows metallic materials used in orthopedic surgery as described by the International Organization for Standardization (ISO) and the American Society for Testing and Materials (ASTM) [1–18]. Figure 1.1 shows typical products used in artificial hip joint and knee joint. Representative metallic materials currently used in orthopedic surgery are stainless steel, Co–Cr alloys, and titanium alloys, and the manufacturing methods can be classified as casting methods and forging methods.

H. Fukuda (✉)
National Institute of Technology, Yuge College, 1000, Shimoyuge,
Yuge, Kamijima-cho, Ochigun, Ehime 794-2593, Japan
e-mail: fukuda@mech.yuge.ac.jp

Table 1.1 Metallic materials used in orthopedic surgery as described by the ISO and the ASTM

Materials	Standard
Stainless steel	ISO 5832–1, Implants for surgery – Metallic materials – Part 1: Wrought stainless steel
	ISO 5832–9, Implants for surgery – Metallic materials – Part 9: Wrought high nitrogen stainless steel
	ASTM F138, Standard Specification for Wrought 18Chromium–14Nickel–2.5Molybdenum Stainless Steel Bar and Wire for Surgical Implants
Co–Cr alloy	ISO 5832–4, Implants for surgery – Metallic materials – Part 4: Cobalt–chromium–molybdenum casting alloy
	ISO 5832–5, Implants for surgery – Metallic materials – Part 5: Wrought cobalt–chromium–tungsten–nickel alloy
	ISO 5832–6, Implants for surgery – Metallic materials – Part 6: Wrought cobalt–nickel–chromium–molybdenum alloy
	ISO 5832–7, Implants for surgery – Metallic materials – Part 7: Forgeable and cold-formed cobalt–chromium–nickel–molybdenum–iron alloy
	ISO 5832–12, Implants for surgery – Metallic materials – Part 12: Wrought cobalt–chromium–molybdenum alloy
	ASTM F75, Standard Specification for Cobalt–28Chromium–6Molybdenum Alloy Castings and Casting Alloy for Surgical Implants
	ASTM F90, Standard Specification for Wrought Cobalt–20Chromium–15Tungsten–10Nickel Alloy for Surgical Implant Applications
	ASTM F799, Standard Specification for Cobalt–28Chromium–6Molybdenum Alloy Forgings for Surgical Implants
	ASTM F1537, Standard Specification for Wrought Cobalt–28Chromium–6Molybdenum Alloys for Surgical Implants
Titanium and titanium alloy	ISO 5832–2, Implants for surgery – Metallic materials – Part 2: Unalloyed titanium
	ISO 5832–3, Implants for surgery – Metallic materials – Part 3: Wrought titanium 6–aluminum 4–vanadium alloy
	ASTM F67, Standard Specification for Unalloyed Titanium, for Surgical Implant Applications
	ASTM F136, Standard Specification for Wrought Titanium–6Aluminum–4Vanadium ELI (Extra Low Interstitial) Alloy for Surgical Implant Applications
	ASTM F1108, Standard Specification for Titanium–6Aluminum–4Vanadium Alloy Castings for Surgical Implants
	ASTM F1813, Standard Specification for Wrought Titanium–12Molybdenum–6Zirconium–2Iron Alloy for Surgical Implant

The materials and manufacturing methods used are of critical importance for orthopedic implants, and they need to be selected appropriately depending on the shape, cost, and performance required of the orthopedic implants in actual use.

For example, the stem of a hip joint prosthesis with no bone cement is supposed to adhere to living bone tissue for a long period of time, and therefore, highly biocompatible titanium alloys are selected; because mechanical strength and
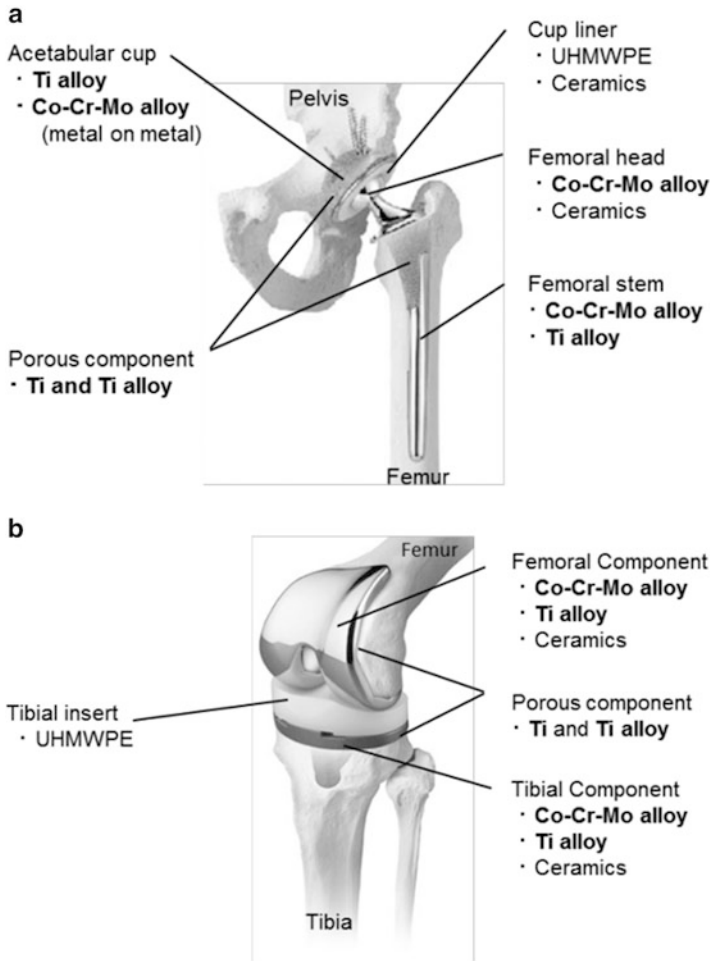
Fig. 1.1 Typical products used in artificial hip joint and knee joint. (**a**) Artificial hip joint. (**b**) Artificial knee joint

ductility are required, the forging method is selected as the manufacturing method. On the other hand, the femoral component of artificial knee joint is used on a sliding portion, and therefore, highly abrasion-resistant Co–Cr alloys are selected; because of the complex shape of the prosthesis, the casting process is selected as the manufacturing method. Over the past few decades, Co–Cr and titanium alloys have become the mainstream materials, and the forging procedure and the casting method have become the mainstream manufacturing methods. However, new biomedical metallic materials [19, 20] and novel manufacturing methods [21, 22] are continually being developed. Particularly, the additive manufacturing process has recently attracted attention as a new manufacturing method for orthopedic

implants [23]. This chapter describes additive manufacturing technology and the development of orthopedic implants utilizing this technology.

1.2 Additive Manufacturing

Additive manufacturing technology was developed in the early 1980s, and it has been used as a means to accelerate the manufacturing of prototypes and design validation models, mainly in the aircraft and automobile industries, which used three-dimensional (3D) data from early on. Currently, complex shapes can be expressed with dimensional accuracy by using metallic powders and resins as materials. However, initially, thermoplastic resins were melted with heat and laminated, and photo-polymerizing resins were irradiated with ultraviolet light in a hardening-only method; materials were limited and dimensional accuracy was low. Later, with technological advances in additive manufacturing in terms of the diversification of materials and the improvement of dimensional accuracy, the application of additive manufacturing has increased. Research and development of additive manufacturing using metallic powder was popular in the 1990s. In the 2000s, use of the method went beyond creating models for design verification; they were also commonly utilized for the direct creation of prototypes for use in performance tests and assembly, in manufacturing processes, and in small amounts of finished products. Figure 1.2 shows various medical devices made by using the additive manufacturing process.

   Initially, the process was often called "rapid prototyping" because it allowed for a rapid construction of models; however, as the technology became widespread, it became known under various names, such as additive fabrication (AF), direct digital manufacturing (DDM), free-form fabrication (FFF), and three-dimensional printing (3DP). Therefore, in 2009, ASTM defined it as additive manufacturing (AM), in the sense that it was a manufacturing method consisting of adding materials as opposed to manufacture by removal, such as in cutting [24]. Table 1.2 shows additive manufacturing process categories defined by ASTM F2729-12a. The additive manufacturing processes, which allow for manufacturing metal components, are powder bed fusion and directed energy deposition. Powder bed fusion is a method for constructing three-dimensional structures by using energy sources such as laser beams and electron beams for sintering or melting the starting raw material powder. Depending on the energy source, powder bed fusion is also known as selective laser melting (SLM) or electron beam melting (EBM). Directed energy deposition is a method for manufacturing three-dimensional structures by using a high-power laser to melt the metal powder while stacking it into layers.
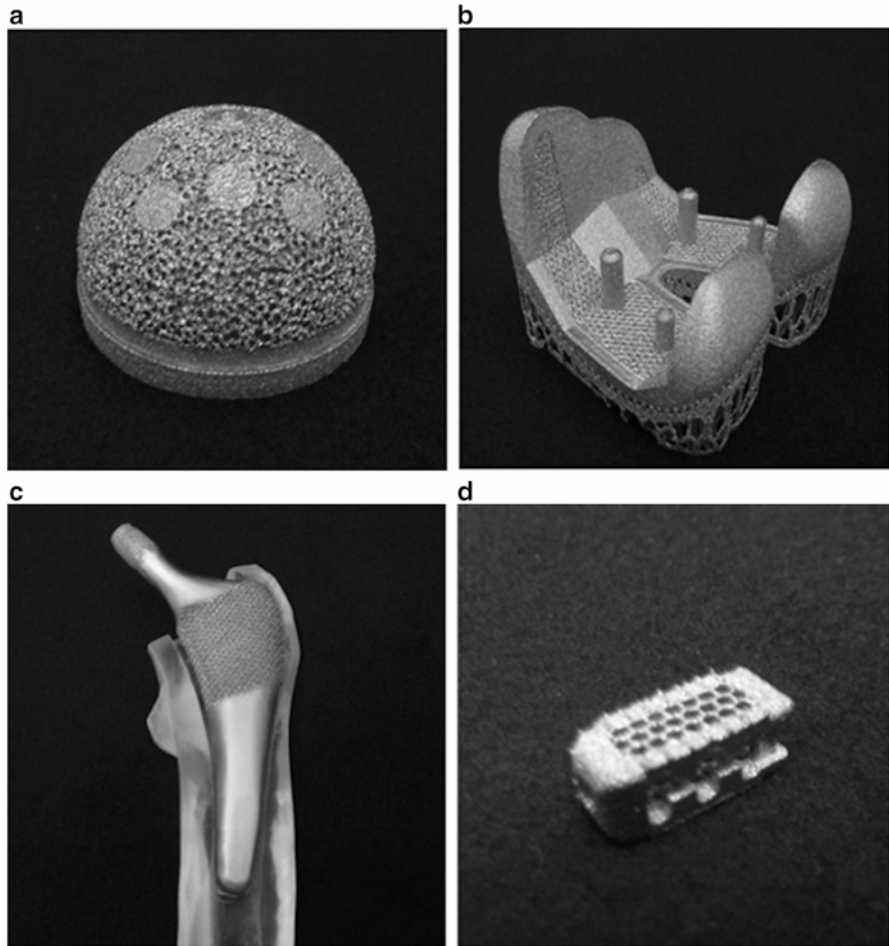
Fig. 1.2 Various medical devices made by using an additive manufacturing process. (**a**) Acetabular cup. (**b**) Artificial knee joint. (**c**) Artificial hip joint. (**d**) Spine cage

1.2.1 Selective Laser Melting

Figure 1.3 shows a representative schematic diagram of an SLM device. There are several types of SLM devices, including EOSINT M 280 by EOS GmbH (Germany) and another type by 3D Systems.

An SLM device is composed of a laser oscillator, a scanning mirror, a blade, a powder supply platform, and a building platform. In order to manufacture metal components by using an SLM device, the first thing to do is to construct a three-dimensional design model of the metal components. The design model is made by using CAD software and computed tomography (CT) data or three-dimensional measurement data. Next, slice data are constructed by dividing the

Table 1.2 Additive manufacturing process categories

Type	Process
Binder jetting	An additive manufacturing process in which a liquid bonding agent is selectively deposited to join powder materials
Directed energy deposition	An additive manufacturing process in which focused thermal energy is used to fuse materials by melting as they are being deposited
Material extrusion	An additive manufacturing process in which material is selectively dispensed through a nozzle or orifice
Material jetting	An additive manufacturing process in which droplets of build material are selectively deposited
Powder bed fusion	An additive manufacturing process in which thermal energy selectively fuses regions of a powder bed
Sheet lamination	An additive manufacturing process in which sheets of material are bonded to form an object
Vat photopolymerization	An additive manufacturing process in which liquid photopolymer in a vat is selectively cured by light-activated polymerization
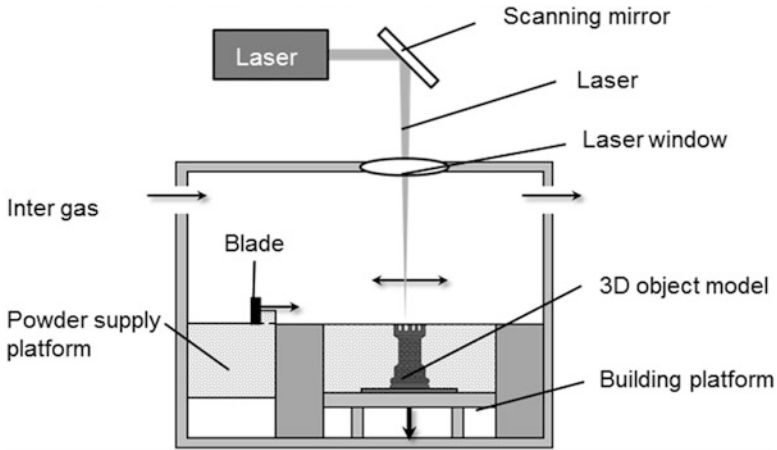
Fig. 1.3 Representative schematic diagram of an SLM device

three-dimensional design model into equal intervals in the direction of its height. Here, the divided interval is the thickness of the laminate per layer. After data on the constructed slices are entered into the SLM device, the parameters of the model are set up, namely, the laser output suitable for the model to be constructed, the scanning speed, the laser's scanning interval, and the hatch angle. To one side of the molding device, powder is supplied to the powder supply platform inside the device, after which N_2 gas or Ar gas is introduced into the device. After the appropriate volume of gas is loaded, an amount of metal powder suitable for one layer is deposited onto the base plate using a blade. The laser, which is emitted from the laser oscillator, is then reflected by a scanning mirror and irradiated onto the thinly paved metal powder layer. Based on the slice data, the laser is scanned by
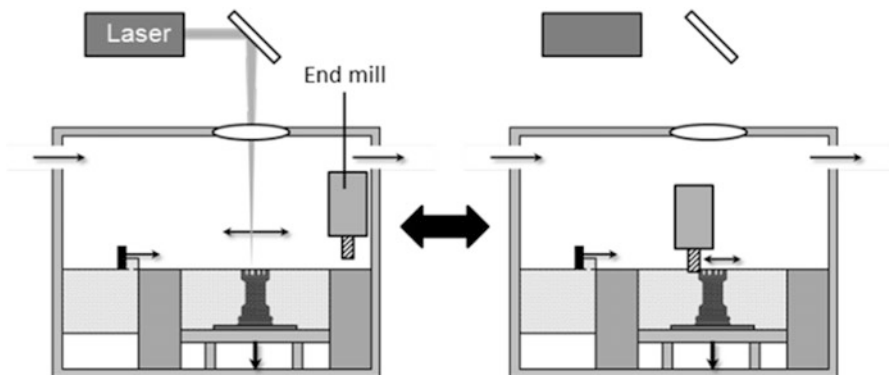
Fig. 1.4 Representative schematic diagram of a metal laser sintering hybrid milling device

controlling the scanning mirror, and the metal powder is melted and solidified into the desired shape. Once one layer of the model is completed, the building platform descends by one layer, and another layer of metal powder is deposited by using the blade. A metal product with a shape similar to that of the three-dimensional design model is molded directly by sequentially and repeatedly melting, solidifying, and depositing metallic powder.

When this method was initially developed, the sintered density was relatively low, and its application was limited to products with no strict requirement for strength. Recently, however, there have been advances in the development of laser oscillators, and with the change from CO_2 lasers to YAG and Yb fiber lasers, the manufacture of products with a higher output, higher precision, and higher density has become possible. Meanwhile, there have also been advances in the development of metal powders, namely, the starting materials. The manufacture of products from titanium and its alloys, cobalt–chromium alloys, maraging steel, and aluminum has become possible, although there are differences depending on the type of modeling device. In order for the laser sintering of aluminum and titanium alloys to be feasible, the oxygen content needed to be markedly reduced; therefore, the size of the modeling area was reduced, and devices using hermetically sealed chambers have been developed. Meanwhile, in order to solve the issues of dimensional precision and surface roughness, which were problems originally associated with the additive manufacturing process, complex processing devices were developed that allowed for the laser sintering and lamination of metal powder, as well as for the cutting and finishing procedures by end milling (Fig. 1.4).

1.2.2 Electron Beam Melting

Figure 1.5 shows a representative schematic diagram of an EBM device. The EBM device is an Arcam Q10, manufactured by Arcam AB (Sweden). An EBM device is
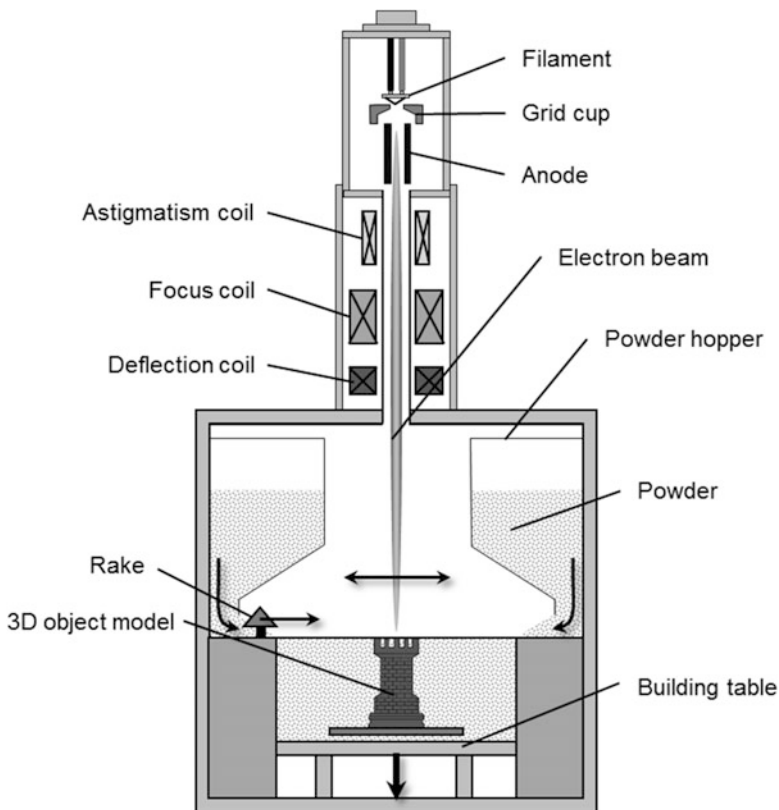
Fig. 1.5 Representative schematic diagram of an SLM device

composed of the following: an electron beam column, which is composed of a filament, grid, and anode; various types of coils, which control the electron beam; a hopper, which supplies the powder; a rake, which levels the powder; and a modeling table. In order to manufacture a metal component using an EBM device, a three-dimensional design model of the metal component is created; based on the resulting data, slice data divided into equal intervals in the direction of the height of the model are created. Up to this step, the procedure is the same as that used in the creation of metal components using an SLM device. The resulting slice data is input into the EBM device, and the modeling parameters are set up, such as the scanning speed and scanning intervals for the electron beam and the beam electric current suitable for the model being created. To one side of the molding device, the metal powder to be used in molding is supplied to the powder hopper inside the molding device and subjected to a vacuum using a vacuum pump. After the desired extent of vacuum is reached, the base plate, which serves as a foundation for the molding

process, is heated by repeatedly irradiating it with an electron beam. When the base plate reaches the desired temperature (conventionally 600–900 °C), an amount of metal powder sufficient for one layer is deposited upon the base plate using a rake. In order to suppress the scattering of metal powder during molding and in order to inhibit the deformation of the model due to residual stress, the entire surface of the deposited metal powder layer is irradiated with an electron beam with a relatively low energy density, which prevents sintering of the metal powder. After irradiation is conducted for the desired duration, an electron beam with a high energy density that allows for melting of the metal powder is applied on the basis of the slice data, and the metal powder is melted and solidified into the desired shape. Once the molding of one layer has been completed, the building table descends by one layer, and the system deposits metal powder for the next layer. The metal powder is sequentially and repeatedly melted, solidified, and deposited, which allows for the direct shaping of metal products with a shape close to that of the three-dimensionally designed model.

The EBM method allows for rapid scanning of the high-output electron beam, and therefore, it allows for faster molding than with the SLM method. Compared to a laser, an electron beam penetrates with little change in the beam width in the direction of the depth of irradiation, and therefore, it allows for melting the paved powder bed efficiently in the direction of the depth; this makes it possible to perform a high-density molding, even when using materials with a high melting point above 2,000 °C. In addition, since the molding is carried out under high vacuum, the products are not affected by oxidation or nitridation, and therefore, this method is suitable for the molding of high-quality metal products.

One of the advantages of EBM is the fact that preheating of the metal powder is performed before fusing it. This is effective in eliminating the residual stress that occurs inside the molded object after melting and solidification, allowing for easy control of the stability of the shape of the molded object.

1.3 Processed Material

The powder material is the most important element in the molding of a component using a powder bed fusion method. No matter how perfect the device and the software are, high-precision molding using the powder bed fusion method is difficult unless the powder used as the starting material has suitable properties in terms of its average particle diameter, bulk density, and crystallinity. In addition, if proper molding conditions such as the environment temperature for molding each material and the laser output cannot be selected, high-precision components cannot be molded.

Figure 1.6 shows a photograph of the metal powder used for powder bed fusion. In powder bed fusion, spherical powders are mostly used. They are manufactured

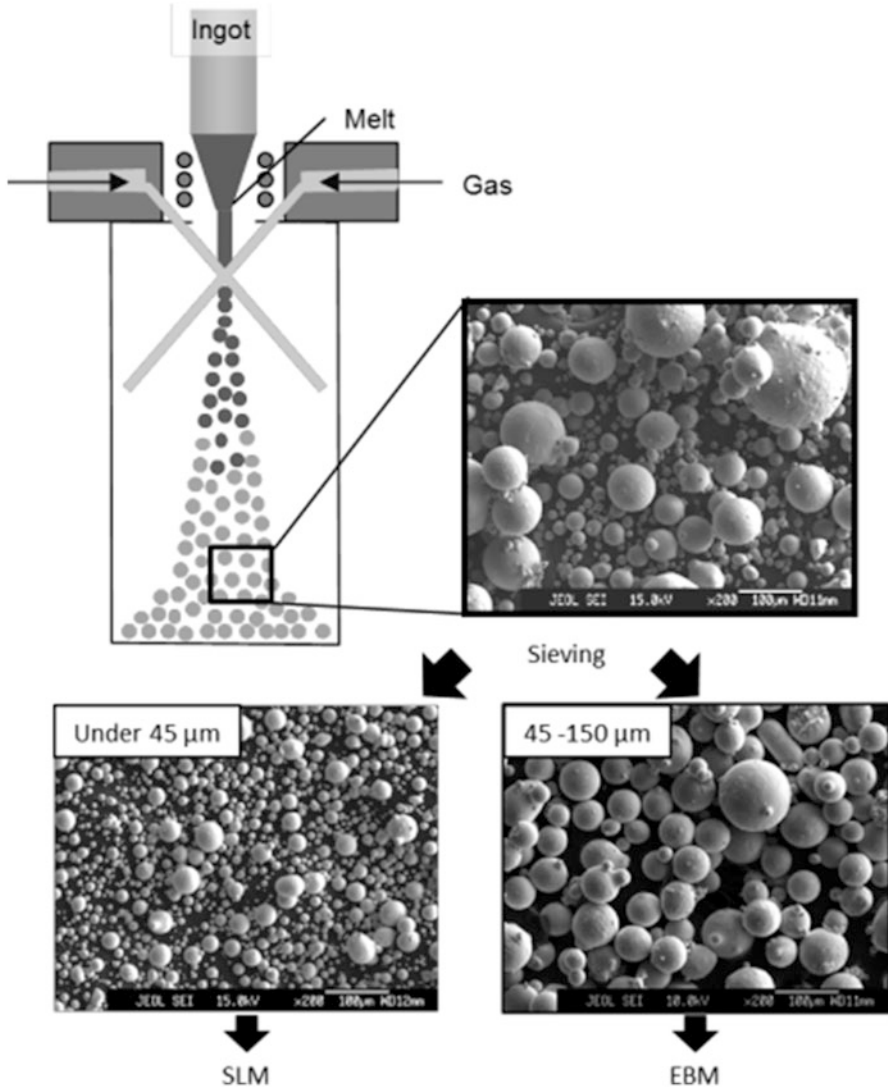**Fig. 1.6** Photograph of the metal powder used for powder bed fusion

by using gas, plasma, or centrifugal atomization methods. Once the powders have been manufactured, they are separated by sieving and are used according to their suitability for the fabricated devices. Next, we report on the application of the powder bed fusion method to biomedical metal materials, namely, Co–Cr alloys and Ti alloys.

1.3.1   Co–Cr Alloy

By using an SLM device, Takaichi et al. [25] examined the mechanical properties of Co–Cr alloys manufactured under various molding conditions and compared them to cast materials made from the same alloy. The 0.2 % proof stress, tensile strength, and elongation of the molded Co–Cr alloys were all higher than those of the cast alloys. Various elements such as carbon and nitrogen have been added in order to improve the mechanical properties of Co–Cr alloy casting materials; however, findings have suggested that this is highly likely to be unnecessary with the SLM method.

Xin et al. [26] compared the cellular responsiveness of mouse fibroblasts to the amount of metal ions eluted from Co–Cr alloys manufactured with the SLM method with that from the corresponding molded objects. The amount of Co and Cr eluted from Co–Cr alloys manufactured using the SLM method showed a significantly stronger inhibition than cast materials. The growth of mouse fibroblasts has also been reported to be high in molded Co–Cr alloys.

Gaytan et al. [27] manufactured sintered bodies of Co–Cr alloys using the EBM method, and they investigated the microstructure and tensile properties of each product. In addition, they attempted to develop a femoral component by using the EBM method and demonstrated the usefulness of EBM.

Sun et al. [28] clarified the structure directional dependence of the mechanical properties of Co–Cr alloy microstructures manufactured using the EBM method. The γ-phase preferential crystal orientation of shaped objects made of Co–Cr alloys manufactured at angles of 0°, 45°, 55°, and 90° was close to [001], [100], [111], and [100], respectively. $M_{23}C_6$ precipitates were aligned in the stacking direction at intervals of about 3 μm. The findings showed that Co–Cr alloys manufactured using the EBM methods need to undergo heat treatment in order to attain a uniform microstructure.

1.3.2   Ti–6Al–4V Alloy

Among research studies on biological metal materials using the powder bed fusion method, most reported studies are on Ti–6Al–4V alloys.

Table 1.3 shows the mechanical properties of Ti–6Al–4V and Ti–6Al–4V ELI alloys manufactured using the SLM and EBM methods [29–31].

Christensen et al. [29] studied the effects of post-molding hot isostatic pressure (HIP) treatment on the molded object. Performing a post-molding HIP treatment is considered to cause a decrease in 0.2 % proof stress and tensile strength. On the other hand, elongation remains unchanged.

In a study conducted by Chaine et al. [30], the test specimen was molded and subjected to post-molding processing by machining. A tensile test was conducted using a test specimen with a polished surface, and the mechanical properties of the

Table 1.3 Mechanical properties of Ti–6Al–4V and Ti–6Al–4V ELI alloys manufactured using the SLM and EBM methods

	YS (MPa)	TS (MPa)	EI (%)	References
Ti–6Al–4V ELI alloy EBM method Used machined specimens	856	924	15	[29]
Ti–6Al–4V ELI alloy EBM method Used HIP and machined specimens	800	876	16	[29]
Ti–6Al–4V ELI alloy EBM method Used machined and polished specimens	–	1,028	14	[30]
Ti–6Al–4V alloy EBM method Used as-build specimens	–	928	3	[30]
Ti–6Al–4V alloy EBM method Used machined specimens	1,130	1,180	>20	[31]
Ti–6Al–4V alloy SLM method Used machined specimens	1,350	1,450	0.5	[31]

two specimens were examined. For the molded specimen whose surface had been polished after post-molding machine processing, the tensile strength and elongation were higher than those found in the specimen used as it was after having been molded.

Murr et al. [31] manufactured Ti–6Al–4V alloys using SLM and EBM devices and compared their conformation and mechanical properties. For objects molded with SLM, the 0.2 % proof stress and tensile strength were higher than those of objects molded with EBM, whereas elongation was inversely related. The differences between the objects were due to the phases comprising the manufactured objects. Objects molded using the SLM method are considered to have an α'' phase and an α' phase. On the other hand, objects molded using the EBM method were composed of two phases, namely, an α phase and a β phase. The difference between those molded objects in terms of their constituent phases is caused by the preheating of the surrounding laminated powder. The preheating during the manufacture of molded objects using the SLM method is carried out at low temperature; the high temperature occurring immediately after solidification causes the existing β phase to be rapidly cooled, becoming an α' phase due to martensitic transformation. Meanwhile, during the manufacture of a molded object by using the EBM method, the preheating consists of a relatively high temperature (400–600 °C); as a result, the β phase occurs immediately after solidification; however, the preheat temperature is later maintained, and therefore, separation into α and β phases progresses.

1.3.3 Ti–15Zr–4Nb–4Ta Alloy

It is important that elements with no indication of toxicity be selected as alloying elements for biomedical metallic materials. Ti–6Al–4V alloys have been widely used as biomedical metallic materials; however, their alloy components comprise the strongly cytotoxic vanadium, as well as aluminum, which was formerly problematic because of its accumulation in the brains of Alzheimer's disease patients; therefore, alloys composed of less toxic elements started to be developed around 1980 [32–34].

Okazaki et al. developed a Ti–15Zr–4Nb–4Ta alloy powder (hereafter referred to as Ti-1544) that had low cytotoxicity and was composed exclusively of elements that improved corrosion resistance. Since the Ti-1544 alloy was composed of elements with low cytotoxicity, it was biologically safe. It was also excellent in terms of corrosion resistance, and it showed a balance between strength and ductility [35]. In addition, it has recently been revealed that by controlling the spatial design and heat treatment appropriately, the Ti-1544 alloy can be made to have apatite-forming ability without using chemical methods via aqueous solutions, such as in alkaline treatments [36]. The Ti-1544 alloy is thus promising as a new biomedical metallic material with apatite-forming ability.

The authors were the first in the world to have achieved the manufacture of molded objects from highly biocompatible Ti-1544 alloy by using the EBM method [37]. Figure 1.7 shows a photograph of the microstructure of Ti-1544 alloy products produced by EBM method. The microstructure of the molded object shows an α phase along the prior β grain boundary and tissue precipitated by an acicular α phase inside the prior β grain. In addition, observations show the prior β grain boundary being elongated in the direction of the lamination. Because the lamination pitch is 0.07 mm, the picture in Fig. 1.7 shows approximately 10 layers worth of stacked layers. This shows that the prior β grain boundary grows between and
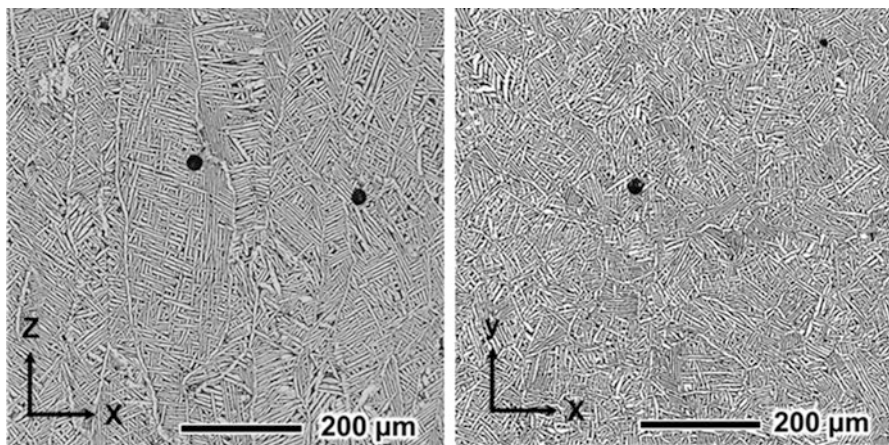

Fig. 1.7 Microstructures of Ti–15Zr–4Nb–4Ta alloy products produced by EBM method

across the stacked layers. This is believed to be due to epitaxial growth between the underlying solidified layer that had previously formed and the solidified layer that had formed on top of the latter. In addition, the additional elements in the Ti-1544 alloy included a large number of elements with high melting points and with marked differences in melting point; however, there was no segregation of the elements. Further, the black points inside the microstructure photograph in Fig. 1.7 are pores that had remained inside the molded object. Although the relative density of the molded object exceeded 99.9 %, the remaining pores were present as spherical shapes inside the molded object. The presence of residual pores inside the molded object might be the result of bubbles of gas generated during the melting process or internal bubbles generated during the preparation of the powder. The tension strength, 0.2 % proof stress, and elongation of molded objects manufactured with the Ti-1544 alloy using the EBM method are 870–890 MPa, 800–840 MPa, and 22–24 %, respectively, values that meet the standard values in accordance with JIS T7401-4 (tension strength, 860 MPa or higher; 0.2 % proof stress, 790 MPa; elongation, 10 % or higher). Therefore, from the perspective of mechanical properties, molded objects made of Ti-1544 alloy manufactured using the EBM method are highly likely to have practical applications.

1.4 Applications

1.4.1 Customized Implants

Most orthopedic implants currently in use have a standardized shape with a predefined width and thickness. However, in addition to individual differences in patients' skeletal conformation, there can be extensive bone loss in some cases due to the diseases such as arthritis, infections, and bone tumors, such that the underlying parent bone is not in good condition; in such cases, the use of standardized orthopedic implants is not indicated. In such cases, so-called custom-made implants, namely, implants with excellent adaptiveness to each individual, are needed. Because custom-made implants can be adapted to each individual patient, they offer excellent advantages, such as bone-sparing treatment, compatibility and individuality, minimally invasive surgery, excellent functional reconstruction, an increase in the number of years of usability of the implant, and early rehabilitation, as well as early social reintegration and a decrease in the probability of repeat surgery. The current problematic issue is that for the mass production of custom-made articular prostheses through conventional casting and machine-cutting processes, the production cost is not worth it. Custom-made prosthetic joints are ordered and manufactured separately for each individual patient, and the shape of these joints is designed to be optimal for each patient's skeletal conformation; as a result, their shape is often complex, with a larger number of free-curved surfaces than those of existing products. If they are constructed with conventional manufacturing methods, the preparation of the mold and the generation of the

tool path would be complicated, and the process would include a larger number of steps than those used for existing products. However, with the powder bed fusion method, products with a shape close to that of the designed three-dimensional CAD model can be manufactured semiautomatically by using an additive manufacturing device, without any particularly complex operation even if there are large numbers of free-curved surfaces. Therefore, the procedure is suitable as a manufacturing method for custom-made prosthetic joints. The following shows a patient-specific ordering-and-manufacturing process applied to the manufacture of custom-made prosthetic joints using the EBM method. The process diagram is shown in Fig. 1.8.
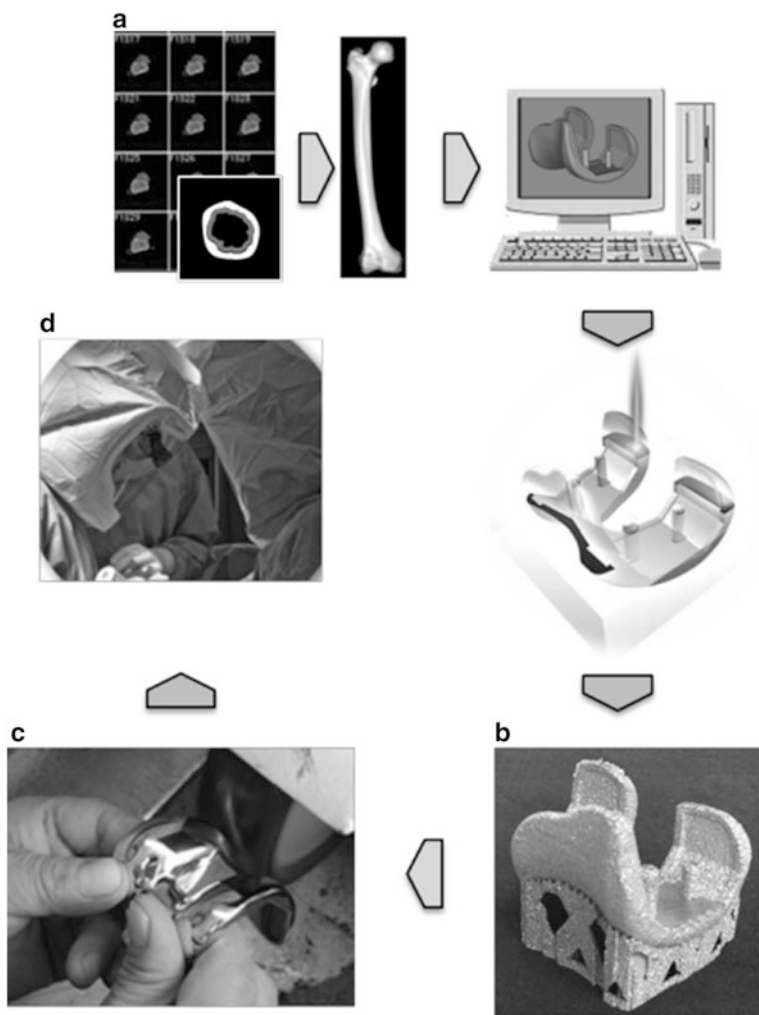

Fig. 1.8 Process diagram of custom-made prosthetic joints using the additive manufacturing. (**a**) Implant reconstruction/design. (**b**) Implant manufacturing (additive manufacturing). (**c**) Post-processing. (**d**) Surgery

1. Images of the diseased location are taken using CT or MRI.
2. A three-dimensional bone model is constructed on a computer on the basis of the medical imaging data.
3. A prosthetic joint that is suitable to each patient's skeletal conformation is designed on the basis of the three-dimensional bone model.
4. If the product needs to be bound to a living bone, three-dimensional porous structures are designed at sites where the latter are needed.
5. The mechanical safety of the prosthetic joint is evaluated by using a finite element method (FEM) analysis.
6. Manufacture is conducted by using the powder bed fusion method on the basis of the three-dimensional CAD data used in the design of the prosthetic joint.
7. Whenever necessary, machine processing is conducted at sites where configurational accuracy is required.
8. The product is subjected to testing, sterilization, and packing. It is then supplied for use in clinical settings.

The above description shows that in terms of production costs, the powder bed fusion method is very useful in the practical realization of custom-made prosthetic joints.

1.4.2 Porous Metallic Biomaterial

"Aseptic loosening of the prosthetic joint" is the main reason for prosthetic joint re-replacement surgery owing to the fact that the elastic modulus (80–120 GPa) of metallic materials used as a substitute for living bone in a prosthetic joint is much larger than the elastic modulus of the cortical bone (10–30 GPa) [38]. As a result, when a prosthetic joint is implanted in a living bone, the metallic material will bear the load, and thus, the load is not transmitted to the surrounding bones (stress shielding), leading to a failure of bone remodeling as well as to osteolysis and deterioration of the bone [39]. In the 1990s, reports from simulation experiments [40] and animal experiments [41] showed that materials with a low elastic modulus were effective in the prevention of stress shielding, and ever since, research and development on metallic materials with a low elastic modulus has been actively conducted. Among biomedical metallic materials already being used in prosthetic joints, those with a low elastic modulus are Ti–15Mo–5Zr–3Al and Ti–12Mo–6Zr–2Fe alloys; they each have an elastic modulus of 80 GPa. Biomedical metallic materials currently being developed include the liquid forms of Ti–29Nb–23Ta–4.6Zr [42] and Ti–24Nb–4Zr–7.9Sn alloys [43], with which an elastic modulus of 40–60 GPa has been achieved. However, none has reached the elastic modulus of cortical bone yet. Meanwhile, there is a method known as the porosification of metallic materials, which is aimed at reducing the elastic modulus of metallic materials [44]. The methods for the manufacture of porous metallic materials include the powder sintering method [45], the space holder method [46], hydrogen

utilization (unidirectional solidification) [47], and powder bed fusion [48, 49], which is a novel manufacturing method. The powder bed fusion method in particular has attracted attention because, on the basis of three-dimensional CAD data, it allows for a near-net-shape direct construction of complex porous structures that are difficult to manufacture with the conventional cutting and plastic deformation processing methods. This makes it possible to control the macroscopic apparent elastic modulus and the yield stress by designing the proper shape, size, and distribution of the pores.

Murr et al. [48] conducted a CT scan of open-cell foams of aluminum, and on the basis of the resulting data, they constructed three-dimensional CAD models of the core cell material and the hollow cell structure, and they constructed a Ti–6Al–4V alloy open-cell structure using the EBM method. The strength, which was calculated on the basis of the microindentation hardness of the manufactured hollow structure, showed values that were 40 % higher than those found in completely dense objects. The relative strength for the relative density of the core cell and hollow cell structures was consistent with the Gibson–Ashby model for open-cell foam materials.

Van Bael et al. [49] designed porous materials with pores measuring 500 μm and 1,000 μm in size and shaped as triangles, squares, and hexagons, and they modeled Ti–6Al–4V alloy open-cell structures using the SLM method. The elastic modulus of those products ranged between 0.4 and 11 GPa, and therefore, porous materials with an elastic modulus ranging from those of cancellous bones to those of cortical bones were achieved.

Pattanayak et al. [50] used human cancellous bone image data obtained from CT scans to create three-dimensional CAD models of porous materials with structures similar to that of the cancellous bone, and the manufacturing process was conducted using the SLM method. The compressive strength of Ti–6Al–4V alloy porous materials manufactured with a cancellous bone-like structure showed values that were higher than those found with titanium alloy porous materials manufactured with the powder sintering method.

Barbas et al. [51] focused on the mechanical anisotropy of bones, and they designed pores in order to express this in titanium porous materials. Based on the design, titanium porous materials were manufactured using the SLM method. After having taken into consideration the crystal anisotropy of titanium in the SLM-modeled object, they arranged a sequence of prisms with diamond-shaped cross sections of a size that would allow for penetration of newly formed bone. As a result, they achieved the manufacture of titanium alloy porous materials with an elastic anisotropy similar to that of bones.

Nakano et al. [52] used the EBM method to prepare a novel embedded directional porous implant made of Ti–6Al–4V alloy for osteogenesis. While focusing on the bone mass and bone quality of the newly formed bone, they conducted bone regeneration tests by embedding the material in rabbits. The cylindrical directional porous implant constructed functioned as scaffold for the conduction of newly formed bone along the direction of the axis of the bone; this induced the attachment of newly formed bone along the axis of the bone and an orientation that was

dependent on the location of the site on the bone. Consequently, it functioned as an implant capable of attaching to the bone over a long period of time without causing bone resorption. Meanwhile, the use of powder bed fusion for the creation of a β-type titanium alloy with low elasticity is also progressing.

Zhang et al. [53] succeeded in the powderization of a low-elasticity Ti–24Nb–4Zr–8Sn alloy using a gas atomization method in the experimental manufacture of an SLM model object with a relative density of 99 % or higher, as well as an acetabular cup. The elasticity modulus of the molded object was comparable to those of hot rolled and forged materials (53 GPa).

1.4.3   Implant with Designed Porous Surface

When implanted in bone tissue, Ti is known to attach closely to bone tissue (osseointegration) under light microscopy [54]. This is why titanium alloys are used as materials for prosthetic joints at sites of long-term adhesion to living bones. However, the current reality is that it takes a titanium alloy several months to fix itself to living bone tissue, and, as a result, stress loading on the prosthetic joint is not possible immediately after its implantation. Therefore, further improvement in the compatibility of titanium with living bone tissue is an issue that needs to be solved. The chemical composition of the surface of the materials and their physical configuration play a major role in the compatibility and adhesion between living bone tissue and biomedical metallic materials. From the perspective of the chemical composition, various modifications to the bioactive surface have been attempted for the purpose of improving the capacity to form new living bone [55]. Bioactive surface modifications can be broadly classified into two types: a method consisting of the coating of apatite, which is similar to bone mineral (hereafter referred to as HAp), directly onto the surface of the material and a method consisting of forming a surface layer or surface composition that promotes HAp formation in vivo. Among the methods, HAp coating by thermal spraying [56] (which represents the first method) and alkaline heat treatment [57] (which represents the second method) have already been put to practical use. However, since both methods include a high-temperature process, the temperature of the substrate increases. In general, the mechanical properties of titanium alloys are known to be strongly influenced by heat treatment [58]. Particularly, heat treatment at a temperature of 500 °C or higher causes marked changes in the mechanical properties and a loss of the properties of interest. Therefore, for titanium alloys, reducing the temperature in the heat treatment during the bioactive surface modification process is an extremely important matter.

Meanwhile, from the perspective of the physical shape of the material surface, porosification and roughening of the surface of the prosthetic joint have been attempted. Surface undulations, which are present at the surface of the material, have an anchoring effect owing to an increase in the bone contact area and mechanical fitting with the living bone tissue. In addition, these undulations have been reported to affect the development and growth behavior of bone cells [59], allowing

for a progression of the cells along the material's uneven surface. For those reasons, techniques allowing for control over the morphology of the surface of biomedical metallic materials are essential for improving their compatibility with living bone tissue. Currently, typical surface morphology control techniques that are being applied to the prosthetic joints include porosification of the surface through Ti plasma spray [60], metal bead coating [61], and fiber mesh coating [62]. Further, surface porosification using the additive manufacturing method has been the focus of attention in recent years, since it allows for control over pore shape, size, and distribution through a design of pore morphology [63]. Figure 1.9 shows a process diagram of implant with designed porous surface using the additive manufacturing method.

1.5 Future Developments

In recent years, more and more patients who had received treatment using prosthetic joints as a result of musculoskeletal disorders seek to live a more active lifestyle, such as running full marathons. Even patients who had been subjected to reconstruction using osteosynthesis devices because of fracture malunions challenge themselves by playing tennis. However, the main role of conventional orthopedic implants is merely to act as a substitute for supporting loads, and the range of motion has been designed to take into consideration only a very limited number of functions for daily living. In other words, patients' requests in recent years have gone beyond efficacy and safety as conventionally assumed in conventional orthopedic implants. Unreasonable use of the devices, namely, for purposes other than those they had been designed for, is likely to lead to a surge in the number of cases of re-replacements due to damage or deterioration in the near future. Therefore, in order to achieve a more active life, it is essential for the patient to recognize that a prosthetic joint behaves as if it were living bone and that it has properties similar to those of bones; at the same time, it is essential that the device be designed individually (high level of freedom) in accordance with each patient's particular skeleton, disease severity, and lifestyle habits and that it exerts its properties and functions with high performance. By themselves, the aforementioned "custom-made prosthetic joint" manufacturable with the EBM method, "prosthetic joints with a three-dimensional communicating porous structure," and "prosthetic joints with a low elasticity modulus" are each promising as prosthetic joints with new functions; however, their combination for the realization of futuristic prosthetic joints acting as actual living bones and with an "ability to fit into the morphology of the skeleton," a "biological ability to attach," and "bone-like mechanical functions" is not just a dream either. Futuristic prosthetic joints will be clearly distinct from prosthetic joints based on conventional types using average skeleton data, and they are expected to be able to provide a heretofore impossible level of activity to patients who have undergone functional reconstruction surgery. In addition, the powder bed fusion method is a very effective and essential technique for the realization of such prosthetic joints.
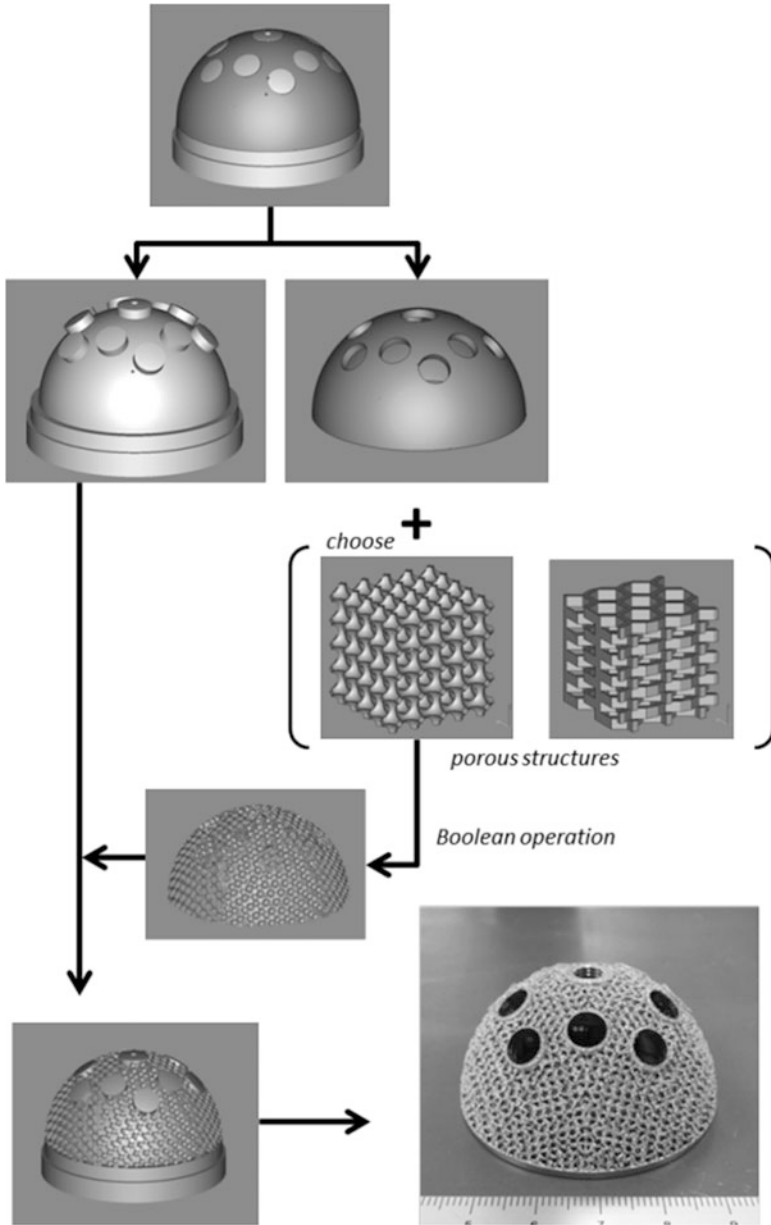
Fig. 1.9 Schematic process diagram of implant with designed porous surface using the additive manufacturing method

References

1. ISO 5832–1 (2007) Implants for surgery -metallic materials – Part 1: Wrought stainless steel. International Organization for Standardization
2. ISO 5832–9 (2007) Implants for surgery -metallic materials – Part 9: Wrought high nitrogen stainless steel. International Organization for Standardization
3. ASTM F138 (2008) Standard specification for wrought 18Chromium-14Nickel-2.5Molybdenum stainless steel bar and wire for surgical implants. American Society for Testing and Materials
4. ISO 5832–4 (1996) Implants for surgery -metallic materials – Part 4: Cobalt-chromium-molybdenum casting alloy. International Organization for Standardization
5. ISO 5832–5 (2005) Implants for surgery -metallic materials – Part 5: Wrought cobalt-chromium-tungsten-nickel alloy. International Organization for Standardization
6. ISO 5832–6 (1997) Implants for surgery -metallic materials- Part 6: Wrought cobalt-nickel-chromium-molybdenum alloy, International Organization for Standardization
7. ISO 5832–7 (1994) Implants for surgery -metallic materials – Part 7: Forgeable and cold-formed cobalt-chromium-nickel-molybdenum-iron alloy. International Organization for Standardization
8. ISO 5832–12 (2007) Implants for surgery -metallic materials – Part 12: Wrought cobalt-chromium-molybdenum alloy. International Organization for Standardization
9. ASTM F75 (2012) Standard specification for Cobalt-28 Chromium-6 Molybdenum alloy castings and casting alloy for surgical implants. America Society for Testing and Materials
10. ASTM F90 (2001) Standard specification for wrought Cobalt-20Chromium-15Tungsten-10Nickel alloy for surgical implant applications. American Society for Testing and Materials
11. ASTM F799 (2011) Standard specification for Cobalt-28Chromium-6Molybdenum alloy forgings for surgical implants. American Society for Testing and Materials
12. ASTM F1537 (2011) Standard specification for wrought Cobalt-28Chromium-6Molybdenum alloys for surgical implants. American Society for Testing and Materials
13. ISO 5832–2 (1999) Implants for surgery – metallic materials – Part 2: Unalloyed titanium
14. ISO 5832–3 (1996) Implants for surgery – metallic materials – Part 3: Wrought titanium 6-aluminium 4-vanadium alloy
15. ASTM F67 (2013) Standard specification for unalloyed Titanium, for surgical implant applications. American Society for Testing and Materials
16. ASTM F136 (2013) Standard specification for wrought Titanium-6Aluminum-4Vanadium ELI (extra low interstitial) alloy for surgical implant applications. American Society for Testing and Materials
17. ASTM F1108 (2004) Standard specification for Titanium-6Aluminum-4Vanadium Alloy castings for surgical implants. American Society for Testing and Materials
18. ASTM F1813 (2013) Standard specification for wrought Titanium–12 Molybdenum–6 Zirconium–2 Iron alloy for surgical implant. American Society for Testing and Materials
19. Bobyn JD, Poggie RA, Krygier JJ, Lewallen DG, Hanssen AD, Lewis RJ, Unger AS, O'Keefe TJ, Christie MJ, Nasser S, Wood JE, Stulberg SD, Tanzer M (2004) Clinical validation of a structural porous tantalum biomaterial for adult reconstruction. J Bone Joint Surg A 86:123–129
20. Nomura N, Tanaka Y, Suyalatu, Kondo R, Doi H, Tsutsumi Y, Hanawa T (2009) Effects of phase constitution of Zr-Nb alloys on their magnetic susceptibilities. Mater Trans 50:2466–2472
21. Thian ES, Loh NH, Khor KA, Tor SB (2002) Microstructures and mechanical properties of powder injection molded Ti-6Al-4V/HA powder. Biomaterials 23:2927–2938
22. Quan Y, Zhang F, Rebl H, Nebe B, Kessler O, Burkel E (2013) Ti6Al4V foams fabricated by spark plasma sintering with post heat treatment. Mater Sci Eng A 565:118–125

23. Lawrence EM, Sara MG, Diana AR, Edwin M, Jennifer H, Krista NA, Patrick WS, Francisco RM, Ryan BW (2012) Metal fabrication by additive manufacturing using laser and electron beam melting technologies. J Mater Sci Technol 28:1–14
24. ASTM F2729 (2012) Standard consumer safety specification for constant air inflatable play devices for home use. American Society for Testing and Materials
25. Takaichi A, Suyalatu NT, Joko N, Nomura N, Tsutsumi Y, Migita S, Doi H, Kurosu S, Chiba A, Wakabayashi N, Igarashi Y, Hanawa T (2013) Microstructures and mechanical properties of Co-29Cr-6Mo alloy fabricated by selective laser melting process for dental applications. J Mech Behav Biomed Mater 21:67–76
26. Xin XZ, Xiang N, Chen J, Xu D, Wei B (2012) Corrosion characteristics of a selective laser melted Co–Cr dental alloy under physiological conditions. J Mater Sci 47:4813–4820
27. Gaytan SM, Murr LE, Martinez E, Martinez JL, Machado BI, Ramirez DA, Medina F, Collins S, Wicker RB (2012) Comparison of microstructures and mechanical properties for solid and mesh Cobalt-base alloy prototypes fabricated by electron beam melting. Metall Mater Trans A 41:3216–3227
28. Sun SH, Koizumi Y, Kurosu S, Li YP, Matsumoto H, Chiba A (2014) Build direction dependence of microstructure and high-temperature tensile property of Co–Cr–Mo alloy fabricated by electron beam melting. Acta Mater 64:154–168
29. Christensen A, Kircher R, Lippincott A (2008) Qualification of electron beam melted (EBM) Ti6AI4V-ELI for orthopaedic applications. Medical device materials IV: proceedings of the materials and processes for medical devices conference. ASM International, pp 48–53
30. Chahine G, Koike M, Okabe T, Smith P, Kovacevic R (2008) The design and production of Ti–6Al–4V ELI customized dental implants. JOM 60:50–55
31. Murr LE, Quinones SA, Gaytan SM, Lopez MI, Rodela A, Martinez EY, Hernandez DH, Martinez E, Medina F, Wicker RB (2009) Microstructure and mechanical behavior of Ti–6Al–4V produced by rapid-layer manufacturing, for biomedical applications. J Mech Behav Biomed Mater 2:20–32
32. Okazaki Y, Ito Y, Kyo K, Tateishi T (1996) Corrosion resistance and corrosion fatigue strength of new titanium alloys for medical implants without V and Al. Mater Sci Eng A 213:138–147
33. Kuroda D, Niinomi M, Morinaga M, Kato Y, Yoshihiro T (1998) Design and mechanical properties of new β type titanium alloys for implant materials. Mater Sci Eng A 243:244–249
34. Okazaki Y, Gotoh E, Nakada H, Kobayashi K (2005) Mechanical property, fatigue strength and clinical trial of dental cast Ti-15Zr-4Nb-4Ta alloy. Mater Trans 46:1545–1550
35. Okazaki Y, Rao S, Ito Y, Tateishi T (1998) Corrosion resistance mechanical properties corrosion fatigue strength and cytocompatibility of new Ti alloys without Al and V. Biomaterials 19:1197–1215
36. Sugino A, Ohtsuki C, Tsuru K, Hayakawa S, Nakano T, Okazaki Y, Osaka A (2009) Effect of spatial design and thermal oxidation on apatite formation on Ti-15Zr-4Ta-4Nb alloy. Acta Biomater 5:298–304
37. Fukuda F, Takahashi H, Kuramoto K, Okazaki Y, Yoshikawa H, Nakano T (2012) Fabrication and clarification of fatigue properties of nontoxic Ti-15Zr-4Nb-4Ta alloy products by electron beam melting method for biomedical application. Jpn J Clin Biom 33:257–264
38. Rho JY, Tsui TY, Pharr GM (1997) Elastic properties of human cortical and trabecular lamellar bone measured by nanoindentation. Biomaterials 18:1325–1330
39. Li C, Granger C, Schutte HD Jr, Biggers SB Jr, Kennedy JM, Latour RA Jr (2002) Progressive failure analysis of laminated composite femoral prostheses for total hip arthroplasty. Biomaterials 23:4249–4262
40. Cheal E, Spector M, Hayes W (1992) Role of loads and prosthesis material properties on the mechanics of the proximal femur after total hip arthroplasty. J Orthop Res 10:405–422
41. Bobyn JD, Glassman AH, Goto H, Krygier J, Miller JBrooks C (1990) The effect of stem stiffness on femoral bone resorption after canine porous-coated total hip arthroplasty. Clin Orthop Relat Res 261:196–213

42. Niinomi M, Nakai M, Hieda J (2012) Development of new metallic alloys for biomedical applications. Acta Biomater 8:3888–3903
43. Hao Y, Li S, Sun S, Zheng C, Fu Q, Yang R (2005) Super-elastic titanium alloy with unstable plastic deformation. Appl Phys Lett 87:091906–1
44. MacAdam GD (1951) Some relations of powder characteristics to the elastic modulus and shrinkage of sintered ferrous compacts. J Iron Steel Inst 168:346–358
45. Nomura N, Kohama T, Oh IH, Hanada S, Chiba A, Kanehira M, Sasaki K (2005) Mechanical properties of porous Ti–15Mo–5Zr–3Al compacts prepared by powder sintering. Mater Sci Eng C 25:330–335
46. Bram M, Stiller C, Buchkremer HP, Stöver D, Baur H (2000) High-porosity Titanium, stainless steel, and superalloy parts. Adv Eng Mater 2:196–199
47. Nakano T, Kan T, Ishimoto T, Ohashi Y, Fujitani W, Umakoshi Y, Hattori T, Higuchi Y, Tane M, Nakajima H (2006) Evaluation of bone quality near metallic implants with and without lotus-type pores for optimal biomaterial design. Mater Trans 47:2233–2239
48. Murr LE, Gaytan SM, Medina F, Martinez E, Martinez JL, Hernandez DH, Machado BI, Ramirez DA, Wicker RB (2010) Characterization of Ti–6Al–4V open cellular foams fabricated by additive manufacturing using electron beam melting. Mater Sci Eng 527:1861–1868
49. Van Bael S, Chai YC, Truscello S, Moesen M, Kerckhofs G, Van Oosterwyck H, Kruth JP, Schrooten J (2012) The effect of pore geometry on the in vitro biological behavior of human periosteum-derived cells seeded on selective laser-melted Ti6Al4V bone scaffolds. Acta Biomater 8:2824–2834
50. Pattanayak DK, Fukuda A, Matsushita T, Takemoto M, Fujibayashi S, Sasaki K, Nishida N, Nakamura T, Kokubo T (2011) Bioactive Ti metal analogous to human cancellous bone: fabrication by selective laser melting and chemical treatments. Acta Biomater 7:1398–1406
51. Barbas A, Bonnet AS, Lipinski P, Pesci R, Dubois G (2012) Development and mechanical characterization of porous titanium bone substitutes. J Mech Behav Biomed Mater 9:34–44
52. Nakano T, Fujitani W, Ishimoto T, Lee JW, Ikeo N, Fukuda H, Kuramoto K (2011) Formation of new bone with preferentially oriented biological apatite crystals using a novel cylindrical implant containing anisotropic open pores fabricated by the electron beam melting (EBM) method. ISIJ Int 51:262–268
53. Zhang LC, Klemm D, Eckert J, Hao YL, Sercombe TB (2011) Manufacture by selective laser melting and mechanical behavior of a biomedical Ti–24Nb–4Zr–8Sn alloy. Scr Mater 65:21–24
54. Brånemark PI, Hansson BO, Adell R, Breine U, Lindström J, Hallén O, Öhman A (1977) Osseointegrated implants in the treatment of the edentulous jaw. Experience from a 10-year period. Scand J Plast Reconstr Surg Suppl 16:1–132
55. Narushima T (2008) Surface modification for improving biocompatibility of titanium materials with bone. J JILM 58:577–582
56. Klein CPAT, Patka P, Wolke JGC, Blieck-Hogervorst JMA, Groot K (1994) Long-term in vivo study of plasma-sprayed coatings on titanium alloys of tetracalcium phosphate, hydroxyapatite and α-tricalcium phosphate. Biomaterials 15:146–150
57. Kokubo T, Miyaji F, Kim HM, Nakamura T (1996) Spontaneous formation of bonelike apatite layer on chemically treated titanium metals. J Am Ceram Soc 79:1127–1129
58. Ikeda M, Komatsu S, Sugimoto T, Hasegawa M (1998) Effect of two phase warm rolling on aging behavior and mechanical properties of Ti–15Mo–5Zr–3Al alloy. Mater Sci Eng A 243:140–145
59. Bruntte DM, Tengval P, Textor M, Thomsen P (2001) Titanium in medicine. Springer, Berlin, pp 361–374
60. Schroeder A, Zypen EV, Stich H (1981) ShutterF. J Max-Fac Surg 9:15–25
61. Davis JR (2003) Handbook of materials for medical device. ASM International, Materials Park, 183

62. Akhavan S, Matthiesen MM, Schulte L, Penoyar T, Kraay MJ, Rimnac CM, Goldberg VM (2006) Clinical and histologic results related to a low-modulus composite total hip replacement stem. J Bone Joint Surg 88:1308–1314
63. Heinl P, Müller L, Körner C, Singer RF, Müller FA (2008) Cellular Ti–6Al–4V structures with interconnected macro porosity for bone implants fabricated by selective electron beam melting. Acta Biomater 4:1536–1544

Chapter 2
Metal Injection Molding (MIM) Processing

Hideshi Miura, Toshiko Osada, and Yoshinori Itoh

Abstract Complex-shaped components can be obtained by net or near-net shaping through the powder metallurgy processing route such as metal injection molding (MIM) process. MIM is an advanced powder processing technique for the mass production of complex-shaped components. This technology also reduces the material used for production and processing cost. Sintered compacts obtained by MIM process show high density over 95 % and excellent mechanical properties. Titanium and its alloys are used in biomedical applications because of their excellent characteristics such as high specific strength, corrosion resistance, biocompatibility, and so on. MIM process is a suitable technique for titanium and its alloys to reduce the processing cost and material cost. In this chapter, tensile and fatigue properties of MIM compacts fabricated with Ti, Ti-6Al-4V, Ti-6Al-4V-4Cr, and Ti-6Al-7Nb are reviewed.

Keywords MIM process • Net shape • Tensile strength • Fatigue limit • Microstructure • Oxygen content • Titanium alloys

2.1   Introduction

Metal injection molding (MIM) combines the most useful characteristics of powder metallurgy (PM) and plastic injection molding to facilitate the production of small, complex-shaped metal components with outstanding mechanical properties.

Injection molding is a productive and widely used technique for shaping plastics. Alternatively, metals have advantages over polymers in mechanical properties and electrical and thermal conductivity. PM also has advantages such as easy alloying by powders and recycle ability. MIM uses the metal powder and binder plastics; thus, this is a combined process of injection molding and PM.

H. Miura (✉) • T. Osada
Department of Mechanical Engineering, Kyushu University, 744 Motooka, Nishi-ku, Fukuoka 819-0395, Japan
e-mail: miura@mech.kyushu-u.ac.jp

Y. Itoh
Hamamatsu Industrial Research Institute of Shizuoka Prefecture, 1-3-3, Shinmiyakoda, Kita-ku, Hamamatsu, Shizuoka 431-2103, Japan

This chapter introduces the MIM process and provides the tensile and fatigue properties of various injection molded titanium alloy compacts.

2.2 Metal Injection Molding

2.2.1 MIM Process

Metal injection molding (MIM) is an advanced manufacturing technology that uses the shaping advantage of injection molding process to be applied to metal. The process has ability to produce the high degree of geometrical complexity of the component with high properties. Because of high final density, often near theoretical density, the MIM products exhibit excellent properties. MIM process is applicable for most of common engineering metals such as carbon steel, stainless steel, tungsten, nickel-based alloys, titanium alloys, etc. Figure 2.1 shows the advantages of the MIM process [1]. MIM has been demonstrated to be a cost-effective manufacturing process of small components (typically less than 50 g for titanium alloys), complex-shaped parts with high production volume, as it can be seen in Fig. 2.2.

The principle of the MIM process is illustrated in Fig. 2.3. Initially, powder and thermoplastic binder are mixed and kneaded in order to obtain the feedstock. This feedstock is heated and injected into a mold using a conventional injection molding machine. After the injection process, the binder is removed by heating, chemical extraction, or catalytic reaction, and then this is followed by sintering process to produce the final parts. The binder removal process is called the debinding process.

The purpose of sintering is to densify the powder and to remove most of the void space left by the binders. Usually the shrinkage during sintering is in the range between 12 and 18 %; therefore, the mold is oversized to meet the required dimension. The MIM component has tolerance ranging from ± 0.05 to ± 0.3 %.
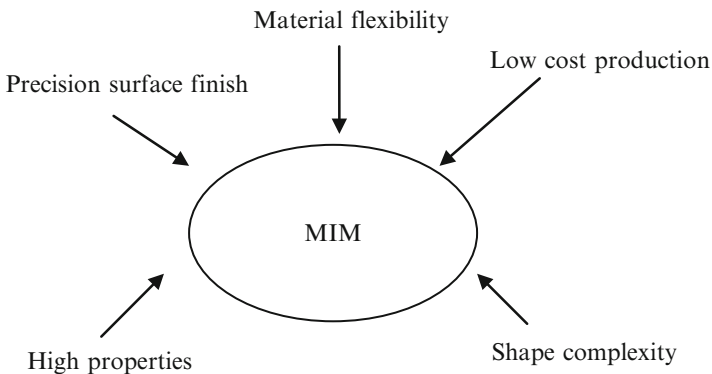

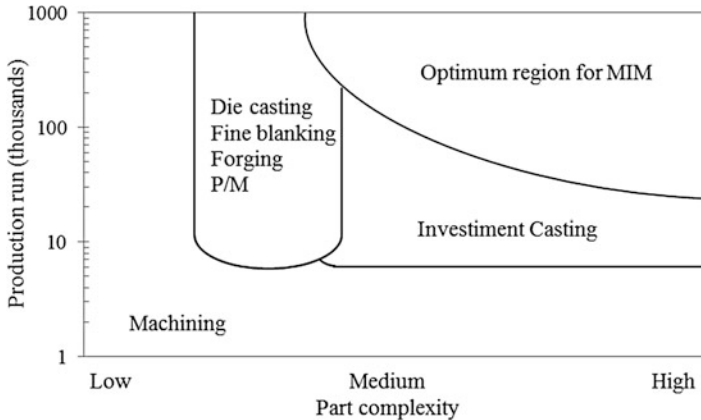**Fig. 2.1** The advantages of MIM process (Redrawn from Ref. [1])

Fig. 2.2 MIM is suited to complex-shaped parts with high production volume (Redrawn from Ref. [1])

After sintering process, the secondary operations such as grinding, machining, and drilling can be omitted. However, it depends on the accuracy of the product. For the mechanical parts, which need tighter tolerance, an approach to achieve tighter tolerance is to machine the critical surface after sintering. Hence, it is only applied for critical features. Surface roughness depends on the tools and also powder size. After sintering process, the sand blasting process can be done to reduce the surface roughness.

Another point is in the MIM process; the feedstock material can be recycled nearly 100 %. This will be beneficial for cost reduction, especially for the expensive materials. The total cost of binders, mold, debinding, and sintering process can be reduced by increasing the amount of production. In other words, the low cost of MIM process is suitable for the mass production. The summary of this section is that, with the capability of producing complex-shaped component with high properties at low cost, MIM process is expected to be one of the suitable processes to fabricate complex biomedical parts.

2.2.2 Biomedical Applications

MIM is suitable for the fabrication of small and complex-shaped parts; thus, several parts for medical applications were produced. Figure 2.4 shows the examples of biomedical components [3–7]. Those are fabricated from stainless steel, Ti alloy, and so on.

MIM is a very clean process compared to conventional manufacturing technologies. Only the possible binder residuals could represent potential candidates as
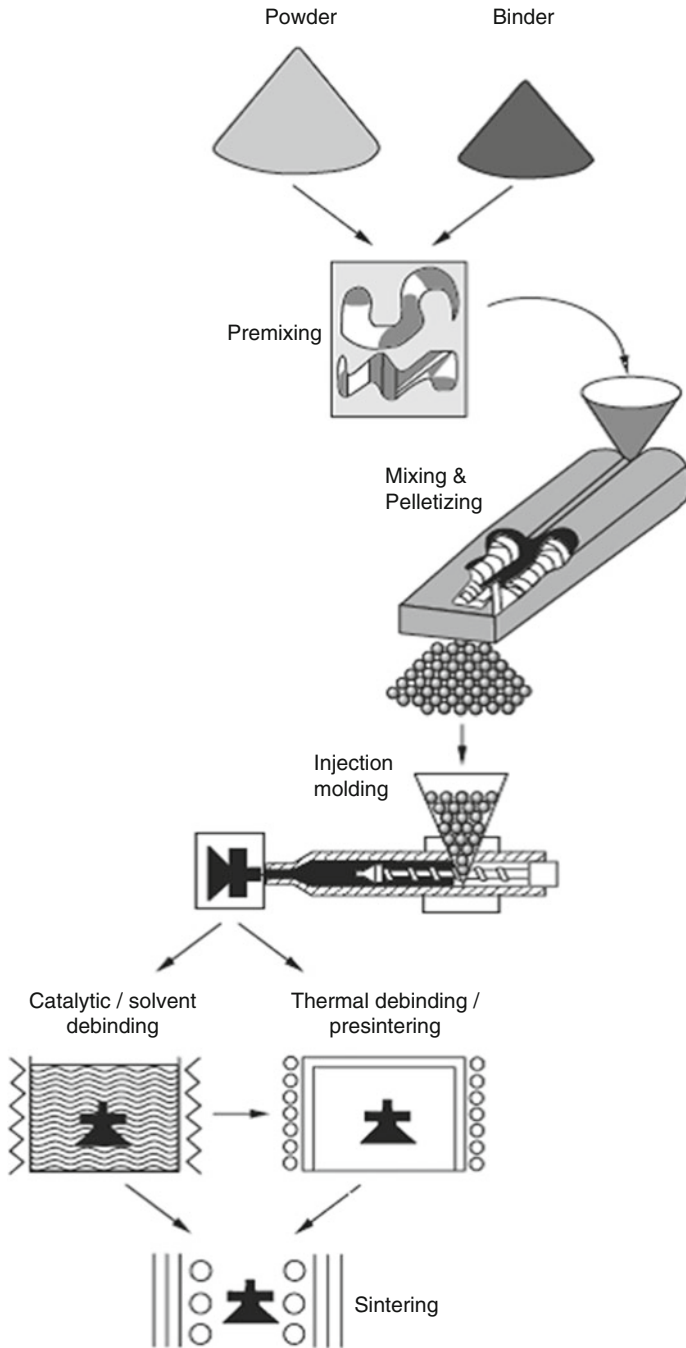
Fig. 2.3 Schematic diagram of MIM process (Reproduced with permission from Ref. [2]. Copyright 1996, Uchida Rokakuho Publishing Co., Ltd.)

Fig. 2.4 MIM products for biomedical applications. (**a**) Orthodontic parts, SUS630, Ti, Al$_2$O$_3$; (**b**) surgical scalpel holder, SUS630; (**c**) fracture fixation plate, SUS316L; (**d**) heart valve, titanium; (**e**) an implant pump, Ti-6Al-4V; (**f**) dental implant, titanium

toxic substances [8]. It is a good start to use exclusively nontoxic biocompatible binder components. Even if the single binder constituents may be harmless, such as paraffin or polyethylene, decomposition at high temperature could generally lead to new toxic substances. However, these substances would be trapped in pores after sintering and would cover the surface. In the first instance, they would have no contact with the body, and in the latter case, they could be removed if necessary. In the end, appropriate tests of the sintered components have to prove this.

MIM for the fabrication of medical implants is also interesting because of the possibility of generating porous components. These are beneficial with regard to

tissue ingrowth. Porosity and pore diameter could be easily controlled. Figure 2.4f shows the implant that has a dense layer covered by a porous layer.

2.2.3   Titanium Alloys Fabricated by MIM

Ti and its alloys show excellent characteristics of low density, high strength, and high biocompatibility, leading to their widespread use for various industrial and biomedical applications. However, they show poor workability, so it is difficult to use them to produce parts with complicated shapes at low processing cost. Therefore, MIM process is a suitable technique for fabricating the complex-shaped parts to reduce the processing cost and material cost. Ti-6Al-4V is well known as the most widely used Ti-based alloy. Meanwhile, MIM can be used to produce various types of Ti alloys using mixed powders [8, 9].

As shown in Fig. 2.4, MIM is favored by a large number of small complex parts. Cosmetic parts had been successfully made from CP Ti powder, but for the structural applications, the oxygen level is still high especially for Ti-6Al-4V alloy. Nowadays, the oxygen content of Ti-6Al-4V products can be controlled to about 0.2 mass% with low oxygen level of starting powders, development of binders, and sintering facilities. This development promises a significant expansion of the titanium MIM marketplace into aerospace, automobiles, surgical instruments, dentistry, and so on.

2.3   Static Mechanical Properties of Ti Alloys Fabricated by MIM

In this section, the properties of injection molded Ti-6Al-4V alloy compacts using alloy powders and various mixed powders were investigated comprehensively to clarify the effect of oxygen content and relative density on the tensile properties.

On the other hand, Ti-6Al-7Nb alloy has been developed for more suitable biomaterial in place of Ti-6Al-4V alloy, because the vanadium (V) is toxic to the human body. There are few reports about MIM Ti-6Al-7Nb alloy, though the cost of starting material powder seems to be expensive because of not using a commercially available powder of gas-atomized Ti-6Al-7Nb alloy powder [10] or Al-53.8Nb pre-alloyed powder [11].

In this section, the metal injection molding process of Ti-6Al-7Nb alloy using an alloy powder and three types of mixed powders, which consisted of commercially available powders, is reviewed. The effects of powders and sintering conditions on the microstructure, relative density, and mechanical properties of injection molded compacts were mainly investigated.

Table 2.1 Chemical composition and mean particle diameter of the powders

		Chemical composition (mass%)					
		Al	V	Fe	O	C	Particle diameter (µm)
Ti		–	–	0.044	0.130	0.008	24.4
Ti-6Al-4V		5.75	4.13	0.017	0.100	0.004	26.1
TiH$_2$		–	–	0.03	0.170	–	15.0
Al-40 V	Fine	Bal.	41.0	0.24	0.47	0.02	6.4
	Coarse	Bal.	39.7	0.33	0.20	0.01	20.0
	Atomized	59.5	Bal.	0.13	0.12	0.02	26.0

2.3.1   Effect of Oxygen Content in Ti-6Al-4V Compacts

2.3.1.1   Experimental Procedures

A gas-atomized pure Ti powder (TILOP-45, Osaka Titanium Technologies Co., Ltd.), ground TiH$_2$ powder with a different particle diameter and shape (TCH452, Toho Titanium Co., Ltd., etc.), two types of ground Al-40V alloy powders with different particle diameters (VAL-3, Nippon Denko Co., Ltd.), gas-atomized Al-40V alloy powder (60Al-40V, Daido Steel Co., Ltd.), and three types of Ti-6Al-4V alloy powders with different particle diameters and oxygen contents (TILOP64-45, Osaka Titanium Technologies Co., Ltd., etc.) were used in the experiment. The chemical compositions, particle diameter, and scanning electron microscope (SEM) images of these powders are shown in Table 2.1 and Fig. 2.5. The TiH$_2$ powder is more cost-effective compared with gas-atomized Ti powder, which should reduce raw material costs [12]. The fine Al-40V powder shows higher oxygen content than the other Al-40V powders.

The pure Ti powder, TiH$_2$ powder, and Al-40V alloy powder were weighed to obtain the chemical composition of Ti-6Al-4V and then were premixed for 3.6 ks by rotating in an argon gas-filled pot mill. The mixtures of Ti-6Al-4V alloy powder were then kneaded with binder [13] (which contained polypropylene, polymethyl methacrylate, paraffin wax, and stearic acid in a weight ratio of 30:40:29:1) using a pressure-type kneading machine (Moriyama Co., Ltd., DV1-5GHH-E) at 443 K for 8.1 ks. The binder loading was 35 vol%, and it increased with increasing TiH$_2$ powder content because of its irregular shape and low density. The compounds obtained were crushed and screened from 2 to 8 mm diameter to prepare feedstocks for injection molding. The feedstocks were then injection molded by injection molding machine (Nissei Plastic Industrial Co., Ltd., ST20S2V) to produce tensile test specimens with a length of 75 mm, a width of 5 mm, and a thickness of 2 mm. After injection molding, solvent extraction debinding was conducted at 343 K for 21.3 ks in *n*-hexane [13] to partially remove the wax and polymethyl methacrylate. By this treatment, the contamination of sintered compacts by carbon derived from the binder system was reduced. Following this treatment, thermal debinding was performed from room temperature to 703 K in reduced pressure under argon gas flow. Continuous sintering was performed in high vacuum (in the order of below 10^{-2} Pa) at various temperatures for 3.6 to 28.8 ks, followed by furnace cooling to
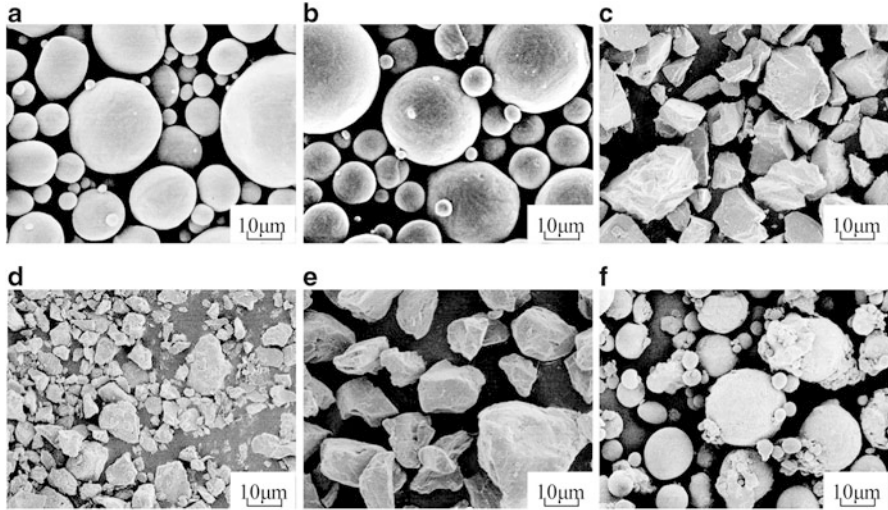
Fig. 2.5 SEM images of (**a**) titanium powder, (**b**) Ti-6Al-4V alloy powder, (**c**) titanium hydride (TiH$_2$) powder, (**d**) fine Al-40V alloy powder, (**e**) coarse Al-40V alloy powder, and (**f**) atomized Al-40V powder

room temperature in high vacuum (in the order of below 10^{-3} Pa). The vacuum furnace (Shimadzu Mectem Inc., PVSGgr20/20) has both its heater elements and vessel made from graphite. The compacts were set on yttria or zirconia substrates in an inner vessel made from molybdenum or zirconia, and the compacts were surrounded by a spongelike Ti powder to prevent their carburization and oxidation.

The relative densities and tensile properties were measured on as-sintered compacts. The density of sintered compacts was measured by the Archimedean method with an automatic densimeter (Toyo Seiki Seisaku-Sho, Ltd., DENSIMETER H), and the relative density was calculated against the full density of Ti-6Al-4V alloy (4.42 Mg/m^3). The tensile testing (in triplicate) was conducted using a universal testing instrument (Shimadzu Corp., AG-50kNIS) with an extensometer gauge length of 25 mm and crosshead speed of 8.33×10^{-5} m/s in air at room temperature. The oxygen content was determined by means of Oxygen/Nitrogen analyzer (Horiba, Ltd., EMGA-520).

2.4 Results and Discussion

Table 2.2 shows the typical properties of sintered Ti-6Al-4V alloy compacts discussed in this section. For details of these properties, refer to previous papers [12, 14–18].

The relative density of the compacts using a mixture of Ti, TiH$_2$, and Al-40V alloy powders increased with increasing TiH$_2$ content. At the same time, the

Table 2.2 Characteristic properties of sintered Ti-6Al-4V alloy compacts

Powder	Sintering condition	Vessel/ substrate	Relative density	Tensile strength	Elongation (%)	Oxygen content (%)
Ti, TiH$_2$, and coarse Al-40 V	1,373 K X 28.8 ks	Mo/ Y$_2$O$_3$	98.3	990	4.9	0.41
		ZrO$_2$/ ZrO$_2$	98.5	930	15.8	0.35
Ti and fine Al-40v	1,473 K X 28.8 ks	Mo/ ZrO$_2$	98.5	890	9.6	0.35
		ZrO$_2$/ ZrO$_2$	97.7	880	14.5	0.27
Ti and coarse Al-40v	1,373 K X 28.8 ks	Mo/ Y$_2$O$_3$	98.4	820	13.7	0.24
Ti and atomized Al-40 V	1,473 K X 14.4 ks		96.7	790	12.3	0.20
Ti-6Al-4V ELI	1,423 K X 28.8 ks		96.4	760	11.0	0.18

powder loading of compacts decreased with increasing TiH$_2$ content because more binder was required to obtain enough flowability in the feedstock for injection molding. The tensile strength and oxygen content of the compacts using a mixture of Ti, TiH$_2$, and Al-40V alloy powders increased with increasing TiH$_2$ content. On the other hand, the elongation of the compacts using a mixture of Ti, TiH$_2$, and Al-40V alloy powders reduced drastically with increasing TiH$_2$ content [12].

The sintered compacts using a mixture of Ti and fine irregular Al-40V alloy powder showed the highest density, and the compacts using a mixture of Ti and coarse, irregular Al-40V alloy powder showed slightly higher density than the compacts using a mixture of Ti and spherical atomized Al-40V alloy powder. The sintered compacts using a mixture of Ti and fine irregular Al-40V alloy powder, which had the highest oxygen content compared with other Al-40V alloy powders, showed high oxygen content [14, 18]. Furthermore, the molybdenum vessel and yttria substrate could be effective to oxidation of the compacts from sintering atmosphere [15], which resulted in enough ductility, even for the prolonged sintering time at high sintering temperature to obtain high density.

The sintered compacts using Ti-6Al-4V alloy powders showed slightly lower relative density compared with the compacts using mixed powders, and their tensile properties were slightly low [16]. However, they were improved by prolonged sintering time and higher sintering temperature or using a small particle size powder [17]. The oxygen content of the sintered compacts using a Ti-6Al-4V ELI (extra-low interstitial) powder reached below 0.2 mass% as shown in Table 2.1 and Table 2.2.

The relative density and oxygen content of the compacts in our previous studies cover a wide range from 90 to 99.8 % and 0.18 to 0.85 mass% O, respectively. As shown in Table 2.2, there is a tendency for the tensile strength of sintered compact to decrease with increasing oxygen content.

Fig. 2.6 Effect of oxygen content on the elongation of Ti-6Al-4V alloy compacts sintered under various conditions with various mixed or Ti-6Al-4V alloy powders
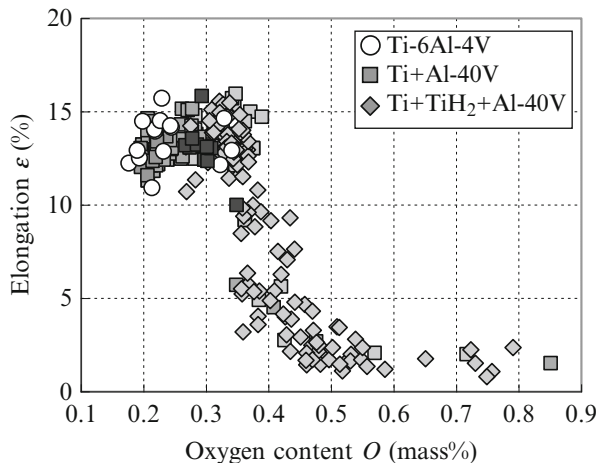

Figure 2.6 shows the effect of oxygen content on the elongation of sintered Ti-6Al-4V alloy compacts using various mixed powders or Ti-6Al-4V alloy powder. The tensile properties of the compacts with relative density below 94.5 % were excluded because of their poor properties and large fluctuation. The elongation of the compacts using any mixed powder or Ti-6Al-4V alloy powder and also any sintering conditions shows the excellent values, in excess of 10 %, when the oxygen content of the sintered compacts is below 0.35 mass%. However, the elongation of the sintered compacts is reduced dramatically if the oxygen content exceeds 0.35 mass%.

Figure 2.7 shows the effect of oxygen content on the elongation of sintered Ti-6Al-4V alloy compacts as a function of relative density for the oxygen content range from 0.1 to 0.35 mass%. The solid line shows the effect of oxygen content on the elongation of sintered Ti-6Al-4V alloy compacts which have relative densities from 97.5 to 98.5 %, as an approximated line. The oxygen content of sintered Ti-6AI-4V alloy compacts has little influence on the elongation when the sintered compacts have ductility greater than 10 % elongation. In addition, the relative density of sintered Ti-6Al-4V alloy compacts has very little influence on the elongation form the result of approximated line calculated for each relative density range.

Figure 2.8 shows the effect of oxygen content on the tensile strength of sintered Ti-6Al-4V alloy compacts using various mixtures of Ti-6Al-4V alloy powder. The tensile strength of the compacts using any mixed powder or Ti-6Al-4V alloy powder and also any sintering condition increases from approximately 800 to 1,000 MPa with increasing oxygen content below 0.5 mass%, but they are drastically reduced from the oxygen content above 0.5 mass%.

Figure 2.9 shows the effect of oxygen content on the tensile strength of sintered Ti-6Al-4V alloy compacts as a function of relative density in the oxygen content range from 0.1 to 0.5 mass%. The solid line and light solid line show the effect of oxygen content on the tensile strength of sintered Ti-6Al-4V alloy compacts with relative densities from 98.5 to 99.5 % and from 94.5 to 95.5 % as an approximated line, respectively. From the difference among each line, the tensile strength of sintered Ti-6Al-4V alloy compacts is improved by 40 MPa with increasing 4 % of

Fig. 2.7 The relationship between the oxygen content under 0.35 mass% and the elongation of Ti-6Al-4V alloy compacts sintered by various conditions with various mixed or Ti-6Al-4V alloy powders
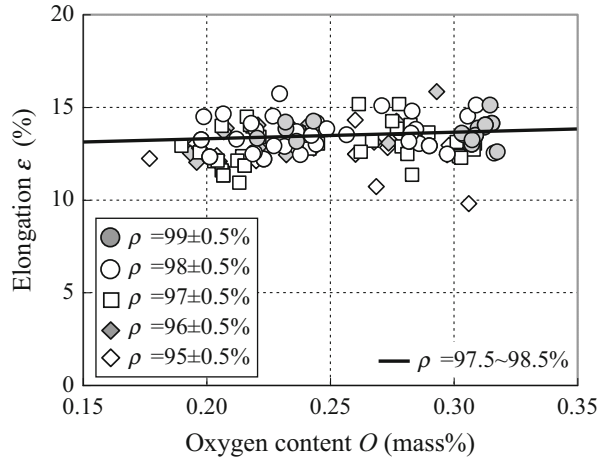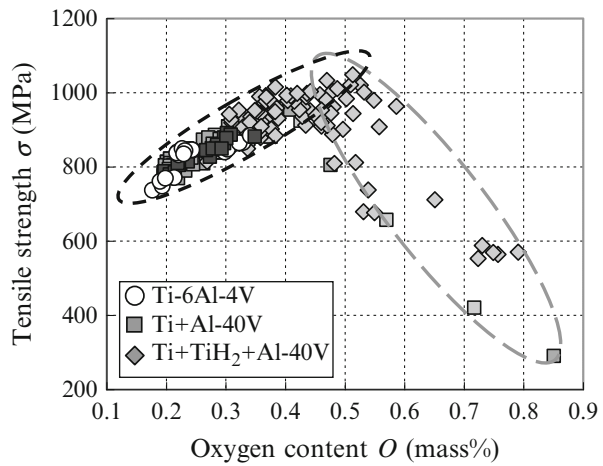

Fig. 2.8 Effect of oxygen content on the tensile strength of Ti-6Al-4V alloy compacts sintered by various conditions with various mixed or Ti-6Al-4V alloy powders

relative density. Furthermore, from the slope of each line, the tensile strength of sintered Ti-6Al-4V alloy compacts is improved by 70 MPa with each increasing 0.1 mass% O. In other words, it was found that the tensile strength of sintered Ti-6Al-4V alloy compacts is greatly affected by oxygen content and relative density of the compacts. From these results, the tensile strength (σ) of sintered Ti-6Al-4V alloy compacts shows an excellent correlation with oxygen content (O) and relative density (ρ) as shown in the following experimental Eq. (2.1):

$$\sigma(MPa) = 700O(\text{mass}\%) + 10\rho(\%) - 315$$
$$(\text{Provided that } O < 0.5 \text{ mass}\% \text{ and } \rho > 94.5 \%) \tag{2.1}$$

To confirm the viability of experimental Eq. (2.1), the comparison was made between calculated tensile strength and experimental values. Figure 2.10 shows the effect of relative density and oxygen content on the tensile strength of Ti-6Al-4V

Fig. 2.9 The relationship
between the oxygen content
and the tensile strength of
Ti-6Al-4V alloy compacts
sintered under various
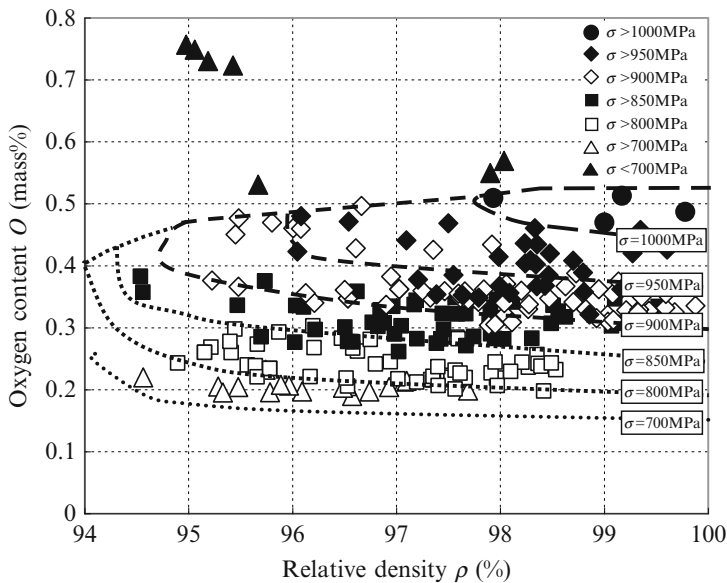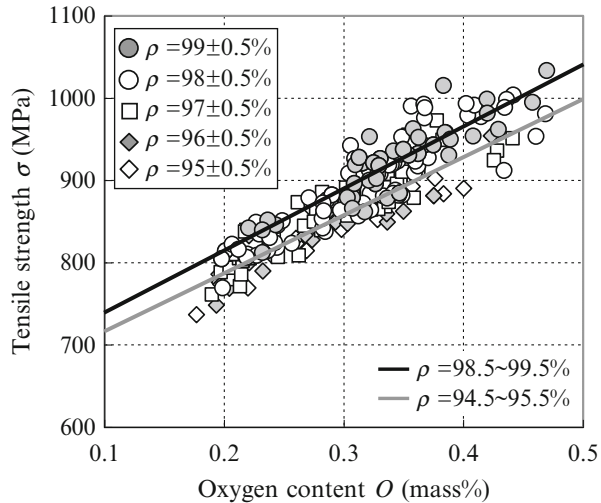conditions with various
mixed or Ti-6Al-4V alloy
powders

Fig. 2.10 Effect of the relative density and oxygen content on the tensile strength of Ti-6Al-4V alloy compacts sintered under various conditions with various mixed or Ti-6Al-4V alloy powders

alloy compacts sintered under various conditions with various mixed or Ti-6Al-4V alloy powders by plotting each experimental value and approximate contour lines. The highest strength sintered compacts are shown in the region of high oxygen and high relative density.
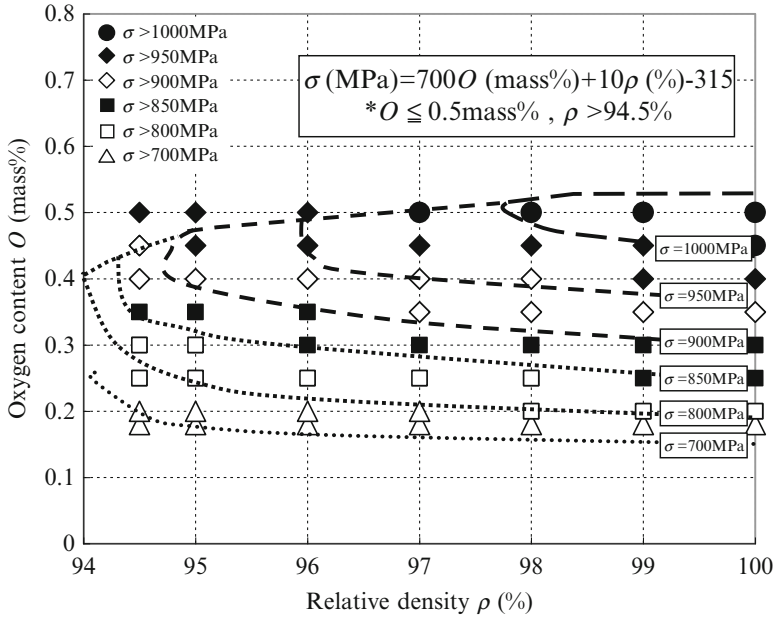
Fig. 2.11 The relationship between the calculated values and the experimental curved lines for tensile strength of sintered Ti-6Al-4V alloy compacts as a function of relative density and oxygen content

Figure 2.11 shows the relationship between calculated values and experimental contours (shown in Fig. 2.10) of tensile strength of sintered Ti-6Al-4V alloy compacts as a function of relative density and oxygen content (provided that oxygen is in the range 0.18–0.5 mass% and relative densities are in the range 94.5–100 %). The calculated values of tensile strength are in fair agreement with the experimental curved line. Thus, the correlation between the tensile strength of sintered Ti-6Al-4V alloy compacts and oxygen content and relative density can be expressed by the experimental Eq. (2.1).

2.4.1 Ti-6Al-7Nb

2.4.1.1 Experimental Procedure

Gas-atomized Ti-6Al-7Nb alloy and pure Ti (from Sumitomo Titanium Corp.), Nb (from Kojundo Chemical Laboratory Co., Ltd.), Ti-Al alloy (Ti-35.7Al, from KCM Corp.), Al-Nb alloy (Al-53.8Nb), and two types of Al powders with different particle diameters (from Minalco Co., Ltd.) were used. The chemical compositions and particle diameter of those powders are shown in Table 2.3, and a scanning electron microscope (SEM) image of Ti-6Al-7Nb alloy powder is shown in

Table 2.3 Chemical compositions and particle diameter of the powders used

Powder		Composition (mass%)			Particle diameter (μm)
		O	C	Fe	
Ti		0.140	0.008	0.044	<45
Al	Coarse	–	–	0.130	<45
	Fine	–	–	0.140	<10
Nb		–	–	0.004	<45
Ti-35.7Al		0.620	–	0.015	<45
Al-53.8Nb		0.064	0.024	–	<45
Ti-6Al-7Nb		0.157	0.023	0.083	<45

Fig. 2.12 SEM image of Ti-6Al-7Nb alloy powder
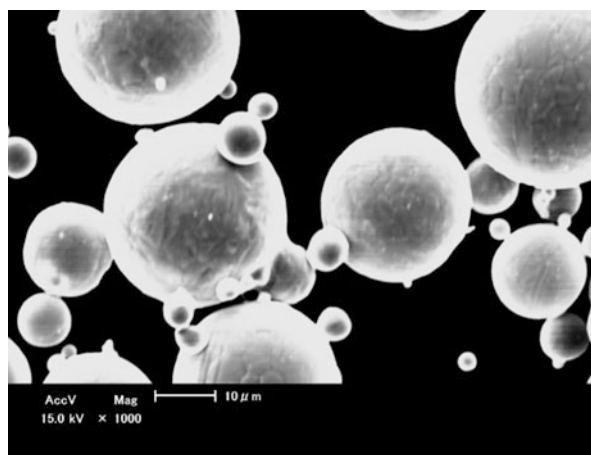
Fig. 2.12. The Ti-Al alloy powder shows higher oxygen content than Ti powder. Those powders were weighed to obtain the chemical compositions of Ti-6Al-7Nb and were premixed for 3.6 ks by pot mill rotator with argon gas-filled polyethylene pot. The powder mixtures were then kneaded with binder (which contained polypropylene, polymethyl methacrylate, paraffin wax, and stearic acid in a weight ratio of 30:40:29:1) by means of a pressure-type kneading machine (Moriyama Co., Ltd., DV1-5GHH-E) at 443 K for 8.1 ks. The powder loading was 65 vol.%. The compounds were molded by injection molding machine (Nissei Plastic Industrial Co., Ltd., ST20S2V) into compacts for tensile test specimen with a length of 75 mm, a width of 5 mm, and a thickness of 2 mm. After injection molding, the extraction debinding with vaporized solvent, which was conducted at 343 K for 21.3 ks in n-hexane, was used to partially remove the wax and polymethyl methacrylate. Following this treatment, thermal debinding was performed from room temperature to 703 K in reduced pressure with argon gas current, and continuous sintering was performed in vacuum (10^{-2} Pa order) at various temperatures for 14.4 ks, followed by furnace cooling. The vacuum furnace has both heater and vessel made from graphite, and the compacts were set on the yttria substrate in the Mo

vessel and were surrounded by a spongelike Ti powder. The relative density and tensile properties were measured on as-sintered compacts. The tensile test was conducted at a crosshead speed of 8.33×10^{-5} m/s in air at room temperature. The oxygen and carbon contents of sintered compacts were determined by means of Oxygen/Nitrogen analyzer (Horiba, Ltd., EMGA-520) and Carbon/Sulfur analyzer (Horiba, Ltd., EMIA-920 V). Microstructural observations of sintered compacts were conducted using an optical microscope. To determine the distribution of each element of sintered compacts, electron probe microanalysis was also performed.

2.4.1.2   Results and Discussion

Figure 2.13 shows the effect of sintering temperature on the relative density of Ti-6Al-7Nb compacts. The relative density of the compacts increases with increasing sintering temperature and reached up to 98 % and 97 % at 1350 °C, respectively, in contrast with 94 % for the compacts using a mixture of Ti, Nb, and coarse Al powders.

Figures 2.14 and 2.15 show the effect of sintering temperature on the oxygen and carbon contents of the Ti-6Al-7Nb alloy compacts. These values have sufficiently low level so that they do not have a detrimental effect on the mechanical properties of sintered compacts. The sintered compacts using a mixture of Ti, Nb, and Ti-Al powders have higher oxygen content derived from Ti-Al alloy powder, which suggests that there is difference in tensile properties between the sintered compacts using a mixture of Ti, Nb, and Ti-Al powders and using a mixture of Ti, Nb, and fine Al powders such as high tensile strength and low elongation.

The tensile properties of Ti-6Al-7Nb alloy compacts sintered at various temperatures are shown in Figs. 2.16 and 2.17. The tensile strength of all the compacts increases with increasing sintering temperature, but it remains nearly constant with increasing sintering temperature above 1,200 °C. The tensile strength of the

Fig. 2.13 Comparison of relative sintering density for sintered compacts using alloy and mixed powders
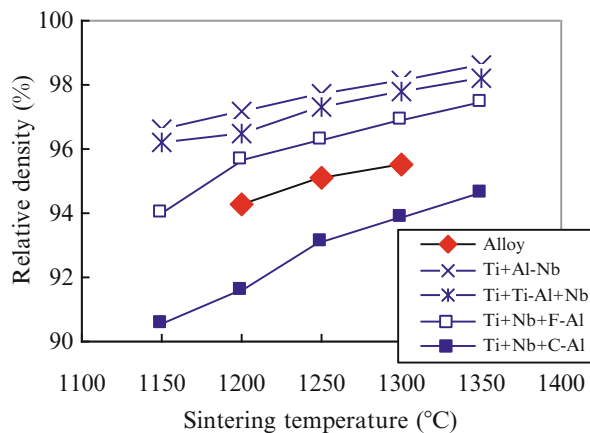
Fig. 2.14 Comparison of
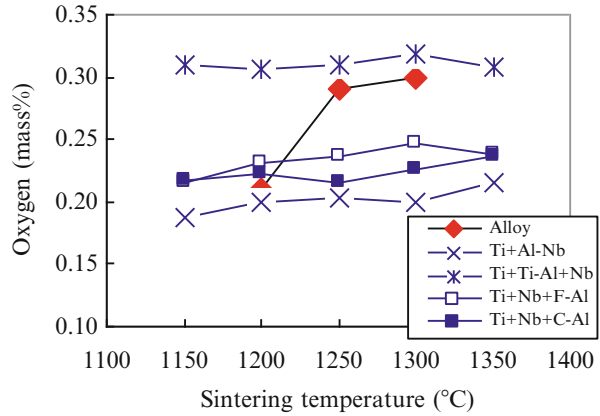oxygen content for sintered
compacts using alloy and
mixed powders

Fig. 2.15 Comparison of
carbon content for sintered
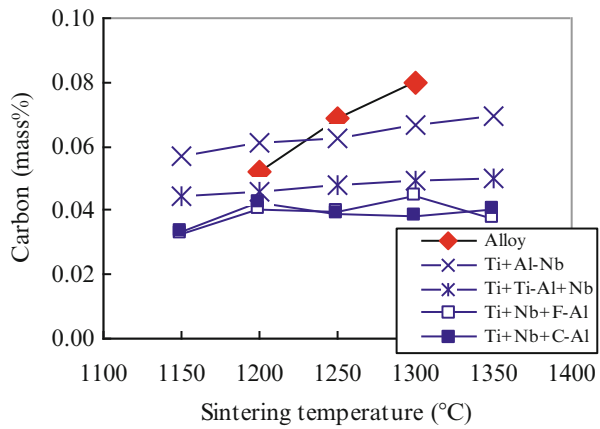compacts using alloy and
mixed powders

Fig. 2.16 Comparison of
tensile strength for sintered
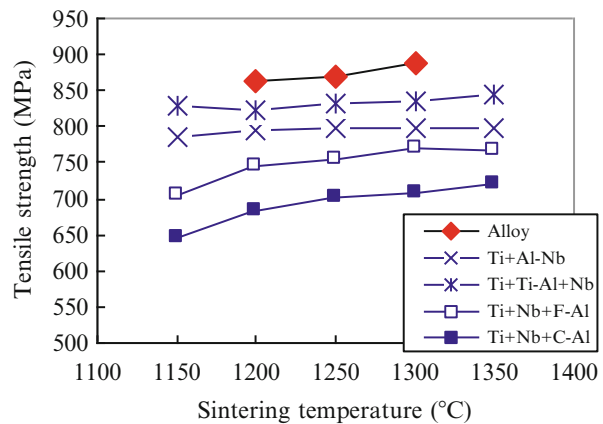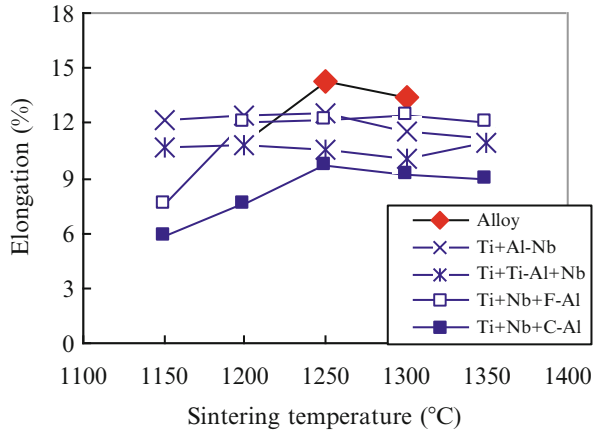compacts using alloy and
mixed powders

Fig. 2.17 Comparison of elongation for sintered compacts using alloy and mixed powders


compacts using alloy powder shows the highest value; however, a mixture of Ti, Nb, and coarse Al powders is lower than that of the compacts using other mixtures, even though it increases with increasing sintering temperature. The tensile strength of the compacts using alloy powders is about 100 MPa higher than that of the compacts using a mixture of Ti, Nb, and fine Al powders. Moreover, a compact using alloy powder shows high elongation of above 14 % at the sintering temperature of 1,250 °C.

Figure 2.18 shows the microstructures of Ti-6Al-7Nb alloy compacts sintered at various temperatures. The microstructures of all sintered compacts consist of acicular alpha and intergranular beta phases. The acicular alpha phases become longer and coarser with increasing sintering temperature, which means that the grain size of prior beta was so large for the compacts sintered above 1,250 °C. On the other hand, the sintered compacts using a mixture of Ti, Nb, and coarse Al powders showed many large pores in the microstructure at all sintering temperature. These pores are considered to be the result of the dissolution of Al particles during sintering steps, which also lead to low relative density and poor tensile properties. In the case of the sintered compacts using Ti, Nb, and fine Al powders, although the pores form by dissolution of Al particles during sintering steps similarly, the size of pores is smaller than that of the sintered compacts using a mixture of Ti, Nb, and coarse Al powders due to the small particle diameter of Al powder. Then, it is considered that the compacts using a mixture of Ti, Nb, and fine Al powders have high density and excellent tensile properties at high sintering temperature range.

The relative density, tensile strength, and elongation of the Ti-6Al-7Nb alloy compacts sintered at 1250 °C for 14.4 ks are 97 %, 850 MPa, and 14 %, respectively. These properties are comparable to those of the wrought materials.

Fig. 2.18 *SEM micrographs* of Ti-6Al-7Nb compact

1200 (°C)   0.1mm

1250 (°C)   0.1mm

1300 (°C)   0.1mm
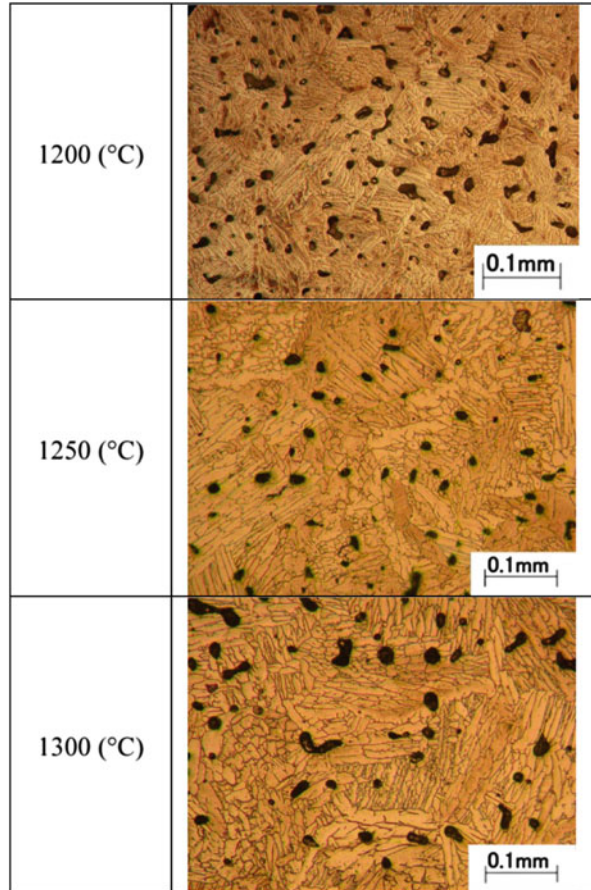
2.4.2 Summary

The metal injection molding process was applied to produce Ti-6Al-4V and Ti-6Al-7Nb alloy compacts. The sintered compacts show higher density over 95 %. It is important to reduce the oxygen content under 0.35 mass% because the elongation would dramatically decrease from that content.

On the other hand, sintered compacts using Ti-6Al-7Nb alloy powder show relatively higher mechanical properties than the compacts using mixed powder. Eventually, the compacts using alloy powder are improved to be 900 MPa of tensile strength with 15 % of elongation, which are comparable to the properties of wrought materials.

2.5   Fatigue Properties of Ti Alloys Fabricated by MIM

The static mechanical properties of injection molded titanium alloy compacts have been reported so far [19–21]; however, there are few reports regarding the dynamic fracture characteristics [22, 23]. As the dynamic fatigue behavior is of great importance in practical use, fatigue characteristics of injection molded Ti alloy compacts are reviewed.

Usually MIM compacts show higher than 95 % of theoretical density (TD) and sometimes near full density. This leads to higher mechanical properties comparable to wrought materials. However, retained pores (a few percentages) with effect as a notch could be the starting points of crack initiation and may decrease the fatigue limit. Recently hot isostatic pressing (HIP) to MIM compacts is conducted to achieve higher mechanical properties [24]. In order to improve the fatigue limit, HIP is also conducted to injection molded compacts.

Moreover, it has been reported that small additions of Cr or B to Ti alloys produce a reduction of grain size [25, 26] due to the pinning effects against grain growth. Also, certain heat treatments contribute to the grain refinement. Grain refinement is beneficial to the improvement of the tensile strength and ductility. Thus, grain refinement is also expected to improve the fatigue limit.

In this section, rotating bending fatigue characteristics of injection molded pure Ti, Ti-6Al-4V, and Cr or B-added Ti-6Al-4V compacts are investigated using HIP and heat treatment.

2.5.1   Materials

Metal powders used were pure titanium, Ti-6Al-4V alloy, Cr, and TiB_2 powders. Table 2.4 shows the characteristics of powders used. Ti-6Al-4V and Cr powders were mixed to form Ti-6Al-4V-4Cr. Also 0.1 mass% of TiB_2 powder was added to Ti-6Al-4V powder. The fabricated specimens were referred to as Ti, Ti64, Ti64Cr, and Ti64B.

Wax-based binders (paraffin wax 69 mass%, polypropylene 10 mass%, ethylene vinyl acetate 10 mass%, carnauba wax 10 mass %, and di-n-butyl phthalate 1 mass %) were used and mixed with each powder. Powder loading was 65 vol.%.

Table 2.4 Particle diameter and oxygen content of the powders used

Powder	Particle diameter (μm)	Oxygen (mass %)
Pure Ti	32.7	0.170
Ti-6Al-4V	33.0	0.115
Cr	9.90	0.450
TiB_2	1.28	1.000

Fig. 2.19 Geometry of rotating bending fatigue specimen in mm
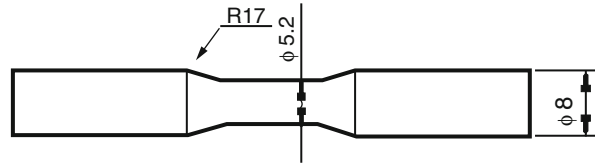
2.5.2 Fatigue Testing

Rotating bending fatigue specimens were prepared through an injection molding process. Specimen geometry of the mold is shown in Fig. 2.19. Before thermal debinding, solvent debinding was conducted in vaporous heptane at 58 °C for 4 h. Then the specimens were thermally debound at 600 °C for 2 h in argon and sintered at 1,150–1,350 °C for 2–8 h in high-vacuum atmosphere using a vacuum debinding and sintering furnace (Shimadzu Mectem Inc., Japan, VHSgr 20/20/20). Each specimen was named after the sintering temperature and time used, for example, 1,350–2 means being sintered at 1,350 °C for 2 h. Moreover, heat treatment was conducted for Ti64Cr specimens. Solution heat treatment was performed at 950 °C for 1 h followed by aging at 560 °C for 4 h. Furthermore, HIP (1,150 °C for 1 h) was conducted for Ti64Cr specimens to reduce porosity. For sintered specimens, density measurement, microstructure observation, oxygen and carbon content analysis, and rotating bending fatigue testing were performed.

2.5.3 Results and Discussion

2.5.3.1 Pure Ti

Figure 2.20 shows the relative density of as-sintered unalloyed Ti specimens. The sintered density increased with increasing sintering temperature and time.

Microstructures of the specimens are shown in Fig. 2.21. The number of pores decreased with increasing sintering time, while the pore size seemed to become bigger. As-sintered Ti shows an equiaxed structure, and grain growth was observed with increasing sintering temperature and time.

The oxygen content in the sintered specimens was almost constant, around 0.2 mass%, which was greater than the original oxygen content of the powder but less than 0.33 mass% (at which the elongation dramatically decreases by static tensile testing [27]). The carbon content was around 0.07 mass%, which means that the binder in green specimen was successfully debound.

Figure 2.22 shows the stress amplitude-number of cycles to failure curves obtained by rotating bending fatigue testing. Fatigue limit increased with increasing sintering temperature and time. Fatigue limit of wrought Ti materials by ASTM grade 3 was about 240 MPa. Therefore, the fatigue limit of injection molded Ti shows 64 % of the fatigue limit of wrought Ti.

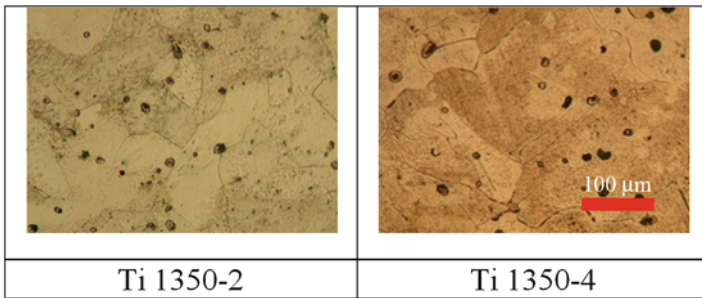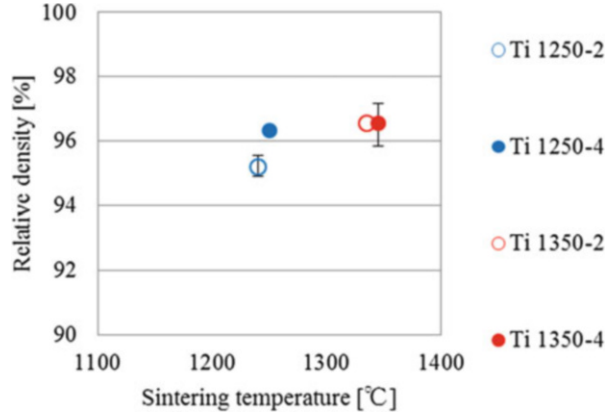**Fig. 2.20** Relationship between relative sintered density and sintering temperature of Ti specimens

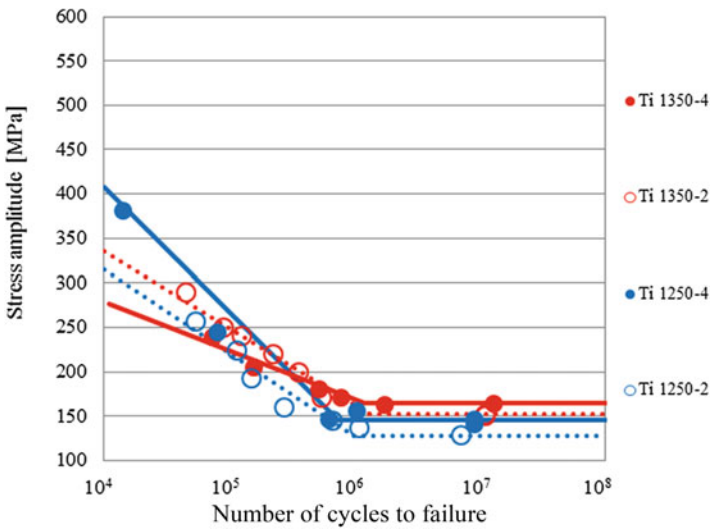**Fig. 2.21** SEM micrographs of Ti specimens

Fig. 2.22 Stress amplitude-number of cycles to failure curves of Ti specimens by rotating bending fatigue testing
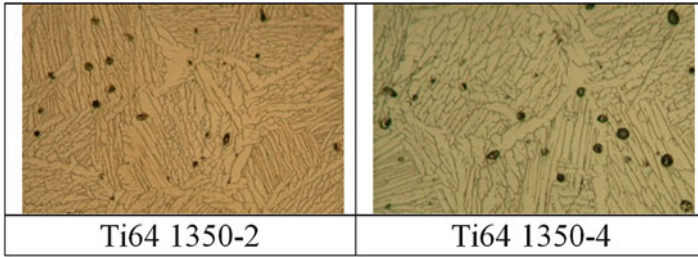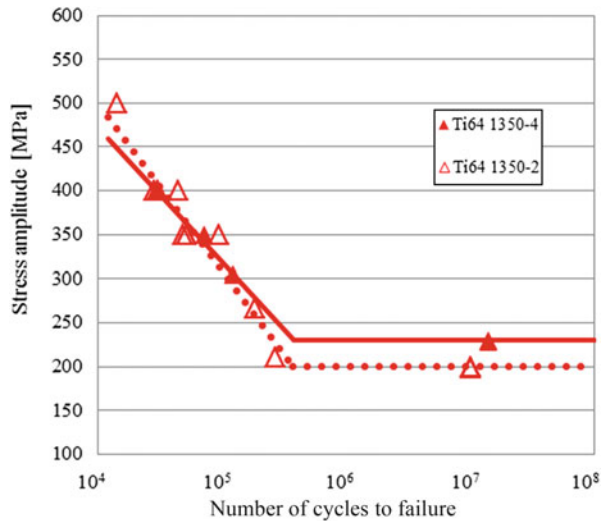
Fig. 2.23 SEM micrographs of Ti64 specimens

Fig. 2.24 Stress amplitude
-number of cycles to failure
curves Ti64 specimens by
rotating bending fatigue
testing

2.5.3.2 Ti-6Al-4V

Sintered densities of the specimens were around 97.5 %. Their microstructures are shown in Fig. 2.23. Pore size seemed to become bigger with increasing sintering time. Ti64 showed the α- and β-lamellar structure. The lamellar structure formed in each prior β-grain, and the prior β-grain size increased with increasing sintering time. Similarly, the oxygen content in the as-sintered specimens was almost constant, below 0.3 mass%. The carbon content was less than 0.1 mass%.

Figure 2.24 shows the stress amplitude-number of cycles to failure curves obtained by rotating bending fatigue testing. Fatigue limit increased with increasing sintering time. The fatigue limit of wrought Ti64 by ASTM grade 5 was 510 MPa. In this case, the fatigue limit of injection molded Ti64 shows 45 % of the fatigue limit of the wrought Ti64, which is very low.

2.5.3.3 Ti-6Al-4V-4Cr

Figure 2.25 shows the sintered density of each specimen, which increased with increasing sintering temperature. Specimens except Ti64Cr 1150–8 showed higher than 96 %TD. Also the specimen treated by HIP showed a relative density over 99 %TD.

The microstructures of the specimens are shown in Fig. 2.26. The number of pores decreased with increasing sintering temperature. A few pores remained even after HIP, and their pore diameter is around 20 μm. HIP can reduce the number of pores; however, it cannot eliminate all pores. Ti64Cr also showed the α- and β-lamellar structure. The prior β-grain size increased with increasing sintering temperature. The oxygen content in the specimens was little changed, below 0.3 mass%. The carbon content was below 0.09 mass%.

Figure 2.27 shows the stress amplitude-number to failure curves of specimens obtained by rotating bending fatigue testing. Fatigue limit increased with increasing sintering temperature. The specimens treated by HT and HIP showed much higher fatigue limit.

2.5.3.4 Ti-6Al-4V-0.03B

The sintered density obtained was around 97 %TD. The resulting α- and β-lamellar structure is shown in Fig. 2.28. The oxygen content in Ti64B was measured to 0.37 mass%, which is higher than the oxygen content of other specimens because of the higher oxygen content of the original TiB_2 powder (1 mass%) introduced.

Figure 2.29 shows the stress amplitude-number of cycles to failure curves obtained by rotating bending fatigue testing. Fatigue limit (fatigue limit at 10^7 cycles) is around 360 MPa.

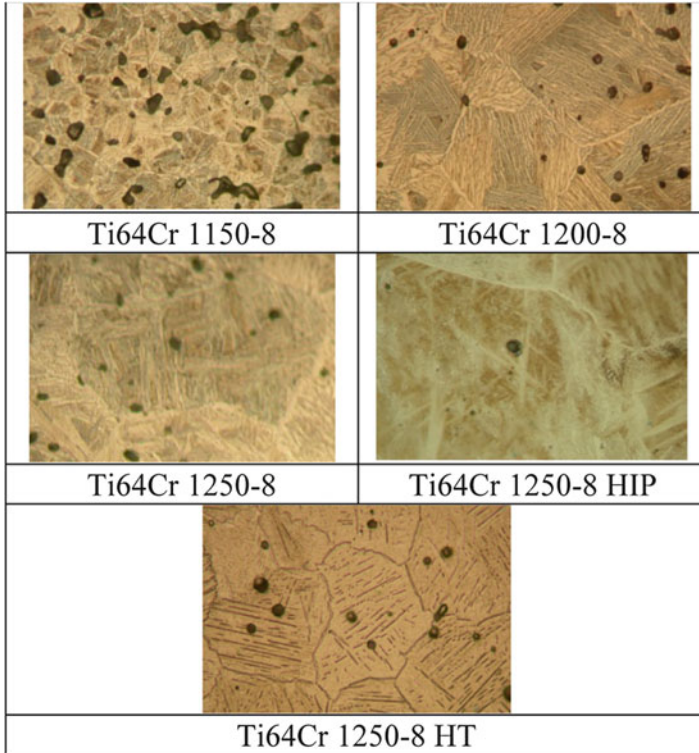**Fig. 2.25** Relationship between relative sintered density and sintering temperature of Ti64Cr specimens
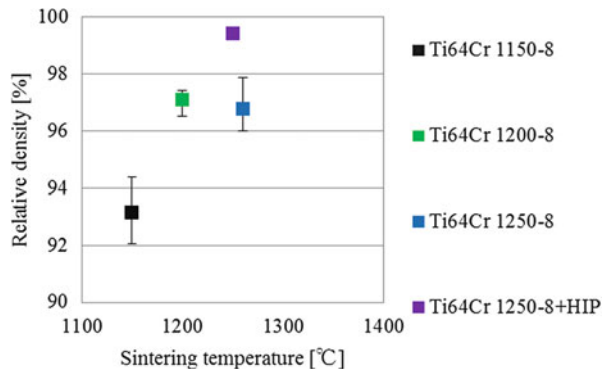
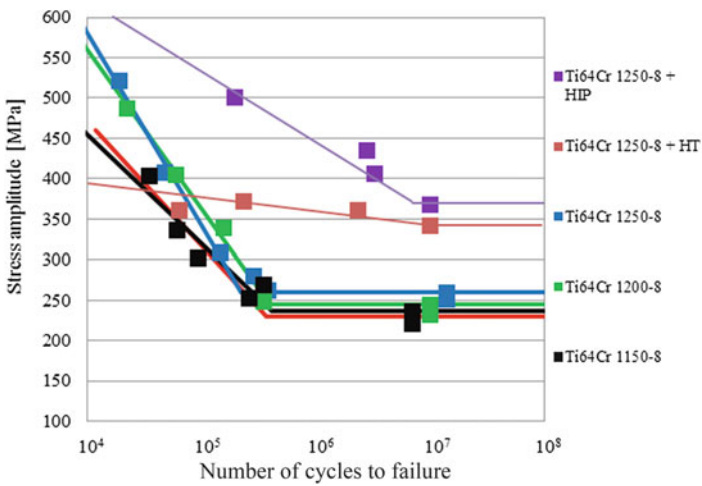**Fig. 2.26** *SEM micrographs* of various Ti64Cr specimens

Fig. 2.27 Stress-number curves of Ti64Cr specimens by rotating bending fatigue testing

Fig. 2.28 SEM micrograph
of Ti64B specimen
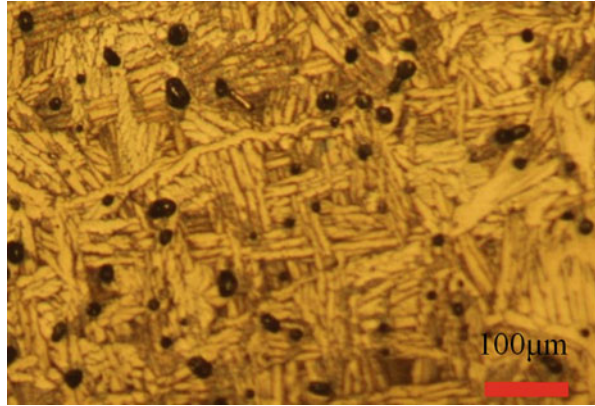
Fig. 2.29 Stress amplitude-
number of cycles to failure
curves of Ti64B specimens
by rotating bending fatigue
testing
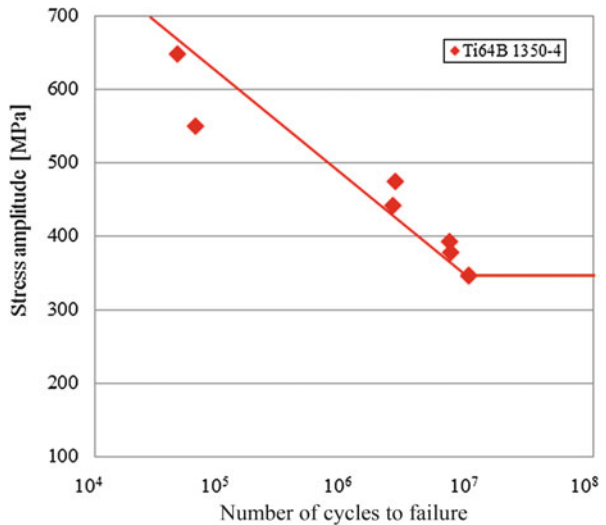
2.5.3.5 Discussion

The sintered densities of all specimens are summarized in Fig. 2.30. They are
around 97 %TD. From the microstructure, the α-lamellae in Ti64Cr are thinner
than that in Ti64. Thus, the addition of Cr powder refined the microstructure.
Moreover, Ti64B shows smaller prior β-grain size than that of Ti64. Finer grain
size is also effective to improve the fatigue properties. Figure 2.31 shows the
relationship between the grain size and sintering temperature. Grain size increased
with increasing sintering temperature and time. Although the grain size of Ti64Cr
was smaller than that of Ti64, the grain size of Ti64Cr 1250–8 after HIP became
larger. On the other hand, certain heat treatment conditions could change the
smaller size. In spite of the higher sintering temperature used, the grain growth of
Ti64B seemed to be negligible.

Fig. 2.30 Relationship between relative density and sintering temperature for various specimens

Fig. 2.31 Relationship between grain size and sintering temperature for various specimens

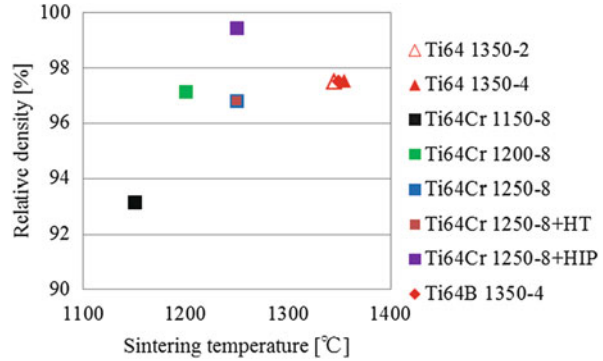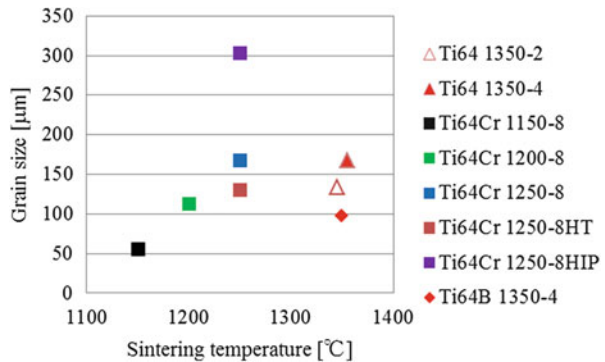The fatigue limit of Ti showed 64 % that of the wrought Ti, while Ti64 showed only 45 % that of the wrought Ti64. It is known that, in harder materials, high notch sensitivity causes the decrease of fatigue limit. The notch sensitivity should become higher for Ti64, which showed lower fatigue limit.

The fatigue limits of all specimens are summarized in Fig. 2.32. Ti64Cr shows 30 MPa higher fatigue limit than that of Ti64, because of the refinement of α-lamellae. Ti64Cr HT shows 100 MPa higher fatigue limit than that of Ti64Cr. Ti64Cr HIP and Ti64B show 55 % improvement in fatigue limit compared to the wrought Ti64; however, they are still weaker than that of the wrought Ti64.

Fatigue ratio is the ratio of fatigue limit to tensile strength. The fatigue ratios of all specimens are shown in Fig. 2.33. The fatigue ratio of wrought Ti materials is around 0.4–0.6, while that of P/M material is usually around 0.3 [28]. From Fig. 2.33, the fatigue ratio of injection molded Ti alloy specimens is around 0.3, including HT- and HIP-treated specimens. Although the microstructural refinement is effective to improve the fatigue limit, the results suggest that even a small amount of remained pores could cause a significant decrease in fatigue limit.

In order to clarify the effect of retained pores on the fracture behavior such as fatigue crack propagation, in situ replica observations were performed. At certain cycles, the rotating was terminated and the surfaces of specimens were replicated using acetyl cellulose film and methyl acetate. Figure 2.34 shows the photograph of

Fig. 2.32 Relationship between fatigue limit and sintering temperature
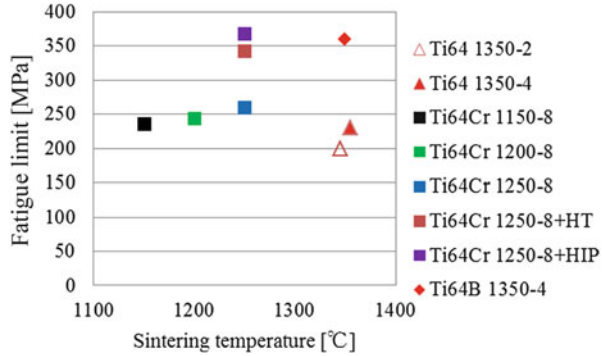
Fig. 2.33 Relationship between fatigue limit and tensile strength (fatigue ratio)
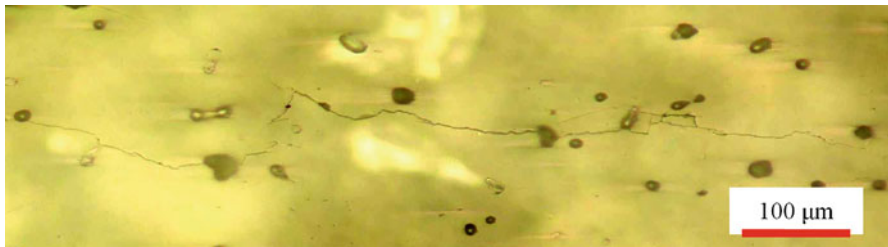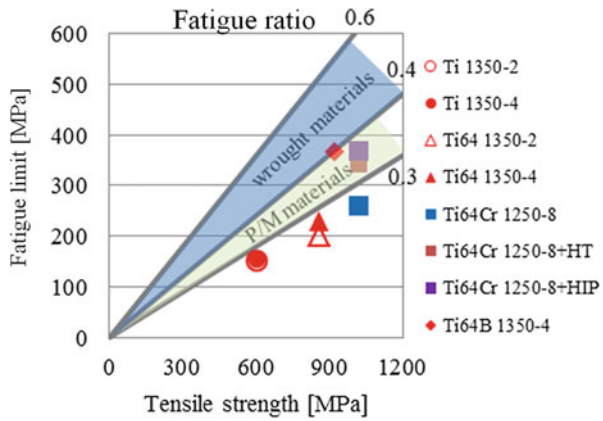
Fig. 2.34 Surface crack by replica observation of Ti64Cr specimen at 80 % of fatigue life

a replica film for Ti64Cr. It was taken at 80 % of fatigue life. There is an 800 μm long crack on the surface of the specimen. Fatigue cracks started from several pores and connected each other, resulting in a longer crack.

Figure 2.35 shows the etched microstructure of the surface of the specimen after fatigue tests to reveal the crack propagation root. Two types of crack propagation were observed: one is transgranular fracture, and the other is intergranular fracture. Normally, a crack that occurred in the wrought materials starts from slipping inside
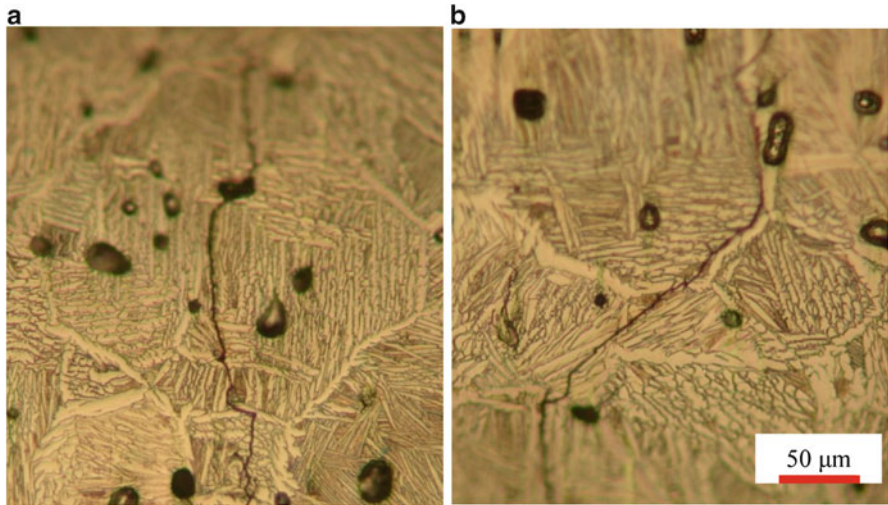
Fig. 2.35 Crack propagation behavior of Ti64Cr specimen. (**a**) Transgranular fracture, (**b**) intergranular fracture

the grain, and then the crack goes along the grain boundary [29]. Crack initiation in the sintered materials occurs differently. They start at pores in a grain or at the grain boundary and then propagate easily to the next pores or along the grain boundary. This causes the lower fatigue limit of the as-sintered specimens.

2.5.4 Summary

In this section, the fatigue properties of the injection molded Ti, Ti-6Al-4V, Ti-6Al-4V-4Cr, and Ti-6Al-4V-0.03B were reviewed. Fatigue limit of pure Ti shows 64 % of the fatigue limit of the wrought material, while Ti64 shows only about 45 %. The high notch sensitivity causes the decrease of fatigue limit of Ti64. By addition of Cr or TiB_2, the fatigue limits of Ti64Cr and Ti64B are higher than that of Ti64 because of the microstructural refinement, especially the α- and β-lamellae. Fracture of injection molded specimens was confirmed by in situ observation, in which the crack initiated from the pores on the surface of the specimen and propagated easily by connecting the pores. HIP treatment improved the fatigue limit because of the further densification; however, a few pores still remained in the matrix which facilitated the crack generation, resulting in still not high fatigue limit.

2.6   Conclusion

Complex-shaped component can be obtained through the powder metallurgy processing route. Especially, metal injection molding (MIM) process is an advanced net-shape processing technique for the mass production of complex-shaped components. This technology also reduces the production cost. Sintered compacts obtained by MIM process show high relative density over 95 % and excellent mechanical properties. MIM process is a suitable technique for titanium and its alloys to reduce the processing cost and material cost.

In this chapter, the tensile and fatigue properties of Ti, Ti-6Al-4V, Ti-6Al-4V-4Cr, Ti-6Al-4V-0.03B, and Ti-6Al-7Nb were reviewed. The sintered compacts showed higher density over 95 %. It was important to reduce the oxygen content under 0.35 mass% because the elongation would dramatically decrease from that content. Sintered compacts using Ti-6Al-7Nb alloy powder showed 900 MPa of tensile strength with 15 % of elongation, which were comparable to the properties of wrought materials. Fatigue limit of pure Ti showed 64 % the fatigue limit of wrought material, while Ti-6Al-4V showed only about 45 %. The high notch sensitivity caused the decrease of fatigue limit of Ti-6Al-4V. By addition of Cr or TiB_2, the fatigue limits of Ti-6Al-4V-4Cr and Ti-6Al-4V-0.03B were higher than that of Ti-6Al-4V because of the microstructural refinement, especially the α- and β-lamellae. HIP treatment improved the fatigue limit because of the further densification; however, a few pores still remained in the matrix which facilitated the crack generation, resulting in still not high fatigue limit. MIM of titanium alloy is still a novel process and under continuous development.

References

1. German RM, Bose A (1997) Injection molding of metals and ceramics. Metal Powder Industries Federation, Princeton
2. Miura H, Takagi K (1996) Powder Metallurgy Science, Uchida Rokakuho,Tokyo
3. Japan Powder Metallurgy Association (2013) http://www.jpma.gr.jp/index.html. Accessed 28 Dec 2013
4. Omar MA, Mustapha M, Ali EAGE, Subuki I, Meh B (2010) Production of medical device using MIM technique. AIP Conf Proc 1217:287–293
5. Fraunhofer Institute for Manufacturing Technology and Advanced Materials (2013) http://www.ifam.fraunhofer.de/en/Bremen/Formgebung_Funktionswerkstoffe/Pulvertechnologie/Projekte/Herzklappen.html. Accessed 28 Dec 2013
6. Ebel T (2008) Titanium and titanium alloys for medical applications: opportunities and challenges. PIM Int 2(2):21–30
7. German RM (2011) Markets, applications, and financial aspects of global metal powder injection molding (MIM) technologies. Proc PowderMet 2011, 04-120-133

8. Heaney DF (2012) Handbook of metal injection molding. Woodhead Publishing in Materials, Cambridge
9. Itoh Y, Harikou T, Sato K, Miura H (2004) Improvement of ductility for injection moulded Ti-6Al-4V alloy. In: Proceedings of 2004 powder metallurgy world congress (PM 2004), compiled by Danninger H, Ratzi R, vol 4. European Powder Metallurgy Association, Vienna, Austria, pp 445–450
10. Itoh Y, Harikou T, Sato K, Miura H (2005) Fabrication of near-α titanium alloy by metal injection molding. J Jpn Soc Powder Powder Metall 52:43–48
11. Itoh Y, Miura H, Sato K, Niinomi M (2007) Effect of mixed powders on the properties of Ti-6Al-7Nb alloy by metal injection molding. Mater Sci Forum 534–536:357–360
12. Itoh Y, Harikou T, Sato K, Komatsu T (2005) Method of preparations for sintered titanium alloy compacts by metal injection molding. JPN Patent No. 2005–281736, Oct 13, 2005
13. Itoh Y, Harikou T, Satoh K, Miura H (2002) Development of the binder systems for solvent and thermal debinding in MIM process. J Jap Soc Powder Metall 49:518–521
14. Itoh Y, Miura H, Toshiaki U, Sato K (2010) The influence of density and oxygen content on the mechanical properties of injection molded Ti-6Al-4V alloys. Adv Powder Metall Particle Mater 1:4.46–4.53
15. Uematsu T, Itoh Y, Sato K, Miura H (2006) Effects of substrate for sintering on the mechanical properties of injection molded Ti-6Al-4V alloy. J Jpn Soc Powder Metall 53:755–759
16. Miura H, Takemasu T, Kuwano Y, Itoh Y, Sato K (2006) Sintering behavior and mechanical properties of injection molded Ti-6Al-4V alloys. J Jpn Soc Powder Metall 53:815–820
17. Arimoto N, Fujita M, Nishioka K, Miura H (2007) New production method by gas-atomized process of titanium alloy powder. Ti-2007 science and technology, compiled by Niinomi M, Akiyama S, Ikeda M, Hagiwara M, Maruyama K, vol 2. The Japan Institute of Metals, Kyoto, pp 1137–1140
18. Itoh Y, Uematsu T, Sato K, Miura H (2008) Effect of Al-40V alloy powders on the properties of injection molded Ti-6Al-4V alloys. J Jpn Soc Powder Metall 55:666–670
19. Osada T, Miura H, Itoh Y, Fujita M, Arimoto N (2008) Optimization of MIM process for Ti-6Al-7Nb alloy powder. J Jpn Soc Powder Metall 55(10):726–731
20. Itoh Y, Miura H, Uematsu T, Sato K (2009) Advanced MIM process for high performance Ti alloy materials. J Solid Mech Mater Eng 3(12):1297–1305
21. Itoh Y, Miura H, Uematsu T, Sato K, Niinomi M (2007) Improvement of the properties of Ti-6Al-7Nb alloy by metal injection molding. Adv Powder Metall Particle Mater Part4:81–86
22. Ferri OM, Ebel T, Bormann R (2009) High cycle fatigue behaviour of Ti–6Al–4V fabricated by metal injection moulding technology. Mater Sci Eng A 504:107–113
23. Osada T, Noda M, Kang H, Tsumori F, Miura H (2012) Dynamic fracture characteristics of injection molded titanium alloy compacts. Int Conf Mater Process Technol 2012:141–146
24. Huang WY, Da Chen C, Chen YN, Shih WJ, Chang CH (2012) Defect detection of metal injection modeling by micro computed tomography. Appl Mech Mater 229–231:1445–1448
25. Itoh Y, Miura H, Uematsu T, Osada T, Sato K (2009) Effect of Fe or Cr addition on the strengthening Ti-6Al-4V alloy by metal injection molding. J Solid Mech Mater Eng 3(6):921–930
26. Hagiwara M, Kitaura T, Ono Y, Yuri T, Ogata T, Kanou O (2012) High cycle fatigue properties of a minor boron-modified Ti6Al4V alloy. Mater Trans 53(8):1486–1494
27. Itoh Y, Uematsu T, Sato K, Miura H (2009) Effect of oxygen content and relative density on the tensile properties of injection molded Ti-6Al-4V alloy. J Jpn Soc Powder Powder Metall 56(5):259–263
28. Hasegawa M (1973) Stainless steel handbook. Nikkan Kogyo Shimbun Ltd, Tokyo
29. Akahori T, Niinomi M, Ozeki A (1998) Effect of microstructure on small fatigue crack initiation and propagation characteristics of Ti-6Al-7Nb alloy. J Jpn Inst Metals 62(10):952–960

Chapter 3
Application of Smart Hot Forging Technique in Producing Biomedical Co–Cr–Mo Artificial Implants

Yunping Li and Chiba Akihiko

Abstract Hot forging processes in producing Co–Cr–Mo artificial implants, which involve large strains and a high strain rate, are usually conducted at temperatures higher than approximately two-thirds the melting point of the material. In order to predict the optimum working condition of the workpiece with complex geometry, a novel technique, smart hot forging technique, has been developed and was successfully applied in optimizing both the microstructure and working condition of Co–Cr–Mo alloy biomedical devices with complex geometry. Smart hot forging technique is established by combining the concepts of both FEM calculation, which can precisely predict both the geometry and working parameter (T, strain, strain rate, etc.), and processing map, which can predict the working state of the workpiece such as the occurrence of crack or shear band. This study emphasized on some fundamental concepts of the processing map as well as friction and adiabatic corrections, which are the basis of this technique.

Keywords Co–Cr–Mo alloy • Biomedical materials • Processing map • Smart hot forging technique • Correction of stress–strain curves

3.1 Introduction

Co–Cr–Mo alloys have been considered to be surgical implant materials for the use of artificial hip and knee joint due to their excellent wear resistance, corrosion resistance, and biocompatibility [1–12]. The representative Co–Cr–Mo alloys for surgical implants are cast Co–Cr–Mo alloys (ASTM F-75) and hot-forged

Y. Li
Institute for Materials Research, Tohoku University, Sendai 980-8577, Japan

Present Address: Materials Science and Engineering, Central South University, Changsha, China
e-mail: lyping@csu.edu.cn

C. Akihiko (✉)
Institute for Materials Research, Tohoku University, Sendai 980-8577, Japan
e-mail: a.chiba@imr.tohoku.ac.jp

Co–Cr–Mo alloys (ASTM F-799 and ASTM F-1537). However, the cast Co–Cr–Mo alloys exhibit limited ductility and fatigue strength, because of casting defects and coarse structure [13]. The homogeneous and fine grain size of Co–Cr–Mo alloys is desirable in order to acquire high mechanical properties [14], for which the hot forging process is a useful method to optimize and control the microstructures. To develop a sound product without defects such as cracks or localized shear bands, it is important to understand the plastic flow behavior and microstructural evolution during hot forging [15]. Moreover, microstructural evolution caused by dynamic recrystallization (DRX) during the hot working process has an advantage in achieving enhanced mechanical properties with ultrafine and equiaxed grains [14, 16]. DRX usually occurs in fcc materials with low stacking fault energy (SFE). Since Co–Cr–Mo alloys have an fcc crystal structure at temperatures higher than approximately 950 °C [17–19] where the SFE of the alloy is very low [19], DRX would be the major hot deformation mechanism. Therefore, investigating the hot deformation behavior and microstructural evolution is very important to achieve high mechanical properties with a fine and equiaxed microstructure [14].

Hot forging processes in producing Co–Cr–Mo artificial implants, which involve large strains and a high strain rate, are usually conducted at temperatures higher than approximately two-thirds the melting point of the material. A fundamental method in investigating the working behavior of materials is analyzing the true stress–true strain curves combined with the microstructure observation, which reflects the intrinsic mechanical properties of materials. In order to understand and constitutively analyze the hot workability of the materials, the processing map based on the dynamic material model (DMM) has been adopted extensively [20]. Processing maps, including both power dissipation and instability maps, are developed on the basis of the DMM [21, 22].

Stress–strain curves are used in developing the processing maps – power dissipation map and instability map. Thus, it is possible to obtain the optimum condition of the forging process without resorting to expensive and time-consuming trial-and-error methods. However, friction between the material and the tools during the working process has to be considered before further investigation [23–31]; this is because practical measurements of the deformation curve depart from the real mechanical response of the materials to a certain degree. In practice, for many metalworking processes, friction is the predominant factor. Friction affects the evaluation of the deformation behavior of materials because the flow stress of the sample is strongly influenced by friction; this is especially true in hot compression processes [32], where the friction is hard to eliminate completely even when the lubricant is added between the sample and anvil surfaces [33]. Therefore, correcting the deformation curve for real behavior is a very important topic for both researchers and engineers in hot working.

In addition, it has been reported that over 90 % of the input energy during deformation is converted into heat due to adiabatic heating. This results in the softening of the flow stress and its decreases as compared to the ideal isothermal deformation conditions [34]. The influence of temperature rise due to adiabatic heating during deformation on stress decrease has also to be taken into a real consideration [34].

Processing map has been proved effective in predicting the optimum condition for hot forging of Co–Cr–Mo alloys [35, 36]. However, in an actual hot forging process, the distributions of strain, stress, temperature, and strain rate in the interior of the workpiece are varied significantly due to its complex geometry or the inconstant forging condition of temperature, strain rate and strain, etc. Such characteristic of the hot forging process greatly limits the further application of the processing map in practical use. In order to predict the optimum working condition of the workpiece with complex geometry, smart hot forging technique, which combines both finite element method (FEM) and processing map, was developed by Chiba and Li [37] and has been applied in the hot forging process of biomedical Co–Cr–Mo implants successfully [38].

Thus, in this chapter, the smart hot forging technique of biomedical Co–Cr–Mo alloys was introduced in detail. This was emphasized on some fundamental concepts of processing map as well as friction and adiabatic corrections, which are the basis of this technique.

3.2 Friction Correction and Adiabatic Correction

3.2.1 Friction Coefficient

Friction correction in this research is considered in the case that a cylindrical sample is compressed along its longitudinal direction. It is usually assumed that the friction coefficient over the interface between the workpiece and the tools is constant during the working process. On the basis of these, Ebrahimi et al. developed an upper bound theory to determine the average Tresca friction coefficient by conducting a barrel compression test [39, 40]. According to this theory, the average Tresca friction coefficient m for a cylindrical sample can be determined by measuring the degree of barreling sample and using the following equation:

$$f = \frac{\frac{R_{th}}{H} \cdot b}{\frac{4}{\sqrt{3}} - \frac{2b}{3\sqrt{3}}} \tag{3.1}$$

where f is the average Tresca friction coefficient for a hot working process: its value ranges from 0 (perfect sliding) to 1 (sticking friction). R_{th} and H are the radius of the sample in the absence of bulging (or condition without friction) and final height of the sample, respectively. The barreling factor, b, is given by the following equation:

$$b = 4 \frac{\Delta R}{R_{th}} \cdot \frac{H}{\Delta H}, \tag{3.2}$$

where ΔR is the difference between the maximum radius (R_m) and the radius of the original flat end surface after expansion (R_t) of the cylindrical sample after

Fig. 3.1 The shape of the cylindrical sample at true strain levels of (**a**) 0.3, (**b**) 0.65, and (**c**) 1.5 at friction coefficient of 0.5 simulated by DEFORM-3D software (Reprinted from Ref. [41], with kind permission from Springer Science + Business Media)
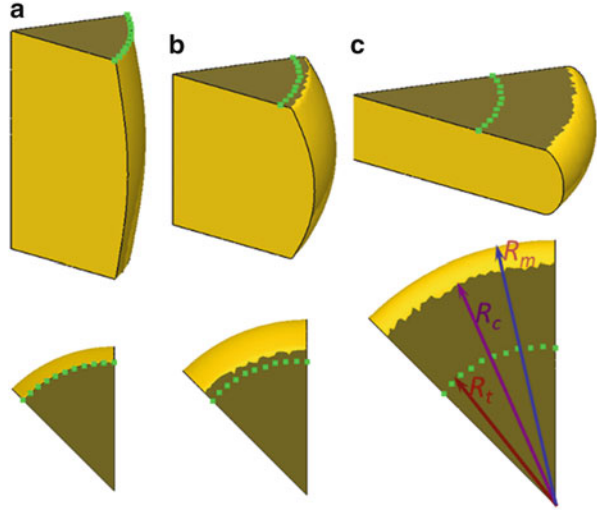
compression and ΔH is the reduction in the height of the cylindrical sample after compression. At low strain levels, the contact surface (radius with R_c) of cylindrical samples with anvil surface after compression was found to be formed mainly by the original flat end surfaces of samples (radius with R_t) (Fig. 3.1a); however, at higher strain levels, the contact surfaces were observed to be formed by both the originally flat end surface after expansion in the middle area and the external lateral surface of the sample (Fig. 3.1b, c) due to barreling and its further contact with the anvil (R_c–R_t). It should be noted that Eq. 3.1 was proposed on the basis of the upper bound theory, and from this theory, the contact surface should be completely generated from the originally flat end surface of the sample after expansion [39]. Therefore, this equation is not applicable at high strain levels according to the abovementioned analysis.

In this study, using the DEFORM-3D FEM software, we simulated the evolution behavior of various parameters of a cylindrical sample such as R_t, R_c, and R_m in hot compression processes by adjusting the average Tresca friction coefficient f. On the basis of the results of simulation, the identification of f was carefully established just by analyzing the abovementioned nondimensional parameters [41]. We simulated the shape of the sample by means of the DEFORM-3D FEM software for various values of f: in this case, f was considered to be constant or, in other words, independent of strain in each compression process. For $f = 0.5$, the simulated shapes of the sample at true strains of 0.3, 0.65, and 1.5 are shown in Fig. 3.1a, b, and c, respectively. When the true strain was 0.3, it was observed that the contact surface of the compressed cylindrical sample was formed mainly by the original flat end surface of the sample after broadening; in this case, R_t was approximately equal to the radius of the deformed contact surface of the sample with the anvil (Fig. 3.1a). However, at strain levels of both 0.65 and 1.5, the contact surface consists of both the original flat end surface (characterized by the dashed line) and the annular surface due to the contact of the lateral surface of sample after barreling.

From the simulation results, R_t, R_m, and R_c as a function of friction coefficient at different strain levels can be calculated, on the basis of which new relationships between the parameters R_t, R_m, original geometrical parameter of the sample (H_0, R_0), and the friction coefficient f could be established [41]. When considering the relationship between f and the geometry of the sample, since there are similar trends between R_c and R_m from the simulation results, we just considered R_m in this study and combined it with other parameters such as the sample height after compression, H, R_t, and the initial height of the sample H_0 into $R_m H/R_t H_0$ for each process as a function of the true strain level, respectively. The plots show gradual decreases in the values with an increasing strain level at each compression process. Let $P = R_m H/R_t H_0$; therefore, the relationship between true strain and P in each compression process can be exactly expressed by a spline equation as follows:

$$P = A + B\varepsilon + C\varepsilon^2, \tag{3.3}$$

where A, B, and C are variables and

$$A = a' + b' f + c' f^2, \tag{3.4}$$

$$B = a'' + b'' f + c'' f^2, \tag{3.5}$$

$$C = a''' + b''' f + c''' f^2. \tag{3.6}$$

These parameters are constants and independent of materials or experimental condition as given in Table 3.1. By inserting Eqs. 3.4, 3.5, and 3.6 into Eq. 3.3, the relationship between f and P can be summarized as

$$\left(a' + a'' \varepsilon + a''' \varepsilon^2 - P\right) + \left(b' + b'' \varepsilon + b''' \varepsilon^2\right)f + \left(c' + c'' \varepsilon + c''' \varepsilon^2\right)f^2 = 0 \tag{3.7}$$

where P is able to be obtained easily by measuring the geometry of the deformed sample and other parameters in this equation are available in Table 3.1 in the case of the current sample.

On the basis of Eq. 3.7, the relationship among the nominal strain, parameter P, and friction coefficient f is plotted in Fig. 3.2 by a contour map; the relationship between these parameters could be observed clearly. For a deformed sample, parameter P and nominal strain could be easily obtained; in this case, f could be read directly from this figure [41]. For example, if a cylindrical sample was compressed to a nominal strain of 0.5 (50 %) and the geometrical parameter P was calculated to be about 0.68, then the friction coefficient f should be about 0.45 as shown in Fig. 3.2.

3.2.2   Friction Correction

Rowe analyzed the influence of interfacial friction between a workpiece and a tool [42] and found that, without the influence of friction for a circular disk, the relationship between the average axial pressure and stress is

Table 3.1 Constant in Eqs. 3.7 and 3.15

Eq. 7	a′	b′	c′	
Value	0.99	0.016	−0.0057	
Eq. 7	a″	b″	c″	
Value	−0.84	0.93	−0.52	
Eq. 7	a‴	b‴	c‴	
Value	0.22	−0.05	0.32	
Eq. 15	a	b	c	d
Value	0.042	−0.24	0.045	0.31

Reprinted from Ref. [41], with kind permission from Springer Science + Business Media

Fig. 3.2 Relationships among nominal strain, friction coefficient f, and parameter P in cylindrical compression tests (Reprinted from Ref. [41], with kind permission from Springer Science + Business Media)
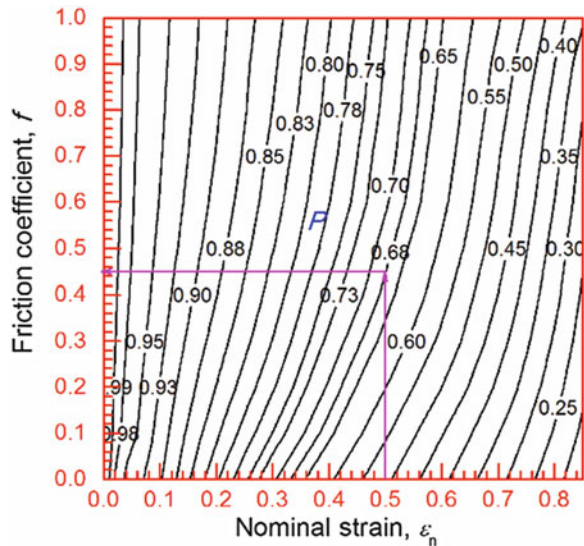
where r and h are the instantaneous radius and height, respectively, of the sample and σ and σ_z are the equivalent axial stresses without and with frictional conditions, respectively. Dieter also proposed a Coulomb stress distribution at both end surfaces of the cylindrical sample [43] and found that the average axial stress (mean height of the friction hill) with respect to the stress without friction is

$$\sigma_z = \sigma\left(1 + \frac{2f}{3\sqrt{3}}\frac{r}{h}\right), \qquad (3.8)$$

$$\sigma = \frac{C_f{}^2\sigma_z}{2\left[\exp(C_f) - C_f - 1\right]}, \qquad (3.9)$$

where

$$C_f = \frac{2\mu r}{h}. \tag{3.10}$$

In the above equation, μ denotes the Coulomb friction coefficient. The relationship between the Tresca friction coefficient f and the Coulomb friction coefficient μ is

$$f = \sqrt{3}\mu. \tag{3.11}$$

It should be noted that Eqs. 3.8 and 3.9 are based on the assumption that there is no barreling at the edges of the sample and that the thickness is small enough so that the average axial stress σ_z/σ may be taken as constant throughout the sample thickness. However, in an actual cylindrical hot working process, the sample thickness is generally greater than its radius. In addition, the stress is considered to vary greatly as a function of the sample height. Therefore, these two theories are not applicable to an actual compressive test. A more precise equation for compensating the stress–strain curve is therefore required for a cylindrical compression test because the stress distributions both within the sample and at the interface between the sample and the anvil vary with the height/radius ratio and with the friction condition.

In the current study, we used the DEFORM-3D FEM software to simulate the evolutionary behavior of flow stress in a sample under compression by adjusting the average Tresca friction coefficient f. To analyze the variation of flow stress with respect to the initial height/diameter ratio of the sample, a series of simulations were performed for samples with various initial heights (same diameter). In this chapter, we propose a pragmatic and simple approach to compensate the stress–strain curve.

Models of the aforementioned samples were generated using DEFORM-3D v6.13. To reduce the calculation time, one-eighth of the cylindrical sample with a mesh number of 30,000 was considered in the FEM model for analysis. The values of the Tresca friction coefficients f selected for each simulation were 0 for perfect sliding and 0.1–1, in increments of 0.1, for restriction condition between the sample top surfaces and the anvils. FEM analysis was carried out to a true strain of about 1.8 (nominal strain of approximately 85 %) [44].

The simulated compression processes were performed using a true strain rate-controlling process of 10^{-3} s^{-1}. In addition, the heat efficiency was chosen to be 0 in the simulation process so that adiabatic heating (temperature rise) would not occur inside the compressed sample (it leads to softening of the flow stress in the deformation process). All of the above settings for the simulation process are based on the fact that the compensation of stress both from adiabatic heating and from the stroke rate effect can be performed independently, as we mentioned above [44].

Let the dimensionless parameters σ_z and σ represent the stress with and without the influence of friction, respectively, during the compression process. Therefore, the ratio σ_z/σ is a parameter expressing the extent to which friction influences the stress of materials. For a sample with Rastegaev geometry, the influence of friction on the flow stress of materials is very small for strain values less than approximately

0.6; however, at high strain levels, the stress increases sharply because of the friction. Oh et al. [45] studied the cylindrical compression of a Ti alloy sample with Rastegaev geometry to a true strain level of approximately 0.6–0.7 using DEFORM-3D FEM software, and their findings suggest that stress variations due to the influence of friction are below 5 % for strain values below 0.6–0.7, which is in good agreement with the current results. However, they did not report any results for higher strain levels. The results of our current study indicate that, at a high strain level, the influence of friction is extremely large. In fact, numerous compression tests were conducted using a high strain level to further refine the microstructure or improve the mechanical properties of the final products. Therefore, analyzing the influence of friction at both high and low strain levels is important. From the plot of σ_z/σ as a function of average Tresca friction coefficient f at different strain levels, we find that f is linear to σ_z/σ, where the slopes K of these lines are closely related to the nominal strain levels. From the abovementioned results and for a specific strain level, the relationship between the ratio σ_z/σ and f is [44]

$$\frac{\sigma_z}{\sigma} = 1 + K(\varepsilon)f, \tag{3.12}$$

where the slope $K(\varepsilon)$ of the line depends on the strain

$$K(\varepsilon) = f(\varepsilon). \tag{3.13}$$

The plot of the slope $K(\varepsilon)$ can be calculated as a function of the true strain. We find that the curve can be expressed by a third-order spline equation:

$$K = f(\varepsilon) = a + b\varepsilon + c\varepsilon^2 + d\varepsilon^3, \tag{3.14}$$

where a, b, c, and d are constants determined by the fitting process and their suitable values are listed in Table 3.1. By substituting Eq. 3.14 into Eq. 3.11, correcting the stress–strain curve for a sample with Rastegaev geometry is obtained:

$$\sigma = \frac{\sigma_z}{1 + (a + b\varepsilon + c\varepsilon^2 + d\varepsilon^3)f}, \tag{3.15}$$

where f can be calculated using the methodology developed in the previous section. The stress without the influence of friction can be compensated by inserting the other parameters of Table 3.1 into Eq. 3.14, regardless of the experimental conditions or of the characteristics of the material.

3.3 Adiabatic Correction

It has been reported that over 90 % of the input energy during high-speed deformation is converted into heat due to adiabatic heating. This results in the softening of flow stress and its decreases as compared to the ideal isothermal deformation conditions [46, 47]. The temperature rise due to adiabatic heating during deformation is usually calculated by [46, 47]

$$\Delta T = \frac{\eta_e}{\rho c} \int_0^\varepsilon \sigma \mathrm{d}\varepsilon = \frac{\eta_e}{\rho c_h} W \qquad (3.16)$$

where ΔT is the temperature rise due to the work done on the sample, ρ is the density of the sample, and c_h is the heat capacity of the material; η_e is the heat efficiency and is empirically dependent on the strain rate as [48]

$$\eta_e = 0.316 \log \dot{\varepsilon} + 0.95. \qquad (3.17)$$

From Eq. 3.17, the temperature rise and the subsequent softening are usually more significant at high strain rates due to the short dissipation time and high input energy. At a certain strain rate and strain level, the flow stress after adiabatic correction can be calculated from

$$\ln(\sigma) = E + \frac{Q}{RT} \qquad (3.18)$$

where $E = \ln(A \cdot \varepsilon^m)$. An example of deformation curve biomedical Co–29Cr–6Mo–0.12C–0.16 N alloy ($T = 1150\,^\circ\text{C}$, strain rate $= 1\,\text{s}^{-1}$) after corrections of both friction and adiabatic heating is shown in Fig. 3.3; in this case, the friction coefficient was calculated to be 0.52, and it can be seen that the influence of friction on the deformation curve is not so significant below the true strain level of 0.6, while the effect of adiabatic heating on deformation curves has a much influence on the entire shape of deformation curves.

3.4 Processing Map

Processing map on the basis of the dynamic material model (DMM) [21, 22] is used to constitutively analyze the hot workability of metallic materials. It is based on the fundamental principles of continuum mechanics of large plastic flow, physical system modeling, and irreversible thermodynamics. "DMM may be viewed as a bridge between the continuum mechanics of large plastic deformation and the development of dissipative microstructures in the material and encompasses the area of deterministic chaos in describing the patterns of the dynamic response of the material in hot deformation" [21]. This model considers that the workpiece during

Fig. 3.3 Stress–strain curves obtained in experimental condition, after friction correction, and after adiabatic correction for biomedical Co–29Cr–6Mo–0.16N alloy at $T = 1,150\,°C$, strain rate $= 1\ s^{-1}$
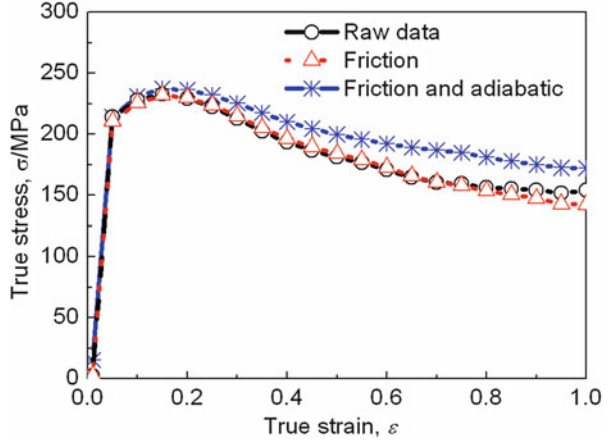
hot working process is a power dissipater and that the instant power dissipated at a given strain rate, $\dot{\varepsilon}$, consists of two complementary parts: the G content and the J co-content, which are related to temperature rise and the microstructure dissipation, respectively (Fig. 3.4). The instantaneous total power dissipation P consists of two complementary parts, G and J as

$$P = G + J \quad \text{or}$$
$$\sigma\dot{\varepsilon} = \int_0^{\dot{\varepsilon}} \sigma d\dot{\varepsilon} + \int_0^{\sigma} \dot{\varepsilon} d\sigma \tag{3.19}$$

where the σ is the flow stress and G content represents the power dissipated by plastic work and is designated the dissipater content. The J content represents the structural mechanisms occurring dynamically during hot deformation and is designated the dissipater co-content.

The factor that partitions the power between J and G is the strain rate sensitivity (m) of the flow stress (σ); the J co-content is given by

$$J = \int_0^{\sigma} \dot{\varepsilon} \cdot d\sigma \rightarrow \frac{\sigma \cdot \dot{\varepsilon} \cdot m}{m+1}. \tag{3.20}$$

Since the value of m varies nonlinearly with temperature and strain rate, the J co-content variation is also nonlinear. The variation may be normalized with respect to a linear dissipator for which m is unity and then the J co-content will assume a maximum value given by $J_{max} = \sigma \cdot \dot{\varepsilon}/2$. For a nonlinear dissipater, the efficiency of power dissipation may be expressed in terms of a dimensionless parameter η. The variation of η with the temperature and strain rate constitutes the power dissipation map, and its domains may be interpreted in terms of specific microstructural evolution processes as the following:

Fig. 3.4 Dynamic constitutive equation for a viscoplastic solid following power law behavior (*upper figure*) and ideal linear dissipator (*lower figure*), at constant temperature and strain (Reprinted from Ref. [21], with permission from Maney publishing)
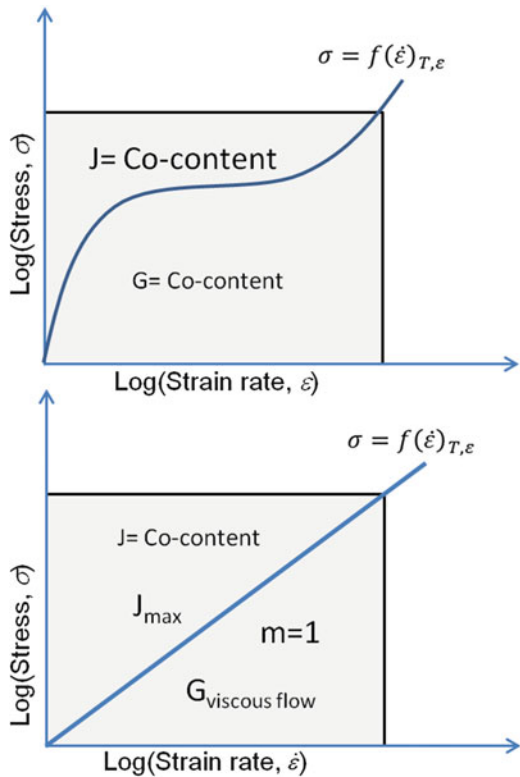

$$\eta = \frac{J}{J_{max}} = \frac{2m}{m+1} \tag{3.21}$$

where at a given temperature T and strain ε, m can be obtained by (Fig. 3.5)

$$m = \frac{d\ln\sigma}{d\ln\dot{\varepsilon}}\bigg|_{T,\varepsilon} \tag{3.22}$$

Thus, η is directly related to the strain rate sensitivity m. The variation of efficiency η with temperature and strain rate constitutes a power dissipation map which exhibits various domains in which specific microstructural mechanisms occur. The efficiency map itself represents the power transactions within a continuum, and the understanding of its origin and its interpretation in terms of atomistic mechanisms requires a correlation with some of the concepts of irreversible thermodynamics. It is possible to extend the theory of deterministic chaos and interpret the behavior in terms of domains of local order separated by bifurcations. Also, it helps in interpreting the microstructures resulting from hot deformation as "dissipative" and characterizes them in terms of atomistic mechanisms.

Fig. 3.5 Schematic figures
showing the method of
obtaining strain rate
sensitivity *m* as a function
of strain rate
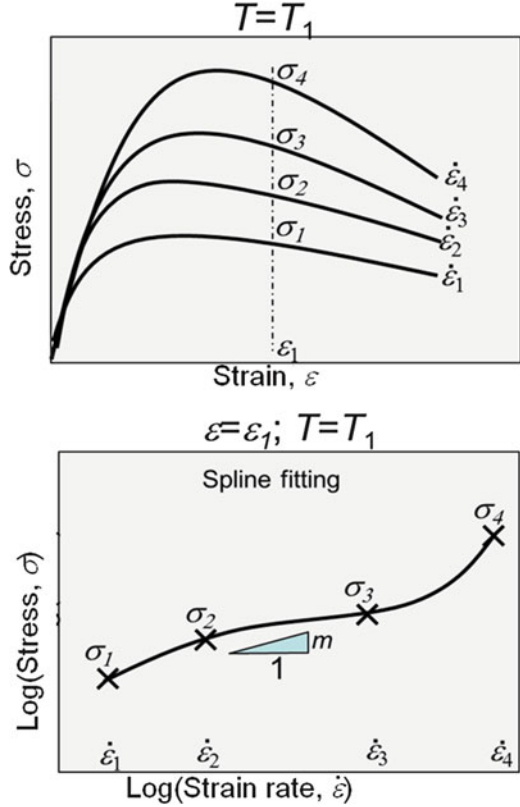
In general, microstructural behaviors during hot deformation are DRX, dynamic recovery (DRV), superplasticity, void formation, precipitation from metastable phase, and so on. These mean that when the microstructures of the workpiece change remarkably, the dissipation efficiencies have high values whether the microstructural changes are beneficial to hot workability or not. Therefore, it is needed to separate them from the harmful ones in order to use the dissipation efficiency maps for deciding the optimum hot working condition.

The occurrence of instability has been proposed by Ziegler [49], who considered that the transition of the plastic flow into an unstable condition is given by

$$\frac{\mathrm{d}D}{\mathrm{d}\dot{\varepsilon}} < \frac{D}{\dot{\varepsilon}} \tag{3.23}$$

where D is the dissipative function that is characteristic of the constitutive behavior of materials; it depends on the dissipative power. D can be replaced with J, and a condition for microstructure-related flow instabilities is obtained as

$$\xi(\dot{\varepsilon}) = \frac{\partial \log(m/m + 1)}{\partial \log \dot{\varepsilon}} + m < 0. \tag{3.24}$$

In the preceding equations, the assumption that the flow stress obeys the power law with $\dot{\varepsilon}$ and temperature, T, is necessary because the changes in the microstructure due to change in the deformation curve can easily be separated from the heat dissipation or the G contour. The parameter $\xi(\dot{\varepsilon})$ may be plotted as a function of the temperature and strain rate, and the region where it is negative will exhibit flow instabilities. The physical meaning of the above instability criterion is that if the system does not generate entropy at a rate that at least matches with the imposed rate, the system will localize the flow and cause flow instabilities. The instability map can be superimposed on the power dissipation maps to obtain the regions of flow instabilities.

In Fig. 3.6, the peak efficiency in the DRX domain is plotted as a function of SFE, and lower-SFE metals have a lower efficiency of power dissipation from the result of Prasad et al. [21]. There is no such kind of research regarding the peak power dissipation efficiency of Co–Cr–Mo alloys from this result; however, we extrapolated the optimum power dissipation efficiency of the current alloy based on its SFE and related parameters, and it is plotted in the same figure by a rectangle, indicating that the peak power dissipation efficiency of Co–Cr–Mo alloys in the DRX domain should be in the range of 20–30 %.

Prior to plotting the processing map, all of the stresses at various conditions were compensated as mentioned above. We took the Co–29Cr–6Mo–0.16N alloy, for example. All the true stress–strain curves obtained from hot compressive test at various conditions are given in Fig. 3.7. After correction by both friction and adiabatic heating, the results are shown in Fig. 3.8. Typical power dissipation map generated from the temperature range 1,000–1,200 °C and strain rate range 0.01–30 s^{-1} for a strain of 0.65 is shown in Fig. 3.9a, b in both three and two dimensions [50]. The contour represents constant power dissipation efficiencies that are expressed in percentage. The maps exhibit a clear domain with peak efficiency at approximately 1,000 °C and 0.01 s^{-1}, and the domain exhibits its peak efficiency at about 50–60 %.

The instability map at strain of 0.65 is plotted in Fig. 3.10 [50]. By comparing the two maps, it is observed that the region in the temperature range 1,050–1,200 °C and strain rate range 1.0–30 s^{-1} has the optimum condition for the forging process (power dissipation coefficient 20–30 % and instability parameter >0). Therefore, the optimum hot working condition for Co–29Cr–6Mo–0.16 N alloy should be in the range of $T = 1,000$–1,200 °C and strain rate above 1 s^{-1} as squared by a shaded rectangle in Fig. 3.10.

In order to evaluate the reliability of the results predicted by the processing map, we selected four typical areas [(a) (1,000 °C, 0.1 s^{-1}), (b) (1,100 °C, 10 s^{-1}), (c) (1,100 °C, 0.1 s^{-1}), and (d) (1,100 °C, 0.01 s^{-1})] for microstructure observation by means of electron backscattered diffraction (EBSD) equipment, where both points b and d are stable conditions and points a and c are unstable condition

Fig. 3.6 (**a**) Correlation of optimum efficiency of power dissipation in dynamic recrystallization domain with normalized SFE in various metals (Reprinted from Ref. [21], with permission from Maney publishing). (**b**) Stacking fault energy as a function of temperature for Co–29Cr–6Mo alloy compared to other alloys (Reprinted from Ref. [15], with kind permission from Springer Science + Business Media)
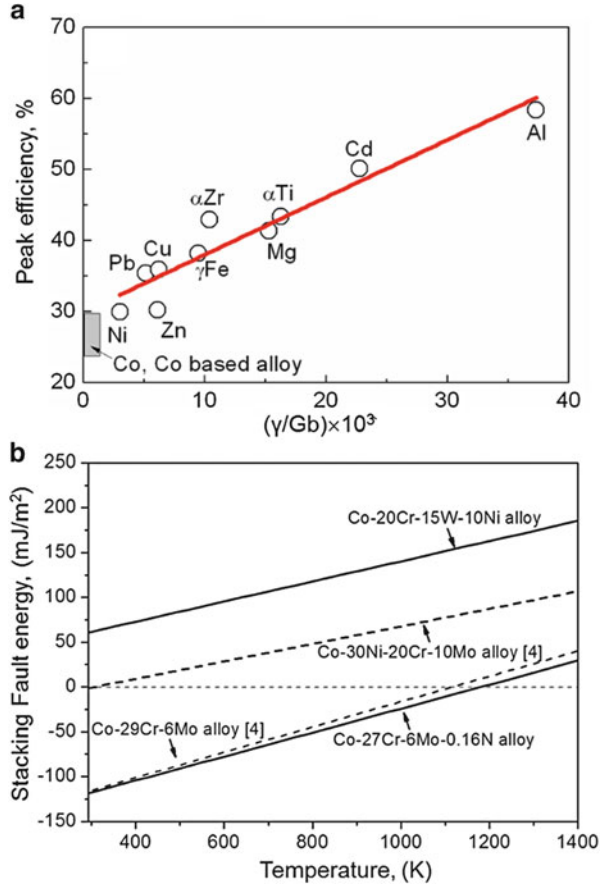
predicted by the processing map. The results are shown in Fig. 3.11 by both grain boundary map and kernel average misorientation (KAM) map. It can be seen that conditions at regions b and d, which are stable as predicted from the processing map, were in good agreement with the microstructure observations, since there is neither shear band or localization of deformation observed in these conditions, and extremely homogeneous DRXed and fine microstructures were obtained. In addition, from their KAM maps, the residual strain in the entire microstructure was observed to be extremely low, indicating the complete DRXed microstructure. The condition in point a ($T = 1,000$ °C, 0.1 s^{-1}) was predicted to be unstable plastic deformation from the processing map; correspondingly, the microstructure was observed to be partially DRXed microstructure with the non-DRX area having high residual strain inside the matrix, implying the localization of deformation. The microstructure observation for point c was predicted to be unstable by the processing map. Although not so obvious as that in region a, the microstructure is
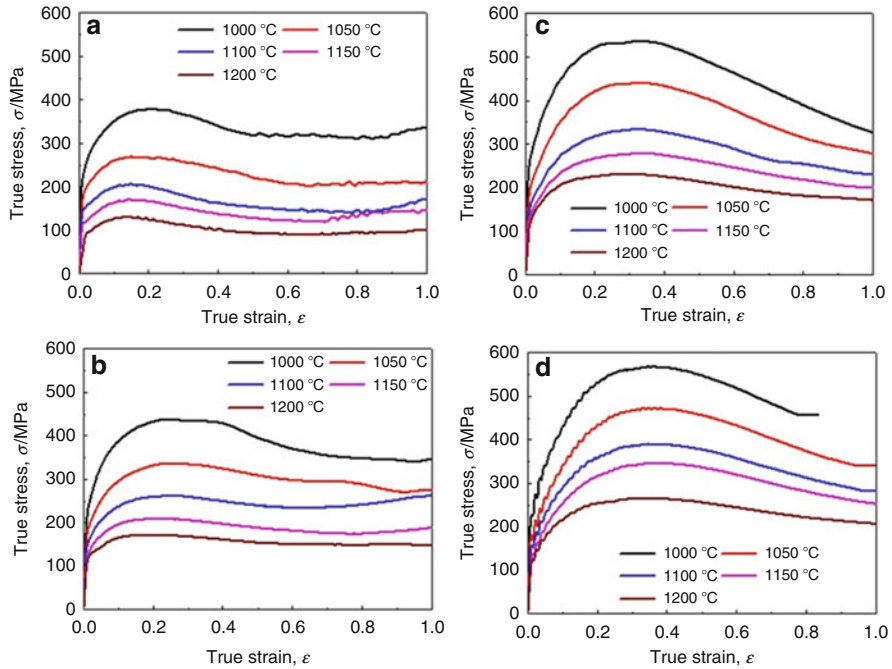
Fig. 3.7 True stress–true strain curves of Co–29Cr–6Mo–0.16N alloy obtained by hot compression tests at strain rate (SR) of (**a**) 0.1 s^{-1}, (**b**) 1.0 s^{-1}, (**c**) 10 s^{-1}, and (**d**) 30 s^{-1}

characterized by both DRXed and non-DRXed microstructure, indicating the uncomplete DRX during hot working process.

As a result, we found that the microstructure evolution of the Co–28Cr–6Mo–0.16N alloy during hot deformation can be well predicted by the processing map consisting of the power dissipation map and the flow instability map. These results would be very helpful to design the hot forging processing of the sound product of Co–28Cr–6Mo–0.16 N alloy, and applying these results to the numerical analysis, for example, the finite element method could more accurately predict the instable regime of the product. This will be reported in Sect. 3.4.

In summary, the results of EBSD observation and the analysis of processing map were well matched. Thus, the processing map constructed in the present study can be utilized for fabrication of a Co–28Cr–6Mo–0.16 N alloy by means of hot forging processes.
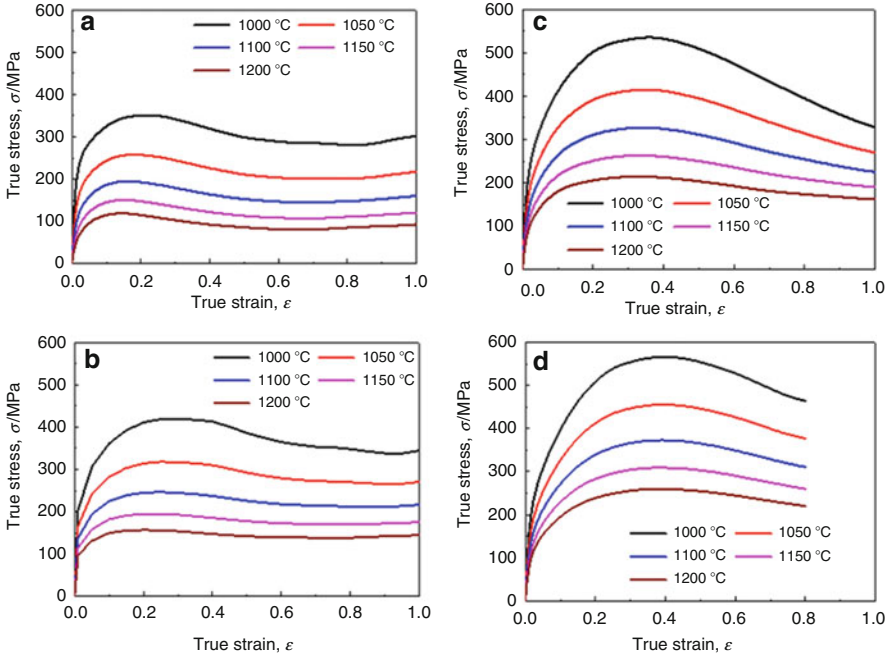
Fig. 3.8 True stress–true strain curves of Co–29Cr–6Mo–0.16N alloy obtained by hot compression tests at strain rate (SR) of (**a**) 0.1 s^{-1}, (**b**) 1.0 s^{-1}, (**c**) 10 s^{-1}, and (**d**) 30 s^{-1} after both friction correction and adiabatic correction

3.5 Biomedical Co–Cr–Mo Artificial Implants Produced by Smart Hot Forging Technique

A schematic flow of smart hot forging technique is shown in Fig. 3.12. This technique combines the concepts of FEM calculation, which can be used to precisely predict the geometry and working state such as T, ε, $\dot{\varepsilon}$, and σ in the interior of the workpiece, and processing map, which can predict the working state inside the workpiece such as the occurrence of crack or DRX during the hot working process. In order to obtain the processing map with high precision, both friction correction and adiabatic heating correction have to be carried out on the true stress–true strain curves by the methods mentioned above. On the basis of the true stress–true strain responses of materials obtained by compressive test, processing maps in a wide range of working conditions (T, ε, $\dot{\varepsilon}$) were constructed and transmitted into a database for the further use in FEM analysis. Constructing the processing map database can be carried out in the processing map maker software which was developed by Li and Chiba et al. [50, 51], where η and ξ can be expressed as a function of working parameters T, ε, and $\dot{\varepsilon}$ as the follows:

$$\xi = f(T, \varepsilon, \dot{\varepsilon}) \tag{3.25}$$

Fig. 3.9 The three-dimensional (the *upper figure*) and two-dimensional power dissipation map (the *lower figure*) of Co–28Cr–6Mo–0.16N alloy at true strain level of 0.65 (Reprinted with permission from Ref. [50]. The Japanese Society for Technology of Plasticity, ISJP)
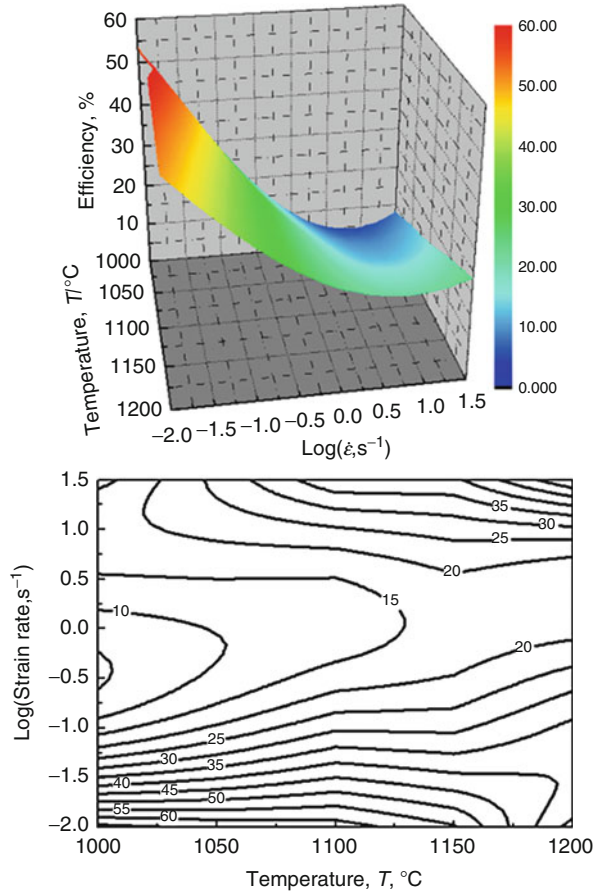
Fig. 3.10 Instability map of Co–28Cr–6Mo–0.16N alloy at true strain level of 0.65 (Reprinted with permission from Ref. [50]. The Japanese Society for Technology of Plasticity, ISJP)
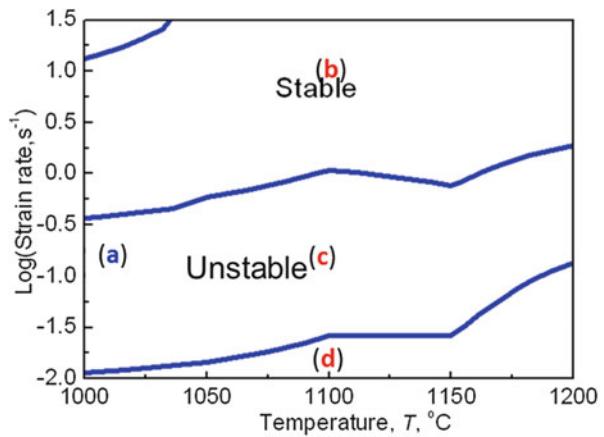
Fig. 3.11 Microstructure observed by EBSD in terms of grain boundary map and kernel average misorientation (KAM) map by the deformation in conditions of **a**, **b**, **c**, and **d** points of Fig. 3.10, respectively (Reprinted with permission from Ref. [50]. The Japanese Society for Technology of Plasticity, ISJP)

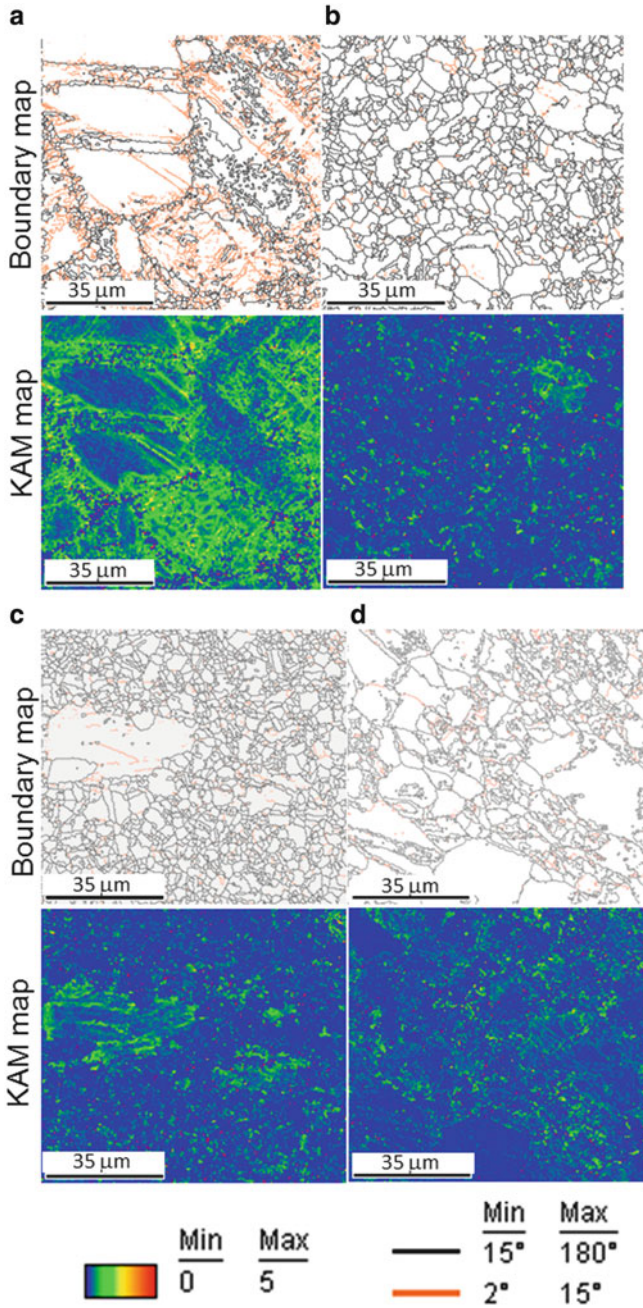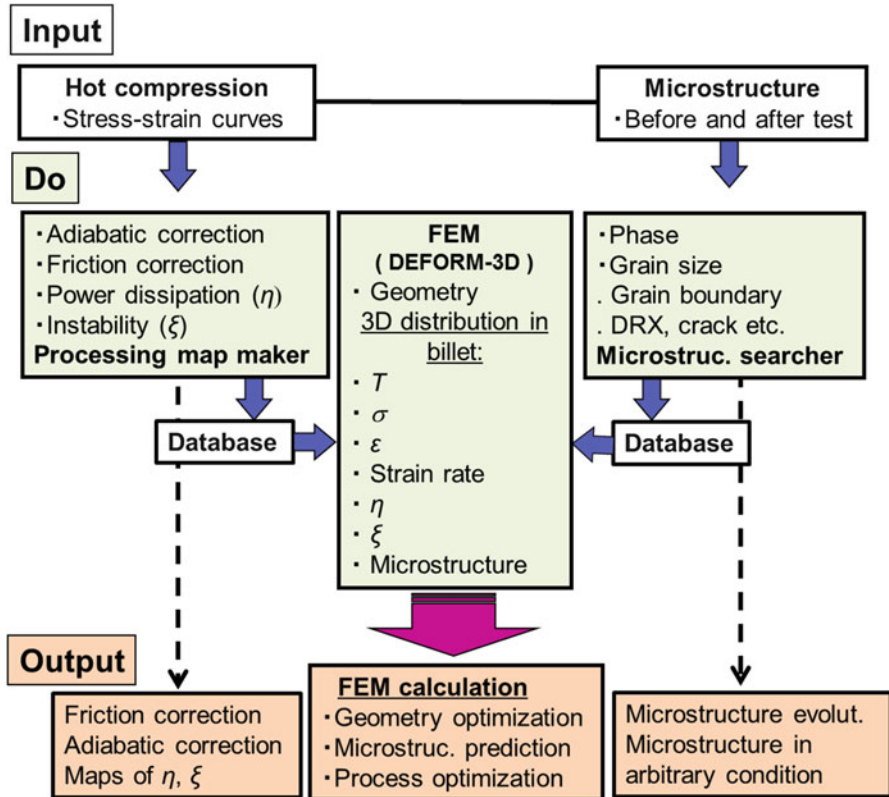**Fig. 3.12** Schematic figures showing the flow of smart hot forging technique

and

$$\eta = f(T, \varepsilon, \dot{\varepsilon}). \qquad (3.26)$$

Through the User Routine function attached on DEFORM-3D software, processing map database can be merged into the database of DEFORM-3D software. This is important in smart hot forging technique, since after the database of both FEM analysis and processing map is interconnected to each other, obtaining the three-dimensional processing map of a whole workpiece with even arbitrary geometry is possible on the basis of the working condition (T, ε, $\dot{\varepsilon}$) derived from the FEM analysis.

On the other hand, hot forging process of the workpiece with complex geometry can be simulated by FEM analysis calculation, where the geometrical evolution as well as the working condition such as T, ε, and $\dot{\varepsilon}$ distribution of the workpiece during the working process can be obtained in detail. Incorporating the processing map database into FEM software (DEFORM-3D), the working state in the interior of the workpiece can be predicted before the actual forging process. This is

meaningful in that not only the working condition of the workpiece such as T, ε, and $\dot{\varepsilon}$, but also that the parameters of the processing map could be obtained at the same time from Eqs. 3.25 and 3.26.

Similar to the processing map, microstructure of materials can be obtained through observing the compressed cylindrical sample in various working conditions by means of EBSD, XRD, or optical microscope (OM). On the basis of microstructure observation in a wide range of working conditions, a database for microstructure can be established by microstructure searcher software [50, 51] and incorporated into DEFORM-3D through the User Routine function attached on the software.

For given materials, by combining the databases of the processing map and microstructure with FEM simulation, both hot working condition and working state as well as the microstructure (given that a database of the microstructure is established) of a workpiece under an arbitrary hot forging process can be predicted with high reliability.

In order to give a further explanation on the details of smart hot forging technique, we take an example of Co–29Cr–6Mo–0.16 N alloy in producing an artificial hip joint femoral head through hot forging process. Extremely high surface hardness is required in artificial hip joint femoral head in order to enhance the wear resistance of the alloy, since it is subjected to a severe wear from its counterparts during service. Alloy rod billet with equal diameter and length of 45 mm was used in the present research. The objective head with a diameter of 30 mm will be machined from the billet after hot forging, where the microstructure of the head surface is hoped to be characterized by high hardness through grain refining (Fig. 3.13). A schematic figure for the mold as well as the relationship between the mold and billet is shown in Fig. 3.14. During hot forging, the billet was pushed by external pressure into the cavity of the mold, where the diameter of the front head of the billet varied from 45 mm into 35 mm in the first step and into 25 mm at the second step in the mold, resulting in one head of the billet severely plastically deformed into a round closed shape.

In order to obtain the optimum hot forging condition, FEM analysis on the hot forging process of the billet was carried out using a commercially available DEFORM-3D software. A model of rigid mold was used in the simulation. Temperature variation of the workpiece due to the contact with the mold and adiabatic heating in the interior of the workpiece was considered during FEM simulation.

The initial temperature of the billet and the mold was set to be 1,200 °C and 100 °C, respectively. Thermal conductivity and friction coefficient f between the billet and the mold were set to be 32 kW/(m^2.K) and 0.5, respectively. The true stress–true strain curves of Co–29Cr–6Mo–0.16 N alloy after both friction correction and adiabatic heating correction in Fig. 3.8 were used in FEM simulation, and the processing map database is established. At a hot forging rate of 40 mm/s, the simulation results in the effective strain distribution, temperature distribution, and the effective strain rate distribution are shown in Fig. 3.15a, b, and c, respectively. On the basis of the distributions of temperature, strain, and strain rate, the processing map of the billet during hot forging process, including both
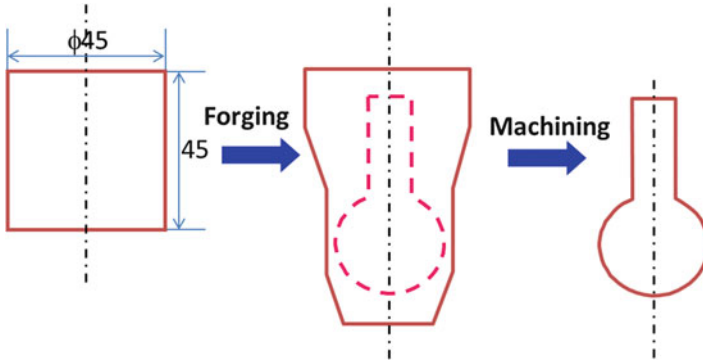
Fig. 3.13 Schematic figures showing the hot forging process of artificial hip joint head made of Co–29Cr–6Mo alloy

Fig. 3.14 Schematic figures showing the hot forging mold of artificial hip joint head
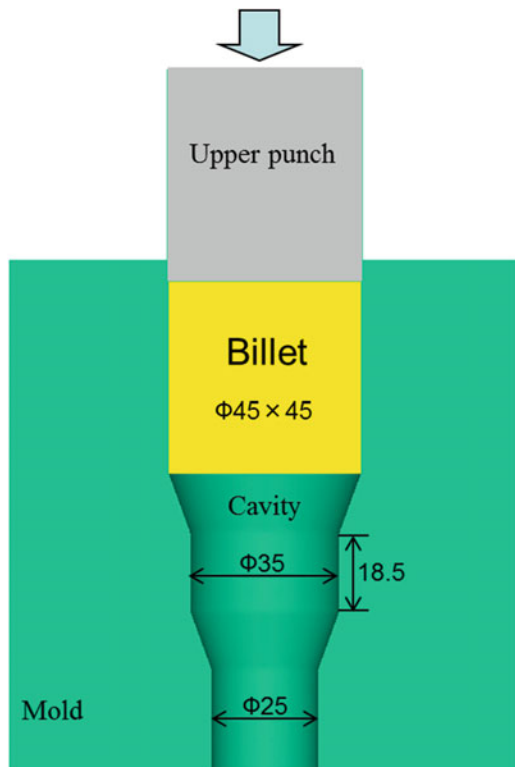
3D power dissipation map and 3D instability map throughout the billet, is shown in Fig. 3.15d, e, respectively.

Under this condition, approximately true strain of 0.4 was introduced homogenously surrounding the plastically deformed region of the artificial hip

Fig. 3.15 The simulation results in the (**a**) effective strain distribution, (**b**) temperature distribution, and the (**c**) effective strain rate distribution in the billet after hot forging at 1,200 °C with a forging rate of 40 mm/s; (**d**) 3D power dissipation map and (**e**) 3D instability map of the billet were derived from the working condition in (**a**) to (**c**)

joint femoral head billet. In addition, during the forging process, the temperature variation is not significant and is above 1,150 °C, and the strain rate is $1–8$ s^{-1} throughout the bi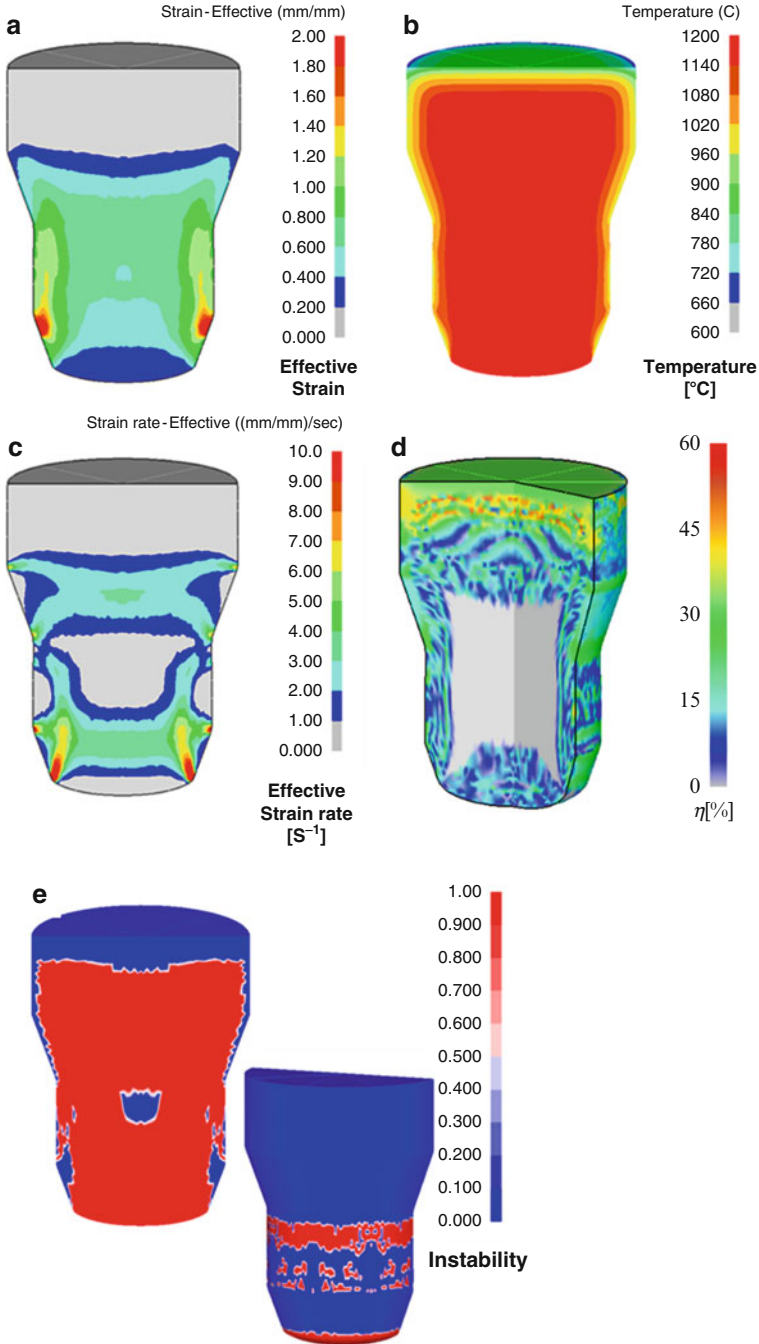llet. However, due to the direct contact between the billet and mold, extremely thin layer of the outmost surface of the billet demonstrated a drastic temperature decrease to below 1,000 °C. According to the 3D power dissipation map and 3D instability map of the billet, derived from the condition of temperature, strain, and strain rate as shown in Fig. 3.13a, b, and c, respectively, the artificial hip joint head surface was subjected to a working state with power dissipation coefficient of 15–30 % and stable condition for the head surface but instable for the billet surface layer which will be removed in the subsequent machining process.

Following the condition used in the simulation process, hot forging of the Co–29Cr–6Mo–0.16 N alloy artificial hip joint femoral head billet was carried out under 300 ton pressure. The profiles of the billet before and after hot forging are shown in top two figures, and the amplified figure of the billet surface and the profile of the billet after removing the outmost surface are shown in two figures below in Fig. 3.16. The billet after hot forging demonstrates a comparable geometry to that of simulation.
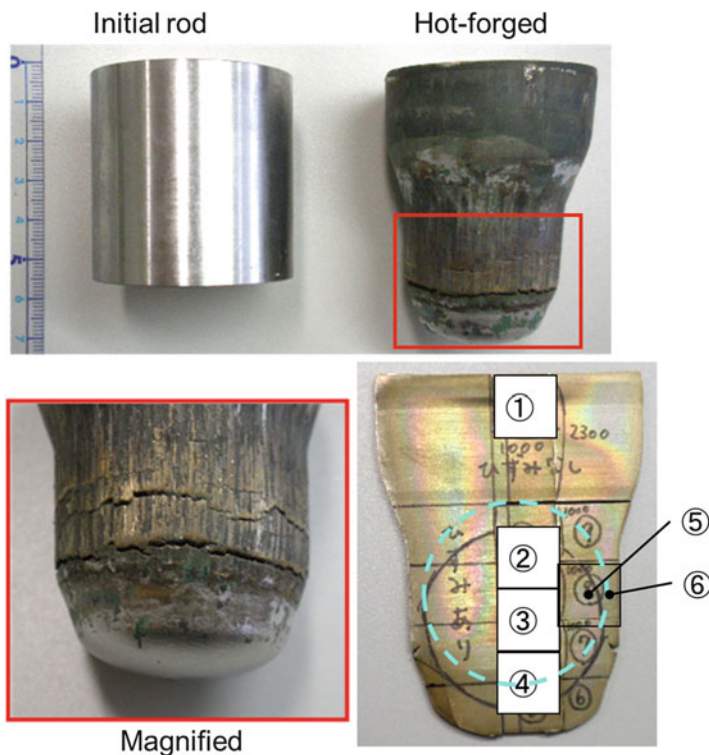
Fig. 3.16 The profiles of the billet before and after hot forging (the *top* two figures) and the amplified figure of the billet surface and the profile of the billet after removing the outmost surface (the *bottom* two figures)

As predicted by the 3D instability map of the billet in Fig. 3.15e, the outmost surface of the billet during hot forging was subjected to an unstable working condition and is characterized by crack. After removing the outmost surface layer of the billet, the substructure is free of crack, which is consistent with the results predicted by FEM simulation as shown in Fig. 3.15e, indicating the high reliability of the smart hot forging technique in predicting the working state of the billet during the hot forging process.

Microstructure characterization of the initial microstructure and various positions of the billet after hot forging (positions are indicated at the bottom right figure of Fig. 3.16) are shown in Fig. 3.17 in terms of inverse pole figure (IPF) map. The

Fig. 3.17 Microstructure characterization of the initial microstructure and various positions of the billet after hot forging (positions are also indicated at the *bottom right* figure of Fig. 3.16)

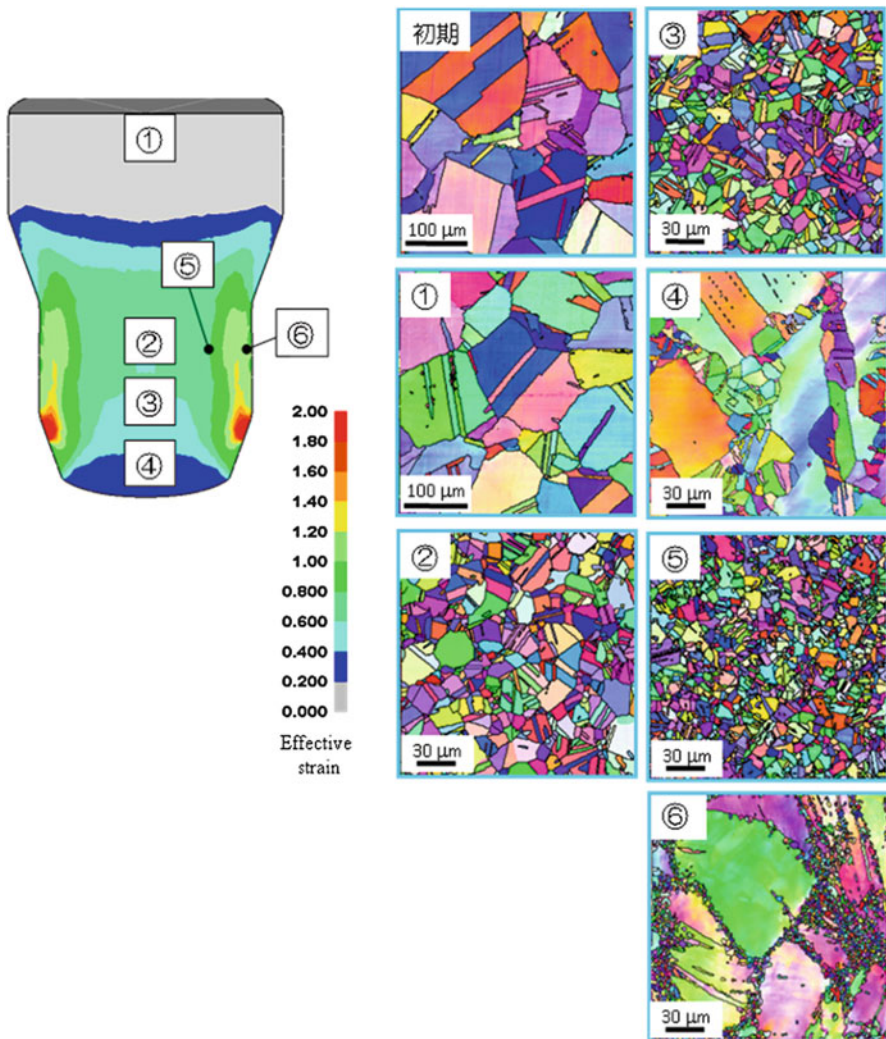initial microstructure of the billet indicates the equiaxed grains with the mean size of approximately 90 μm. Position ① at the center of the billet subjected to a slight deformation (Fig. 3.15a) indicates a comparable microstructure to the initial microstructure. Positions ② to ⑤, which were predicted to be the stable working condition, demonstrate the DRXed microstructure characterized by finer grain size compared to the initial microstructure. In contrast, position ⑥, which was predicted to be the unstable working condition, demonstrated DRX-free microstructure characterized by a localized deformation.

References

1. Chen Y, Li YP, Kurosu S, Yamanaka K, Tang N, Chiba A (2014) Effects of microstructures on the sliding behavior of hot-pressed CoCrMo alloys. Wear 319:200–210
2. Chen Y, Li YP, Kurosu S, Tang N, Koizumi Y, Chiba A (2014) Effects of phase constitution and carbide morphology on wear behavior of high-carbon biomedical CoCrMo alloys under lubricated conditions. Wear 310:51–62
3. Chiba A, Kumagai K, Nomura N, Miyakawa S (2007) Pin-on-disk wear behavior in a like-on-like configuration in a biological environment of high carbon cast and low carbon forged Co-29Cr-6Mo alloys. Acta Mater 55:1309–1318
4. Hsu HC, Lian SS (2003) Wear properties of Co–Cr–Mo–N plasma-melted surgical implant alloys. J Mater Process Technol 138:231–235
5. Li YP, Phacharaphon T, Tang N, Koizumi Y, Chiba A (2014) Effects of Al, Ti and Zr doping on oxide film of Co-29Cr-6Mo alloy used as Al die-casting molds. Corros Sci 84:147–158
6. Li YP, Tang N, Phacharaphon T, Koizumi Y, Chiba A (2013) Characterisation of oxide films formed on Co-29Cr-6Mo alloy used in die-casting moulds for aluminum. Corros Sci 73:72–79
7. Tang N, Li YP, Koizumi Y, Kurosu S, Chiba A (2014) Effect of nitriding treatment on corrosion behaviour of Co–Cr–Mo alloy in liquid Al. Corros Sci 78:244–250
8. Tang N, Li YP, Koizumi Y, Kurosu S, Chiba A (2013) Interfacial reaction between Co-Cr-Mo alloy and liquid Al. Corros Sci 75:262–268
9. Tang N, Li YP, Phacharaphon T, Koizumi Y, Chiba A (2014) Thermo-mechanical fatigue test of a wrought Co-based alloy as potential tooling material for die casting. Mater Sci Eng A 615:164–168
10. Tang N, Li YP, Koizumi Y, Kurosu S, Chiba A (2014) Surface nitriding of a Co–Cr–Mo alloy in nitrogen. Mater Chem Phys 145:350–356
11. Zhang X, Li YP, Tang N, Onodera E, Chiba A (2014) Corrosion behaviour of CoCrMo alloys in 2 wt% sulphuric acid solution. Electrochimica Acta 125:543–555
12. Shettlemore MG, Bundy KJ (2001) Examination of in vivo influences on bioluminescent microbial assessment of corrosion product toxicity. Biomaterials 22:2215–2228
13. Dobbs HS, Robertson JLM (2004) Heat-treatment of cast Co-Cr-Mo for orthopedic implant use. J Mater Sci 18:391–401
14. Yamanaka K, Mori M, Chiba A (2012) Enhanced mechanical properties of as-forged Co-Cr-Mo-N alloys with ultrafine-grained structures. Metall Mater Trans 43A:5243–5257
15. Yamanaka K, Mori M, Kurosu S, Matsumoto H, Chiba A (2009) Ultrafine grain refinement of biomedical Co-29Cr-6Mo alloy during conventional hot-compression deformation. Metall Mater Trans 40A:1980–1994
16. Li YP, Yamashita Y, Tang N, Liu B, Kurosu S, Matsumoto H, Koizumi Y, Chiba A (2012) Influence of carbon and nitrogen addition on microstructure and hot deformation behavior of biomedical Co-Cr-Mo alloy. Mater Chem Phys 133:849–854

17. Kurosu S, Matsumoto H, Chiba A (2010) Isothermal phase transformation in biomedical Co-29Cr-6Mo alloy without addition of carbon or nitrogen. Metall Mater Trans 41A:2613–2625
18. Yamanaka K, Mori M, Chiba A (2013) Nanoarchitectured Co–Cr–Mo orthopedic implant alloys: Nitrogen-enhanced nanostructural evolution and its effect on phase stability. Acta Biomater 9:6259–6267
19. Li YP, Yu J, Koizumi Y, Kurosu S, Chiba A (2012) Role of nitrogen addition in stabilizing the γ phase of Co-29Cr-6Mo alloy. Mater Chem Phys 133:29–32
20. Monajati H, Jahazi M, Yue S, Taheri AK (2005) Deformation characteristics of isothermally forged UDIMET 720 nickel-base superalloy. Metall Mater Trans 36A:895–905
21. Prasad YVRK, Seshacharyulu T (1998) Modelling of hot deformation for microstructural control. Int Mater Rev 43:243–258
22. Prasad YVRK, Gegel HL, Doraivelu SM, Malas JC, Morgan JT (1984) Modeling of dynamic material behavior in hot deformation: forging of Ti-6242. Metall Trans 15A:1883–1892
23. Suzuki T, Li YP, Koizumi Y, Chiba A (2013) Quantitative evaluation in hot workability of SUS303 free-cutting steel. Mater Sci Eng A 563A:117–124
24. Liu B, Matsumoto H, Li YP, Koizumi Y, Liu Y, Chiba A (2012) Dynamic phase transformation during hot-forging process of a powder metallurgy α + β titanium alloy. Mater Trans 53:1007–1010
25. Liu B, Li YP, Matsumoto H, Liu YB, Liu Y, Chiba A (2011) Thermomechanical characterization of P/M Ti-Fe-Mo-Y alloy with a fine lamellar microstructure. Mater Sci Eng A 528:2345–2352
26. Kartika I, Li YP, Matsumoto H, Chiba A (2009) Constructing processing maps for hot working of Co-Ni-Cr-Mo superalloy. Mater Trans 50:2277–2284
27. Gao Z, Grandhi RV (2000) Microstructure optimization in design of forging processes. Int J Mach Tools Manuf 40:691–710
28. Monajati H, Jahazi M, Bahrami R, Yue S (2004) The influence of heat treatment conditions on γ′ characteristics in Udimet® 720. Mater Sci Eng A373:286–293
29. Briottet L, Jonas JJ, Montheillet F (1996) A mechanical interpretation of the activation energy of high temperature deformation in two phase materials. Acta Mater 44:1665–1672
30. Bay N (1987) Friction stress and normal stress in bulk metal-forming processes. J Mech Work Technol 14:203–223
31. Male AT, Depierre V (1970) The validity of mathematical solutions for determining friction from the ring compression test. J Lubr Technol 92:389–397
32. Bowden FP, Rabor D (1950) The friction lubrication of solid, 1st edn. Oxford University Press, London, pp 1
33. Schey JA (1983) Tribology in metalworking: friction, lubrication and wear. American Society for Metals, Metals Park, p 1
34. Koul AK, Immarigeon JP (1987) Modelling of plastic flow in coarse grained nickel-base superalloy compacts under isothermal forging conditions. Acta Metall 35:1791–1805
35. Chiba A, Lee SH, Matsumoto H, Nakamura M (2009) Construction of processing map for biomedical Co-28Cr-6Mo-0.16N alloy by studying its hot deformation behavior using compression tests. Mater Sci Eng A 513–514:286–293
36. Yamashita Y, Li YP, Matsumoto H, Koizumi Y, Chiba A (2011) Construction of processing map for biomedical Co-29Cr-6Mo-0.23C-0.14N alloy by using compression tests. Mater Trans 52:780–786
37. Li YP, Tanaka Y, Onodera E, Chiba A (2012) Hot working prediction system and hot working prediction method. International Patent, WO2013-128646, March 2012
38. Onodera E, Kurosu S, Li YP, Matsumoto H, Chiba A (2010) Hot forging process of artificial hip joint made of Ni-free Co-29Cr-6Mo-0.12N alloy by means of intelligent hot forging processing method. J JSTP 51:227–232
39. Ebrahimi R, Najafizadeh A (2004) A new method for evaluation of friction in bulk metal forming. J Mater Proc Technol 152:136–143

40. Toroghinejad MR, Ashrafizadeh F, Najafizadeh A, Humphreys A, Liu D, Jonas JJ (2003) Effect of rolling temperature on the recrystallization texture of warm rolled steels. Metall Mater Trans 34A:1163–1174
41. Li YP, Onodera E, Chiba A (2010) Evaluation of friction coefficient by simulation in bulk metal forming process. Metall Mater Trans 41A:224–232
42. Rowe GW (1965) An introduction to the principles of metalworking. Edward Arnold, London
43. Dieter GE (1986) Mechanical metallurgy, 3rd edn. McGraw Hill Book Co., New York
44. Li YP, Onodera E, Matsumoto H, Koizumi Y, Yu S, Chiba A (2011) A new method of compensation for friction investigated by FEM analysis. ISIJ Int 51:782–787
45. Oh SI, Semiatin SL, Jonas JJ (1992) An analysis of the isothermal hot compression test. Metall Trans 23A:963–975
46. Li YP, Matsumoto H, Chiba A (2009) Correcting the stress–strain curve in stroke-rate controlling forging process. Metall Mater Trans 40A:1203–1209
47. Li YP, Onodera H, Matsumoto H, Chiba A (2009) Correcting the stress–strain curve in hot compression process to high strain level. Metall Mater Trans 40A:982–990
48. Mataya M, Sackschewsky V (1994) Effect of internal heating during hot compression on the stress–strain behavior of alloy 304L. Metall Mater Trans 25:2727–52
49. Ziegler H (1965) Progress in solid mechanics, vol 4. Wiley, New York, pp 91–193
50. Li YP, Onodera E, Matsumoto H, Chiba A (2010) Compensation for friction and temperature increase due to adiabatic heating during hot compression testing and construction of "processing map" of biomedical Co29-Cr-6Mo-0.16N alloy. J JSTP 51:221–227
51. Li YP, Chiba A, Tanaka Y, Onodera E (2012) Processing map creation program. International Patent, WO2013-094225, Feb 2012

Chapter 4
Electroforming as a New Method for Fabricating Degradable Pure Iron Stent

**Agung Purnama, Afghany Mostavan, Carlo Paternoster,
and Diego Mantovani**

Abstract The first example of a documented electroforming process dates back to 1837 when a layer of electrodeposited copper was found on the surface of a printing plate. Since then, it became a basic manufacturing process to produce delicate metallic components such as nickel thin foils for solar panels, perforated screen-printing cylinders used for fabric and carpet printings, digital recording devices, etc. Recently, electroforming is used for the fabrication of iron-based materials designed for cardiovascular stents. Electroformed iron shows a higher corrosion rate in simulated biological environment; this behaviour is supposed to be influenced by its microstructure which is finer than that of iron produced with traditional techniques. A high corrosion rate can be beneficial for cardiovascular stent applications: a complete stent dissolution in 12–18 months can effectively prevent both late thrombosis and further treatment of paediatric patients, usually requiring a continuous vessel remodelling. Faster corrosion rate of iron-based material is advantageous for cardiovascular stent application in order to avoid late stent thrombosis and arterial growth mismatch in young patients leading to a secondary revascularization procedure. Electroformed iron has mechanical properties comparable to those of stainless steel (stent reference metal) with the advantage of the total dissolution of the material after the accomplishment of its function: for this reason, this metal can be considered as a valid alternative to magnesium-based materials. Nevertheless, electroforming is influenced by parameters such as electrolyte bath composition, current density, pH, temperature, additives, cathode, etc. that have a significant effect on the structure of the produced materials.

A. Purnama • A. Mostavan • C. Paternoster • D. Mantovani (✉)
Laboratory for Biomaterials and Bioengineering (CRC-I), Department of Mining, Metallurgy and Materials Engineering & CHU de Québec Research Center, Laval University, Adrien-Pouliot 1745-G, 1065 Avenue de la Médecine, G1V0A6 Québec, Canada
e-mail: Diego.Mantovani@gmn.ulaval.ca

4.1 Introduction

Electroforming is a special form of electroplating, specifically defined by the American Electroplaters and Surface Finishers (AESF) Society as the production or reproduction of an article by electrodeposition upon a mandrel or mould that is subsequently separated from the deposit [1]. Electroforming was first recognized during the electrodeposition of copper onto a printing plate in 1837 [2]. Electroforming is considered as an alternative manufacturing process to casting, forging, drawing, machining and other traditional production techniques. Its outstanding ability to reproduce complex shapes and small dimension manufacturs makes electroforming a competitive process compared to other ones, suitable to be efficiently implemented in an industrial production system [1].

Generally, electroplating is applied to obtain coatings with conductive properties, enhanced corrosion resistance or a decorative purpose. In the case of electroforming, electrodeposited layers are used as free-standing elements, reproducing exactly the geometrical features and dimensions of the final piece. The use of stable permanent moulds allows a precise reproduction of the model features and a high reproducibility of the formation process. After deposition, electroformed layers need to be removed from the cathode because they are used as self-standing pieces; hence, the electroformed deposits are often thicker compared to the electroplated ones [3]. The cathode is the electrode acting as a mould or mandrel, and it reproduces the precise geometry and dimensions of the final piece to be obtained. Since electroformed deposits need to be easily removed from the mandrel, a strong adhesion after the electroforming process should be avoided. Nevertheless, a net detachment of the electroformed layer from the mandrel could not be easily achieved. To solve this problem, mechanical separation procedures are often adopted, as well as chemical and thermal approaches.

Electroforming involves a multidisciplinary background, and it comprises four major features, including imaginative conception, engineering, electrochemistry and materials. The imaginative conception assumes the crucial design that integrates engineering concept and practicability. The engineering part consists of design, manufacture and component adjustment for the various systems. The electrochemistry part includes the choice of mandrel, electrolyte bath, temperature, pH, additive, current, etc. Finally, the material part consists of characterization of grain size, alloy composition, hardness, elongation, porosity, corrosion resistance, tensile strength, etc. [2].

4.2 Basics of Electroforming

Electroplating involves the electrochemical dissolution of the metal at the anode, which is transferred to the cathode, as described in Fig. 4.1. The anode serves as a metal ion source that equilibrates the metal deposition on the cathode. For this
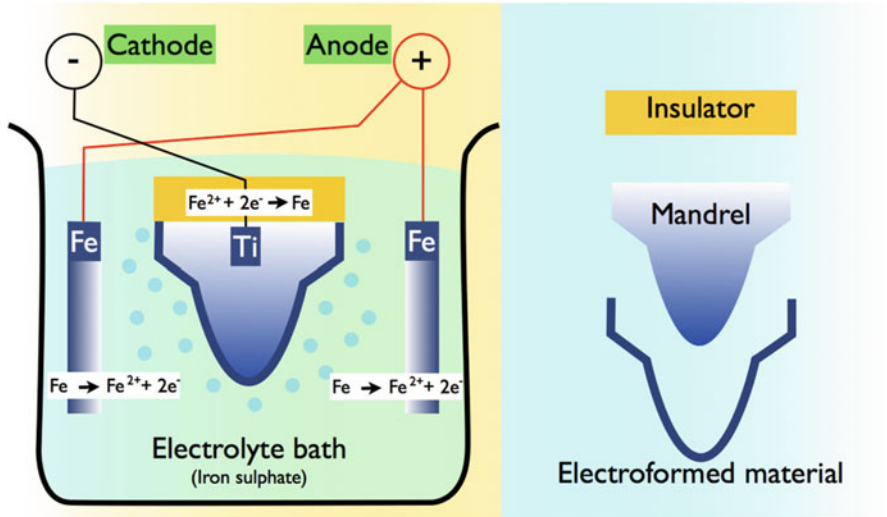
Fig. 4.1 General setting of electroforming cell consisting of anode, cathode and electrolyte

reason, the anode undergoes an oxidation process releasing metallic ions into the solution. On the other side, metallic ions are deposited on the surface of the cathode throughout a reduction process. The thickness of the deposited layer can be calculated with Faraday's equation (Eq. 4.1) [4] where T is the thickness (cm), I is the applied current (A), and t is the deposition time (s); A_{wt} is the atomic weight (g/mol), n is the number of electron involved in the reaction, and F is the faraday constant (96,487 C/mol); ρ is the material density (g/cm^3) and A is the surface area of the cathode (cm^2):

$$T = \frac{I \cdot t \cdot A_{wt}}{n \cdot F \cdot \rho \cdot A} \tag{4.1}$$

The transfer of matter from the anode to the cathode is realized in an electrolyte solution, which contains ions of the same metallic element that has to be deposited. Electrolyte solution plays an important role in determining the quality of the products. There are at least two typical electrolyte solutions, chloride- and sulphate-based baths. Depending on the metal being electroformed, the result might vary depending on the type of bath. Kim et al. [5] reported that chloride bath shows a higher current efficiency compared to that of sulphate bath when they are used to manufacture CoFe, NiCo and CoNiFe alloys, probably due to the catalytic activity of chloride ions in the deposition of Ni and Fe through the formation of an ion bridge between the electrode and the metallic ions being discharged [5]. Moreover, the use of chloride bath has been reported to produce a ductile deposit at higher temperatures for iron electroforming, making it a common electrolyte solution for industrial processing. However, the use of sulphate bath has been reported to produce pure iron deposit with smoother surfaces and a low

amount of pitting leading to thicker layers [4]. Therefore, careful selection of electrolyte bath is highly required as a function of the material being deposited.

The shape of the deposit reproduces that of the cathode/mandrel; low adherence between the substrate and the deposit is required to easily remove the electroformed manufact. Metallic materials currently used for the realization of a mandrel are, for example, titanium and stainless steel. This can be obtained by creating a passive layer on the surface of the mandrel allowing an easier detachment of the deposit; for this reason, sodium dichromate solution is often applied on the surface of a mandrel made of stainless steel or nickel [3]. Moreover, when an insulating material is used as a mandrel, the main challenge is to make the surface conductive in order to attract the metal ions. Generally, the conductivity of such a material can be modified or improved by the application of silver film with painting or spraying [2].

Additionally, mandrels can be divided into two categories: permanent and temporary ones [3]. Permanent mandrels are made of metallic or nonmetallic materials that can be formed into a precise shape with the advantage of a high resistance against mechanical damage and/or chemical corrosion. Examples of materials used for permanent mandrels are stainless steel and photosensitive resins that are important materials for compact disc (CD) industry, since they allow the reproduction of highly accurate surface details. In contrast to permanent mandrels, temporary ones are expected to be dissolved after the electroforming process. For this reason, metals with low melting temperature such as bismuth and tin are normally chosen. Otherwise, reactive metallic materials such as aluminium can also be envisaged because they can be dissolved in concentrated basic solutions (sodium hydroxide). This procedure leaves the electroformed nickel intact because of its resistance to strong alkaline solution [2].

4.3 Industrial Applications

The final products of electroforming can be easily found in everyday life. Electroforming is involved in the making of screen-printing cylinder that gives motives to our clothes, blankets, wall papers, coffee cups and even for banknotes. Electroforming is also used to create televisions, radios and computers' circuit boards, and also it is used in the process for the production of the holographic logo available on credit cards. The music recording industry uses electroforming in the process of CD making. The patterns on the above-mentioned final products all come from electroformed masters [2, 6].

1. Audiovisual compact discs (CDs): a single CD consists of a helical track with 30 billion pits only 0.1 μm deep and 0.4–0.6 μm wide. Size accuracy and position precision on the track are required in order to maintain a high sound quality.
2. Electroformed foil products: nickel thin foil is vastly used for printed circuit boards with welded connection. Nickel foil is also used to fabricate solar energy absorbers.

3. Mesh products: electroformed mesh products with particular patterns are used for screen-printing cylinders in the typography industry to produce fabrics and carpets.
4. Macro electroforms: macro electroforms are used to produce individual large components in the aerospace industry as well as in the automotive industry.
5. Small electroforms: electroforming enables the development of micro engineering applications to produce micron-scale components for automotive, aerospace and biomedical industry. An innovative factual application is the production of small electric motors used in cardiovascular disease treatment. These miniaturized machines can pass arteries to scour the walls and remove the plaque deposit.

4.4 Electroforming of Pure Iron

Pure iron has been proposed as a biodegradable metal due to its superior mechanical properties when compared to those of its counterpart—magnesium alloys. Various fabrication methods have been applied to produce iron as a biodegradable implant including casting [7], powder metallurgy [8] and electroforming [9]. From the processing point of view, electroforming is associated with a low production cost and a simpler manufacturing process compared to other ones. Electroforming was then considered as an interesting fabrication method to be explored for biodegradable implant application. The first electroformed iron application for biodegradable cardiovascular stents was reported by Moravej et al. [9]. It is considered to be an ideal process for stent making, since a precise dimension is required to produce a thin-walled bulk material with superior purity and adjustable microstructures.

Some parameters need to be optimized during the electroforming process such as electrolyte composition, current density, pH and temperature. The electrolyte is a very important factor, since it is the source of metallic ions. Several electrolytes such as iron sulphate, iron chloride, iron sulphate–chloride, iron sulfamate, iron fluoborate or alkaline solutions [4] are currently used in industrial applications. Furthermore, the electrolyte composition has a significant influence on the properties of deposited iron. As previously reported [9], an electrolyte with $400 \ \mathrm{gL}^{-1}$ $FeCl_2$ and $80 \ \mathrm{gL}^{-1}$ $CaCl_2$ in de-ionized water was selected to produce electroformed iron. The solution known as Fischer–Langbein is a common electrolyte used to produce a ductile electroformed iron. Moreover, additives such as saccharin and sodium dodecyl sulphate are added, respectively, as stress-reducing and wetting agents (anti-pitting), enhancing the quality of the deposits.

Other important parameters about iron electroforming are pH, temperature, current density and cathode material. The pH is controllable by the addition of HCl, H_2SO_4 or NaOH. It was shown that for $0 \leq \mathrm{pH} \leq 3$, iron chloride baths have a significant effect on mechanical properties of electroformed iron. Electrolytes with $\mathrm{pH} < 0$ produce highly stressed and brittle deposits compared to those obtained with $\mathrm{pH} \geq 3$. The temperature of the electrolyte has an effect on electrodeposits' grain size and texture, as well as on the mechanical properties. Higher temperatures are

associated to ductile deposits, but they tend to produce larger grain size layers with reduced hardness, tensile strength and internal stress [5].

Current density can control the nucleation rate during the electroforming process. Increasing the current density increases the difference in the electrode potential between its equilibrium potential and its operating potential—overpotential—thus increasing the nucleation rate [4]. Cathode chemical composition and surface state are also important parameters, influencing the microstructure and properties of the deposits. In electroforming process, less adhesive cathode is preferred since the deposited film has to be separated from the cathode after deposition. The selection of cathode depends on the desired shape and material dimension. The material of cathode needs to be conductive in order to transfer the electrical current required for electrodeposition [3].

In the work carried out by Moravej et al. [10], the deposition was carried out with a pH = 1, a bath temperature of 90 °C and a current density of 2 A dm^{-2}. These parameters have been proved to produce an electroformed foil with high ductility and a lower surface roughness. Commercially pure titanium was selected as cathode material due to its reduced adherence to iron, allowing a rapid mechanical removal from the cathode. Foils produced with these parameters were studied to compare their microstructure, mechanical properties and corrosion behaviour with those of rolled iron and stainless steel 316 L. The results showed that grain size and texture were the main factors influencing mechanical properties and corrosion behaviour in simulated biological solution. Electron back-scattered diffraction (EBSD) revealed that electroformed iron showed a highly oriented (111) fibre texture, and it has columnar grains with an average size of ~4 μm (Fig. 4.2). From the mechanical point of view, the yield strength of electroformed iron was comparable to that of 316 L SS, even though its ductility was lower because of the internal stress. Therefore, annealing was performed to induce recrystallization due to the presence of residual stresses in microstructure of the material, which has a higher concentration of structural defects. The elongation at break changed significantly from 8 % as produced to 18 % after annealing at 550 °C for 1 h and 30 % after annealing at 600 °C for 1 h. The average grain size after heat treatment at 550 °C was ~6 μm, significantly smaller than that of iron produced by melting, which after recrystallization-induced heat treatment presented an average grain size of ~25 μm. Static and dynamic degradation test on electroformed iron showed a faster degradation rate compared to that one produced by melting. The enhanced corrosion behaviour of the former was correlated to its finer structure, while the latter has a lower density of grain boundaries that makes the material less susceptible to chemical attacks. Another cause of the higher rate corrosion of electroformed iron is the high density of structural defects [10].
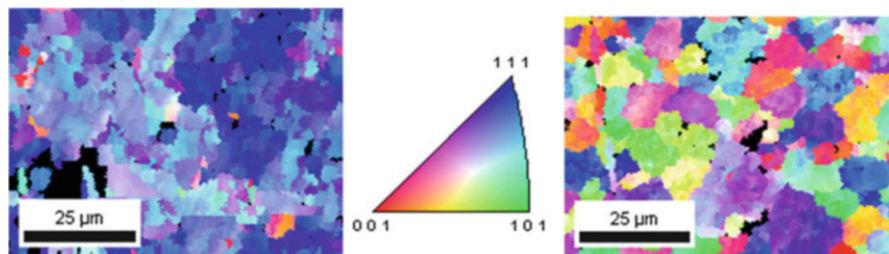
Fig. 4.2 Orientation map of electroformed iron surface. *Left*: electroformed; *right*: after annealing at 550 °C (Reprinted from Ref. [10], Copyright 2010, with permission from Elsevier)

4.5   Electroforming of Binary and Ternary Alloy

Metal alloying was used to improve mechanical properties and to accelerate corrosion rate, especially for iron. Hermawan et al. [8] were the first who introduced Mn as an alloying element for iron-based alloys cardiovascular stent. The results showed that Fe-35Mn has superior mechanical properties close to those of 316 L SS, the gold standard for cardiovascular stents. The corrosion rate of Fe-35Mn doubled compared to that of rolled pure iron. Furthermore, Schinhammer et al. [11] developed a new alloy with Mn and Pd. These elements create a noble intermetallic phase (Fe, Mn) Pd which is responsible for both an increased degradation rate and enhanced mechanical properties. Liu et al. [12] studied Fe–X binary alloys with another approach. They studied the effect of Mn, Co, Al, W, Sn, B, C and S on pure iron. They concluded that C, S, W and Co could be successfully used as potential alloying elements for biodegradable iron-based biomaterials. In another study, Wegener et al. [13] produced Fe–C, Fe–P, Fe–B and Fe–Ag alloys. The effect of P was beneficial for density and strength and useful to increase the degradation rate.

Mechanical properties and corrosion behaviour of electroformed iron still need to be improved and fully understood. Another suitable strategy for the modification of electroformed material properties is the deposition of layers with an alloying element that shows a gradual amount variation over thickness. This deposition system could create different phases and microstructures influencing the mechanical properties and corrosion behaviour. The electroforming of binary and ternary alloys has been explored in several publications [4, 14–21]; at least 22 elements have been proposed by Schlesinger et al. [4] for the realization of iron-based alloys. In biodegradable metal applications, it is important to choose a nontoxic element for the human body. For this reason, some elements that are safe to be alloyed with iron by electroforming include carbon, phosphorus, zinc, boron and cobalt. Table 4.1 shows some data about binary and ternary alloys, which have been applied for various purposes.

The properties of binary and ternary alloys are influenced by the kind of solid solution formed. For mechanical properties, elements can form interstitial or substitutional solid solutions, depending on the difference of atomic size between

Table 4.1 Various applications of Fe-based alloys

	Bath composition (g/ml)	pH	Temp (°C)	Current density (A/dm^2)	Application
Fe	$FeCl_2$ 0.4	1–3	86–198	10	Protective shield
[14]	$CaCl_2$ 0.08				
Fe–Co	$FeCl_2$ 11.8	0.3	25–90	6	Micro electro mechanical system
[15]	$CoCl_2$: balance				
	$CaCl_2$ 9				
Fe–Ga	$Ga_2(SO_4)_3$ 1.5	3	25	N/A	Magnetostriction material
[16]	$FeSO_4$ 0.19				
	H_3BO_3 8.1				
	$C_6H_5Na_3O_7$ 0.58				
	$HC_6H_7O_6$ 0.23				
Fe–Ni	$FeCl_2$ 400	0.5	95	5–20	Moulding
[17]	$NiCl_2$ 30				
	$CaCl_2$ 80				
Fe–Ni	$FeSO_4.7H_2O$ 3.29	2	70	0.1–10	Magnetic materials
[18]	$NiSO_4.6H_2O$ 0.95				
	$NaCl$ 0.05				
Ni–Fe	$NiSO_4.6H_2O$ 0.38	0.2–3	50	2–8	Lithography
[19]	$FeSO_4$ 0.014				
	H_3BO_3 0.025				
	$NiCl_2$ 0.001				
	$C_7H_5NO_3S$ 0.001				
	$NaC_{12}H_{25}SO_4$ 0.0005				
Co–Fe	$FeSO_4.7H_2O$ 0.006	3	30	0.3	Magnetic film
[20]	$CoSO_4.7H_2O$ 0.056				
	$C_7H_5NO_3S$ 0.004				
	$NaCl$ 0.03				
	H_3BO_3 0.025				
Ni–Fe–P	$H_4N_2NiO_6S_2$ 0.346	1–3	50–70	5	Electronic component
[21]	$H_4FeN_2O_6S_2$ 0.001				
	H_3PO_4 0.0007				
	H_3BO_3 0.040				
Fe–C–B	$FeCl_2$ 0.126	3.5	50	5	Antifriction

Table 4.1 (continued)

	Bath composition (g/ml)	pH	Temp (°C)	Current density (A/dm^2)	Application
[4]	H$_3$BO$_3$ 0.040				
	C$_4$H$_6$O$_5$ 0.0007				
	C$_2$H$_{10}$BN 0.003				
Fe–C–P	FeCl$_2$ 0.020	3.5	50	3	Antifriction
[4]	C$_6$H$_8$O$_7$ 0.0012				
	C$_6$H$_8$O$_6$ 0.003				
	H$_3$PO$_4$ 0.015				

the solute (added element) and the solvent (iron). If the solute atoms are equal or smaller than the solvent ones, they can fill the interstices between the host atoms. This process causes the distortion of the lattice, and it is responsible for the phenomenon known as solid solution hardening. Another hardening mechanism is present in substitutional solid solution; this kind of hardening occurs for solute atoms large enough to replace solvent atoms in their lattice positions (Hume–Rothery rules). Furthermore, if solute and solvent form a second phase finely dispersed throughout the matrix of the base metal, the mechanical properties of the matrix are increased. For corrosion properties, the presence of different phases other than the solvent one is responsible for phenomena of micro galvanic corrosion.

4.6 Microtube Fabrication

Electroforming has been used as a micro-fabrication technique to produce thin-walled tubes of small diameter. For medical applications, electroforming can factually produce stents. By this process, it is possible to easily make layers with a thickness in the range 100–200 μm; electroforming is also suitable to produce layers with a thickness of a few mm [22], depending on the deposition condition and on the deposited material. Moreover, since it is possible to produce minitubes with a single step process, electrodeposition drastically reduces the multiple working steps needed in traditional metal working processes (from billet or ingot casting to hard drawing into a tubular shape).

Moravej et al. [23] obtained an electroformed iron tube using a tin cylindrical cathode. Since the cathode had a low melting point, it was removed by melting at 300 °C. Subsequently, grinding and polishing were applied on the internal surface of the iron tube to remove the remaining tin as shown in Fig. 4.3.

Laser cutting was applied after cathode melting to shape the stent in its final form (Fig. 4.4). Annealing and polishing by acid pickling were then carried out to,
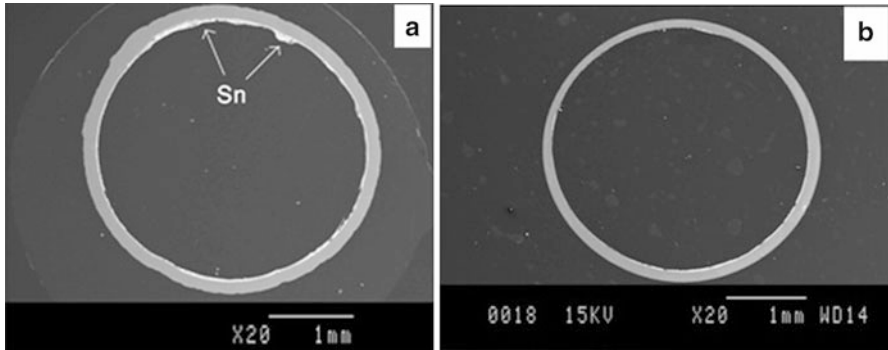
Fig. 4.3 Cross section of an electroformed tube: before grinding (**a**) and after internal grinding (**b**) (Reprinted under the policy of MDPI publisher—Open Access Publishing with proper citation from Ref. [23])
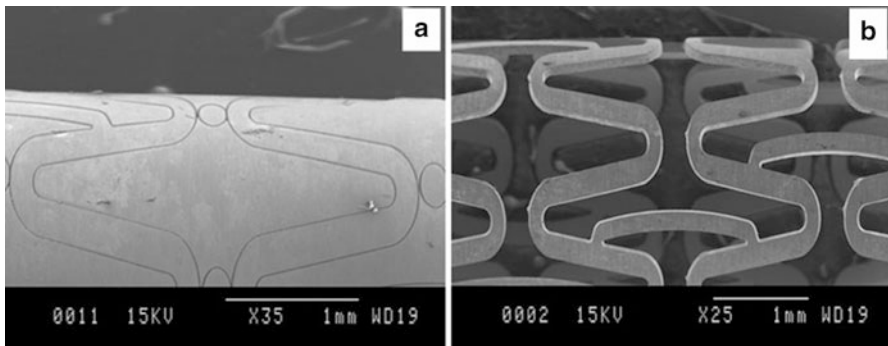

Fig. 4.4 SEM micrograph of annealed cut iron tube (**a**) before laser cutting and (**b**) after acid pickling (Reprinted under the policy of MDPI publisher—Open Access Publishing with proper citation from Ref. [23])

respectively, homogenize the structure and relieve the stresses in the heat-affected zone and to remove burrs and debris as a result of laser cutting. In conclusion, a completely functional cardiovascular stent was produced by electroforming and laser cutting with fine microstructure and equiaxed grains with an average grain size of 5 µm.

4.7 Advantages and Disadvantages of Electroforming

The major advantages of electroforming are reproducibility, precision, fabrication of complex shapes with homogeneous thickness and the possibility to produce manufacturs with a broad range of size. The reiterated use of the same permanent mandrel allows a high reproducibility (few µm of thickness difference among all the pieces produced with the same cathode) for each replicate [1]. Additionally,

complex shapes components are also feasible with electroforming method without involving traditional and advanced fabrication process such as pressing, drilling, machining, deburring, welding, etc. reducing remarkably the manufacture costs to those needed for a reusable electrolyte bath. Moreover, electroforming covers a large-scale production in the sense of quantity since identical mandrel could be produced by electroforming itself and be used subsequently in the same bath to produce identical components simultaneously [24]. Furthermore, producing large components is also possible making it as a fabrication technique with an extensive range of size that is more advantageous when compared to the other fabrication methods such as casting, powder metallurgy and others. Interestingly, electroforming allows the fabrication of alloys with different structures such as sandwich-structured alloys giving the access to tunable mechanical properties and corrosion behaviour.

Along with its superior advantages, electroforming also presents some disadvantages such as the presence of internal stresses, which are produced during the process and results in cracking and peeling of the deposits from the cathode. This limitation is often removed by the addition of stress-reducing additives such as saccharin, sodium lauryl sulphate or thiourea [5]. It has been reported that the addition of saccharin significantly reduces the internal stress of electrodeposited FeNiCo films on NiFe cathodes [25]. In the same way, saccharin has been reported to decrease the passivation performance of CoFe alloy resulting in an enhanced corrosion behaviour, compared to that shown by the same alloy produced with the same bath without saccharin [26]. Moreover, electroformed components are often found to have a nonhomogenous thickness, but this problem is solved by applying a supplementary anode into recessed area to increase the local deposition rate [2]. The separation of electroformed components from the cathode is sometimes difficult; hence, mechanical as well as chemical or thermal treatments are frequently employed to solve this problem [3]. Another critical parameter for the electroforming process is the deposition time. Low current densities are often used to avoid the formation of a high number of defects [27], but for this reason, the deposition time is often prolonged. Some techniques have been reported to overcome this inconvenience, either by operating parallel production lines or by rotating the mandrel with high relative velocity. This expedient increases the permissible applicable current density without increasing the defect density but decreasing the deposition time [28].

4.8 Degradation Behaviour and Biocompatibility Aspects of Electroformed Iron

The degradation behaviour of electroformed iron plays a key role in determining its biocompatibility. Through the degradation process, electroformed iron dissolves over time, leaving a fully remodelled artery. The dissolving process of iron generates degradation products released in the body in the form of ions, hydroxides, gases

and particulates. These degradation products could potentially harm the surrounding tissues especially if they are generated abundantly and within a relatively short period. In order to understand how electroformed iron could harm the surrounding cells, it is important to assess the biodegradation mechanisms. The mechanism of biodegradation for electroformed iron or simply iron in general can be separated into the following steps (adapted from [29]).

4.8.1 Initial Degradation

After the stent placement into the artery, iron is oxidized to metallic ions in anodic spots according to Eq. 4.2. This anodic reaction generates electrons, which are subsequently engaged in the cathodic reaction that reduces the oxygen that dissolved in the body liquid (Eq. 4.3). These reactions occur all over the surface due to the different potentials between the metal matrix and the intermetallic phases or surface defects (such as grain boundaries):

$$Fe \rightarrow Fe_{2+} + 2e^- \tag{4.2}$$

$$2H_2O + O_2 + 4e^- \rightarrow 4OH^- \tag{4.3}$$

4.8.2 Hydroxide Layer Formation

Metal ions from Eq. 4.2 then react with the hydroxyl ions from Eq. 4.3, generating insoluble iron hydroxides on the surface following Eq. 4.4:

$$Fe^{2+} + nOH^- \rightarrow Fe(OH)_n \tag{4.4}$$
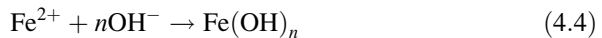
4.8.3 Pit Formation

Since the formation of the hydroxide layer on the surface is not homogeneous, negative chloride ions penetrate the hydroxide layer forming metal chloride, to compensate the increase of metal ions. Iron chlorides are then hydrolysed by water resulting in the formation of free acid (Eqs. 4.5 and 4.6), which leads to an autocatalytic reaction and to the formation of pits:

$$Fe^{2+} + 2Cl^- \rightarrow FeCl_2 \tag{4.5}$$

$$FeCl_2 + 2H_2O \rightarrow Fe(OH)_2 + 2HCl \tag{4.6}$$
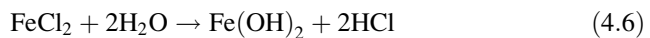
4.8.4 Calcium/Phosphorus Layer Formation

Calcium ions and phosphates forming apatite are then deposited on the stable hydroxide layers; this is due to the saturation of calcium and phosphate in the body fluid and to the local pH change.

4.8.5 Degradation and Layer Disintegration

As the degradation layers are formed, endothelization of the degradable metallic stent (DMS) and device incorporation in body tissues occurs. Cell action causes the disintegration of the corrosion layers into irregular particles that can be enclosed in the fibrous tissue by macrophages, depending on the size of the debris. The DMS degrades progressively under the activity of cells, as previously described, until it completely disappears.

The application of electroformed metal for medical devices is still limited, probably due to brittleness, presence of impurities and internal stress, which are produced during the electroforming process. For this reason, there are only several metals that are commercially produced by electroforming such as copper, nickel and iron [6]. Only electroformed iron has been thoroughly explored for the fabrication of cardiovascular stents. As a degradable metal, electroformed iron has been reported to have a fine grain structure of 4 μm resulting in high yield strength, 360 MPa, and ultimate tensile strength of 423 MPa, higher than those of other metallic biodegradable metals. Moreover, annealing at 550 °C was found to improve its ductility [9]. Electroformed iron showed a degradation rate of 0.25 mmpy, which is higher than iron produced by traditional techniques (0.14 mmpy). Even though electroformed iron did not affect cellular metabolic activity, it had a significant effect on cellular proliferation [10]; this effect is considered as advantageous to avoid in-stent restenosis [10, 30].

4.9 Future Perspective

Up to now, electroforming has been found to produce layer with microstructural and mechanical properties compatible for cardiovascular devices. Even though the degradation rate of electroformed iron is faster than that of rolled iron, it is considered to be not sufficiently high since 10–12 months is the period usually needed for artery remodelling [29]. Considering that the average stent strut is around 100 μm, the ideal in vivo degradation rate should be in the range of 0.08–0.12 mmpy. Previous experiences and experts suggest that in vitro degradation should be increased by a factor of 6 to evaluate the in vivo value, giving the idea that the expected in vitro degradation rate is 0.48–0.72 mmpy.

In order to increase the degradation rate of electroformed pure iron and to achieve the expected dissolution rate, some elements could be integrated as impurities. Some of these are manganese, palladium, carbon, tungsten and cobalt. A content of 35 % (mass %) manganese was used to create a Fe–Mn alloy with accelerated degradation rate compared to that of pure iron [31]; the addition of 10 % (mass %) manganese and 1 % palladium (mass %) to pure iron was also reported to decrease the corrosion resistance [11]. In the same sense, the addition of 3 % (at %) of carbon, tungsten and cobalt into pure iron resulted in a significant increase of its degradation rate [12]. In relation to this issue, a current challenge for the electroforming method is to integrate a specific amount of alloying elements to pure iron in order to have the expected corrosion rate together with appropriate mechanical properties. For this reason, optimization process and bath composition need to be deeply studied.

Another interesting issue is the fabrication of small diameter tubular structures (minitubes) whose production through electroforming could be extremely simplified, if compared to the steps needed with the traditional techniques. The fabrication of complex forms can reasonably be achieved by electroforming, depending on the shape of the involving cathode. The direct fabrication of minitubes could simplify the manufacturing procedures of cardiovascular stent production, having a strong impact on time and economical aspects of the fabrication process.

4.10   Conclusion

Electroformed iron has revealed its potential for cardiovascular stent applications. The degradation rate of this material is significantly higher than that of rolled pure iron, and its mechanical properties are comparable to those of stainless steel, but a relevant improvement of its degradation rate is envisaged. For this reason, other elements could be integrated during the electroforming process acting as impurities and increasing the material degradation rate. Manganese, palladium, carbon, tungsten and cobalt are all known elements accelerating the degradation rate of electroformed iron. The correct integration of these elements is one of the issues of the present study of electroforming processes, as they need an extensive experimental assessment in order to achieve optimized systems. The development of electroformed iron enriches the choice of biodegradable metals available for cardiovascular stent [32] and expectedly useful for other applications such as bone implants [33, 34].

References

1. McGeough JA, Leu MC, Rajurkar KP, De Silva AKM, Liu Q (2001) Electroforming process and application to micro/macro manufacturing. CIRP Ann Manuf Technol 50:499–514
2. Sole MJ (1994) Electroforming: methods, materials, and merchandise. Miner Metals Mater 46:29–35

3. Hart T, Watson A (2002) Electroforming. Metal Finish 100(Suppl 1):372–383
4. Schlesinger M, Paunovic M (2000) Modern electroplating. Wiley, New York
5. Kim D, Park DY, Yoo BY, Sumodjo PTA, Myung NV (2003) Magnetic properties of nanocrystalline iron group thin film alloys electrodeposited from sulfate and chloride baths. Electrochim Acta 48:819–830
6. Harty SF, McGeough JA, Tulloch RM (1981) A review of the electroforming of iron and nickel alloy. Surf Technol 12:39–55
7. Peuster M, Wohlsein P, Brugmann M, Ehlerding M, Seidler K, Fink C et al (2001) A novel approach to temporary stenting: degradable cardiovascular stents produced from corrodible metal–results 6–18 months after implantation into New Zealand white rabbits. Heart 86:563–569
8. Hermawan H, Alamdari H, Mantovani D, Dube D (2008) Iron-manganese: new class of degradable metallic biomaterials prepared by powder metallurgy. Powder Metall 51:38–45
9. Moravej M, Prima F, Fiset M, Mantovani D (2010) Electroformed iron as new biomaterial for degradable stents: development process and structure-properties relationship. Acta Biomater 6:1726–1735
10. Moravej M, Purnama A, Fiset M, Couet J, Mantovani D (2010) Electroformed pure iron as a new biomaterial for degradable stents: in vitro degradation and preliminary cell viability studies. Acta Biomater 6:1843–1851
11. Schinhammer M, Hanzi AC, Loffler JF, Uggowitzer PJ (2009) Design strategy for biodegradable Fe-based alloys for medical applications. Acta Biomater. doi: 10.1016/jactbio200910071039
12. Liu B, Zheng YF (2011) Effects of alloying elements (Mn, Co, Al, W, Sn, B, C and S) on biodegradability and in vitro biocompatibility of pure iron. Acta Biomater 7:1407–1420
13. Wegener B, Sievers B, Utzschneider S, Müller P, Jansson V, Rößler S et al (2011) Microstructure, cytotoxicity and corrosion of powder-metallurgical iron alloys for biodegradable bone replacement materials. Mater Sci Eng B 17:1789–1796
14. Lai SHF, McGeough JA, Lau P (1977) Electroforming of iron foil. J Mech Work Technol 1:231–243
15. Myung MV, Park DY, Urgiles DE, George T (2004) Electroformed iron and Fe-Co alloy. Electrochim Acta 49:4397–4404
16. Ng JHG, Record PM, Shang X, Wlodarczyk KL, Hand DP (2015) Optimised co-electrodeposition of Fe-Ga alloys for maximum magnetostriction effect. Sens Actuator A223:91–96
17. Harty SF, McGeough JA, Tulloch RM (1981) A review of the electroforming of iron and iron-nickel alloy. Surf Technol 12:39–55
18. Nakamura K, Umetani M, Hayashi T (1985) Electrodeposition of iron-rich Ni-Fe alloys from sulfate and chloride baths. Surf Technol 25:111–119
19. Yeh YM, Tu GC, Fang TH (2004) Nanomechanical properties of nanocrystalline Ni-Fe mold insert. J Alloys Compd 372:224–230
20. Ricq L, Lallemand F, Gigandet MP, Pagetti J (2001) Influence of sodium saccharin on the electrodeposition and characterization of CoFe magnetic film. Surf Coat Technol 138:278–283
21. Seo MH, Kim DJ, Kim JS (2015) The effect of pH and temperature on Ni-Fe-P alloy electrodeposition from a sulfamate bath and the material properties of the deposits. Thin Solid Film 489:122–129
22. Colombo A, Karvouni E (2000) Biodegradable stents "Fulfilling the mission and stepping away". Circulation 102:371–373
23. Moravej M, Mantovani D (2011) Biodegradable metals for cardiovascular stent application: interests and new opportunities. Int J Mol Sci 12:4250–4270
24. Parkinson R (1998) Electroforming-a unique metal fabrication process. The Nickel Development Institute, Toronto
25. Tabakovic I, Inturi V, Riemer S (2002) Composition, structure, stress, and coercivity of electrodeposited soft magnetic CoNiFe films. J Electrochem Soc 149:C18–C22

26. Ricq L, Lallemand F, Gigandet MP, Pagetti J (2001) Influence of sodium saccharin on the electrodeposition and characterization of CoFe magnetic film. Surf Coat Technol 138:278–283
27. Gow KV, Iyer SP, Wu HH, Castelliz KM, Hutton GJ (1979) Microstructure, internal stress, and mechanical properties of electrodeposited iron foils. Surf Technol 8:333–346
28. Watson SA (1991) Modern electroforming in Europe. American Electroplaters' and Surface Finishers' Society, 292–311
29. Hermawan H, Purnama A, Dube D, Mantovani D (2010) Fe-Mn alloys for metallic biodegradable stents: degradation and cell viability studies. Acta Biomater 6:1852–1860
30. Mueller PP, May T, Perz A, Hauser H, Peuster M (2006) Control of smooth muscle cell proliferation by ferrous iron. Biomaterials 27:2193–2200
31. Hermawan H, Moravej M, Dube D, Fiset M, Mantovani D (2007) Degradation behavior of metallic biomaterials for degradable stents. Adv Mater Res 15:113–118
32. Sing NB, Mostavan A, Hamzah E, Mantovani D, Hermawan H (2014) Degradation behavior of biodegradable Fe35Mn alloy stents. J Biomed Mater Res Part B Appl Biomater. doi: 10.1002/jbm.b.33242
33. Nasution AK, Murni NS, Sing NB, Idris MH, Hermawan H (2014) Partially degradable friction-welded pure iron-stainless steel 316L bone pin. J Biomed Mater Res Part B Appl Biomater. doi: 10.1002/jbm.b.33174
34. Ulum MF, Arafat A, Noviana D, Yusop AH, Nasution AK, Abdul Kadir MR, Hermawan H (2014) In vitro and in vivo degradation evaluation of novel iron-bioceramic composites for bone implant application. Mater Sci Eng 36:336–344

Part II
Surface Modification

Chapter 5
Bioactive Ceramic Coatings

Hirotaka Maeda and Toshihiro Kasuga

Abstract Some kinds of metals, such as titanium and its alloys, bond directly to living bone without fibrous tissue. One of the key techniques for enhancing bone-forming ability of the metallic biomaterials is to modify their surface using bioactive ceramics. This chapter introduces various coatings on the metals to give high bioactivity, which is to have an effect on bonding to living bone. The first section is concerned with bioactive ceramic coatings using calcium phosphates or calcium silicates. These coatings show high bonding strength and enhance the biocompatibility, which refers to ability of materials to interact with living tissue and cells, in vivo and in vitro. The next section describes bioactive glass and glass-ceramic coatings on the metal surface. These materials have a significant advantage in that their chemical/physical properties can be controlled by the choice of the chemical composition. The third section is concerned with modification of Ti and its alloys for forming bioactive oxide layers.

Keywords Bioactivity • Calcium phosphate • Calcium silicate, • Bioactive glass • Titanium oxide

5.1 Introduction

Some kinds of metals, such as titanium and its alloys, are widely used as materials for orthopedic and dental implants because of their nontoxicity and advantageous mechanical properties. They can bond directly to living bone without fibrous tissue for a long period after implantation. The surface modification of the metals can assist the osseointegration with surrounding tissues.

Various kinds of ceramics and glasses, such as hydroxyapatite (HA) and Bioglass®, bond to living bone with mechanically high strengths in a short period without fibrous tissue, which are often called bioactive ceramics. One of the specific characteristic properties is to form hydroxycarbonate apatite (HCA) layer on the

H. Maeda (✉) • T. Kasuga
Department of Frontier Materials, Graduate School of Engineering,
Nagoya Institute of Technology, Gokiso, Showa-ku, Nagoya, Aichi 466-8555, Japan
e-mail: maeda.hirotaka@nitech.ac.jp

Table 5.1 Ion concentration of SBF in comparison with those of human blood plasma

Ion	Ca^{2+}	Na^+	Mg^{2+}	K^+	Cl^-	HCO_3^-	HCO_4^-	SO_4^{2-}
SBF (mM)	2.5	142.0	1.5	5.0	148.8	4.2	1.0	0.5
Human blood plasma (mM)	2.5	142.0	1.5	5.0	103.0	27.0	1.0	0.5
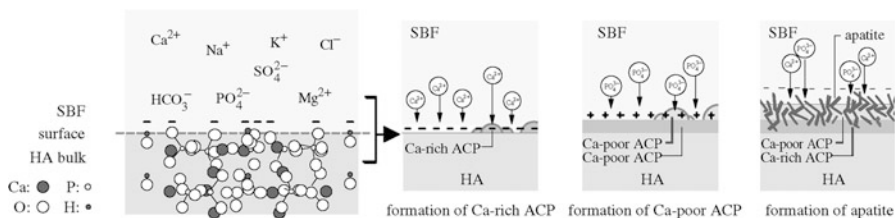
Fig. 5.1 Schematic presentations of the origin of the negative charge on the HA surface (in case of the (100) projection of crystal structure), and the process of bonelike apatite formation thereon in SBF (Reproduced from Ref. [4] by permission of The Royal Society Interface)

surface when they are exposed to physiological fluid [1]. The HCA crystals form the bonding between the ceramics and living bones.

In in vitro evaluation of bioactivity, an acellular simulated body fluid (SBF), which is produced by Kokubo, can reproduce the formation of HCA on bioactive ceramics in vivo [2]. SBF is a Tris buffer solution, which includes 50 mM of $(CH_2OH)_3CNH_2$ and 45.0 mM of HCl, with ion concentrations equal to those of human blood plasma excepting that of HCO_3^- and Cl^-, and its HCO_3^- concentrations are lower and Cl^- is higher than those of human blood plasma [3]. The difference of ion concentrations between SBF and human blood plasma is shown in Table 5.1. The formation mechanism of HCA on HA in vitro model using SBF has been proposed as shown in Fig. 5.1 by Kim et al. [4]. HCA forms via amorphous calcium phosphates as the precursor. The HCA formation is related with electrostatic interaction between calcium and phosphate ions in SBF and the surface of HA.

Bioactive ceramics are suitable for bone substitutes owing to their properties in vivo. However, the fracture resistance is not enough to replace the bone under load bearing. A bioactive ceramic coating on metals takes advantages of the excellent mechanical properties of the metals and accelerates the osseointegration. Some kinds of bioactive ceramic coatings on metals are introduced in this chapter.

5.2 Bioactive Ceramic Coatings

5.2.1 Hydroxyapatite

HA, which shows a similar chemical composition and crystal structure as apatite in the human bone, has been used in clinical bone graft procedures for the past

25 years because of their high bone-bonding ability. Therefore, HA coating is one of the key techniques for the surface modification of metallic implants. Several techniques have been used to fabricate HA coatings on metallic implants, for example, plasma spraying, sputtering, slurry dipping, electrophoretic deposition, and biomimetic coating. Advantages and disadvantages of various methods for HA coatings on Ti–6Al–4V substrate are shown in Table 5.2, as reported by Mohseni et al. [5].

The Food and Drug Administration (FDA) approves plasma spraying only as the HA coating technique. In a plasma-spraying method, ceramic powders are suspended into plasma flame, and then, the melted powders are sprayed on the surface of substrates. This method has advantages on rapid deposition rate and less risk of the thermal degradation than other high-temperature process. De Groot et al. firstly reported HA coatings on a titanium substrate by plasma-spraying technique [6]. In vivo tests showed that bone bonding to the HA coatings was almost the same as HA bulk ceramics. However, it is well known that the fracture occurs almost entirely at the interface between HA and metal substrate under push-out test condition. The plasma-sprayed coatings show poor adhesion strength between the coatings and substrates, compared with other coating techniques. The improvement of the strength is to use high spraying power because the coatings have a dense microstructure. It has been reported that the coatings showed a higher bonding strength by reduction in the residual stress originated from the substrate temperature and cooling condition [7]. For enhancing the mechanical properties of plasma-sprayed HA coatings, yttria-stabilized zirconia powders were mixed with HA powders as a starting material [8]. The bonding strength, fracture toughness, and Young's modulus of the composite coatings were improved with increasing the zirconia content. This paper suggested that the molten state of zirconia particles plays an important role in increasing the mechanical properties of the composite coatings. Another report on alternative plasma spraying has shown that a thin and good adhesive HA coating on titanium substrate was successfully fabricated by pulsed laser deposition using sintered HA [9].

Sputtering, which is a physical vapor deposition method, utilizes gas plasma, such as argon, to remove materials from a target as a source and to deposit them as a thin film coating on a substrate. The sputtering can successfully fabricate homogeneous thin coatings with high adhesive strengths. On the other hand, it is well known that the sputtered coatings show a low crystallinity and a higher Ca/P ratio than stoichiometric HA. Van Dijk et al. reported thin HA coatings on titanium substrate by radiofrequency (RF) magnetron sputtering [10]. The annealing conditions played an important role in the change in crystalline phases of as-sputtered coatings. Addition of water vapor under the annealing using argon flow accelerated crystallization and phase transformation. The HA coating on Ti–6Al–4V substrate fabricated by sputtering showed the highest adhesion strength among those fabricated by common techniques [5].

Electrophoretic deposition (EPD) is one of the colloidal processing techniques using electrophoresis mechanism for moving charged particles in a suspension under electric fields. EPD shows advantages in fabrication of ceramic coatings

Table 5.2 Different techniques to deposit HA coating

Technique	Thickness	Advantages	Disadvantages
Plasma spraying	<20 μm	Rapid deposition; sufficiently low cost; fast bone healing; less risk for coating degradation	Poor adhesion; alternation of HA structure due to coating process; nonuniformity in coating density; extreme high temperature up to 1,200 °C, phase transformation and grain grow of substance due to high-temperature procedure; increase in residual stress; unable to produce complete crystalline HA coating
Thermal spraying	30–200 μm	High deposition rates; low cost	Line of sight technique; high temperatures induce decomposition; rapid cooling produces amorphous coatings; lack of uniformity; crack appearance; low porosity; coating spalling and interface separation between the coating and the substrate
Sputter coating	0.5–3 μm	Uniform coating thickness on flat substrates; dense coating; homogenous coating; high adhesion	Line of sight technique; expensive, time consuming; produces amorphous coatings; low crystallite which accelerates the dissolution of the film in the body
Pulsed laser deposition	0.05–5 mm	Coating with crystalline and amorphous; coating with dense and porous; ability to produce wide range of multilayer coating from different materials; ability to produce high crystalline HA coating; ability to restore complex stoichiometry; high degree of control on deposition parameters	Line of sight technique; splashing or particle deposition; need surface pretreatment; lack of uniformity
Dip coating	<1 μm	Inexpensive; coatings applied quickly; can coat complex substrates; high surface uniformity; good speed of coating	Requires high sintering temperatures; thermal expansion mismatch; crack appearance
Sol–gel	0.1–2.0 μm	Can coat complex shapes; low processing temperatures; relatively cheap as coatings are very thin; simple deposition method; high purity; high corrosion resistant; fairly good adhesion	Some processes require controlled atmosphere processing; expensive raw materials; not suitable for industrial scale; high permeability; low wear resistance; hard to control the porosity

(continued)

Table 5.2 (continued)

Technique	Thickness	Advantages	Disadvantages
Electrophoretic deposition	0.1–2.0 mm	Uniform coating thickness; rapid deposition rate; can cost complex substrates; simple setup; low cost; high degree of control on coating morphology and thickness; good mechanical strength; high adhesion for n-HA	Difficult to produce crack-free coatings; requires high sintering temperatures; HA decomposition during sintering stage
Hot isostatic pressing	0.2–2.0 mm	Produces dense coatings; produce net-shape ceramics; good temperature control; homogeneous structure; high uniformity; high precision; no dimensional or shape limitation	Cannot coat complex substrates; high temperature required; thermal expansion mismatch; elastic property differences; expensive; removal/interaction of encapsulation material
Ion beam-assisted deposition	<0.03 μm	Low-temperature process; high reproducibility and reliability; high adhesion; wide atomic intermix zone at coating–substrate interface	Crack appearance on the coated surface

Reprinted from [5], Copyright 2014, with permission from Elsevier

having dense packing and homogeneous microstructure. Zhitomirsky et al. reported firstly that HA powders, which were prepared by a chemical precipitation, were successfully deposited by an EPD method using isopropyl alcohol as a solvent of the suspension on Ti–6Al–4V with anodic films [11]. Many works have been conducted on the sizes and morphology of HA, the conditions of the electric field, the concentration of the suspension, and the kinds of the solvent and dispersant for HA coatings prepared by EPD [12, 13]. EPD could successfully fabricate HA coatings with 90 μm in thickness on porous titanium substrate [14]. HA coatings on metallic titanium and stainless steel substrates prepared by an EPD and sintering showed more than 10 MPa of interfacial shear stress measured in accordance to ASTM standard F1044-87, indicating a good adhesion [15]. The shear strengths of the HA coating on the stainless steel were higher than those on the metallic titanium because of the less damaging effect derived from residual stress after sintering.

It has been reported that porous structure of HA coatings is one of the important keys for improving the fixation of implant through bone ingrowth into their pores [16]. HA coatings with controlled porosity on 316L stainless steel were prepared by an EPD using carbon black particles as a porogen [17]. In isopropanol as a solvent of suspension, HA/carbon black composite particle showed net positive surface charge by heterocoagulation of the HA nanoparticles with positive charge on carbon black particles with negative charge. The deposition rate depended on the concentration of carbon black in the suspension. The microstructures of the coatings deposited from the suspension before and after sintering were changed under

the condition of the suspension, as shown in Fig. 5.2. In the case of EPD coating without sacrificial phases, the control of pore size and porosity in the coatings is limited. When sacrificial phases are used in the EPD method, the porous properties of the coatings can be controlled by changes in the particle size distribution of particles as sacrificial phases and their concentration in the suspension.

EPD method is attracting increasing attention as an effective coating technique using functional biopolymer, for example, chitosan and alginate, at room temperature. The composite coatings consisting of alginate and Bioglass® have been reported to be successfully fabricated on 316L stainless steel by using direct current and alternating current in an EPD method [18]. The preparation of composites consisting of bioactive ceramics and biopolymer by EPD is well established, as reviewed elsewhere [19].

5.2.2 Other Calcium Phosphates

Much attention has been paid to HCA as a novel biomaterial, since HCA is very similar to the apatite phase in living bone in its chemical composition and crystal structure and shows high osteoconductivity, as well as good bioresorbability [20]. This has been introduced as a preparation method for HCA coating on the metals, polymers, and ceramics based on immersion in SBF, termed "a biomimetic method" [21, 22].

This method has an advantage over conventional coating techniques in the materials that can be homogeneously coated with nano-sized HCA without the need of a heating process. Two indispensable conditions are needed for the formation of HCA coating on materials using SBF as follows [23]:

1. Existence of surface functional groups that induce nucleation of HCA, for example, Si–OH, Ti–OH, and COOH
2. Increase in the supersaturation of HCA in SBF

HCA coatings have been successfully fabricated on commercially metallic titanium after at least 1 week of soaking in SBF utilizing Ti–OH groups on the surface [24]. SBF concentrated more than five times with CO_2 gas has been prepared to accelerate HCA coating process [25]. The use of SBF $\times$ 5 can deposit homogeneous calcium phosphate coating within 1 day. Table 5.3 shows kinetic study and precipitate phases of the formed coatings using various SBFs. Mg^{2+} ion was a stronger inhibitor for HCA formation than carbonate ion under the SBF $\times$ 5 condition.

The HCA coating process using SBF can be also applicable to polymer substrates. Tanahashi et al. have succeeded in dense and uniform HCA coating with more than 3 MPa of adhesive strength on poly(ethylene terephthalate) (PET), polyether sulfone, and poly(vinyl alcohol) hydrogel [26]. This process has two steps, as shown in Fig. 5.3. A polymer substrate, which was in contact with CaO–SiO_2 glass particles, was soaked in SBF for forming HCA nuclei on the substrates.
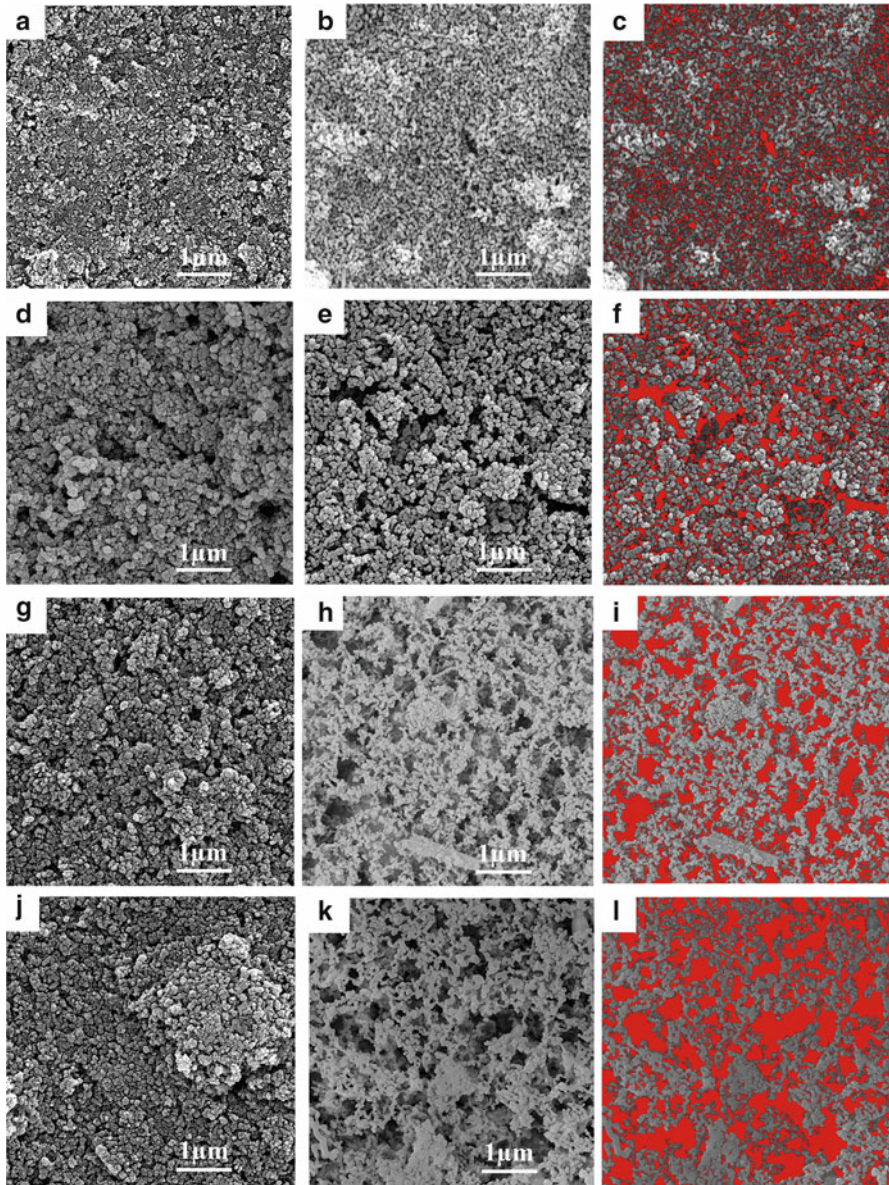
Fig. 5.2 SEM images of the coatings deposited at 60 V and 30 s from suspensions with 20 g/L HA and different concentration of carbon black particles: 0 g/L (**a–c**), 5 g/L (**d–f**), 10 g/L (**g–i**), and 20 g/L (**j–l**) before sintering (**a**, **d**, **g**, and **j**) and after sintering at 700 °C for 1 h (**b**, **e**, **h**, and **k**). (**c**, **f**, **i**, and **l**) are the results obtained from the image analyzing of (**b**, **e**, **h**, and **k**), respectively (Reprinted from [17], Copyright 2014, with permission from Elsevier)

Table 5.3 Kinetics of precipitation and coating formations of the various experiments

Experiment	Precipitation formation		Coating formation		Precipitate structure	Slope (/h)
	pH	Time (h)	pH	Time (h)		
SBF × 5	6.7	$4^1/_2$	6.8	$5^1/_2$	AmCO$_3$-CaP[b]	0.11
SBF × 5 (Mg × 0)	6.7	6	/	/	CO$_3$-Ap[c]	0.14
SBF × 5 (Mg × 3)	6.7	4	6.8	$4^1/_2$	AmCO$_3$-CaP[b]	0.15
SBF × 5 (Mg × 8, HCO$_3$ × 0)	6.6	$15^1/_2$	6.6	$15^1/_2$	DCPD[a]	0.12
SBF × 5 (Mg × 8, HCO$_3$ × 8)	6.4	1	7.0	10	CO$_3$-Ap/calcite	0.12

Reprinted from [25], Copyright 2014, with permission from Elsevier
[a]DCPD: brushite
[b]AmCO$_3$-CaP: amorphous carbonated CaP
[c]CO$_3$-Ap: carbonated apatite
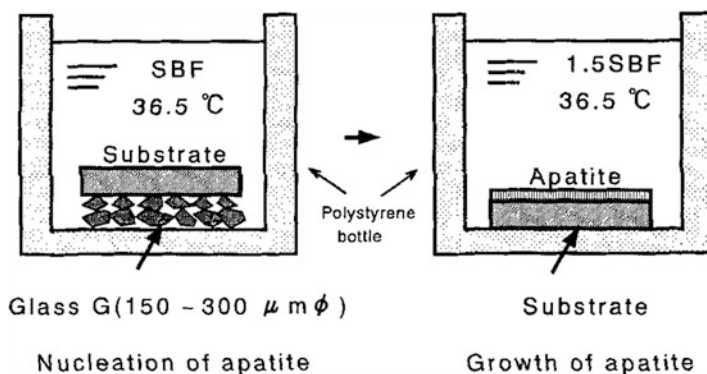
Fig. 5.3 Biomimetic methods for forming the bonelike apatite layer on various substrates (Reprinted with permission from Ref. [26], Copyright 1994, American Ceramic Society)

And then, the treated substrate was soaked in 1.5 times SBF for the growth of HCA nucleus. Individual constituents' fine fibers consisting of PET could be uniformly coated with HCA layer. This had flexibility without peeling off the HCA coating.

Another HCA coating method has been also reported to use calcium carbonate particles of vaterite crystalline structure combined with a biomimetic method. Homogeneous vaterite particles with around 0.5 μm in diameter were deposits on the surface of different polymer substrates, such as ligaments and 3-D macroporous foams, by a slurry dipping technique using ethanol as a solvent, as shown in Fig. 5.4. The polymer substrates covered with a HCA layer were prepared by soaking of the polymer/vaterite composites in SBF within 7 days. This method can induce HCA coatings for surface modification of various polymers, for example, poly(ε-caprolactone), poly(DL-lactide), and polyester [27, 28].
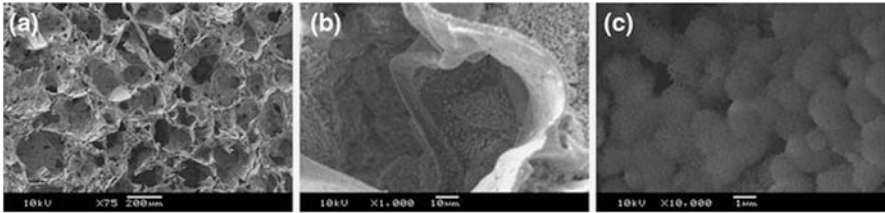
Fig. 5.4 SEM images of vaterite/PDLLA composite foams prepared using ethanol slurry dipping process, after immersion in SBF for 7 days showing formation of the HCA layer at (**a**) low, (**b**) medium, and (**c**) high magnification (Reprinted from Ref. [27], with kind permission from Springer Science + Business Media)

In the series of synthetic calcium phosphate ceramics, many researchers have investigated on β-tricalcium phosphate (β-TCP) and biphasic calcium phosphate (BCP) because they show bioactivity and higher solubility compared with HA. BCP is a mixture of HA and β-TCP, and their solubility depends on the β-TCP/HA ratio [29]. β-TCP or BCP coatings are successfully fabricated by plasma spraying and RF magnetron sputtering [30, 31]. Bone formation has been observed at the surface of these coatings in vivo.

5.2.3 Calcium Silicates

Wollastonite ($CaSiO_3$) has been investigated on bone substitutes for more than 20 years because of its excellent biocompatibility. Moreover, wollastonite shows higher HCA-forming ability in SBF than bioactive glasses [32]. Porous wollastonite $CaSiO_3$ ceramics have been also reported to be superior to β-TCP in terms of degradability and inducing bone formation in vivo [33]. Wollastonite coatings containing amorphous phase on titanium alloys were fabricated by atmosphere plasma spraying [34]. Figure 5.5 shows SEM micrographs of as-sprayed wollastonite coatings. The coatings had microcracks, pores with several tens micrometer in size, and rough surfaces without cracks between coatings and substrate. HCA formed on the coatings after 1 day of soaking in SBF.

Dicalcium silicate (Ca_2SiO_4) coatings on titanium alloys by plasma spraying show a higher bonding to the substrate than HA coatings [35]. That is, dicalcium silicate acts as a bond coat to improve the bonding strength between HA coatings and titanium alloys. When γ-Ca_2SiO_4 is used as a coating material on Ti–6Al–4V, as-plasma-sprayed coatings consist of β-Ca_2SiO_4 and glassy phase and have around 40 MPa of the bonding strength to the substrate [36]. HCA forms on the dicalcium silicate coatings via silica-rich layer after soaking in SBF within 2 days. The HCA formation in SBF of the plasma-sprayed calcium silicate coatings has been proposed to play an important role in the formation of a hydrated silica layer with functional groups due to ionic exchange between Ca^{2+} ions in the coatings and proton in SBF.
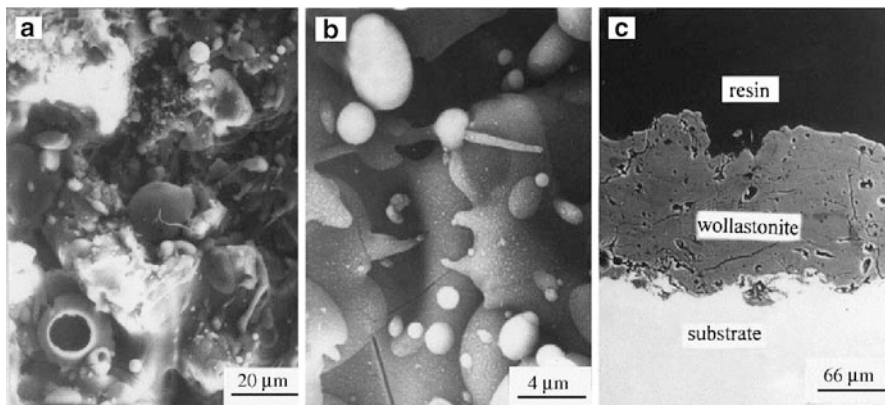
Fig. 5.5 SEM photographs of as-sprayed wollastonite coatings: (**a**) and (**b**) surface morphology; (**c**) cross section (Reprinted from [34], Copyright 2014, with permission from Elsevier)

As other calcium silicate series, dense diopside $CaMgSi_2O_6$ bulk ceramics have been reported to induce bone formation in vivo [37]. The calcined diopside $CaMgSi_2O_6$ powders derived from a sol–gel method have been successfully coated on metallic titanium after a thermal treatment for application to dental implants [38].

5.3 Bioactive Glass Coatings

5.3.1 Silicate-Based Glasses

The first bioactive glass with Na_2O–CaO–P_2O_5–SiO_2 system was discovered by Hench et al. [39]. The glass composition is 46.1 mol% of SiO_2, 24.4 mol% of Na_2O, 26.9 mol% of CaO, and 2.6 mol% of P_2O_5, which is named as Bioglass® and 45S5. The glass can form bond with living bone [40]. Interest has increased in bioactive glasses, and there is some flexibility in the composition of glass-based materials. In the past decade, bioactive glasses have been reported to be able to enhance the bone-forming ability of osteoblasts by gene activation [41]. The preparation and cell compatibilities on bioactive glasses are well established, as reviewed elsewhere [42, 43]. These materials have a significant advantage in that their chemical, physical, and biological properties can be manipulated by chemical compositions.

It is also well known that glass-ceramics containing crystalline apatite and wollastonite (glass-ceramic A–W) in the MgO–CaO–SiO_2–P_2O_5 system bond with living bone in a short period under load-bearing condition in vivo [44]. This type of glass-ceramic showed excellent mechanical properties due to precipitation of wollastonite crystals in matrix [45]. Bioactive glasses and glass-ceramics are two of the coating materials for improving the performance in vivo of metallic implants.
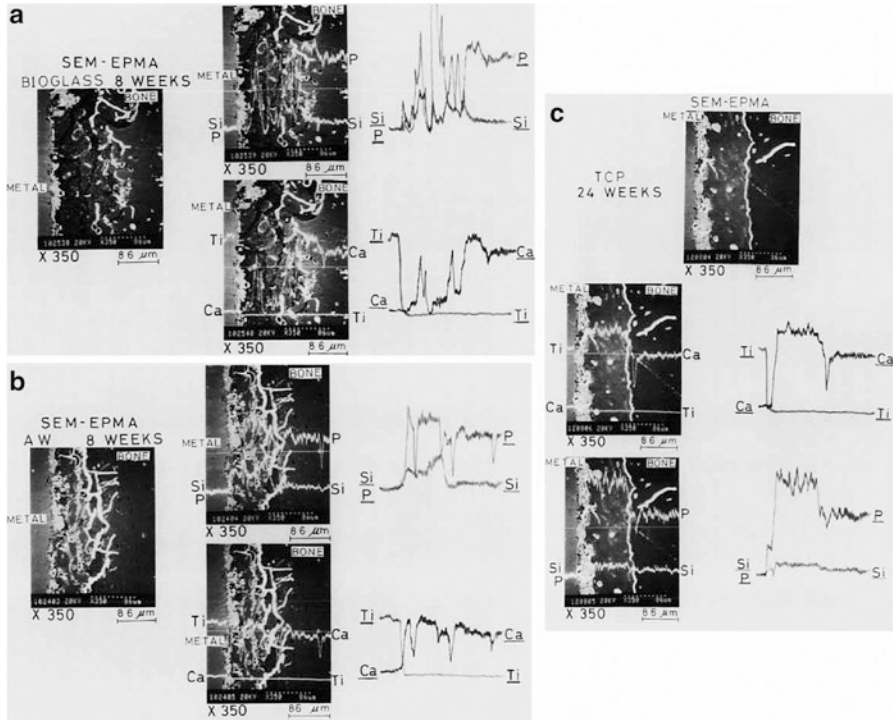
Fig. 5.6 Scanning electron micrographs and electron probe microanalysis (full scale: Ca, 1,000 cps; Si, P, 500 cps; Ti, 200 cps) of plasma-sprayed titanium alloys. (**a**) Interface of Bioglass® coating layer and bone tissue at 8 weeks after implantation. (**b**) Interface of glass-ceramic A–W coating layer and bone tissue at 8 weeks after implantation. (**c**) Interface of β-TCP coating layer and bone tissue at 24 weeks after implantation (Reproduced from Ref. [46] by permission of John Wiley & Sons Ltd)

Bioglass® (45S5), glass-ceramic A–W, and β-TCP coatings on titanium alloys fabricated by plasma spraying induce bonding between living bone and the coatings at an early stage after implantation [46]. Figure 5.6 shows scanning electron micrographs and electron probe microanalysis of the plasma-sprayed coatings. Calcium phosphate layer forms at the interface between the glass-ceramic A–W and bone. In the case of Bioglass® coating, there existed a silicon-rich layer and calcium phosphate layer at the interface. The β-TCP coating bonds without calcium phosphate layer to the bone. Each plasma-sprayed coating showed bioactivity with different bone-bonding mechanisms. On the other hand, histological evaluation showed a gap and detachment between the metals, and the coatings were observed in each plasma-sprayed coatings after 8 weeks of implantation. The breakages after detachment tests occurred in the plasma-sprayed coatings and between the substrates and the coatings. In addition, the plasma-sprayed titanium alloys with glass-ceramic A–W showed lower failure loads, which mean the adhesive strength

between the coating and substrate using detachment tests, after implantation than bulk glass-ceramic A–W.

An enameling technique is proposed as an alternative method to coat the metallic implants with a bioactive glass. This is a simple method to deposit bioactive glasses on the metals using suspensions containing the glasses and to heat the deposited metals for making glass flow and adhering. Pazo et al. reported firstly bioactive glass coatings on titanium alloys by a simple enameling method [47]. Three types of glasses in the SiO_2–Na_2O–K_2O–CaO–MgO–P_2O_5 system showed an excellent adhesion to the alloys without interfacial fracture by heating between 800 and 850 °C. In the case of less than 750 °C of heating, the coatings had porous structure and poor adhesive strengths. When the alloys deposited with glasses were heated at more than 850 °C and treated more than 1 min, dewetting and/or interfacial reaction occurred, as shown in Fig. 5.7. In this technique, two important factors are needed to design for the composition of glass as a starting material.

The tuning of the glass composition is needed to be matched with the thermal expansion of the metal (Ti: 9.4×10^{-6} °C^{-1} at 400 °C). The metallic titanium and its alloys transform from α- to β-phase, e.g., at 955–1,010 °C for Ti–6Al–4V. To conduct the heat treatment below the transformation temperatures, it is desirable that the softening temperature of the glass is enough to low. Reactivity between the glass and the metal can be also controlled by an atmosphere in addition to temperature and time during the heat treatment, as shown in Fig. 5.8 [48]. Good adhesion in Fig. 5.8 means dense coatings without delamination even after Vickers indentation tests. The coatings prepared by using glasses containing silica contents less

Fig. 5.7 SEM photographs of cross sections of 56.5SiO_2–11.0Na_2O–3.0K_2O–15.0CaO–8.5MgO–6.0P_2O_5 glass coatings fired in air with (**a**) good adhesion (800 °C/30 s) and (**b**) excessive interfacial reactions (800 °C/2 min) (Reproduced from Ref. [48] by permission of John Wiley & Sons Ltd)
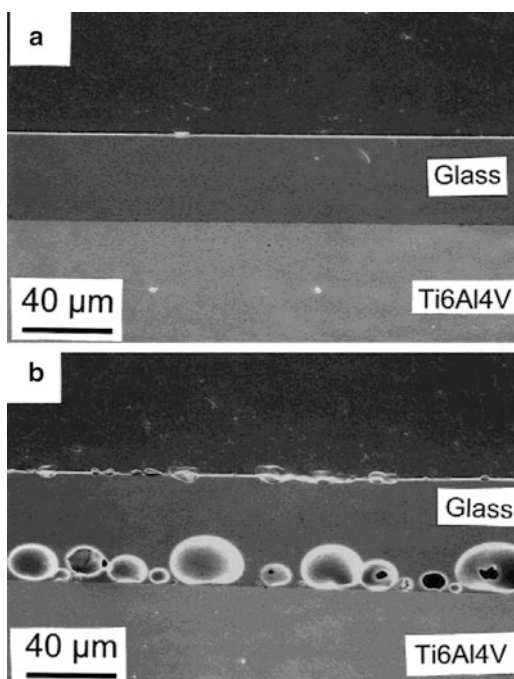
than 53 wt% in the SiO_2–Na_2O–K_2O–CaO–MgO–P_2O_5 system form HCA after soaking in SBF. To enhance the HCA-forming ability of the silica-based coatings prepared by a simple enameling method, HA and Bioglass® particles have been proposed to be embedded on the coatings [49].

Bioactive coating consisting of HCA with silica species releasing ability on metallic titanium was synthesized by a biomimetic method using water glass and vaterite [50]. The layers derived from water glass on metallic titanium act as intermediate layers consisting of silicon and titanium, as shown in Fig. 5.9, resulting in good adhesion without cracks between the coatings and the substrate.

Fig. 5.8 Influence of firing time and temperature on the adhesion of coatings manufactured with $56.5SiO_2$–$11.0Na_2O$–$3.0K_2O$–$15.0CaO$–$8.5MgO$–$6.0P_2O_5$ glass: (○) no sintering, (◇) delamination, (□) good adhesion, and (+) excessive interfacial reaction (Reproduced from Ref. [48] by permission of John Wiley & Sons Ltd)
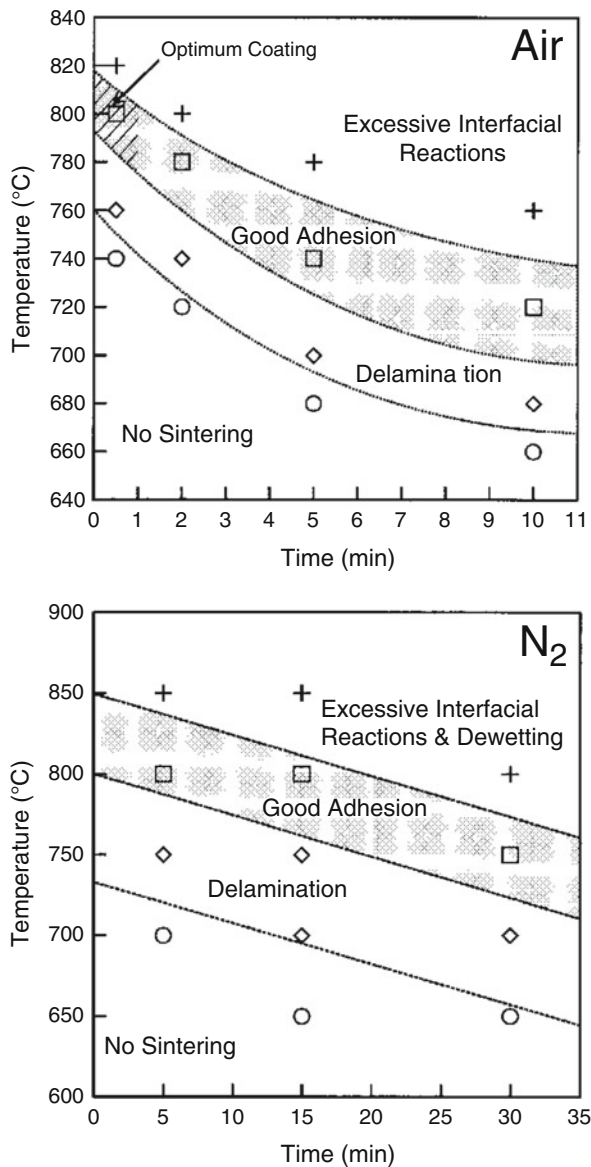
Fig. 5.9 Cross-sectional field emission gun scanning electron micrograph and energy-dispersive spectrometry analysis of the titanium substrate coated with water glass after heat treatment at 300 °C for 2 h (Reprinted with permission from Ref. [50], Copyright 2011, American Ceramic Society)
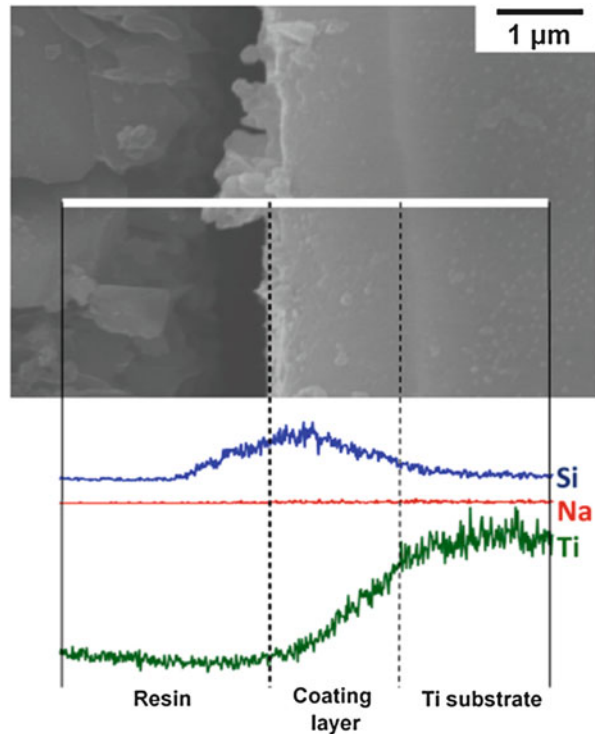
To use vaterite was most suitable for HCA coatings on the metallic titanium modified with water glass among polymorphs of calcium carbonates (calcite and aragonite) and calcium chloride as calcium resources. The HCA coatings with silicon species derived from water glass enhance cell proliferation in cell culture tests using mouse osteoblast-like cells, compared with HCA coatings without silicon species.

5.3.2 Phosphate-Based Glasses

Phosphate glasses in the $CaO–Na_2O–P_2O_5$ system have high solubility and chemical similarity to inorganic phase of the human bone. To control their solubility, various oxides, such as TiO_2, ZnO, and MgO, are incorporated into the phosphate-based ternary system [51–53]. In the case of metaphosphate glass, no HCA forms on the surface after soaking in SBF [54].

Kasuga et al. reported calcium pyrophosphate glass with unique structure in $60CaO–30P_2O_5–7Na_2O–3TiO_2$ system with bioactivity [55]. The glass consists of orthophosphate $(PO_4)^{3-}$ and pyrophosphate $(P_2O_7)^{4-}$ units without metaphosphate $(PO_3)^{2-}$ units; the phosphate groups are connected with Ca^{2+} ions [56].

When the calcium pyrophosphate glass was soaked in SBF, HCA layer formed on the glass surface [57]. Large-sized glass-ceramics containing β-tricalcium phosphate and β-calcium pyrophosphate can be prepared by heating the calcium pyrophosphate glass powder compacts [58]. Some glass-ceramics derived from the calcium pyrophosphate glasses have HCA-forming ability in SBF [59].

The bioactive calcium pyrophosphate glass-ceramic can be successfully coated on titanium alloys without cracks by heating the deposited meal with two chemical compositions of calcium pyrophosphate glass powders [60]. The chemical compositions of the glass powders influence densification of the coatings, as shown in Fig. 5.10. The joining between the glass-ceramic and the metal was controlled by viscous flow of the glassy phase in the glass-ceramic and by reaction of the glassy phase with an oxide phase formed around the surface layer [61]. The coatings showed excellent tensile bonding strength with more than 20 MPa owing to the reaction phase, independently of the chemical compositions. The glass-ceramic coatings derived from $60CaO–30P_2O_5–7Na_2O–3TiO_2$ glass formed HCA on their surface after soaking in SBF and bonded directly to living bone in vivo test [62].
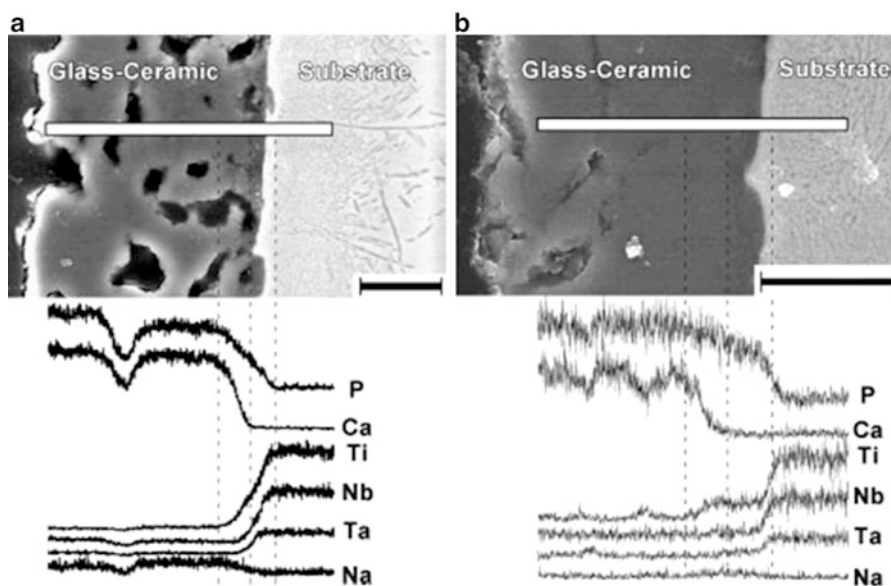
Fig. 5.10 Cross-sectional scanning electron microscopic images at the surface of the substrate of the samples prepared by heating at 800 °C in air and element concentrations measured by energy-dispersive spectrometry (EDS) analysis along the *line* indicated in the images: (a) the sample obtained using $50CaO–40P_2O_5–7Na_2O–3TiO_2$ glass; (**b**) the sample obtained using $60CaO–30P_2O_5–7Na_2O–3TiO_2$ glass. Zr concentration profiles were not measured since the EDS peak position of the L-line from Zr overlaps with that of the K-line from P. Zr content in the substrate is small. The scale bar is 5 μm (Reproduced from Ref. [60], by permission of Wiley-VCH Verlag GmbH & Co. KGaA)

5.4 Oxide Modification of Ti and Its Alloys

5.4.1 Chemical Treatments

Titania gel can induce HCA formation after soaking in SBF [63]. It is considered that oxide gel coating is one of the key factors for surface modification with bioactivity of titanium and its alloys. Two types of chemical treatments to prepare oxide gel layer are introduced as follows:

Kokubo et al. reported that amorphous sodium titanate layers form on titanium metal and its alloys after NaOH and heat treatment [64, 65]. The NaOH treatment leads to the formation of porous structure, as shown in Fig. 5.11. The microstructure and crystalline phase of the as-NaOH-treated substrate changed by heat treatment. The HCA-forming ability in SBF depended on the heating condition of the NaOH-treated substrates. Sodium-free titanium oxide with specific surface structure of anatase and rutile showed much higher HCA-forming ability than sodium-containing titanate in SBF [66]. Recently, metallic titanium subjected to NaOH and $CaCl_2$ treatment has been reported to enhance HCA-forming ability in SBF due to replacement of sodium ions in sodium titanate layer with calcium ions [67].

It is well known that titanium can form titanium oxide gel via a reaction with hydrogen peroxide [68]. Titanium oxide gel layers on metallic titanium surface are prepared by chemical treatment using a solution containing H_2O_2 and HCl at 80 °C for a short period, and subsequently heat treatment in air [69]. The thickness of the titania gel layers increases linearly with increase in chemical treatment time. The temperature during the chemical treatment influences the microstructures of titanium oxide gel layers, as shown in Fig. 5.12. The as-chemical-treated titanium oxide gel layers transformed predominantly of anatase below 600 °C and rutile above 700 °C by the heat treatment. In in vitro test using SBF, the titanium oxide gels heated at between 400 and 500 °C indicate excellent HCA-forming ability. Several papers have been published on acidic chemical treatment of metallic titanium using HF/HNO_3 and H_2SO_4/HCl solution instead of H_2O_2/HCl solution [70, 71].

5.4.2 Anodic Oxidation

Anodic oxidation is a traditional method to modify the surface structure and properties of titanium for application to catalysts and valves. The method, which can be applied to any shaped titanium, enables us to prepare titanium oxide layers of more than 1 μm of thickness on the whole surface. Ishizaki et al. reported that the anodic titanium oxide layers containing calcium and phosphorous elements were deposited on titanium in aqueous solution containing β-glycerophosphate and calcium acetate [72]. Subsequent hydrothermal treatment at 300 °C of the anodic titanium oxide layers allowed HA coatings with needlelike morphology on the surface. The film thickness and the amount of HA crystals were strongly influenced by the ratio for β-glycerophosphate and calcium acetate in the electrolytic solution. The coatings maintained a higher adhesive strength of more than 30 MPa even after
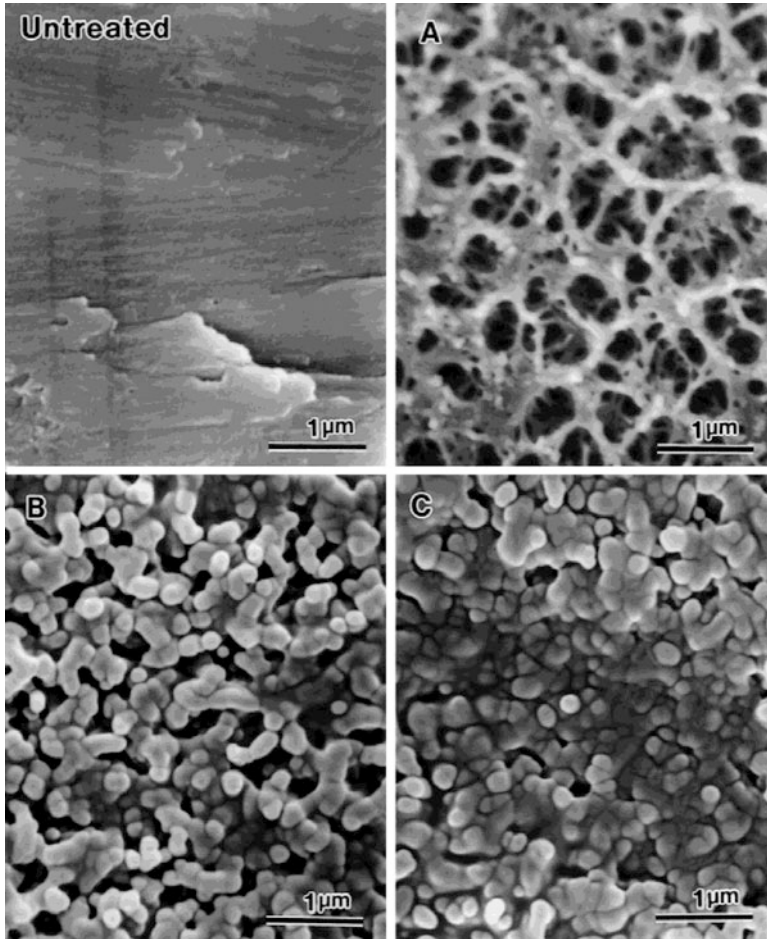
Fig. 5.11 Scanning electron micrographs of the surface of titanium substrates that were subjected to (**a**) 5.0 M NaOH treatment at 60 °C for 24 h, (**b**) the same NaOH treatment and subsequently heat treatment at 600 °C for 1 h, and (**c**) the same NaOH treatment and subsequently heat treatment at 800 °C for 1 h compared to that of untreated titanium substrate (Reproduced from Ref. [65] by permission of John Wiley & Sons Ltd)

300 days of soaking in Tris buffer solution because of existence as an intermediate layer between HA layer and the substrate.

Anodic oxidation of metallic titanium in H_2SO_4 solution forms titanium oxide layer containing anatase and rutile as crystalline phases with porous structure on their surface, as shown in Fig. 5.13 [73]. The anodic titanium oxide layers form HCA crystals on their surface after soaking in SBF. The direct current and concentration of H_2SO_4 solution in the anodic oxidation have influence on the microstructure, titanium oxide phase, and HCA-forming ability. In the case of acetic acid as an electrolytic solution, macroscopic grooves form on the surface of amorphous layer prepared by anodic oxidation [74].
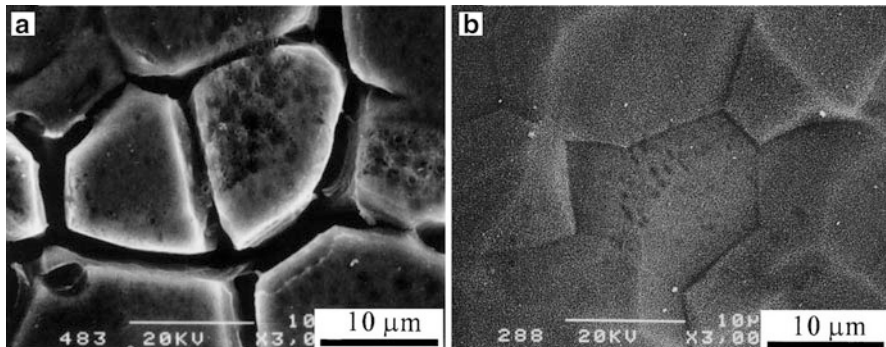
Fig. 5.12 Scanning electron micrographs of the titanium surface after treatment with the $H_2O_2/$HCl solution at (**a**) 25 °C for 1 day and (**b**) 80 °C for 30 min, showing the severe intergranular corrosion for the former and uniform titania gel layer without intergranular for the latter (Reprinted from [69], Copyright 2002, with permission from Elsevier)
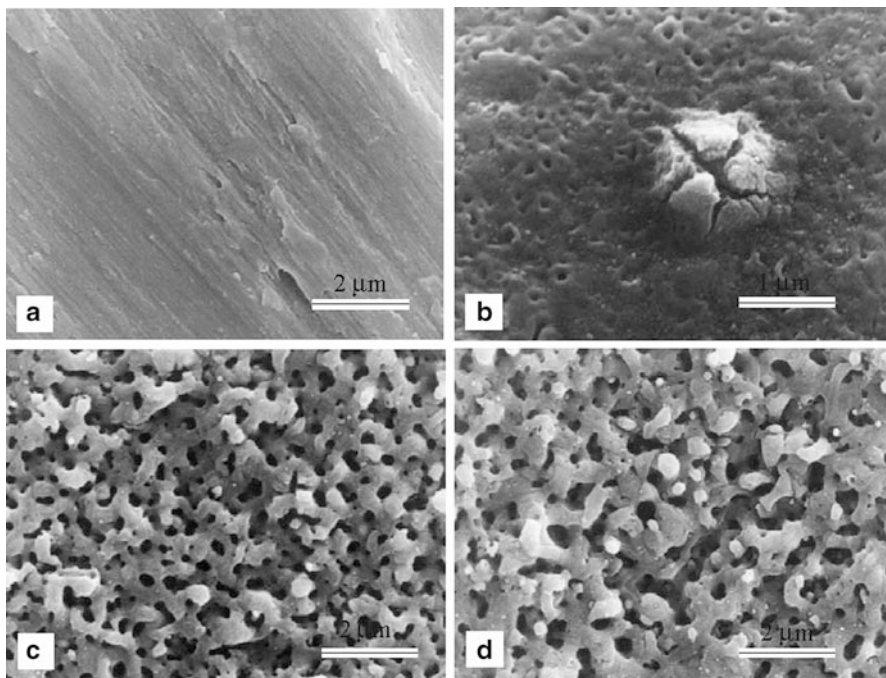

Fig. 5.13 Scanning electron micrographs of (**a**) metallic titanium without treatment and metallic titanium anodically oxidized at (**b**) 90 V, (**c**) 155 V, and (**d**) 180 V in 1 M H_2SO_4 for 1 min (Reprinted from [73], Copyright 2004, with permission from Elsevier)

5.4.3 Sol–Gel Coatings

The sol–gel process is based on inorganic polymerization and one of the key techniques for preparing oxide ceramics. The coatings on titanium substrate is prepared by dip- or spin-coating methods using sol containing hydrolyzed titanium alkoxide, e.g., tetraisopropylorthotitanate ($Ti(CH_3)_2(CHO)_4$), hydrochloric acid as a catalyst, and ethanol as a solvent. After the coating process, two-step heat treatment leads to the formation of gel layer and crystallization. Figure 5.14 shows the reaction schematically during the sol–gel coating process. In the case of fabricating thicker layers, it is necessary to repeat the coating and heat treatment
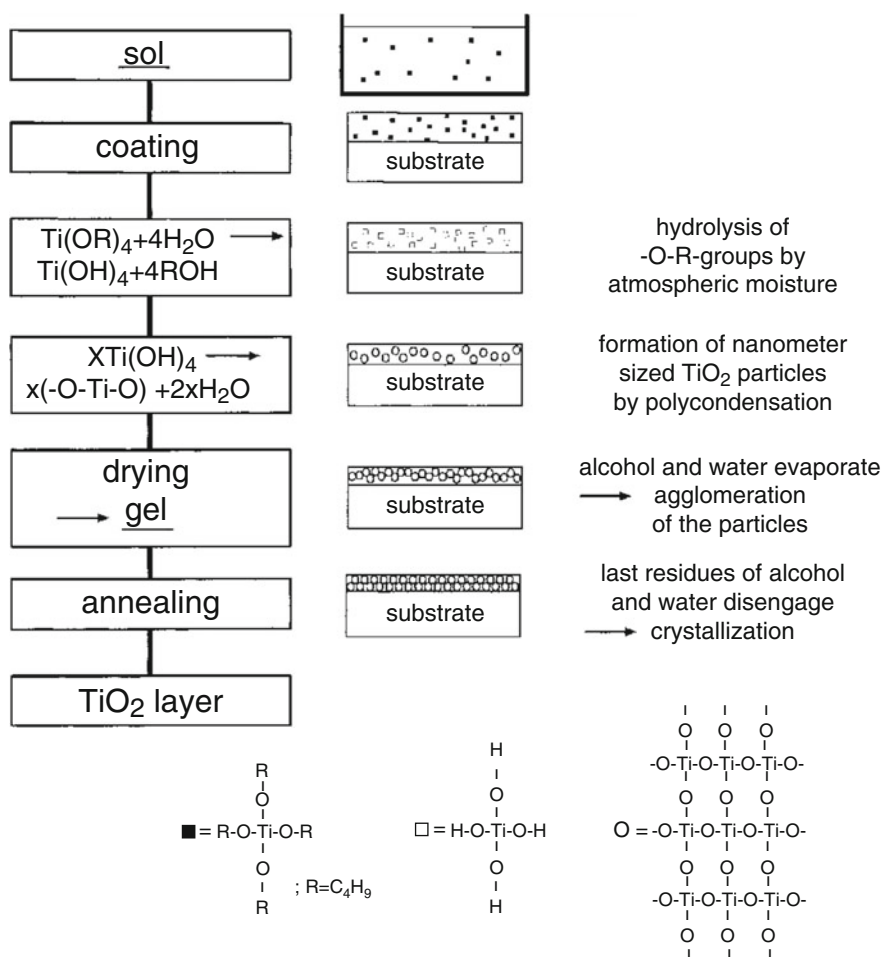
Fig. 5.14 Schematic description of sol–gel chemistry (Reproduced from Ref. [78] by permission of John Wiley & Sons Ltd)

for gel formation several times. Sol–gel-derived titanium oxide coating on metallic titanium induces HCA formation on its surface after soaking in SBF [75]. The coatings need to have adequate thicknesses to induce HCA formation in SBF. The temperatures during the heat treatment of the gel layer for crystallization had an effect on HCA-forming ability in SBF [76]. HA coatings on a titanium substrate with sol–gel-derived titanium oxide improved the bonding strength to the substrate and its corrosion resistance, compared with HA coatings on a titanium substrate [77]. The HA coating on the titanium oxide layer increases alkaline phosphatase expression of human osteosarcoma cells.

5.5 Summary

In this chapter, various types of surface modifications of metallic substrates, such as titanium and its alloys and stainless steel, were introduced. Bioactive ceramic coatings on the metals enhance dramatically HCA-forming ability on their surface, compared with the substrates. A sputtering method can fabricate a thin film with higher adhesive strengths compared with other techniques. HCA layers are prepared on the metals, polymers, and ceramics by a biomimetic method using SBF. An enameling method is suitable for bioactive glasses and glass-ceramic coatings on metals. The formation of titanium oxide gels on the metals plays an important role in improving bioactivity.

References

1. Neo M, Kotani S, Nakamura T, Yamamuro T, Ohtsuki C, Kokubo T, Bando Y (1992) A comparative study of ultrastructure of the interface between four kinds of surface-active ceramic and bone. J Biomed Mater Res 26:1419–1432
2. Kokubo T (1990) Surface chemistry of bioactive glass–ceramics. J Non-Cryst Solids 120:138–151
3. Kokubo T (1998) Apatite formation on surfaces of ceramics, metals and polymers in body environment. Acta Mater 46:2519–2527
4. Kim H-M, Himeno T, Kawashita M, Kokubo T, Nakamura T (2004) The mechanism of biomineralization of bone-like apatite on synthetic hydroxyapatite: an in vitro assessment. J R Soc Interface 1:17–22
5. Mohseni E, Zalnezhad E, Bushroa AR (2014) Comparative investigation on the adhesion of hydroxyapatite coating on Ti-6Al-4 V implant: a review paper. Inter J Adhes Adhes 48:238–257
6. de Groot K, Geesink R, Klein CPAT, Serekian P (1987) Plasma sprayed coatings of hydroxy-apatite. J Biomed Mater Res 21:1375–1381
7. Yang YC, Chang E (2001) Influence of residual stress on bonding strength and fracture of plasma-sprayed hydroxyapatite coatings on Ti-6Al-4V substrate. Biomaterials 22:1827–1839
8. Fu L, Khor KA, Lin JP (2002) Effects of yttria-stabilized zirconia on plasma-sprayed hydroxyapatite/yttria-stabilized zirconia composite coatings. J Am Ceram Soc 85:800–806

9. Lo WJ, Grant DM, Ball MD, Welsh BS, Howdle SM, Antonov EN, Bagratashvili VN, Popov VK (2000) Physical, chemical, and biological characterization of pulsed laser deposition and plasma sputtered hydroxyapatite thin films on titanium alloy. J Biomed Mater Res 50:536–545

10. van Dijk K, Schaeken HG, Wolke JGC, Jansen JA (1996) Influence of annealing temperature on RF magnetron sputtered calcium phosphate coatings. Biomaterials 17:405–410

11. Zhitomirsky I, Gal-Or L (1997) Electrophoretic deposition of hydroxyapatite. J Mater Sci Mater Med 8:213–219

12. Borum-Nicholas L, Wilson OC (2003) Surface modification of hydroxyapatite. Part I Dodecyl alcohol. Biomaterials 24:3671–3679

13. Xiao XF, Liu RF (2006) Effect of suspension stability on electrophoretic deposition of hydroxyapatite coatings. Mater Lett 60:2627–2632

14. Ducheyne P, Radin S, Heughebaert J (1990) Calcium phosphate ceramic coatings on porous titanium: effect if structured and composition on electrophoretic deposition, vacuum sintering and in vitro dissolution. Biomaterials 11:244–254

15. Wei M, Ruys A, Swain M, Kim S, Milthorpe B, Sorrell C (1999) Interfacial bond strength of electrophoretically deposited hydroxyapatite coatings on metals. J Mater Sci Mater Med 10:401–409

16. Nguyen HQ, Deporter DA, Pilliar RM, Valiquette N, Yakubovich R (2004) The effect of sol–gel formed calcium phosphate coatings on bone ingrowth and osteoconductivity of porous-surfaced Ti alloy implants. Biomaterials 25:865–876

17. Farrokhi-Rad M, Loghmani SK, Shahrabi T, Khanmohammadi S (2014) Electrophoretic deposition of hydroxyapatite nanostructured coatings with controlled porosity. J Eur Ceram Soc 34:97–106

18. Chen Q, Cordero-Arias L, Roether JA, Cabanas-Polo S, Virtanen S, Boccaccini AR (2013) Alginate/Bioglass® composite coatings on stainless steel deposited by direct current and alternating current electrophoretic deposition. Surf Coat Technol 233:49–56

19. Boccaccini AR, Keim S, Ma R, Li Y, Zhitomirsky I (2010) Electrophoretic deposition of biomaterials. J R Soc Interface 7:S581–S613

20. Doi Y, Shibutani T, Moriwaki Y, Kajimoto T, Iwayama Y (1998) Sintered carbonate apatites as bioresorbable bone substitutes. J Biomed Mater Res 39:603–610

21. Oyane A, Kawashita M, Nakanishi K, Kokubo T, Minoda M, Miyamoto T, Nakamura T (2003) Bonelike apatite formation on ethylene-vinyl alcohol copolymer modified with silane coupling agent and calcium silicate solutions. Biomaterials 24:1729–1735

22. Kawashita M, Nakao M, Minoda M, Kim H-M, Beppu T, Miyamoto T, Kokubo T, Nakamura T (2003) Apatite-forming ability of carboxyl group-containing polymer gels in a simulated body fluid. Biomaterials 24:2477–2484

23. Ohtsuki C, Kokubo T, Yamauro T (1992) Mechanism of apatite formation on CaO-SiO$_2$-P$_2$O$_5$ glasses in a simulated body fluid. J Non-Cryst Solids 143:84–92

24. Li P, Ducheyne P (1998) Quasi-biological apatite film induced by titanium in a simulated body fluid. J Biomed Mater Res 41:341–348

25. Barrere F, van Blitterswijk CA, de Groot K, Layrolle P (2002) Nucleation of biomimetic Ca-P coatings on Ti6Al4V from a SBF $\times$ 5 solution: influence of magnesium. Biomaterials 23:2211–2220

26. Tanahashi M, Yao T, Kokubo T, Minoda M, Miyamoto T, Nakamura T, Yamamuro T (1994) Apatite coating on organic polymer by a biomimetic process. J Am Ceram Soc 77:2085–2808

27. Maeda H, Maquet V, Kasuga T, Chen QZ, Roether JA, Boccaccini AR (2007) Vaterite deposition on biodegradable polymer foam scaffolds for inducing bone-like hydroxyapatite coatings. J Mater Sci Mater Med 18:2269–2273

28. Maeda H, Maquet V, Chen QZ, Kasuga T, Jawad H, Boccaccini AR (2007) Bioactive coatings by vaterite deposition on polymer substrates of different composition and morphology. Mater Sci Eng C 27:741–745

29. Daculsi G, LeGeros RZ, Nery E, Lynch K, Kerebel B (1989) Transformation of biphasic calcium phosphate in vivo: ultrastructural and physico-chemical characterization. J Biomed Mater Res 23:883–894

30. Daculsi G, Delectrin J (1994) Biological transformation of calcium phosphate coating in human. Microcharacterization using scanning electron microscopy and high resolution transmission electron microscopy. Cells Mater 4:63–71

31. Boyd AR, O'Kane C, O'Hare P, Burke GA, Meenan BJ (2013) The influence of target stoichiometry on early cell adhesion of co-sputtered calcium phosphate surfaces. J Mater Sci Mater Med 24:2845–2861

32. Siriphannon P, Hayashi S, Yasumori A, Okada K (1999) Preparation and sintering of $CaSiO_3$ from coprecipitated powder using NaOH as precipitant and its apatite formation in simulated body fluid solution. J Mater Res 14:529–536

33. Xu S, Lin K, Wang Z, Chang J, Wang L, Lu J, Ning C (2008) Reconstruction of calvarial defect of rabbit using porous calcium silicate bioactive ceramics. Biomaterials 29:2588–2596

34. Liu X, Ding C, Wang Z (2001) Apatite formed on the surface of plasma-sprayed wollastonite coating immersed in simulated body fluid. Biomaterials 22:2007–2012

35. Lamy D, Pierrc AC, Heimann RB (1996) Hydroxyapatite coatings with a bond coat of biomedical implants by plasma project. J Mater Res 11:680–689

36. Liu X, Tao S, Ding C (2002) Bioactivity of plasma sprayed dicalcium silicate coatings. Biomaterials 23:963–968

37. Nakajima S (1990) Experimental studies of healing process on reinforcement ceramic implantation in rabbit mandible. Shikwa Gakuho 90:525–553 (in Japanese)

38. Nonami T, Takahashi C, Yamazaki J (1995) Synthesis of diopside by alkoxide method and coating on titanium. J Ceram Soc Jpn 103:703–708 (in Japanese)

39. Hench LL, Polak JM (2002) Third-generation biomedical materials. Science 296:1014–1017

40. Hench LL, Splinter RJ, Allen WC, Greenlee TK (1971) Bonding mechanisms at the interface of ceramic prosthetic materials. J Biomed Mater Res Symp 334:117–141

41. Xynos ID, Edgar AJ, Buttery LDK, Hench LL, Polak JM (2000) Ionic products of bioactive glass dissolution increase proliferation of human osteoblasts and induce insulin-like growth factor II mRNA expression and protein synthesis. Biochem Biophys Res Commun 276:461–465

42. Jones JR (2013) Review of bioactive glass: from Hench to hybrids. Acta Biomater 9:4457–4486

43. Hoppe A, Güldal NS, Boccaccini AR (2011) A review of the biological response to ionic dissolution products from bioactive glasses and glass-ceramics. Biomaterials 32:2757–2774

44. Nakamura T, Yamamuro T, Higashi S, Kokubo T, Ito S (1985) A new glass-ceramic for bone replacement: evaluation of its bonding to bone tissue. J Biomed Mater Res 19:685–698

45. Kokubo T, Ito S, Shigematsu M, Sakka S, Yamamuro T (1985) Mechanical properties of a new type of apatite-containing glass-ceramic for prosthetic application. J Mater Sci 20:2001–2004

46. Kitsugi T, Nakamura T, Oka M, Senaha Y, Goto T, Shibuya T (1996) Bone-bonding behavior of plasma-sprayed coatings of Bioglass[R], AW-glass ceramic, and tricalcium phosphate on titanium alloy. J Biomed Mater Res 30:261–269

47. Pazo A, Saiz E, Tomsia AP (1998) Silicate glass coatings on Ti-based implants. Acta Mater 46:2551–2558

48. Gomez-Vega JM, Saiz E, Tomsia AP (1999) Glass-based coatings for titanium implant alloys. J Biomed Mater Res 46:549–559

49. Gomez-Vega JM, Saiz E, Tomsia AP, Marshall GW, Marshall SJ (2000) Bioactive glass coatings with hydroxyapatite and Bioglass® particles on Ti-based implants. 1. Processing. Biomaterials 21:105–111

50. Obata A, Kasuga T, Jones JR (2011) Hydroxyapatite coatings incorporating silicon ion releasing system on titanium prepared using water glass and vaterite. J Am Ceram Soc 94:2074–2079

51. Navarro M, Ginebra M-P, Planell JA (2003) Cellular response to calcium phosphate glasses with controlled solubility. J Biomed Mater Res A 67A:1009–1015

52. Shu C, Wenjuan Z, Xu G, Wei Z, Wei J, Dongmei W (2010) Dissolution behavior and bioactivity study of glass ceramic scaffolds in the system of $CaO-P_2O_5-Na_2O-ZnO$ prepared by sol–gel technique. Mater Sci Eng C 30:105–111

53. Ahmed I, Parsons A, Jones A, Walker G, Scotchford C, Rudd C (2010) Cytocompatibility and effect of increasing MgO content in a range of quaternary invert phosphate-based glasses. J Biomater Appl 24:555–575

54. Ohtsuki C, Kokubo T, Takahara K, Yamamuro T (1991) Compositional dependence of bioactivity of glasses in the system $CaO-SiO_2-P_2O_5$: its in vitro evaluation. J Ceram Soc Jpn 99:1–6

55. Kasuga T (2005) Bioactive calcium pyrophosphate glasses and glass-ceramics. Acta Biomater 1:55–64

56. Kasuga T, Abe Y (1999) Calcium phosphate invert glasses with soda and titania. J Non-Cryst Solids 243:70–74

57. Kasuga T, Hosoi Y, Nogami M, Niinomi M (2001) Apatite formation on calcium phosphate invert glass in simulated body fluid. J Am Ceram Soc 84:450–452

58. Kasuga T, Abe Y (1998) Novel calcium phosphate ceramics prepared by powder-sintering and crystallization of glasses in the pyrophosphate region. J Mater Res 13:3357–3360

59. Kasuga T, Sawada M, Nogami M, Abe Y (1999) Bioactive ceramics prepared by sintering and crystallization of calcium phosphate invert glasses. Biomaterials 20:1415–1420

60. Kasuga T, Nogami M, Niinomi M (2003) Calcium phosphate glass-ceramics for bioactive coating on a β-titanium alloy. Adv Eng Mater 5:498–501

61. Kasuga T, Mizuno T, Watanabe M, Nogami M, Niinomi M (2001) Calcium phosphate invert glass-ceramic coatings joined by self-development of compositionally gradient layers on a titanium alloy. Biomaterials 22:577–582

62. Kasuga T, Nogami M, Httori T, Niinomi M, Hench LL (2005) Enhancing effect of autoclaving on bioactivity of β-titanium alloy coated with calcium phosphate glass-ceramic. Key Eng Mater 284–286:243–246

63. Li P, Ohtsuki C, Kokubo T, Nakanishi K, Soga N, de Groot K (1994) The role of hydrated silica, titania, and alumina in inducing apatite on implants. J Biomed Mater Res 28:7–14

64. Kokubo T, Miyaji F, Kim H-M, Nakamura T (1996) Spontaneous formation of bonelike apatite layer on chemically treated titanium metals. J Am Ceram Soc 79:1127–1129

65. Kim H-M, Miyaji F, Kokubo T, Nishiguchi S, Nakamura T (1999) Graded surface structure of bioactive titanium prepared by chemical treatment. J Biomed Mater Res 45:100–107

66. Uchida M, Kim HM, Kokubo T, Nakamura T (1999) Apatite-forming ability of titania gels with different structure. Bioceramics 12:149–152

67. Kizuki T, Takadama H, Matsushita T, Nakamura T, Kokubo T (2010) Preparation of bioactive Ti metal surface enriched with calcium ions by chemical treatment. Acta Biomater 6:2836–2842

68. Tengvall P, Lundstrom I, Sjoqvist L, Elwing H (1989) Titanium-hydrogen peroxide interaction: model studies of the influence of the inflammatory response on titanium implants. Biomaterials 10:166–175

69. Wang X-X, Hayakawa S, Tsuru K, Osaka A (2002) Bioactive titania gel layers formed by chemical treatment of Ti substrate with a H_2O_2/HCl solution. Biomaterials 23:1353–1357

70. Wu JM, Hayakawa S, Tsuru K, Osaka A (2004) Low temperature preparation of anatase and rutile layers on titanium substrates and their ability to induce in vitro apatite deposition. J Am Ceram Soc 87:1635–1642

71. Kawai T, Takemoto M, Fujibayashi S, Neo M, Akiyama H, Yamaguchi S, Pattanayak DK, Matsushita T, Nakamura T, Kokubo T (2012) Bone-bonding properties of Ti metal subjected to acid and heat treatments. J Mater Sci Mater Med 23:2981–2992

72. Ishizaki H, Ogino H (1995) Characterization of thin hydroxyapatite layers formed on anodic titanium oxide films containing Ca and P by hydrothermal treatment. J Biomed Mater Res 29:1071–1079
73. Yang B, Uchida M, Kim H-M, Zhang X, Kokubo T (2004) Preparation of bioactive titanium metal via anodic oxidation treatment. Biomaterials 25:1003–1010
74. Xie L, Yin G, Yan D, Liao X, Huang Z, Yao Y, Kang Y, Liu Y (2010) Structure, morphology and fibroblasts adhesion of surface-porous titanium via anodic oxidation. J Mater Sci Mater Med 21:259–266
75. Li P, Kangasniemi I, de Groot K, Kokubo T (1994) Bonelike hydroxyapatite induction by a gel-derived titania on a titanium substrate. J Am Ceram Soc 77:1307–1312
76. Peltola T, Pätsi M, Kangasniemi I, Yli-Urpo A (1998) Calcium phosphate induction by sol–gel-derived titania coatings on titanium substrates in vivo. J Biomed Mater Res 42:504–510
77. Kim H-W, Koh Y-H, Li L-H, Lee S, Kim H-E (2004) Hydroxyapatite coating on titanium substrate with titania buffer layer processed by sol–gel method. Biomaterials 25:2533–2538
78. Velten D, Biehl V, Aubertin F, Valeske B, Possart W, Breme J (2002) Preparation of TiO_2 layers on cp-Ti and Ti6Al4V by thermal and anodic oxidation and by sol–gel coating techniques and their characterization. J Biomed Mater Res 59:18–28

Chapter 6
Biofunctionalization of Metals with Polymers

Takao Hanawa

Abstract If the advantages of metals and polymers are mixed and disadvantages are eliminated by manufacturing metal–polymer composite materials, humankind will obtain ideal materials having excellent mechanical properties and biofunctions. Two kinds of metal–polymer composite materials are feasible to design: one is a combination of bulk polymeric materials and bulk metallic materials and the other is immobilization of polymers to metal surfaces. In this chapter, the above metal–polymer composite materials for biomedical use are demonstrated, and the corresponding researches are reviewed, including chemical immobilization and electrodeposition of biofunctional polymer; immobilization of biomolecules such as peptide, protein, collagen, hydrogel, and gelatin; bonding of polymers with metal through silane-coupling agent; and polymers condensed in porous titanium.

6.1   Introduction

Metals show high strength, elongation, fracture toughness, and durability, which are specific advantages against ceramics and polymers. Therefore, metals are widely used for medical devices especially implants (devices inserted in the human tissues) to prevent the fracture or degradation of devices during use. However, metals are typically artificial materials and have no biofunction, which makes them fairly unattractive as biomaterials.

On the other hand, polymers are widely used as biomaterials because of their high degree of flexibility, biocompatibility, and technologic properties [1]. Also, it is relatively easy to design biofunctional polymers based on biomimic techniques, because biofunctional polymers exist in the human body as parts of biomolecules, cells, tissues, and organs.

T. Hanawa (✉)
Department of Metallic Biomaterials, Institute of Biomaterials and Bioengineering, Tokyo Medical and Dental University, 2-3-10 Kanda-surugadai, Chiyoda-ku, Tokyo 101-0062, Japan
e-mail: hanawa.met@tmd.ac.jp

Therefore, some of polymeric materials are widely known as biocompatible and biofunctional materials. The fast technological evolution of polymers has made it possible to apply these materials to medical devices over the last three decades; in fact, many devices made from metals have been replaced by others made from polymers. In spite of this fact, about 80 % of implant devices are still made from metals, and this percentage remains unchanged because of their high strength, toughness, and durability. Medical devices consisting of metals cannot be replaced by polymers at present.

If the above advantages of metals and polymers are mixed and disadvantages are eliminated by manufacturing metal–polymer composite materials, humankind will obtain ideal materials having excellent mechanical properties and biofunctions. Two kinds of metal–polymer composite materials are feasible to design: one is a combination of bulk polymeric materials and bulk metallic materials and the other is immobilization of polymers to metal surfaces. In this chapter, the above metal–polymer composite materials for biomedical use are demonstrated, and the corresponding researches are reviewed.

6.2 Immobilization of Poly(ethylene glycol)

6.2.1 Chemical Immobilization

The immobilization of biofunctional polymers on noble metals such as Au is usually conducted using the bonding –SH or –SS– group; however, this technique can only be used for noble metals. The adhesion of platelets and adsorption of proteins, peptides, antibodies, and DNA are controlled by modifications of the above technique.

On the other hand, poly(ethylene glycol) (PEG) is a biofunctional molecule on which adsorption of proteins is inhibited [2]. Therefore, immobilization of PEG to metal surface is an important event to biofunctionalize the metal surface. A class of copolymers based on poly(L-lysine)-g-poly(ethylene glycol), PLL-g-PEG, has been found to spontaneously adsorb from aqueous solutions onto TiO_2, $Si_{0.4}Ti_{0.6}O_2$, and Nb_2O_5 to develop blood-contacting materials and biosensors [3, 4]. In another case, TiO_2 and Au surfaces are functionalized by the attachment of poly(ethylene glycol)–poly(DL-lactic acid), PEG–PLA, and copolymeric micelles. The micelle layer can enhance the resistance to protein adsorption to the surfaces up to 70 % [5]. Surface modification of stainless steel by grafting of poly(ethylene glycol) was reported by Zhang et al. [6]. In their method, the surface of stainless steel was first modified by a silane-coupling agent (SCA), (3-mercaptopropyl) trimethoxysilane. The surface of the silanized stainless steel (SCA-SS) was subsequently activated by argon plasma and then subjected to UV-induced graft polymerization of poly(ethylene glycol)methacrylate (PEGMA). The PEGMA graft-polymerized stainless-steel coupon (PEGMA-g-SCA-SS) has a high graft

concentration, and the high PEG content was found to be very effective to prevent the absorption of bovine serum albumin and γ-globulin. These processes require several steps but are effective for immobilization; however, no promising technique for the immobilization of PEG to a metal surface has been so far developed. Photoreactive PEG is photoimmobilized on titanium (Ti) [7].

6.2.2 Electrodeposition

Both terminals of PEG (MW: 1,000) are terminated with $-NH_2$ ($NH_2-PEG-NH_2$). The cathodic potential is charged to Ti from the open-circuit potential to -0.5 V vs. a saturated calomel electrode (SCE) and is maintained at this potential for 300 s. During charging, the terminated PEGs electrically migrate to and are immobilized on the Ti cathode, as shown in Fig. 6.1a. Not only electrodeposition but also immersion leads to the immobilization of PEG onto a Ti surface. However, more terminated amines combine with Ti oxide via an NH–O bond by electrodeposition, while more amines randomly exist as NH_3^+ in the PEG molecule by immersion (Fig. 6.1b) [8, 9]. An atomic force microscopic image is also shown in Fig. 6.1c. The amounts of the PEG layer immobilized onto the metals are governed by the concentrations of the active hydroxyl groups on each surface oxide in the case of electrodeposition, which is governed by the relative permittivity of the surface oxide in the case of immersion [10]. The PEG-immobilized surface inhibits the adsorption of proteins and cells, as well as the adhesion of platelets [11] and bacteria [12] (Fig. 6.2), indicating that this electrodeposition technique is useful for the biofunctionalization of metal surfaces. It is also useful for all electroconductive materials and materials even having complex surface topography.

6.3 Immobilization of Biomolecules

6.3.1 Immobilization of Biomolecules

Immobilization of biomolecules is a natural approach to obtain cell and tissue compatibility and biofunctions. It has been found that these coatings act as local mediators of cell adhesion and, in consequence, as a stimulating factor for the growth and proliferation of the cells normally found around the substituted tissue. The tight attachment at the surface of the metallic implant and the conservation of the biological function of the proteins involved are prerequisites for obtaining these highly desirable properties. On the other hand, organic coatings have been scarcely used on metallic implants, because manufacturers hesitate to commercialize the
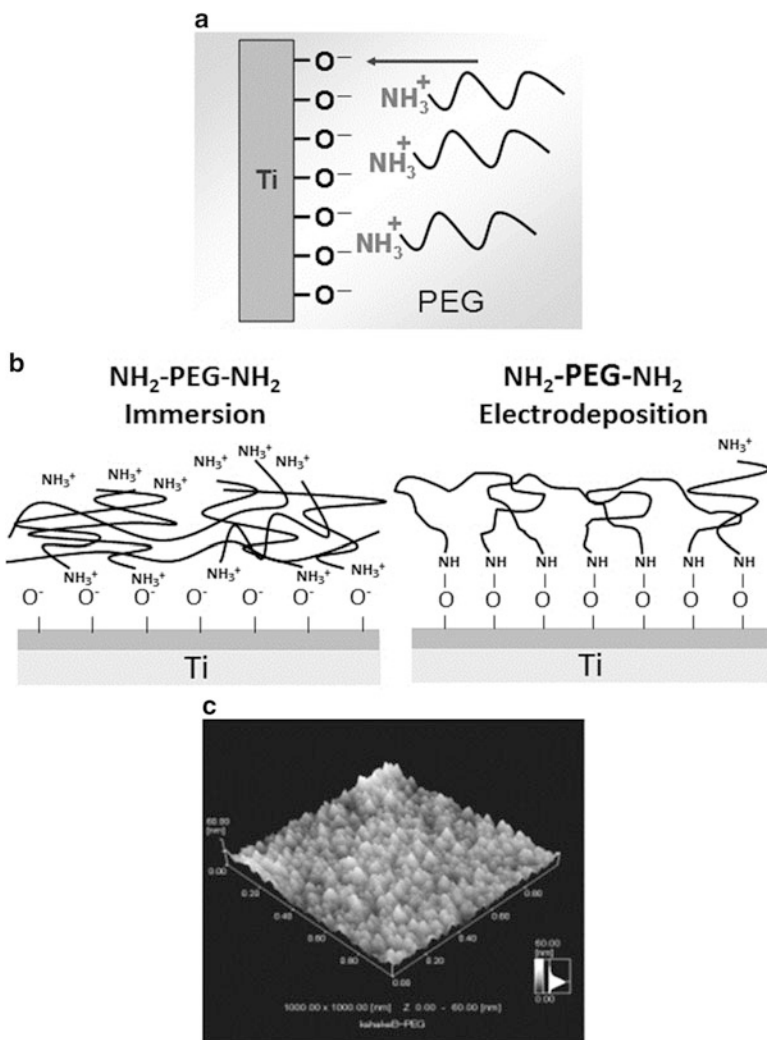
Fig. 6.1 Immobilization of NH$_2$–PEG–NH$_2$ by electrodeposition. The terminated PEGs electrically migrate to and are immobilized on the Ti cathode (**a**). More terminated amines combine with Ti oxide via an NH–O bond by electrodeposition, while more amines randomly exist as NH$_3^+$ in the PEG molecule by immersion (**b**). An atomic force microscopic image of the PEG-immobilized Ti surface (**c**)

biomolecules immobilized by metallic implant due to the problems on storage, safety, sterilization, etc.

The immobilization of biomolecules on the metallic surface can be achieved using self-assembled monolayers as cross-linkers. Self-assembled monolayers provide chemically and structurally well-defined surfaces that can often be manipulated using standard synthetic methodologies [13]. Thiol on self-assembled
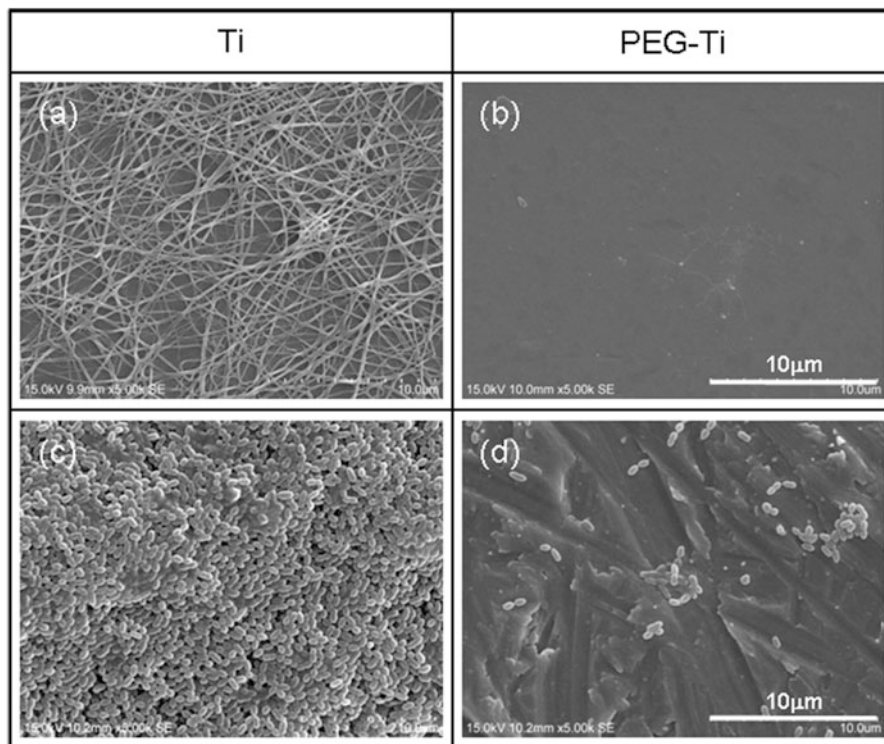
Fig. 6.2 Inhibition of platelet adhesion and biofilm formation on Ti through immobilization of NH$_2$–PEG–NH$_2$ by electrodeposition. (**a**) Platelet adhesion and fibrin network on untreated Ti, (**b**) inhibition of platelet adhesion on PEG-immobilized Ti by electrodeposition, (**c**) biofilm formation on untreated Ti, and (**d**) inhibition of biofilm formation on PEG-immobilized Ti by electrodeposition

monolayers [14, 15] and siloxane-anchored self-assembled monolayers [16] has been particularly well studied. A problem related to the application of immobilized biomolecules via silanization techniques is the hydrolysis of siloxane films when exposed to aqueous (physiological) conditions [17]. More recently, alkyl phosphate films that retain robust under physiological conditions [18] have been used to provide an ordered monolayer on tantalum oxide surfaces [19, 20], and alkalphosphonic acids have been used to coat the native oxide surfaces of metals and their alloys inducing iron [21], steel [22], and Ti [23].

6.3.2   Peptide

In a living tissue, the most important role played by the ECM has been highlighted to favor cell adhesion [24]. Studies have shown that interactions occur between cell

membrane receptors and adhesion proteins derived from the bone matrix, such as type I collagen or fibronectin [25]. These proteins are characterized by a RGD (Arg-Gly-Asp) motif which specially transmembrane connections between the actin cytoskeleton and the RGD motif, and the whole system can activate several intracellular signaling pathways modulating cell behavior (e.g., proliferation, apoptosis, shape, mobility, gene expression, and differentiation) [26].

Due to the main role of the RGD sequence in cell adhesion, several research groups have developed biofunctionalized surfaces by immobilization of RGD peptides. Grafting RGD peptides has been performed on different biomaterials, such as Ti [27–29], and has been shown to improve osteoconduction in vitro. Methodologies differ by the conformation of RGD and by the technique used for peptide immobilization [24, 25, 28–30]. Since the graft of an RGD peptide is known to be efficient in bone reconstruction [31], the challenge is to develop simple and cheap methods to favor cell anchorage on biomaterial surfaces [29, 30]. Self-assembled molecular monolayers bearing RGD moieties have been grafted to numerous surfaces, using either silanes [32], phosphonates on oxidized surfaces [29], or thiols on Au [30], but have encountered some application problems for large-scale production. Phosphonates are known to adsorb on Ti. To be mechanically and physiologically stable, phosphonate layers have to be covalently bound to the material surface using drastic conditions [33, 34] which are not compatible with biomolecule stability. Monolayers of RGD phosphonates have been achieved using a complex multistep process which necessitates to tether a primer onto Ti surface, then a linker, and finally the peptide [35]. To immobilize RGD to the electrodeposited PEG on Ti, PEG with an $-NH_2$ group and a $-COOH$ group (NH_2–PEG–COOH) must be employed. One terminal group, $-NH_2$, is required to bind stably with a surface oxide on a metal. On the other hand, the other terminal group, $-COOH$, is useful to bind biofunctional molecules such as RGD as shown in Fig. 6.3 [36]. This RGD/PEG/Ti surface accelerates the calcification by MC3T3-E1 cell [37]. The calcification level is the highest on the RGD/PEG/Ti surface
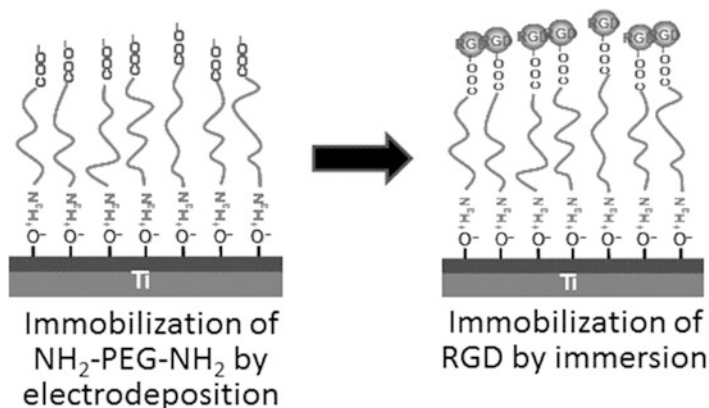

Fig. 6.3 Immobilization of RGD peptide on Ti through electrodeposited NH_2–PEG–COOH
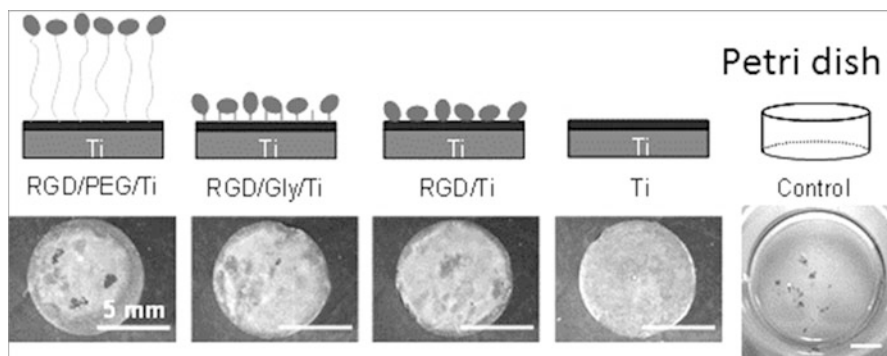
Fig. 6.4 Immobilization mode of RGD peptide on Ti and calcification by MC3T3-E1 cell on each specimen

(Fig. 6.4), and the bone formation on the RGD/PEG/Ti surface is accelerated compared to RGD/Ti surface in rabbit [38].

Glycine (G)–arginine (R)–glycine (G)–asparaginic acid (D)–serine (S) sequence peptide (GRGDS peptide) is coated through the chloride activation technique to enhance adhesion and migration of osteoblastic cells [39]. The expression levels of many genes in MC3T3-E1 cells are altered.

6.3.3 Proteins and Collagen

Among the relevant molecules involved in biochemical modification of bone-contacting surfaces, growth factor, such as bone morphogenetic protein-2 (BMP-2), is of primary interest. BMP-2 has been known to play an important role in bone healing processes and to enhance therapeutic efficiency. Ectopic bone formation by BMP-2 in animals has been well established following the first reports of BMP-2 by the Urist research group [40–42]. Synthetic receptor binding motif mimicking BMP-2 is covalently linked to Ti surfaces through a chemical conjunction process [43]. A complete and homogeneous peptide overlayer on the Ti surfaces; the content is further measured by gamma counting. Biological evaluations show that the biochemically modified Ti is active in terms of cell attachment behavior. Ti surfaces can enhance the rate of bone healing as compared with untreated Ti surface. Bone morphogenetic protein-4 (BMP-4) is immobilized on a Ti–6Al–4V alloy through lysozyme to improve the hard tissue response [44]. Proteins are silane-coupled to the oxidized surfaces of the Co–Cr–Mo alloy, the Ti–6Al–4V alloy, Ti, and the Ni–Ti alloy to improve tissue compatibility [45].

Biomolecules are also used to accelerate bone formation and soft tissue adhesion on a material. Type I collagen is immobilized by immersion in the collagen solution [46]. Type I collagen production increases with modification by ethane-1,1,2-
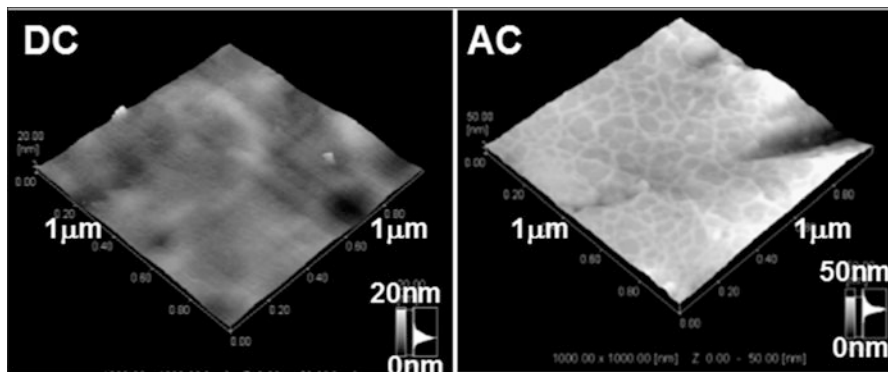
Fig. 6.5 Atomic force microscopic images of Ti surfaces with electrodeposited collagen using DC potential or AC potential

triphosphonic acid and methylenediphosphonic acid grafted onto Ti [47]. Type I collagen is grafted with glutaraldehyde as a cross-linking agent [48]. For the electrodeposition, it is found that an alternating current (AC) between −1 and +1 V vs. SCE with 1 Hz is more effective than direct current (DC) to immobilize type I collagen to Ti and durability in water is high [49] as shown in Fig. 6.5.

Fibronectin is immobilized directly on Ti using a tresyl chloride activation technique [50]. L-threonine and O-phospho-L-threonine are immobilized on acid-etched Ti surface [51].

6.3.4   Hydrogel and Gelatin

Immobilization or coating of hydrogel to metal surface is currently being attempted to add a drug delivery ability to orthopedic implant and stents or fluorescent sensing ability to microchips. Currently, synthetic polymeric hydrogels like poly-(hydroxyethylmethacrylate) (pHEMA) and poly(hydroxyethylacrylate) (pHEA) are widely used as compliant materials particularly in the case of contact with blood or other biological fluids [52]. Despite having good flexibility in the swollen state, hydrogels usually lack suitable mechanical properties, and this could greatly impair their use as coating materials for surgical procedure. Moreover, in case of inadequate adhesion between the hydrogel coating and the metal surface, a break-age at the coating–steel interface might occur [53]. A spray-coated method has been set up with the aim to control the coating of pHEMA onto the complex surface of a 316L steel stent for percutaneous coronary intervention (PCI) [54]. The pHEMA coating evaluation of roughness wettability together with its morphological and chemical stability after three cycles of expansion–crimping along with preliminary results after 6 months demonstrates the suitability of the coating for surgical implantation of stent.

An alternative and very promising synthetic route is represented by electrochemical polymerization, which leads to direct thin film coatings on the metal substrates with interesting applications either for corrosion protection or for the development of bioactive films [55–58]. As far as orthopedic field is concerned, in recent years, many procedures based on surface modification have been suggested to improve the biocompatibility and biofunctionality of Ti-based implant [59]. 2-hydroxy-ethyl-methacrylate (HEMA), a macromer poly(ethylene-glycol diacrylate) (PEGDE), and PEGDE copolymerized with acrylic acid were used to obtain hydrogels. A model protein and a model drug were entrapped in the hydrogel and released according to pH change [60].

6.4 Other Polymer Coatings

6.4.1 Bonding of Polymers with Metals Through Silane-Coupling Agent

The interfacial chemical structure governing the bonding strength, especially at the nanometer level, is one of the most challenging aspects to the development of composite materials. The combination of a Ti alloy with a resin for crown facings has been attempted [61]. In particular, silane-coupling agents containing S–H groups and Si–O–CH$_3$ groups are widely used to combine dental alloys with resins [62]. The S–H group works as a bonding agent with polymers, while the Si–O–CH$_3$ group works as a bonding agent with metals. The mechanical properties and durability of composite resin increase with the silanized filler [63–66]. However, in most studies on materials using silane-coupling agents in the field of dentistry, only the bonding strength is evaluated and discussed, and there are few reports that examine and discuss the chemical structures at the bonding interface and how they influence the bonding strength.

Studies on silane-coupling agents to combine polymers with metals have been performed in other fields. An aluminum–vegetable oil composite using a silane-coupling agent has been developed [67, 68]. Rubber-to-metal bonding by a silane-coupling agent was investigated [69]. In addition, the surface modification of stainless steel by grafting poly(ethylene glycol) using a silane-coupling agent has been reported [6]. However, only the chemical structure is investigated in these studies. In other words, the relationship between the bonding strength and the interfacial chemical structure containing a silane-coupling agent layer has not been studied.

The unequivocal relationship between the shear bonding strength and the chemical structure at the bonding interface of a Ti–SPU composite through a silane-coupling agent (γ-mercaptopropyl trimethoxysilane (γ-MPS)) is investigated [70]. The bonding interface between SPU and Ti substrate is determined by the thickness of γ-MPS layer as shown in Fig. 6.6. On the other hand, the shear bond

Fig. 6.6 Difference in bonding interface structure between thin (*left*) and thick (*right*) γ-MPS layers
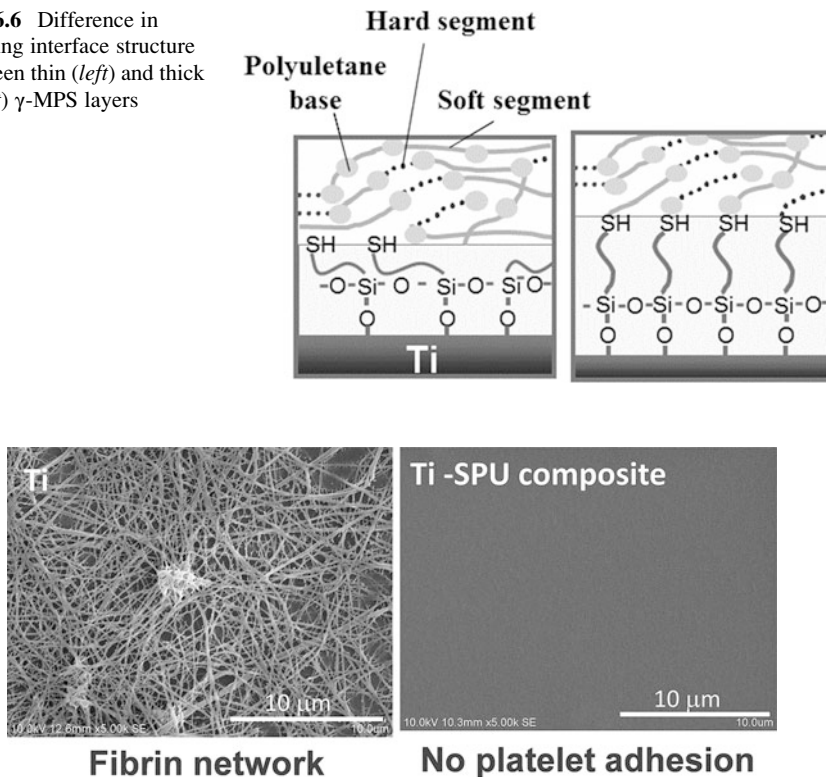

Fig. 6.7 Inhibition of platelet adhesion and fibrin network formation on SPU-coated Ti

strength of the Ti/SPU interface increased with ultraviolet (UV) irradiation according to the increase of the cross-linkage in SPU. Platelet adhesion to Ti is inhibited by SPU, as shown in Fig. 6.7. This technique is used for the creation of a new meta-based material having high strength, high toughness, and biofunction. UV irradiation to a Ti–SPU composite is clearly a factor governing the shear bond strength of the Ti/SPU interface [71]. In addition, active hydroxyl groups on the surface oxide film are clearly factors governing the shear bond strength [72]. After good bonding between metal and polymer is produced, biofunctionalization techniques developed in the field of polymers could be applied to the composite materials.

The effects of different kinds of terminal functional groups and the thickness of the silane layers (SIL) on the adhesive strength between Ti–29Nb–13Ta–4.6Zr (TNTZ) alloy and SPU were investigated by means of shear bonding tests. The following silane-coupling agents were employed in this study: 3-methacryloxypropyltrimethoxysilane (γ-MPTS), aminopropyltriethoxysilane (APS), and γ-MPS. Furthermore, the shear bonding strength of the TNTZ/SIL/ SPU interface was also characterized after immersion in water for 30 days. Silane-coupling treatment produces a tenfold increase in the shear bonding strength,

independent of the type of terminal functional groups and the thickness of the silane layers. The TNTZ/SIL/SPU composites are partially fractured at the interfaces of the TNTZ/SIL, while the rest of the fracture occurs at the interfaces of the SIL/SPU in single sample. The shear bonding strength decreases after immersion in water for 30 days when APS and γ-MPS are used as the silane-coupling agents, because stable chemical bonding is not achieved between the silane layer and SPU, whereas the bonding of the γ-MPTS composite is not affected by exposure to water [73]. The number of hydroxyl groups increases with an increase in treatment time at a H_2O_2 concentration of 5 %. On the other hand, an increase from 5 to 30 % in H_2O_2 concentration leads to a decrease in the number of hydroxyl groups on the TNTZ surface, because at higher H_2O_2 concentrations, the reaction that consumes the hydroxyl groups is dominant. The shear bonding strength is doubled compared with the untreated TNTZ/SIL/SPU interface. Although the shear bonding strength decreases after immersion in water for 30 days when APS and γ-MPS are used, TNTZ/γ-MPTS/SPU composites exhibit good durability to water and maintain an equivalent shear bonding strength before immersion in water [74]. The adhesive strength of the SPU coating on the nanotube structure formed on TNTZ by anodization for 3,600 s increases by 50 %. These improvements in the adhesive strength of SPU are the result of an anchor effect introduced by the nanostructures formed by anodization. Fracture occurs at the interface of the nanoporous structure and the SPU coating layer. In contrast, in the case that SPU coating has been performed on the nanotube structure, fracture occurs inside the nanotubes [75].

6.4.2 Polymers Condensed in Porous Titanium

The Young's modulus of metallic materials is relatively larger than that of cortical bone: about 200 GPa in stainless steels and Co–Cr–Mo alloys, about 100 GPa in α-type and (α + β)-type Ti alloys, and 15–20 GPa in cortical bone. When fractured bone is fixed with metallic bone fixator such as bone plate and bone nail, during healing a load to fixation part is mainly received by metallic fixators because of the difference in their Young's modulus. This phenomenon is well known as so-called "stress shielding" in orthopedics. This large Young's modulus generates other problems. When a metal is used as a metallic spacer in spinal fixation, the spacer is mounted in matrix bone. In the case of dental implant, occlusal pressure is not absorbed by the implant and directly conducts to jaw bone.

To solve the above problems, metals with low Young's modulus are required. Two approaches are feasible: the decrease of the Young's modulus of a metallic material itself and decrease of the apparent Young's modulus by forming a porous body. In the latter case, the pores are sometimes filled by polymers to control the apparent Young's modulus. Ultra-high-molecular-weight polyethylene (UHMWPE) [76] and poly(methyl methacrylate) (PMMA) [77] are attempted to fill the pores in porous Ti. Figure 6.8 shows porous Ti whose pores are filled by UHMWPE.

Fig. 6.8 Fracture by
bending of porous Ti whose
pores are filled by
UHMWPE (Provided by
Dr. Naoyuki Nomura,
Tohoku University)
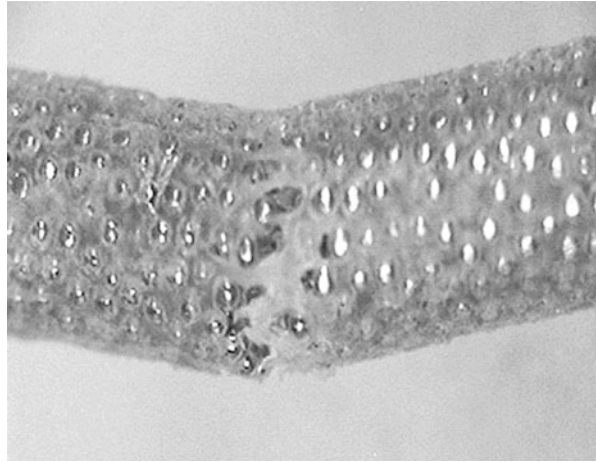
6.5   Conclusions

Metallic materials are widely used in medicine for not only orthopedic and dental
implants but also cardiovascular devices and other purposes. The metal surface may
be biofunctionalized by various techniques such as the immobilization of
biofunctional molecules and the creation of metal–polymer composites. These
techniques make it possible to apply metals to a scaffold in tissue engineering.
Artificial materials such as metal–polymer composites will continue to be used as
biomaterials in the future, because of their excellent tissue compatibility and
biofunctions. Some of metal–polymer composites are reviewed in other textbooks
[78–80].

References

1. Ratner BD, Hoffman AS, Schoen FJ, Lemons JE (eds) (2004) Biomaterials science: an introduction to materials in medicine. Elsevier, Amsterdam
2. Mahato RI (2005) Biomaterials for delivery and targeting of proteins and nucleic acids. CRC Press, Roca Raton
3. Kenausis GL, Vörös J, Elbert DL, Huang N, Hofer R, Ruiz-Taylor L, Textor M, Hubbell JA, Spencer ND (2000) Poly(L-lysine)-g-poly(ethylene glycol) layers on metal oxide surfaces: attachment mechanism and effects of polymer architecture on resistance to protein adsorption. J Phys Chem B104:3298–3309
4. Huang NP, Michel R, Vörös J, Textor M, Hofer R, Rossi AD, Dlbert L, Hubbell JA, Spencer ND (2001) Poly(L-lysine)-g-poly(ethylene glycol) layers on metal oxide surfaces: surface-analytical characterization and resistance to serum and fibrinogen adsorption. Langmuir 17:489–498

5. Huang NP, Csucs G, Emoto K, Nagasaki Y, Kataoka K, Textor M, Spencer ND (2002) Covalent attachment of novel poly(ethylene glycol)-poly(DL-lactic acid) copolymeric micelles to TiO$_2$ surfaces. Langmuir 18:252–258

6. Zhang F, Kang ET, Neoh KG, Wang P, Tan KL (2001) Surface modification of stainless steel by grafting of poly(ethylene glycol) for reduction in protein adsorption. Biomaterials 22:1541–1548

7. To Y, Hasuda H, Sakuragi M, Tsuzuki S (2007) Surface modification of plastic, glass and titanium by photoimmobilization of polyethylene glycol for antibiofouling. Acta Biomater 3:1024–1032

8. Tanaka Y, Doi H, Iwasaki Y, Hiromoto S, Yoneyama T, Asami K, Imai H, Hanawa T (2007) Electrodeposition of amine-terminated-poly(ethylene glycol) to Ti surface. Mater Sci Eng C27:206–212

9. Tanaka Y, Doi H, Kobayashi E, Yoneyama T, Hanawa T (2007) Determination of the immobilization manner of amine-terminated poly(ethylene glycol) electrodeposited on a Ti surface with XPS and GD-OES. Mater Trans 48:287–292

10. Tanaka Y, Saito H, Tsutsumi Y, Doi H, Imai H, Hanawa T (2008) Active hydroxyl groups on surface oxide film of Ti, 316l stainless steel, and cobalt-chromium-molybdenum alloy and its effect on the immobilization of poly(ethylene glycol). Mater Trans 49:805–811

11. Tanaka Y, Matsuo Y, Komiya T, Tsutsumi Y, Doi H, Yoneyama T, Hanawa T (2010) Characterization of the spatial immobilization manner of poly(ethylene glycol) to a titanium surface with immersion and electrodeposition and its effects on platelet adhesion. J Biomed Mater Res 92A:350–358

12. Tanaka Y, Matin K, Gyo M, Okada A, Tsutsumi Y, Doi H, Nomura N, Tagami J, Hanawa T (2010) Effects of electrodeposited poly(ethylene glycol) on biofilm adherence to titanium. J Biomed Mater Res 95A:1105–1113

13. Balachnder N, Sukenik SN (1990) Monolayer transformation by nucleophilic substitution: applications to the creation of new monolayer assemblies. Langmuir 6:1621–1627

14. Bain C, Troughton Y, Tao YT, Evall J, Whitesides GM, Nuzzo RG (1989) Formation of monolayer films by the spontaneous assembly of organic thiols from solution onto gold. J Am Chem Soc 111:331–335

15. Dubois LH, Nuzzo RG (1992) Synthesis, structure, and properties of model organic surfaces. Ann Rev Phys Chem 43:437–463

16. UlMan A (1996) Formation and structure of self-assembled monolayers. Chem Rev 96:1533–1554

17. Xiao SJ, Textor M, Spencer ND (1998) Covalent attachment of cell-adhesive, (Arg-Gly-Asp)-containing peptides to titanium surfaces. Langmuir 14:5507–5516

18. Gawalt ES, Avaltroni MJ, Danahy MP, Silverman BM, Hanson EL, Midwood KS, Schwarzbauer JE, Schwartz J (2003) Bonding organics to Ti alloys: facilitating human osteoblast attachment and spreading on surgical implant materials. Langmuir 19:200–204

19. Brovelli D, Hahner G, Ruis L, Hofer R, Kraus G, Waldner A, Schlosser J, Oroszlan P, Ehart M, Spencer ND (1999) Highly oriented, self-assembled alkanephosphate monolayers on tantalum (V) oxide surfaces. Langmuir 15:4324–4327

20. Textor M, Ruiz L, Hofer R, Rossi K, Feldman K, Hahner G, Spencer ND (2000) Structural chemistry of self-assembled monolayers of octadecylphosphoric acid on tantalum oxide surfaces. Langmuir 16:3257–3271

21. Fang JL, Wu NJ, Wang ZW, Li Y (1991) XPS, AES and Raman studies of an antitarnish film on tin. Corrosion 47:169–173

22. Van Alsten JG (1999) Self-assembled monolayers on engineering metals: structure, derivatization, and utility. Langmuir 15:7605–7614

23. Gawalt ES, Avaltroni MJ, Koch N, Schwartz J (2001) Self-assembly and bonding of alkanephosphonic acids on the native oxide surface of titanium. Langmuir 17:5736–5737

24. Verrier S, Pallu S, Bareille R, Jonczyk A, Meyer J, Dard M, Amedee J (2002) Function of linear and cyclic RGD-containing peptides in osteoprogenitor cells adhesion process. Bio-materials 23:585–596

25. Reyes CD, Petrie TA, Burns KL, Schwartz Z, Garcia AJ (2007) Biomolecular surface coating to enhance orthopaedic tissue healing and integration. Biomaterials 28:3228–3235

26. Hynes RO (2002) Integrins: bidirectional, allosteric signaling machines. Cell 110:673–687

27. Bagno A, Piovan A, Dettin M, Chiarion A, Brun P, Gambaretto R, Fontana G, Di Bello C, Palu G, Castagliuolo I (2007) Human osteoblast-like cell adhesion on titanium substrates covalently functionalized with synthetic peptides. Bone 40:693–699

28. Elmengaard B, Bechtold JE, Soballe K (2005) In vivo study of the effect of RGD treatment on bone on growth on press-fit titanium alloy implants. Biomaterials 26:3521–3526

29. Rammelt S, Illert T, Bierbaum S, Scharnweber D, Zwipp H, Schneiders W (2006) Coating of titanium implants with collagen. RGD peptide and chondroitin sulfate. Biomaterials 27:5561–5571

30. Auernheimer J, Zukowski D, Dahmen C, Kantlehner M, Enderle A, Goodman SL, Kessker H (2005) Titanium implant materials with improved biocompatibility through coating with phosphate-anchored cyclic RGD peptides. ChemBioChem 6:2034–2040

31. Ferris DM, Moodie GD, Dimond PM, Gioranni CW, Ehrlich MG, Valentini RF (1999) RGD-coated titanium implants stimulate increased bone formation in vivo. Biomaterials 20:2323–2331

32. Xiao SJ, Textor M, Spencer ND, Wieland M, Keller B, Sigrist H (1997) Immobilization of the cell-adhesive peptide Arg-Gly-Asp-Cys (RGDC) on titanium surfaces by covalent chemical attachment. J Mater Sci Mater Med 8:867–872

33. Gawalt ES, Avaltroni MJ, Koch N, Schwartz J (2001) Self-assembly and bonding of alkanephosphonic acids on the native oxide surface of titanium. Langmuir 17:5736–5738

34. Silverman BM, Wieghaus KA, Schwartz J (2005) Comparative properties of siloxane vs phosphonate monolayers on a key titanium alloy. ACS J Surf Colloid 21:225–228

35. Schwartz J, Avaltroni MJ, Danahy MP, Silverman BM, Hanson EL, Schwarzbauer JE, Midwood KS, Gawalt ES (2003) Cell attachment and spreading on metal implant materials. Mater Sci Eng C23:395–400

36. Tanaka Y, Saito H, Tsutsumi Y, Doi H, Nomura N, Imai H, Hanawa T (2009) Effect of pH on the interaction between zwitterion and titanium oxide. J Colloid Interface Sci 330:138–143

37. Oya K, Tanaka Y, Saito H, Kurashima K, Nogi K, Tsutsumi H, Tsutsumi Y, Doi H, Nomura N, Hanawa T (2009) Calcification by MC3T3-E1 cells on RGD peptide immobilized on titanium through electrodeposited PEG. Biomaterials 30:1281–1286

38. Park JW, Kurashima K, Tustusmi Y, An CH, Suh YJ, Doi H, Nomura N, Noda K, Hanawa T (2011) Bone healing of commercial oral implants with RGD immobilization through electrodeposited poly(ethylene glycol) in rabbit cancellous bone. Acta Biomater 7:3222–3229

39. Yamanouchi N, Pugdee K, Chang WJ, Lee SY, Yoshinari M, Hayakawa T, Abiko Y (2008) Gene expression monitoring in osteoblasts on titanium coated with fibronectin-derived pep-tide. Dent Mater J 27:744–750

40. Urist MR (1965) Bone: formation by autoinduction. Science 150:893–899

41. Lee YM, Nam SH, Seol YJ, Kim TI, Lee SJ, Ku Y, Rhyu IC, Chung CP, Han SB, Choi SM (2003) Enhanced bone augmentation by controlled release of recombinant human bone morphogenetic protein-2 from bioabsorbable membranes. J Periodontol 74:865–872

42. Wikesjo UM, Lim WH, Thomson RC, Cook AD, Wozney JM, Hardwick WR (2003) Peri-odontal repair in dogs: evaluation of a bioabsorbable space-providing macroporous membrane with recombinant human bone morphogenetic protein-2. J Periodontol 74:635–647

43. Seol YJ, Park YJ, Lee SC, Kim KH, Lee JY, Kim TI, Lee YM, Ku Y, Rhyu IC, Han SB, Chung CP (2006) Enhanced osteogenic promotion around dental implants with synthetic binding motif mimicking bone morphogenetic protein (BMP)-2. J Biomed Mater Res 77A:599–607

44. Puleo DA, Kissling RA, Sheu MS (2002) A technique to immobilize bioactive proteins, including bone morphogenetic protein-4 (BMP-4), on titanium alloy. Biomaterials 23:2079–2087
45. Nanci A, Wuest JD, Peru L, Brunet P, Sharma V, Zalzal S, McKee MD (1998) Chemical modification of titanium surfaces for covalent attachment of biological molecules. J Biomed Mater Res 40:324–335
46. Nagai M, Hayakawa T, Fukatsu A, Yamamoto M, Fukumoto M, Nagahama F, Mishima H, Yoshinari M, Nemoto K, Kato T (2002) In vitro study of collagen coating of titanium implants for initial cell attachment. Dent Mater J 21:250–260
47. Viornery C, Guenther HL, Aronsson BO, Pöchy P, Descouts P, Grötzel M (2002) Osteoblast culture on polished titanium disks modified with phosphonic acids. J Biomed Mater Res 62:149–155
48. Chang WJ, Qu KL, Lee SY, Chen JY, Abiko Y, Lin CT, Huang HM (2008) Type I collagen grafting on titanium surfaces using low-temperature grow discharge. Dent Mater J 27:340–346
49. Kamata H, Suzuki S, Tanaka Y, Tsutsumi Y, Doi H, Nomura N, Hanawa T, Moriyama K (2011) Effects of pH, potential, and deposition time on the durability of collagen electrodeposited to titanium. Mater Trans 52:81–89
50. Pugdee K, Shibata Y, Yamamichi N, Tsutsumi H, Yoshinari M, Abiko Y, Hayakawa T (2007) Gene expression of MC3T3-E1 cells on fibronectin-immobilized titanium using tresyl chloride activation technique. Dent Mater J 26:647–655
51. Abe Y, Hiasa K, Takeuchi M, Yoshida Y, Suzuki K, Akagawa Y (2005) New surface modification of titanium implant with phosphor-amino acid. Dent Mater J 24:536–540
52. Cadotte AJ, DeMarse TB (2005) Poly-HEMA as a drug delivery device for in vitro neutral network on micro-electrode arrays. J Neural Eng 2:114–122
53. Belkasm JS, Munro CA, Shoichet MS, Johnston M, Midha R (2005) Long-term in vivo biochemical properties and biocompatibility of poly(2-hydroxyethyl methacrylate-co-methyl methacrylate) nerve conduits. Biomaterials 26:1741–1749
54. Indolfi L, Causa F, Netti PA (2009) Coating process and early stage adhesion evaluation of poly(2-hydroxy-ethyl-methacrylate) hydrogel coating of 316L steel surface for stent applications. J Mater Sci Mater Med 20:1541–1551
55. Fenelo AM, Breslin CB (2003) The electropolymerization of pyrrole at a CuNi electrode: corrosion protection properties. Corros Sci 45:2837–2850
56. Mengoli G (1979) Feasibility of polymer film coatings through electroinitiated polymerization in aqueous medium. Adv Polym Sci 33:1–31
57. De Giglio E, Guascito MR, Sabbatini L, Zambonin G (2001) Electropolymerization of pyrrole on titanium substrates for the future development of new biocompatible surfaces. Biomaterials 22:2609–2616
58. Rammelt U, Nguyen PT, Plieth W (2003) Corrosion protection by ultrathin films of conducting polymers. Electrochem Acta 48:1257–1262
59. De Giglio E, Gennaro I, Sabbatini L, Zambonin G (2001) Analytical characterization of collagen- and /or hydroxyapatite-modified polypyrrole films electrosynthesized on Ti-substrates for the development of new bioactive surfaces. J Biomater Sci Polym Ed 12:63–76
60. De Giglio E, Cometa S, Satriano C, Sabbatini L, Zambonin G (2009) Electrosynthesis of hydrogel films on metal substrates for the development of coatings with tunable drug delivery performance. J Biomed Mater Res 88A:1048–1057
61. Taira Y, Imai Y (1995) Primer for bonding resin to metal. Dent Mater 11:2–6
62. Smith NA, Antoun GG, Ellis AB, Crone WC (2004) Improved adhesion between nickel-titanium shape memory alloy and polymer matrix via silane coupling agents. Compos Part A Apply Sci 35:1307–1312
63. Abboud M, Casaubieilh L, Morval F, Fontanille M, Duguet E (2000) PMMA-based composite materials with reactive ceramic fillers: IV. Radiopacifying particles embedded in PMMA beads for acrylic bone cements. J Biomed Mater Res 53:728–736

64. Yoshida K, Tanagawa M, Atsuta M (2001) Effects of filler composition and surface treatment on the characteristics of opaque resin composites. J Biomed Mater Res 58:525–530

65. Kanie T, Arikawa H, Fujii K, Inoue K (2004) Physical and mechanical properties of PMMA resins containing γ-methacryloxypropyltrimethoxysilane. J Oral Rehabil 31:161–171

66. Ferracane JL, Berge HX, Condon JR (1998) In vitro aging of dental composites in water-effect of degree of conversion, filler volume, and filler matrix coupling. J Biomed Mater Res 42:465–472

67. Bexell U, Olsson M, Jhansson M, Samuelsson J, Sundell PE (2003) A tribological study of a novel pre-treatment with linseed oil bonded to mercaptosilane-treated aluminum. Surf Coat Technol 166:141–152

68. Bexell U, Olsson M, Sundell PE, Jhansson M, Carlsson P, Hellsing MA (2004) ToF-SIMS study of linseed oil bonded to mercaptosilane-treated aluminum. Appl Surf Sci 231–232:362–365

69. Jayaseelan SK, Ooji WJV (2001) Rubber-to-metal bonding by silanes. J Adhes Sci Technol 15:967–991

70. Sakamoto H, Doi H, Kobayashi E, Yoneyama T, Suzuki Y, Hanawa T (2007) Structure and strength at the bonding interface between a titanium-segmented polyurethane composite through 3-(trimethoxysilyl) propyl methacrylate for artificial organs. J Biomed Mater Res 82A:52–61

71. Sakamoto H, Hirohashi Y, Saito H, Doi H, Tsutsumi Y, Suzuki Y, Noda K, Hanawa T (2008) Effect of active hydroxyl groups on the interfacial bond strength of titanium with segmented polyurethane through -mercaptopropyl trimethoxysilane. Dent Mater J 27:81–92

72. Sakamoto H, Hirohashi Y, Doi H, Tsutsumi Y, Suzuki Y, Noda K, Hanawa T (2008) Effect of UV irradiation on the shear bond strength of titanium with segmented polyurethane through -mercapto propyl trimethoxysilane. Dent Mater J 27:124–132

73. Hieda J, Niinomi M, Nakai M, Kamura H, Tsutsumi H, Hanawa T (2012) Effect of terminal functional groups of silane layers on adhesive strength between biomedical Ti-29Nb-13Ta-4.6Zr alloy and segment polyurethanes. Surf Coat Technol 206:3137–3141

74. Hieda J, Niinomi M, Nakai M, Kamura H, Tsutsumi H, Hanawa T (2013) Improvement of adhesive strength of segmented polyurethane on Ti–29Nb–13Ta–4.6Zr alloy through H_2O_2 treatment for biomedical applications. J Biomed Mater Res Part B Appl Biomater 101B:776–783

75. Hieda J, Niinomi M, Nakai M, Cho K, Mohri T, Hanawa T (2014) Adhesive strength of medical polymer on anodic oxide nanostructures fabricated on biomedical β-type titanium alloy. Mater Sci Eng C36:244–252

76. Nomura N, Baba Y, Kawamura A, Fujinuma S, Chiba A, Masahashi N, Hanada S (2007) Mechanical properties of porous titanium compacts reinforced by UHMWPE. Mater Sci Forum 539–543:1033–1037

77. Nakai M, Niinomi M, Akahori T, Yamanoi H, Itsuno S, Haraguchi N, Itoh Y, Ogasawara T, Onishi T, Shindo T (2008) Effect of silane coupling treatment on mechanical properties of porous pure titanium filled with PMMA for biomedical applications. J Jpn Inst Metal 72:839–845

78. Possart W (1998) Adhesion of polymers. In: Hansen JA, Breme HJ (eds) Metals as biomaterials. Wiley, New York, pp 197–218

79. Worch H (1998) Special thin organic film. In: Hansen JA, Breme HJ (eds) Metals as biomaterials. Wiley, New York, pp 177–196

80. Xiao SJ, Kenausis G, Textor M (2001) Biochemical modification of titanium surfaces. In: Brunrtte DM, Tenvall P, Textor M, Thomsen P (eds) Titanium in medicine. Springer, Amsterdam, pp 417–455

Chapter 7
Adhesive Strength of Bioactive Surface Layer

Noriyuki Hisamori

Abstract Bioactive capability of Ti-alloy for implant application has been developed by producing thin hydroxyapatite (HAp) film on its surface. The adhesive strength between the base metal and the HAp film has to be evaluated to ensure the reliability of the implant. But the method of evaluation is not yet established because of its difficulty to cause adhesive fracture between base metal and HAp thin film. In this chapter, tensile load is applied to the HAp film on Ti-6Al-4V alloy substrate normal to its thickness by using a specimen bonded with adhesives. Surfactant is applied near the interface between Ti-6Al-4V substrate and HAp film by adhesives to avoid coverage of the interface. Thus the accuracy of this method is improved by preventing adhesive overflow from bonded surface to the side of the specimen. As a result, fracture occurs at interface between Ti-alloy and the HAp film. This method is proved to be useful for evaluating bond strength between Ti-alloy and HAp film and verifying the fracture of the adhesive layer.

Keywords Ti-6Al-4V alloy • Hydroxyapatite • Adhesive strength • Interfacial fracture • Bioactive surface layer • Bond layer

7.1 Introduction

It is commonly recognized that about three months' time is necessary to secure metallic implant to the bone tissue [1, 2]. Functional layer deposited on the surface of the metal-based implant improves the bone actively which can be used to shorten this period of time. Therefore, there are several methods of forming hydroxyapatite (HAp) on the surface of the metallic implant material. Hydroxyapatite layer reacts with the body fluids in the human body environment, giving bone-conducting function to metallic implant material [3–5]. However, failures due to delamination at the interface between the HAp film and the metal implant are reported [6, 7]. Therefore, to consider practical use of implant, evaluation of strength of the

N. Hisamori (✉)

Department of Engineering and Applied Sciences, Faculty of Science and Technology, Sophia University, 7-1 Kioi-cho, Chiyoda-ku, Tokyo 102-8554, Japan
e-mail: hisamori@sophia.ac.jp

Fig. 7.1 Schematic of
specimen setup to measure
the bond strength and the
ideal position of fracture
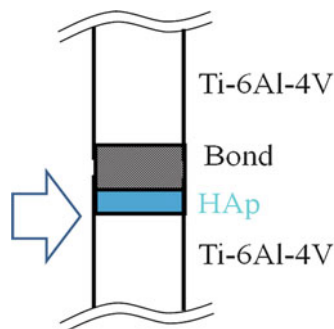
interface between the metal and the HAp film is extremely important. However, the
evaluation methods of the bond strength of thin film have not yet been established.

The strength evaluation of the interface between the metal and the HAp film is
reportedly difficult [8], because fracture does not necessarily occur at the interface
between the metal and the HAp film. There is a method of assessing the strength of
the interface between a substrate and a thin film of functional implant device by
tensile test using adhesive [9, 10]. However, in this test, it is difficult to induce
fracture at the interface between the metal and the HAp film, and the obtained
interface strength is unstable. In addition, the scattering is large. In this chapter, we
suggest a new testing method which is able to measure bond strength between
Ti-6Al-4V alloy and HAp thin film reliably. We focus on a process of preparing
specimen and evaluation of adhesive strength between Ti-alloy and HAp thin film
(Fig. 7.1).

7.2 Materials and Specimens

Ti-6Al-4V is used as the substrate metal. Solid bar specimens of four types in
different diameters (φ4.0, φ7.0, φ10.0, and φ15.0) are used. HAp layer is coated by
plasma spraying on end the bar specimen's surface after blast treatment (Fig. 7.2)
[11, 12]. Figure 7.3 shows a SEM micrograph of the surface after plasma spraying.
The thickness of the HAp film is about 50 μm (HAp thin film). The spraying is
repeated 20 times under the following conditions: supply voltage 68 V, spraying
distance 140 mm, and HAp particles 15 g/min. To measure the interface strength
between the HAp thin film and blast surface, a tensile test piece is made using an
adhesive. A Ti-6Al-4V piece is bonded on the top of the HAp-coated specimen with
two types of bond (EP-138 and Super Bond) by using a jig shown in Fig. 7.4. Holes
of jig are made with severe tolerance to ensure the alignment of specimen. A spring
is attached to the top of the jig for applying constant contact force. Also, the
surfactant is used to peel off the excessive adhesive agent leaked to the side of

Fig. 7.2 Photograph of surface before bonding (*left*: HAp-coated surface, *right*: blast surface)

Fig. 7.3 SEM photograph of plasma-sprayed HAp surface

5μm
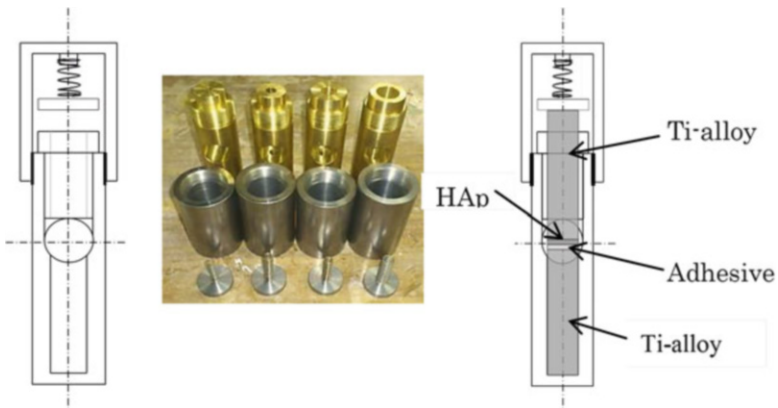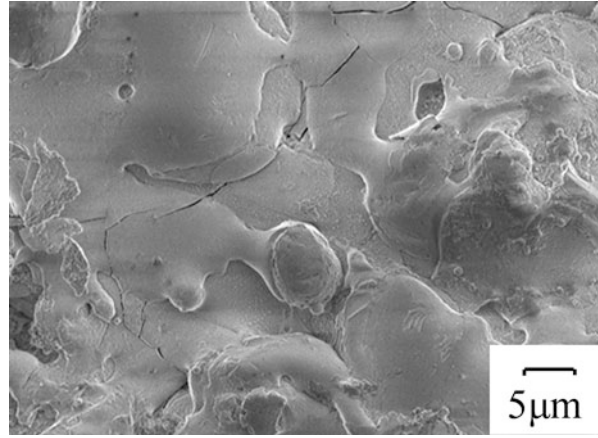
Fig. 7.4 *Schematics and appearance* of bonding device

the specimen easily after testing. This procedure is important because overflowing adhesive will cover interface between Ti-alloy and HAp film and, therefore, prevent interfacial fracture. A constant stress of 0.138 MPa was applied to the specimen. After applying the adhesive EP-138, the specimen is heat treated at 120 °C for
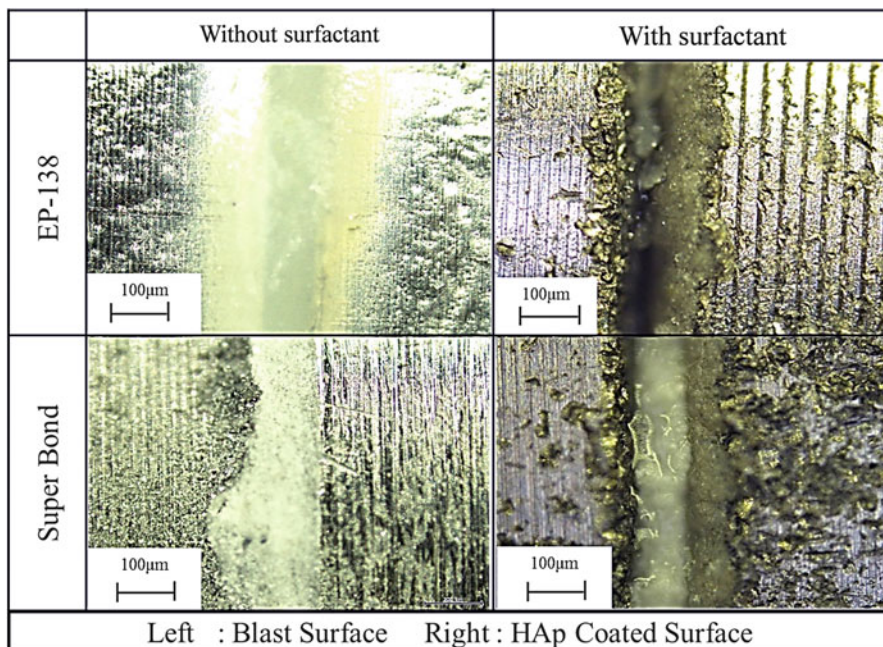
Fig. 7.5 Appearance of the interface of bonded specimen

30 min. Super Bond is hardened within 10 min at room temperature. Figure 7.5 shows the appearance of the interface after bonding. Adhesive layers can be observed at the center of the photograph. The specimens without surfactant show overflow of adhesives from the interface, while those with surfactant do not. Therefore, surfactant protects the interface that is subjected to the examination. However, in removing the surfactant after adhesion, care should be taken.

7.3 Experimental Procedure of Measuring Bond Strength Between Ti-Alloy and HAp

Figure 7.6 shows bonded specimen used to measure bond strength. Tensile load is applied to this specimen under constant crosshead speed (2.5 mm/min). Care is taken to attach the specimen to testing machine to avoid bending or torsional load. If necessary, strain gauges are attached to the specimen to measure stresses within specimen. After tensile test, fracture surfaces are observed by scanning electron microscope (SEM) to confirm whether interfacial fracture occurs or not.
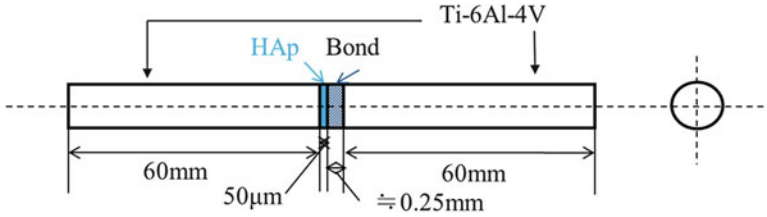
Fig. 7.6 Shape of tensile test specimen

7.4   Bond Strength Between Ti-Alloy and HAp

Figure 7.7 shows bond strength obtained by tensile test. Magnitude of bond strength is almost the same regardless of the diameter of the specimen. Bond strength varies depending on diameter of specimen. However, bond strength shows rather large scatter. The bond strength obtained with EP-138 is slightly higher than that of Super Bond. Scattering is larger on the diameter of φ7.0 and φ4.0. To investigate the cause of scatter, crystal structure of HAp thin film is identified by X-ray diffraction. X-ray diffraction patterns of specimens of different diameters are shown in Fig. 7.8. Crystal structure of HAp thin film is the same regardless of the specimen diameter. Therefore, HAp does not cause scattering of bond strength. Crystallinity of the HAp film will affect the bond strength. If the HAp coating has low crystallinity, interface strength value becomes low. Therefore, construction and spraying technique of HAp on substrate are important factors.

The factors affecting scatter of bond strength in terms of the method of tensile test were considered. Bond strength obtained with specimens of diameters φ4.0 and φ7.0 shows larger scatter than other diameters. Axial deviation is considered to be a reason. The axis of specimen of both sides of HAp and bond layer shift each other about 10–50 μm. This shift produces un-axial load to the interface, and interfacial fracture occurs at lower load than anticipated. This may harm the accuracy of the test. Small diameter specimens are more susceptible for this inaccuracy. Therefore, the tolerance between the jig and the specimen is an important factor in the adhesion process of the test piece.

On the other hand, adhesives protruding out on the side of the specimen near the interface tend to raise adhesion strength. Adhesives overflowing from bonded surface are considered to be a reason for dispersion. The use of surfactants prevents the adhesive protruding out near the interface between Ti-alloy and HAp film, but it is not always effective. Adhesive that remained on interface possibly suppresses interfacial fracture and affects the value of bond strength. If the same quantity of adhesive remains on the interface, the ratio between protruding adhesive and the total cross-sectional area within the interface becomes larger when the diameter of specimen is smaller. Specimens of diameters φ4.0 and φ7.0 are more susceptible to this phenomenon and may show higher adhesion strength. Thus, the adhesive suppresses interfacial failure.

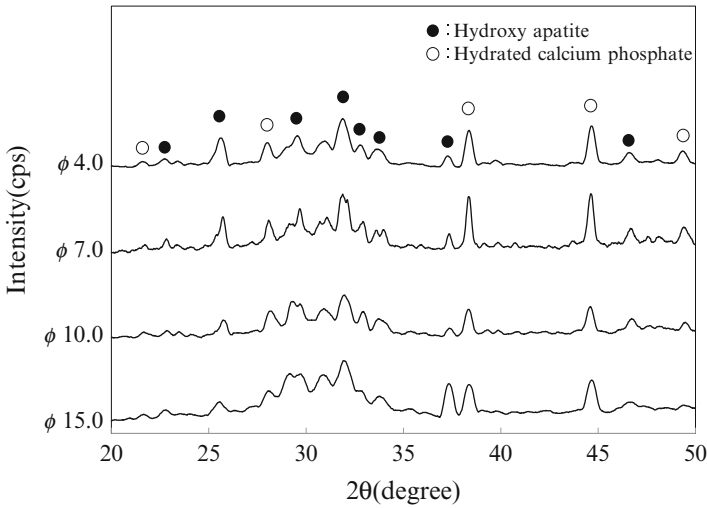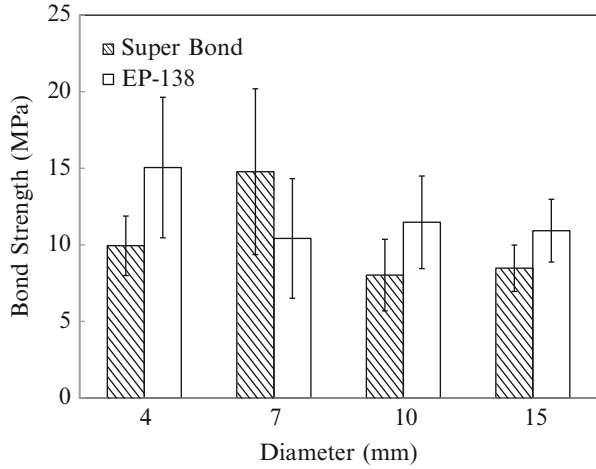**Fig. 7.7** Bond strength
between Ti-alloy and HAp

Fig. 7.8 Result of X-ray diffraction analysis of HAp film on specimens of different diameters

It is difficult to remove all overflowing adhesives and obtain flawless alignment of bonded test pieces. Therefore, larger diameter of specimen will be suitable to minimize these effects and obtain more accurate bond strength. Thus, to determine the bond strength with smaller scatter, it is necessary to choose the specimen diameter carefully and manufacture precise tensile test jig. Because it is difficult to exclude all of these factors causing errors, a certain degree of scatters has to be accepted. Peeling off (fracture) at the interface between the HAp thin film and titanium alloy is important. It is a key to consider the test methods to accurately measure the bond strength.
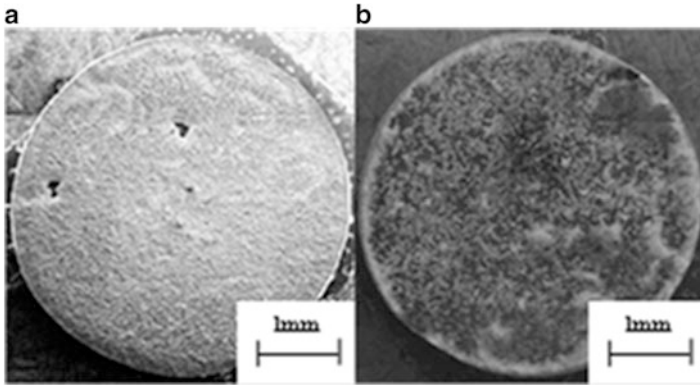
Fig. 7.9 SEM photographs of peeled surface (fracture surface): (**a**) Ti-6Al-4V blast surface and (**b**) HAp-coated surface

7.5 Observation of Peeled Surface (Fracture Surface)

When fracture occurred at the interface between Ti-alloy and HAp film, HAp will be peeled off from HAp-coated surface, and Ti-alloy will appear on the surface. After tensile test, almost all of HAp is peeled off as shown in Fig. 7.9. In the previous section, the test method that can measure bond strength of Ti-alloy and HAp film correctly is verified. The result indicates that the effects of the adhesive and axial misalignment on bond strength are minimized on the method. As shown in Fig. 7.9, peeling occurs at the interface between the HAp thin film and Ti-6Al-4 V. Also, the use of the surfactant enables peeling to occur at the interface. The two photographs at the left in Fig. 7.10 show the peeled surface where surfactant was not used. It can be seen that the area peeled at the interface is smaller compared with the two photographs at the right that were obtained with specimen with surfactant. This is due to the fact that the adhesives protrude to the interface, affecting the value of bond strength, and cause scatter of the measured value.

7.6 Surface Treatment for Improving the Bone Compatibility

Maximum temperature of the plasma can reach 10,000 °C or higher. Therefore, the crystal structure of HAp changes due to thermal decomposition and bond strength to substrate decrease. This is caused by the formation of the amorphous calcium phosphate of low crystallinity. Low-pressure plasma spraying can prevent this phenomenon.

Spraying of HAp was performed in a vacuum chamber. Figure 7.11a shows the cross section of the layer formed by plasma-sprayed HAp on the titanium substrate.
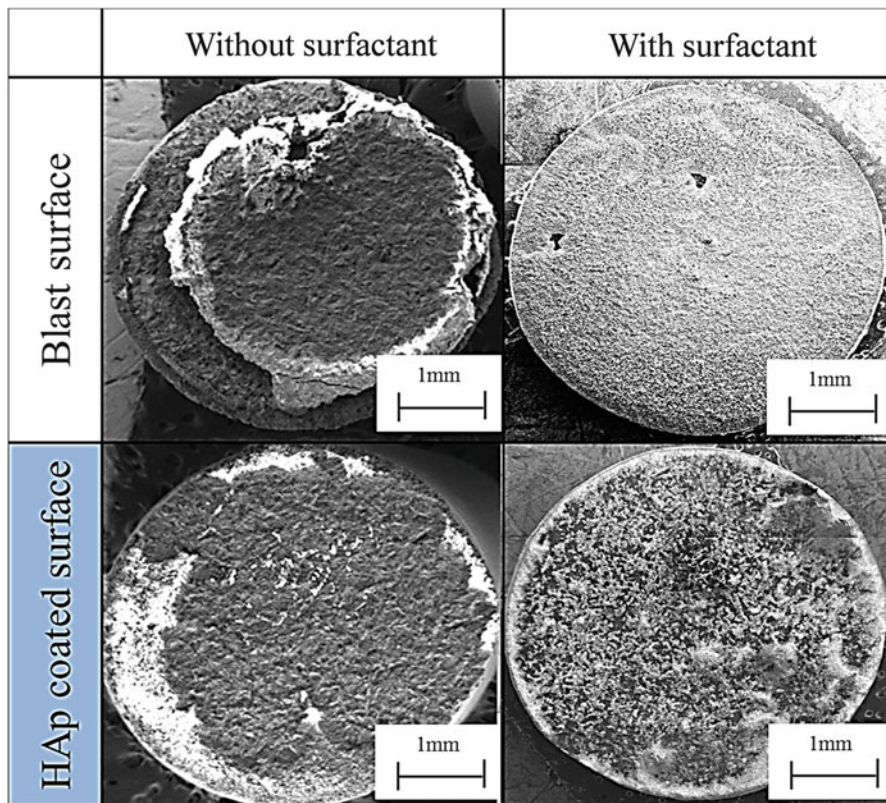
Fig. 7.10 SEM photographs of peeled surface (fracture surface)

Figure 7.11b shows the cross section of two-layer coating formed with plasma-sprayed HAp after plasma spraying of titanium for enhanced adhesion of HAp layer [13]. Because the thickness of the HAp film varies from 10 to 200 μm, both adhesion and bond strength may change; testing bond strength in a unified manner has been required [14]. Other method of film formation is the high-velocity oxygen fuel (HVOF) spraying. By using oxygen gas combustion, the flight speed of the thermal spraying powder is faster than that of plasma spraying. The density of formed layer and the adhesion to the substrate are improved. There is also the cold spray method. It is a method of high-speed collision without melting the HAp particles and, therefore, holds the crystallinity of HAp. Research has been conducted such as sputtering [15] or the powder jet deposition method [16] of forming a film at room temperature by injecting particles. By using these methods, HAp-coated titanium showed good fixation to the bone. It is proven to be effective in the initial period of implant, but the peeling has been a problem in the long term. Research and development on surface modification and application techniques of bioactive performance of the metal-based materials will be actively carried out in the future.

Fig. 7.11 Cross-sectional observation which is coated with a thin film HAp plasma spray to the titanium substrate: (**a**) Ti substrate + HAp and (**b**) Ti substrate + Ti + HAp
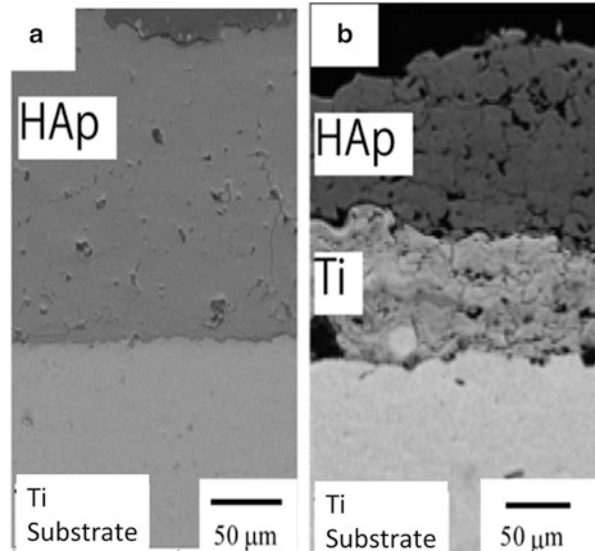
7.7 Summary

1. Bond strength between Ti-alloy and HAp thin film can be measured by the method based on a tensile test, which is proposed by our group.
2. To obtain accurate bond strength, diameter size of specimen should be large. It minimizes the effects of adhesive overflowing and imperfect alignment.

Our method is similar to the ASTM F1147-05 [17]. However, this standard is intended for a film made in various ways. The subject of our method is a thin film that has been produced by plasma spraying. In addition, determination of the bond strength is assured by restricting a fracture within a film. In addition, there is ASTM F 1044–05 [18]. That evaluates the bond strength by shear. We also have to evaluate the bond strength in shear. However, the ASTM standards include some ambiguous factors: substrate surface, surface condition prior to coating, coating method, bonding method, heat treatment, and a fixing method to the tensile testing machine. As a result, a large error occurs in bond strength values obtained. It makes organizing the results difficult. We are planning to clarify these points. And we are considering how this method can be easily used in many fields.

References

1. Gruen T (1979) "Modes of failure" of cemented stem type femoral components: a radiographic analysis of loosening. Clin Orthop Relat Res 141:17–27
2. Takayama A, Naito M, Akiyoshi Y, Kumano T, Shitama H, Shinoda A, Kiyama T, Maeyama A, Teratani T (2007) The short-term follow up study of the cementless THA using the CentPillar Stem. Hip joint 33:249–251

3. Neo M, Kotani S, Fujita Y, Nakamura T, Yamamuro T, Bando Y, Ohtsuki C, Kokubo T (1992) Differences in ceramic–bone interface between surface-active ceramics and resorbable ceramics: a study by scanning and transmission electron microscopy. J Biomed Mater Res 26:255–267
4. Hisamori N (2014) Introduction of biomaterials for beginners −1: present condition of biomaterials and its application. J Soc Mater Sci Jpn 63:417–423
5. Kokubo T, Miyaji F, Kim HM, Nakamura T (1996) Spontaneous formation of bonelike apatite layer on chemically treated titanium metals. J Am Ceram Soc 79:1127–1129
6. Reis RL, Monteiro FJ, Hastings GW (1994) Stability of hydroxylapatite plasma-sprayed coated Ti-6Al-4V under cyclic bending in simulated physiological solutions. J Mater Sci Mater Med 5:457–462
7. Tomita N, Kitakura T, Onmori N, Ikada Y, Aoyama E (1999) Prevention of fatigue cracks in ultrahigh molecular weight polyethylene joint components by the addition of vitamin E. J Biomed Mater Res Part A 48:474–478
8. Toyoda M (1990) On strength of interface of bonded joints of dissimilar materials. J Mech Heterog Mater 59:34–40
9. Fukuda M (1992) Experimental study on the histocompatibility and bonding strength to bone of zirconia dispersed hydroxyapatite ceramics: strength to bone of zirconia dispersed hydroxy-apatite ceramics. Jpn J Oral Maxillofac Surg 38:1718–1737
10. Inoue Y, Ono T, Noutomi A, Izuha A, Toyoda M, Tsukamoto M (1991) Applicability of stress singularity parameter for evaluating adhesive strength of coating film. (Phase 1). Adhesive strength evaluation of plasma sprayed coatings by tensile pin test: applicability of stress singularity parameter for evaluating adhesive strength of coating film (Phase 1). Quar J Jpn Weld Soc 9:167–173
11. Inagaki M, Kameyama T (2007) Biomaterial coatings using plasma processing. J Plasma Fusion Res 83:595–600
12. Heimann RB (2006) Thermal spraying of biomaterials. Surf Coat Technol 201:2012–2019
13. Laonapakul T, Otsuka Y, Nimkerdphol RA, Mutoh Y (2012) Acoustic emission and fatigue damage induced in plasma sprayed hydroxyapatite coating layer. J Mech Behav Biomed Mater 8:123–133
14. Hisamori N (2013) Interface strength evaluation method of medical metal material with thin-film coating. Mechanical Engineering Conference 2013 Japan (MECJ-13). CD-ROM F041004 (2013) Trans Jpn Soc Mech Eng
15. Ueda K, Narushima T, Goto T, Katsube T, Nakagawa H, Kawamura H, Taira M (2007) Evaluation of calcium phosphate coating films on titanium fabricated using RF magnetron sputtering. Mater Trans 48:307–312
16. Sasaki K, Kuriyagawa T (2006) Caries treatment procedure based on nano-precision mechanical manufacturing. J Jpn Soc Biomater 24:244–250
17. ASTM F 1147–05. Standard test method for tension testing of calcium phosphate and metallic coatings 1
18. ASTM F 1044–05. Standard test method for shear testing of calcium phosphate coatings and metallic coatings 1

Chapter 8
Surface Improvement for Biocompatibility of Biomedical Ti Alloy by Dealloying in Metallic Melt

Masahiro Hirohashi, Kyosuke Ueda, Takeshi Wada, Takayuki Narushima, and Hidemi Kato

Abstract Dealloying is known to be a powerful method to produce porous materials mainly with noble metals because the mechanism involves the selective dissolution of specific element(s) through corrosion in acid/alkali aqueous solutions. Recently, an alternative dealloying method has been developed using a metallic melt in place of the corrosive aqueous solution. In this study, using the novel dealloying method using a metallic melt, a toxic element, Ni, was successfully removed from the surface of NiTi, which has been used for biomedical metals, for improving their biocompatibility. Although the toxic ion release per unit surface area decreased, the total amount from the treated sample did not decrease effectively because of the substantial surface area developed using the dealloying method. The dealloying method followed by the oxidation treatment was found to decrease the ion release. By optimizing the dealloying conditions to suppress surface area development, drastic improvement in the biocompatibility of these Ti alloys is expected.

Keywords Dealloying • Nitinol • Surface improvement • Biocompatibility

8.1   Introduction

Metals have often been used for biomedical applications such as operating tools and implants (fixtures, wires and stents, etc.) because of their higher strength and toughness than other types of materials and also because of additional

---

M. Hirohashi
Graduate Student, Graduate School of Engineering, Tohoku University,
Sendai 980-8579, Japan

K. Ueda • T. Narushima
Department of Materials Processing, Tohoku University, Sendai 980-8579, Japan

T. Wada • H. Kato (✉)
Institute for Materials Research, Tohoku University, Sendai 980-8577, Japan
e-mail: hikato@imr.tohoku.ac.jp

characteristics such as superelasticity or shape memory function. Many of these applications are made of the stainless steels and Co and Ti alloys, which reluctantly contain toxic elements such as Ni, Co, V, Al, etc. to sustain the functions. Recently, many efforts have been put to develop new alloys without toxic elements. Surface improvement is an alternative method to address this problem, e.g., producing a surface barrier on NiTi to suppress Ni ion release by gas nitriding (causing TiNi and $Ti_2NiH_{0.5}$ compound layers) [1], chemical vapor deposition (CVD) (causing paracyclophane layers [2]), plasma ion implantation (causing surface layer of carbon [3] and phosphorus oxide [4]), solgel (causing TiO_2 layer [5]), and H_2O_2 (causing titania scale mainly composed of rutile and anatase [6]) methods. Although these methods can work, the resulting barrier is not sufficiently thick and is typically on the order of several hundred nm. To produce a thicker barrier, a laser spraying method has been shown to perform well [7]. However, the equipment is expensive and/or the running costs are high. Recently, our research group developed a novel dealloying method to dissolve a specific element from an alloy into a metallic melt, metallurgically, and succeeded in preparing nano-/microporous metals [8–12]. In this study, we apply this dealloying method to remove toxic elements from the surface of biomedical alloys and then investigate the resulting effect on the biocompatibility.

8.1.1 Conventional Dealloying Method

Nano-/mesoporous metals have been prepared by the dealloying (or leaching) method, which involves the selective elusion of constituent element(s) from an alloy in a corrosive aqueous solution followed by the self-organization of a porous structure by the remaining element(s). In the 1920s, for example, M. Raney succeeded in preparing porous Ni by dipping a Ni–Si alloy precursor in a sodium hydroxide aqueous solution for removal of the Si element [13]. The resulting porous product is known as the Raney Ni catalyst, which has been used for curing oils and fats. Porous metals subsequently prepared by this method have been called "Raney metals" and have been used for various kinds of catalysts. Because the mechanism of this method involves corrosion in an aqueous solution, this method can be typically applied to the preparation of porous structures with noble metals having a higher potential than the standard hydrogen electrode or for iron group elements such as Fe [14], Co [15], and Ni using the electrochemical approach. In 1979, Forty prepared porous gold by dipping a Au–Ag alloy precursor in a nitric acid aqueous solution to remove the Ag element selectively and determined that the self-organization of the porous structure was mainly achieved by surface diffusion of the remaining Au element [16]. Later, this proposed self-organization was validated by Erlebacher et al. by means of kinetic Monte Carlo simulations [17].

Although this dealloying method is simple and easy, targets are limited to the noble or iron group elements. If we attempt to apply this method to the less noble

"base" elements, the remaining elements are easily oxidized, and the process does not result in the formation of a porous structure.

8.1.2   Dealloying in a Metallic Melt

Since Raney's work, researchers have sought alternative methods to produce porous structures using base metals. To overcome this limitation, we have succeeded in using a metallic melt in place of a corrosive aqueous solution [8]. This method can also be applicable to base metals, which serve as the remaining element, because metallic melts do not ideally contain oxygen. The problem is how we design the selective dissolution of an element from an alloy precursor in a metallic melt. To understand this problem, we focus on the mixture or separation of materials. When we mix two elements, the free energy change due to this event is

$$\Delta G_{\mathrm{mix}} = \Delta H_{\mathrm{mix}} - T\Delta S_{\mathrm{mix}}, \tag{8.1}$$

where ΔH_{mix} is the heat of mixing, ΔS_{mix} is the entropy of mixing, and T is the absolute temperature. Usually, the entropy increases after mixing. Therefore, if $\Delta H_{\mathrm{mix}} < 0$, then $\Delta G_{\mathrm{mix}} < 0$, and the mixing reaction can occur spontaneously from a thermodynamic point of view. On the other hand, if $\Delta H_{\mathrm{mix}} > 0$, the sign (positive or negative) of ΔG_{mix} depends on the temperature. If the temperature is adequately controlled to make the enthalpy term larger than the entropy term, then $\Delta G_{\mathrm{mix}} > 0$, and we can avoid the mixture of the two elements. Here we dip an A–B binary alloy precursor into a metallic melt consisting of element C. If the heat of mixing between elements B and C is negative, i.e., $\Delta H_{\mathrm{mix},\,B-C} < 0$, and if the heat of mixing between elements A and C is positive, i.e., $\Delta H_{\mathrm{mix},\,A-C} > 0$, then by controlling temperature adequately only element B dissolves from the precursor into the C melt; since element A is rejected from the C melt, it is expected to self-organize into a porous structure by surface diffusion in the same manner as that of the ordinary dealloying method in an aqueous solution [16]. Figure 8.1 shows a schematic of this
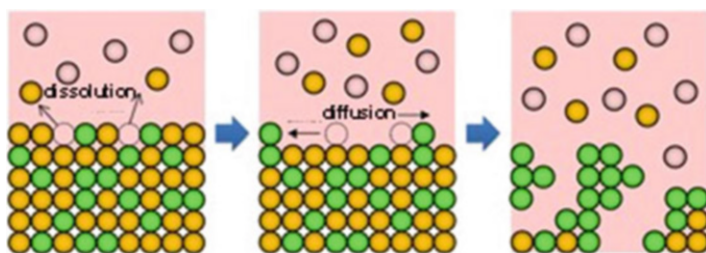
Fig. 8.1 Schematic of the dealloying method using a metallic melt, where atom B (*orange*) dissolves into a melt composed of C atoms (*pink*) and the remaining atom A (*yellowish green*) self-organizes into a porous structure by surface diffusion

Fig. 8.2 Triangle relationship of the enthalpies of mixing among elements A, B, and C for dealloying in a metallic melt
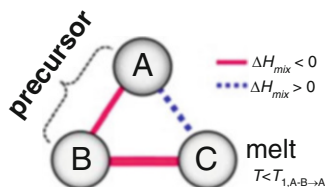
novel dealloying method that involves the selective dissolution of B atoms (orange) in the C atom melt (pink) and surface diffusion of the remaining A atoms (yellowish green). Figure 8.2 summarizes this "triangle" relationship in terms of the heat of mixing among elements A, B, and C required for the dealloying reaction in a metallic melt. Because the heat of mixing is expressed usually with temperature and chemical composition, we have to calculate the rigid value with considering these parameters for the heat of mixing with these parameters for designing the dealloying reaction. However, this is sometimes complicated. The heat of mixing between the transition metals and the transition metals and metalloids can be obtained from the table in Ref. [18], the values of which are approximately calculated by the Miedema model and that of other metals can be obtained from the table constructed by Takeuchi et al. [19]. In our study, we first identify the candidates for elements A, B, and C from these values, and we then confirm the relationships A–B and B–C (mixture) and A–C (separation) by the related binary phase diagrams. The following are demonstrations of the design of the dealloying reaction in a metallic melt for preparing porous hcp-Ti (α-Ti) and bcc-Ti (β-Ti) alloys as examples.

8.2 Porous α-Ti and β-Ti Alloy Prepared by Dealloying with a Metallic Melt

8.2.1 α-Ti [8]

The values of heat of mixing between various elements are tabulated in Table 8.1, which include some RE (rare earth) metal candidates. Here, A = Ti and candidates for the other suitable elements appropriate to the triangle relationship described by Fig. 8.2 are selected from the table to be B = Cu and C = Mg. As shown in Fig. 8.3a, the Ti–Cu binary system includes a solid solution and intermetallic compounds; thus, this binary system can be used for the precursor. It is confirmed from the related phase diagrams [20] shown in Fig. 8.3b, c that Mg alloys with Cu (Fig. 8.3b), which is expected to dissolve from the precursor, while on the other hand, Mg separates from the Ti element over wide composition and temperature ranges (Fig. 8.3c). The nominal composition of the precursor is determined to be $Ti_{30}Cu_{70}$ at%. The ingot is prepared by arc-melting high-purity Ti (99.99 mass%) and Cu (99.99 mass%) metals in an argon atmosphere. Thin ribbons of the Ti–Cu

Table 8.1 Enthalpies of mixing (kJ/mol) among A = Ti, B = Ni, and C = Mg, Ca, and Ce (rare earth), where A, B, and C satisfy the triangle relationship shown in Fig. 8.2

	A	B	C			
	Ti	Cu	Ni	Mg	Ca	Ce
Ti		−9	−35	+16	+43	+18
Cu				−3	−13	−21
Ni				−4	−7	−28
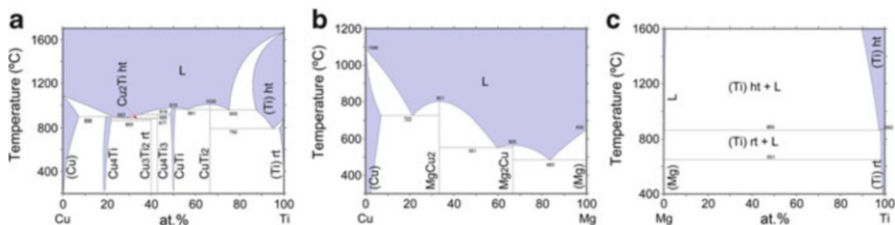
Fig. 8.3 Binary phase diagrams for Ti–Cu (**a**), Cu–Mg (**b**), and Mg–Ti (**c**)
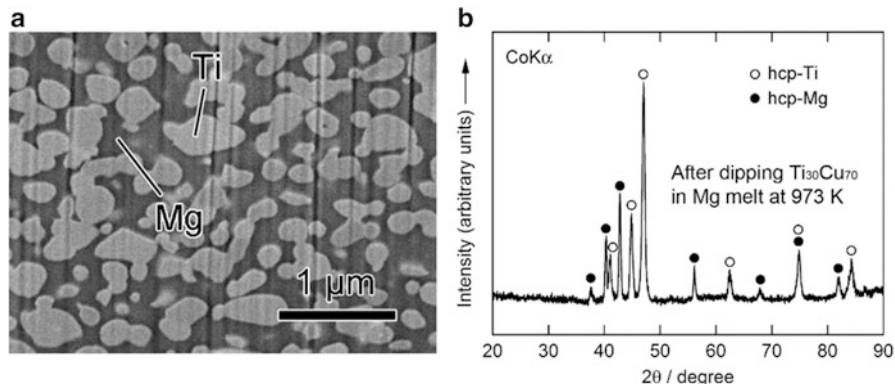
Fig. 8.4 Scanning electron microscope (SEM) image of a polished surface of Ti$_{30}$Cu$_{70}$ (at%) alloy dipped in a Mg melt at 973 K for 5 s (**a**) and a corresponding XRD pattern from the surface (**b**) (Reprinted from Ref. [8], Copyright 2011, with permission from Elsevier)

alloy about 10 mm wide and 30 μm thick were prepared by the melt-spinning method. The x-ray diffraction (XRD) pattern of the ribbon is a broad halo pattern (not shown), which is a characteristic of an amorphous structure; however, it has been confirmed that the dealloying reaction does not depend so much on the precursor structure, and crystalline alloy structures are also acceptable. About 10 g of Mg (99.9 mass%) was inductively heated in a carbon crucible under an argon atmosphere to create a pure liquid. The Mg melt must be maintained at a temperature less than 1,233 K, which is the lowest liquid temperature of the Ti$_{57}$Cu$_{43}$ (at%) alloy (see Fig. 8.3a), to avoid mixing the Ti–Cu alloy system with a titanium concentration from 30 at% to 100 at% together with the melt in a liquid state. Here, we set the melt temperature at 973 K and the dipping time to 5 s. Figure 8.4 shows (a) a scanning electron microscopy (SEM) image of a polished
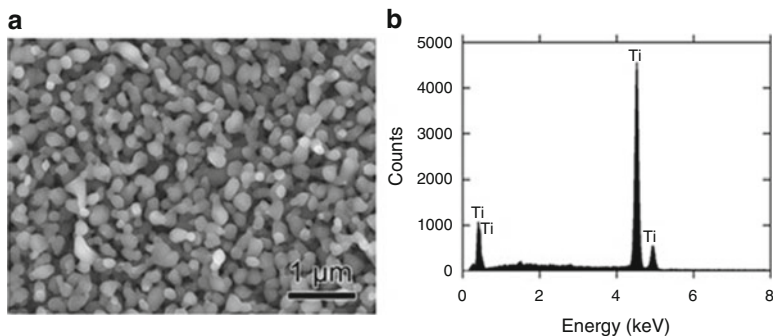
Fig. 8.5 SEM image of the bending fracture surface of porous Ti prepared by dipping the $Ti_{30}Cu_{70}$ (at%) alloy into a Mg melt followed by leaching the Mg phases in a nitric acid aqueous solution (**a**) and the EDX result obtained from the central part of the fracture surface (**b**) (Reprinted from Ref. [8], Copyright 2011, with permission from Elsevier)

Fig. 8.6 Schematic of typical composite structures: bicontinuous (**a**) and isolated (**b**)
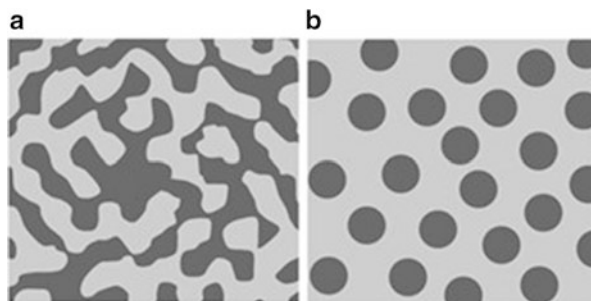
cross section of the ribbon precursor dipped in the Mg melt and (b) the XRD pattern of the bulk precursor dipped in the Mg melt under nearly the same conditions as the ribbon precursor shown in (a). It is recognized that the $Ti_{30}Cu_{70}$ alloy precursor became a nanocomposite consisted of hcp-Ti regions of about 200 nm in size surrounded by hcp-Mg regions after dipping in the Mg melt, which can be confirmed by the XRD pattern shown in Fig. 8.4b. The nanocomposite was dipped in a nitric acid aqueous solution to remove the Mg phase, and then the bending fracture surface was evaluated by SEM-energy dispersive x-ray spectroscopy (SEM-EDX). The results in Fig. 8.5 show that the nanocomposite became a porous structure of pure Ti consisting of hcp-Ti particles of ~200 nm size partially bonded together, and no Mg phase was detected even around the central part of the fracture surface. Evidently, the nitric acid aqueous solution penetrated from the surface of the sample and dissolved all traces of Mg phase inside the material. In other words, the original Ti/Mg nanocomposite was a completely bicontinuous structure, as schematically shown in Fig. 8.6a, in comparison with the isolated structure shown in Fig. 8.6b, and all pores remaining after the removal of Mg are connected

Fig. 8.7 Transmission electron microscope (TEM) image of porous Ti with its corresponding electron diffraction pattern in the inset (Reprinted from Ref. [8], Copyright 2011, with permission from Elsevier)
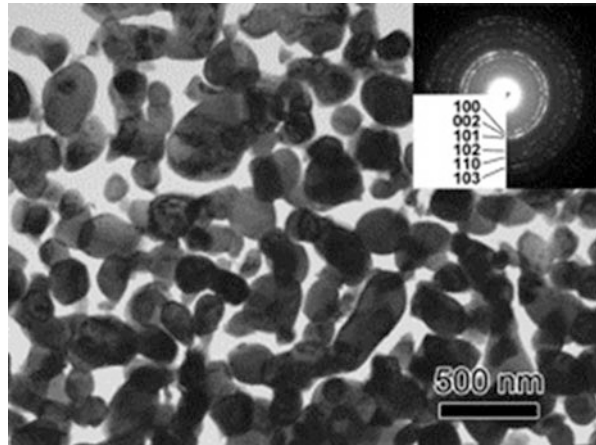
to the outside of the sample. Figure 8.7 shows a transmission electron microscopy (TEM) image and a selected area electron diffraction pattern of the nanoporous Ti. The presence of Ti particles of a diameter of about 200 nm without grain boundaries indicates that the particles are single crystals. Thus, the porous structure was formed by partially connected Ti single crystals. Based on the same reaction design, open-cell-type nanoporous metals were formed from base metals such as Fe, Cr [10], Nb [11], and even a metalloid of Si [21], confirming the universality of this reaction design of dealloying in a metallic melt. Figure 8.8 shows SEM images of the fracture surfaces of these various nanoporous base metals, and the insets demonstrate the triangle relationships used in the preparation of each nanoporous metal.

Here, we summarize the preparation procedures for nanoporous metals and nanocomposites by dealloying in a metallic melt, as they are schematically shown in Fig. 8.9:

1. Selection of A–B–C elements, which satisfy the triangle relationship of the heats of mixing (tables of values of heat of mixing and equilibrium phase diagrams can be used)
2. Preparation of the A–B alloy precursor
3. Selective dissolution of element B from the A–B precursor into the C metal melt (formation of the porous structure)
4. Removal of the C element by etching with an acid or alkaline solution (the remaining A component must be inert in the solution)

For preparing nanocomposites, the 4th step of the process is not required.
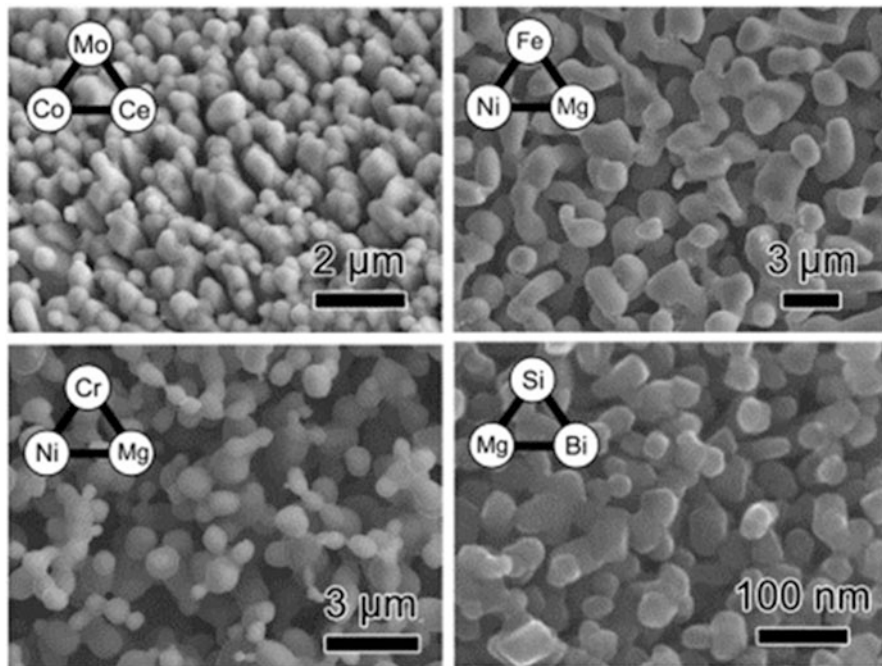
Fig. 8.8 SEM images of the fracture surfaces of porous base metals, Mo, Fe, Cr, and Si together with the corresponding triangle relationship of the enthalpies of mixing used for the preparation
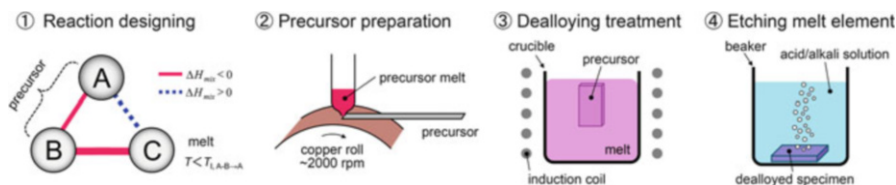

Fig. 8.9 Schematic of the process of porous metal preparation using dealloying within a metallic melt

8.2.2 *β-Ti Alloy [9]*

In the above section, we outlined the newly proposed concept of dealloying where a metallic melt is used as the dealloying medium. By employing three metal elements that satisfy the triangle relationship of the heats of mixing shown in Fig. 8.2 and also referring to the equilibrium phase diagram database, we confirmed that dealloying actually occurs using a metallic melt, and an open-cell-type nanoporous Ti was successfully prepared, which has never been achieved by conventional dealloying in an aqueous solution. In the next step, we apply our dealloying method for preparing open-cell-type nanoporous metal alloys. To realize this application,

Fig. 8.10 Triangle relationship of the enthalpies of mixing among Ti, Zr, Cr, Cu, and Mg
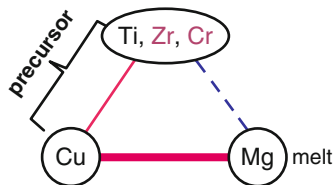
the triangle relationship is extended wherein the role of element A in Fig. 8.2 is expanded to incorporate additional elements A′, A″, ..., which are similar to element A in terms of their values of heat of mixing with B and C. Based on this strategy, we expect the formation of nanoporous A-A′-A″... alloys under the appropriate dealloying conditions. Here, we demonstrate the preparation of a β-type nanoporous Ti alloy by extending the preparation method for nanoporous Ti described previously. Generally, Ti has a hcp crystal structure at room temperature but has a bcc structure as a high temperature phase. By adding bcc stabilizers, a Ti alloy having a bcc structure, namely, the β-type Ti alloy, can be obtained even at room temperature. Among the potential bcc stabilizers, if those elements which are similar to Ti in terms of its heat of mixing with Cu and Mg are employed as the additional elements in the Ti–Cu precursor, these bcc stabilizers will not dissolve into the Mg melt during dealloying treatment and would thus remain, forming the β-Ti alloy phase with a nanoporous structure. Among these bcc stabilizers, we selected Cr and also Zr as a neutral element for the additional elements because similar to Ti, Cr and Zr can mix with Cu but separate from Mg. These elements satisfy the triangle relationship of the values of heat of mixing shown in Fig. 8.10. A pseudo-binary alloy with a composition of $(Ti_{0.847}Zr_{0.055}Cr_{0.098})_{20}Cu_{80}$ (at%) was employed as the precursor. The dissolving component, Cu, is added to the remaining component, $Ti_{84.7}Zr_{5.5}Cr_{9.8}$ (at%) alloy, which is reported to form the β-Ti alloy at room temperature [22]. Using this precursor, the dealloying reaction in the Mg melt was investigated.

Figure 8.11a (top) shows XRD patterns of the 40 μm thick $(Ti_{0.847}Zr_{0.055}Cr_{0.098})_{20}Cu_{80}$ melt-spun ribbon precursor. The phases present in the as-spun ribbon precursor were a mixture of crystalline Cu and Cu_3Ti. Figure 8.11a (bottom) and 8.11b shows XRD patterns and a back-scattering SEM image from a cross section of the $(Ti_{0.847}Zr_{0.056}Cr_{0.098})_{20}Cu_{80}$ alloy dealloyed in the Mg melt at 973 K for 15 min, respectively. The XRD measurement was performed with the bulk sample prepared under the same conditions as the melt-spun ribbon to enhance the accuracy. These analyses reveal that the precursor composed of Cu and Cu_3Ti phases transformed into a nanocomposite of α-Mg and β-Ti composed of regions about 500 nm in size by dealloying the Cu element in the Mg melt. Figure 8.12 shows (a) bending fracture surface, (b) enlarged surface, (c) EDX spectrum, and (d) TEM image with the electron diffraction pattern in the inset for the porous Ti-based alloy prepared by etching α-Mg from the β-Ti/α-Mg composite using a 3 mol/l nitric acid solution for 30 min followed by washing/drying.
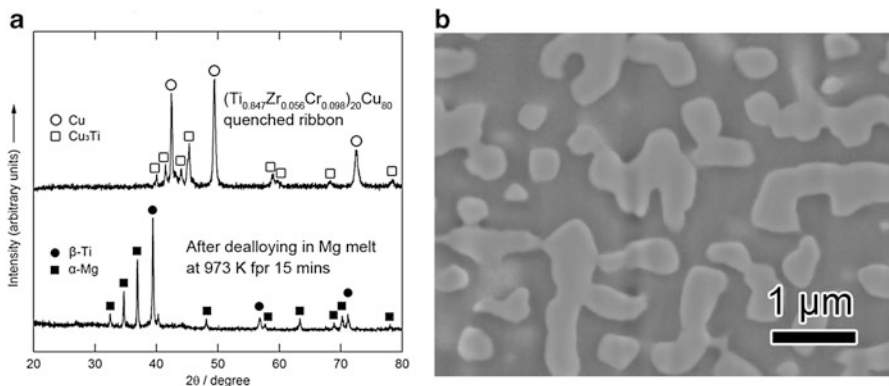
Fig. 8.11 XRD patterns of $(Ti_{0.847}Zr_{0.055}Cr_{0.098})_{20}Cu_{80}$ (at%), as melt spun (*top*) and dealloyed in a Mg melt at 973 K for 15 min (*bottom*) (**a**), and SEM image of the polished surface of the dealloyed sample (**b**) (Reprinted from Ref. [9], Copyright 2011, with permission from Elsevier)
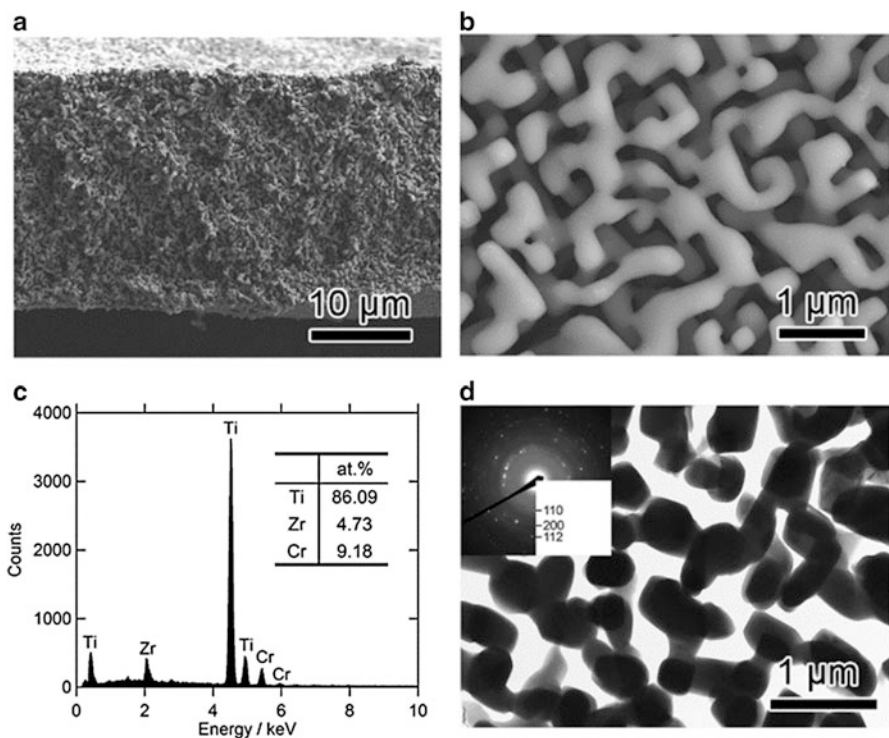

Fig. 8.12 SEM image of the fracture surface of the porous β-Ti alloy (low magnification (**a**) and high magnification (**b**)), EDX spectrum obtained from the surface (**c**), and TEM image of the porous β-Ti alloy together with the electron diffraction pattern in the inset (**d**) (Reprinted from Ref. [9], Copyright 2011, with permission from Elsevier)
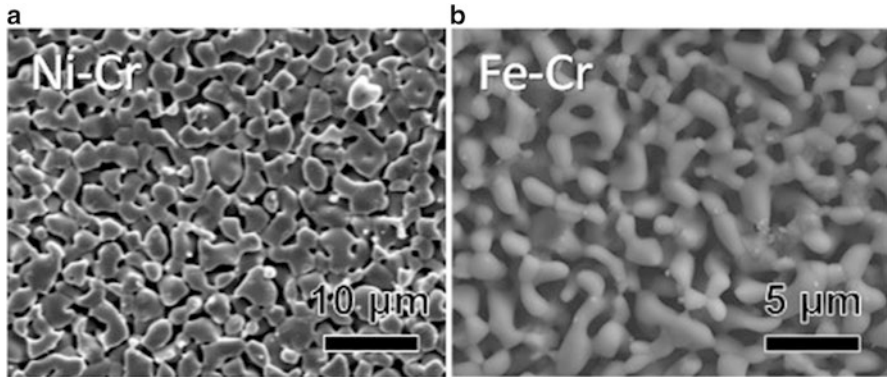
Fig. 8.13 SEM images of the fracture surface of porous Ni–Cr (*left*) and Fe–Cr (*right*) prepared by dealloying within a metallic melt

The SEM image of the cross section (Fig. 8.12a) indicates that the porous structure of a ligament size of about 500 nm is uniformly spread throughout. The corresponding EDX spectrum (Fig. 8.12c) shows that the porous alloy has a composition of $Ti_{86.09}Zr_{4.73}Cr_{9.18}$ (at%), which is nearly the same as that of the initial alloy precursor. No Mg was detected from the fracture surface, indicating that the α-Mg/β-Ti composite alloy had a bicontinuous structure; hence, the resulting nanoporous Ti alloy had an open-cell structure, which is the same as the case of nanoporous α-Ti described previously. These results confirm that the triangle relationship of the heats of mixing shown in Fig. 8.2 can be applied for preparation of nanoporous alloys, as shown in Fig. 8.10. Using this strategy, we have succeeded in preparing open-cell-type nanoporous alloys of base metals such as Ni–Cr alloy [23] and Fe–Cr stainless steel [10], as shown in Fig. 8.13, which have never been prepared by the conventional dealloying method.

8.3 Surface Improvement of Biomedical Ti Alloys by Dealloying with a Metallic Melt

8.3.1 Ni–Ti (Nitinol) [24]

8.3.1.1 Dealloying Treatment in a Metallic Melt

We intend to remove the toxic Ni element from the surface of a Ni–Ti alloy, which has been used for various biomedical applications due to its excellent superelasticity [25]. In order to remove the Ni element from the Ni–Ti alloy by the dealloying reaction, the elements in the triangle relationship given in Fig. 8.2 are designated as A = Ti, B = Ni, and C = Mg, Ca, and RE metals. Here, we selected

Fig. 8.14 Triangle
relationship of enthalpies of
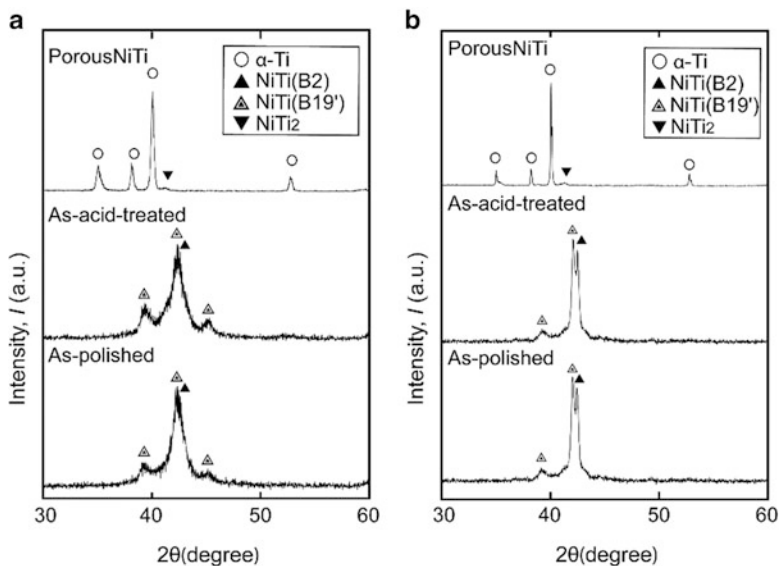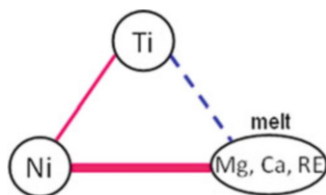mixing among Ti, Ni, and
Ce

Fig. 8.15 XRD patterns of As-polished, As-acid-treated, and porous NiTi using the α-2θ (**a**) and
θ-2θ (**b**) methods (Reprinted from Ref. [24]. Copyright 2010, with permission from Tohoku
University, Japan)

Ce (melting point = 1,071 K) as the C element from the potential candidates, which
yields the triangle illustrated in Fig. 8.14. The Ce melt bath was prepared in a
commercial Ti crucible by the high-frequency induction melting method at 1,073 K
under an argon atmosphere. A polished NiTi disk (~1.2 mm in thickness) was tied
by a molybdenum wire and then immersed in the Ce melt bath for 0.24 ks to remove
the toxic Ni element from the surface. After this dealloying treatment, the disk was
immersed in an acid aqueous solution composed of $H_2O:HNO_3:HCl = 15:8:3$ (vol.)
for 2.8 ks at ambient temperature to remove the Ce phases from the surface. After
the disk was cleaned by ethanol and ultra-purified water using an ultrasonic cleaner
and subsequently dried, the surface modified disks, hereafter referred to as "porous
NiTi," were obtained.

Figure 8.15 shows XRD patterns of the surface of the modified disks using the θ-
2θ and α-2θ methods for the interior and surface investigations, respectively. The
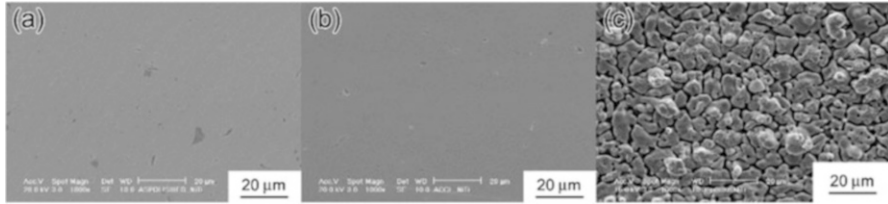"As-polished" disk, prior to both the dealloying and acid treatments, is found to be

Fig. 8.16 SEM images of the surfaces of As-polished (**a**), As-acid-treated (**b**), and porous NiTi (**c**) (Reprinted from Ref. [24]. Copyright 2010, with permission from Tohoku University, Japan)

Fig. 8.17 EDX spectra of the surface of (**a**) As-polished, (**b**) As-acid-treated, and (**c**) porous NiTi (Reprinted from Ref. [24]. Copyright 2010, with permission from Tohoku University, Japan)
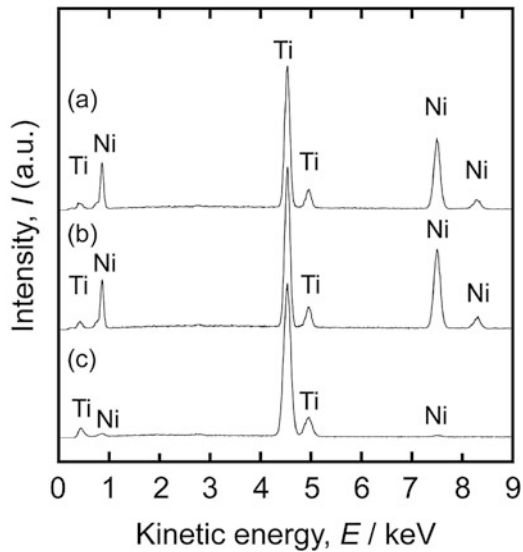
composed of NiTi with both austenite (B2) and martensite (B19′) phases. The XRD pattern of the α-2θ method exhibits the B19′ peaks more prominently than that of the θ-2θ method. This indicates that the B19′ phase exists around the surface more than the interior; thus, this phase is considered to be generated during the polishing treatment by a stress-induced mechanism. The porous NiTi disk was found to be composed of α-Ti and a $NiTi_2$ intermetallic compound. Figure 8.16 shows surface SEM images of the As-polished (a), As-acid-treated (b), and porous NiTi (c) disks. The porous NiTi disk is thereby confirmed to have a porous surface with a porosity of ~1 μm. From the EDX analysis results shown in Fig. 8.17, the concentration of the Ni element detected from the porous NiTi disk surface clearly decreases due to the dealloying treatment in the Ce melt bath. Table 8.2 shows the concentrations of Ni and Ti in each sample derived from the EDX results. The As-polished sample shows nearly Ni:Ti = 1:1, being the same as the nominal alloy composition. On the other hand, the porous NiTi shows Ni:Ti = 1:9 confirming a decrease in the Ni content. Figure 8.18 shows an SEM image of a cross section of the porous NiTi.

Table 8.2 EDX quantitative analyses of the surface of As-polished, As-acid-treated, and porous NiTi

Specimen	Concentration of elements (at%)		
	Ni	Ti	Total
As-polished	50.67	49.33	100
As-acid-treated	51.71	48.29	100
Porous NiTi	13.47	86.53	100

Fig. 8.18 SEM image of a cross section of the porous NiTi. Arrows indicate TiC precipitates (Reprinted from Ref. [24]. Copyright 2010, with permission from Tohoku University, Japan)
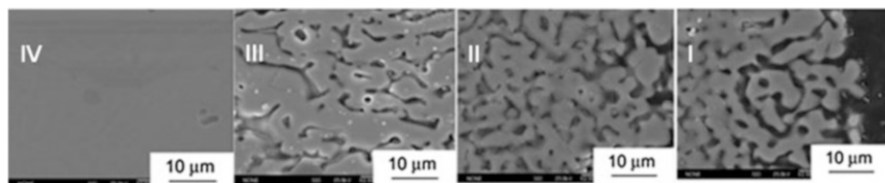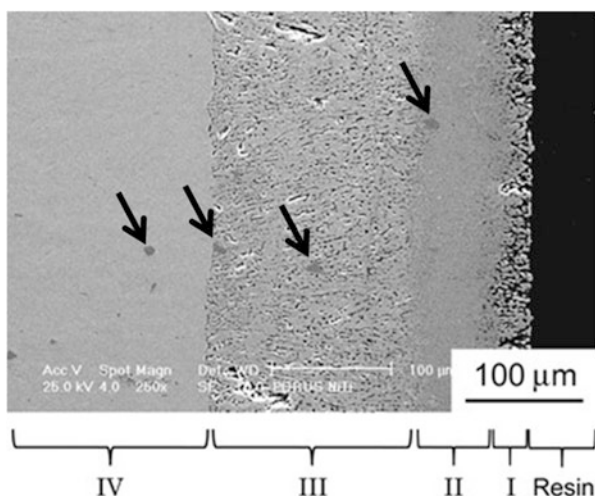

Fig. 8.19 High magnification SEM images of a cross section of the porous NiTi. I~IV correspond to the regions numbered in Fig. 8.18 (Reprinted from Ref. [24]. Copyright 2010, with permission from Tohoku University, Japan)

After the dealloying treatment, a multilayered structure having different porous features is observed at a depth of 200–300 μm. Hereafter, these layers are denoted as Regions I, II, III, and IV, from the outermost surface to the interior, respectively. Enlarged SEM images for each region are shown in Fig. 8.19. Region I exhibits a porous structure and its thickness is about 20 μm. Regions II and III also have a porous structure, but Region II has finer pores than Region III. The thickness of Regions II and III is 60 and 120 μm, respectively. Region IV represents the substrate. TiC precipitates of about 10 μm diameter, appearing as dark-gray regions in Fig. 8.18, originated from the NiTi substrate and can be observed in Regions II

Fig. 8.20 Line analysis of a cross section of the porous NiTi sample. I~IV correspond to the regions numbered in Fig. 8.18 (Reprinted from Ref. [24]. Copyright 2010, with permission from Tohoku University, Japan)
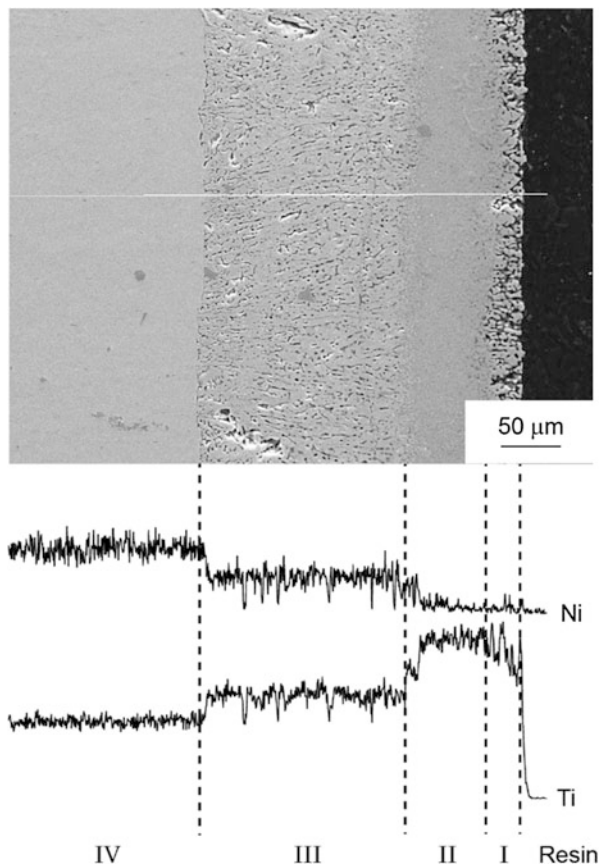
and III, suggesting that the substrate material remained in these regions due to incomplete dealloying treatment. Figure 8.20 shows an EDX composition profile from a line analysis passing from Region IV to Region I in the porous NiTi. The concentration of Ni was found to decrease stepwise while the Ti concentration increased. The Ni concentration in Regions I and II is nearly zero and is about 30 % in Region III. These results indicate that dealloying of Ni occurred from Region I to III to a 200 μm depth. A preliminary experiment using a 40 μm thick NiTi ribbon with a Ce melt revealed that the time required to completely remove Ni from the allow sample using the dealloying method was 0.24 ks; thus, the dealloying rate is estimated to be $\sim8.3 \times 10^{-2}$ μm/s. Therefore, from these preliminary results, we would expect dealloying to form a porous layer about 20 μm thick on the disk sample. However, in fact, after dealloying, the multilayer structure composed of different porous features was formed to a 200 μm depth. Figure 8.21 shows XRD patterns measured from the porous NiTi after mechanically polishing the surface down to several depths. Each position of the XRD pattern on the left-hand side corresponds to the depth from the surface on the right-hand side SEM image. From
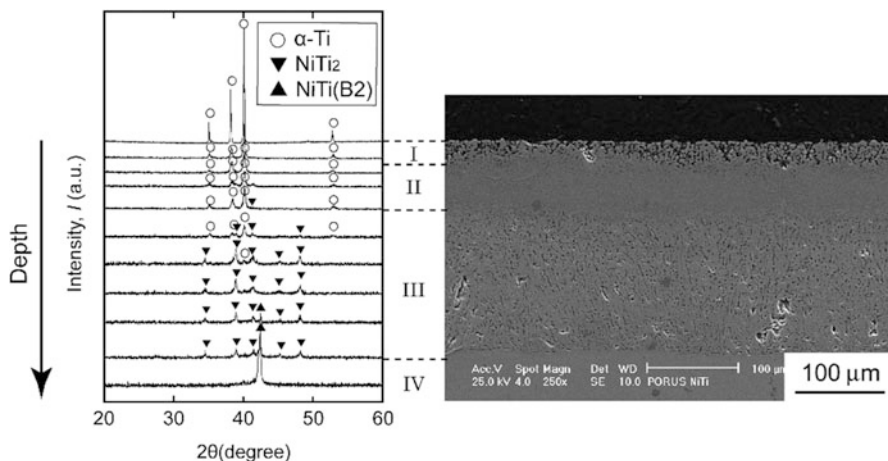
Fig. 8.21 θ-2θ XRD depth profile of the surface of the porous NiTi. I~IV correspond to the regions numbered in Fig. 8.18 (Reprinted from Ref. [24]. Copyright 2010, with permission from Tohoku University, Japan)

Fig. 8.22 Schematic of the temperature schedule for the oxidization treatment process in air (Reprinted from Ref. [24]. Copyright 2010, with permission from Tohoku University, Japan)
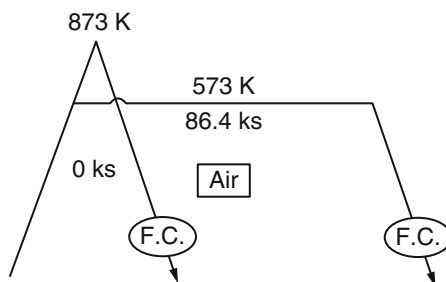
the XRD analysis, Regions I and II were identified as α-Ti phase. Region III was identified as NiTi$_2$ phase. Region IV was identified as an austenite phase, confirming this region as the original NiTi substrate layer.

8.3.1.2 Oxidization Treatment in Air

Surface oxidation of Ti alloy is known for effective way to suppress metal ion release in the simulated body fluid [5, 6]. So in this study, we oxidized surface of the dealloyed porous NiTi alloy for further suppression of Ni ion release and investigated the synergetic effect of dealloying and oxidation on Ni ion release. Oxidization treatment was performed in air using an electric furnace. Figure 8.22 shows the heating program utilized for the oxidization treatment. The As-polished, As-acid-treated, and porous NiTi samples were used. Prior to the oxidization treatment, the samples were washed under ultrasonic vibration in ultra-purified
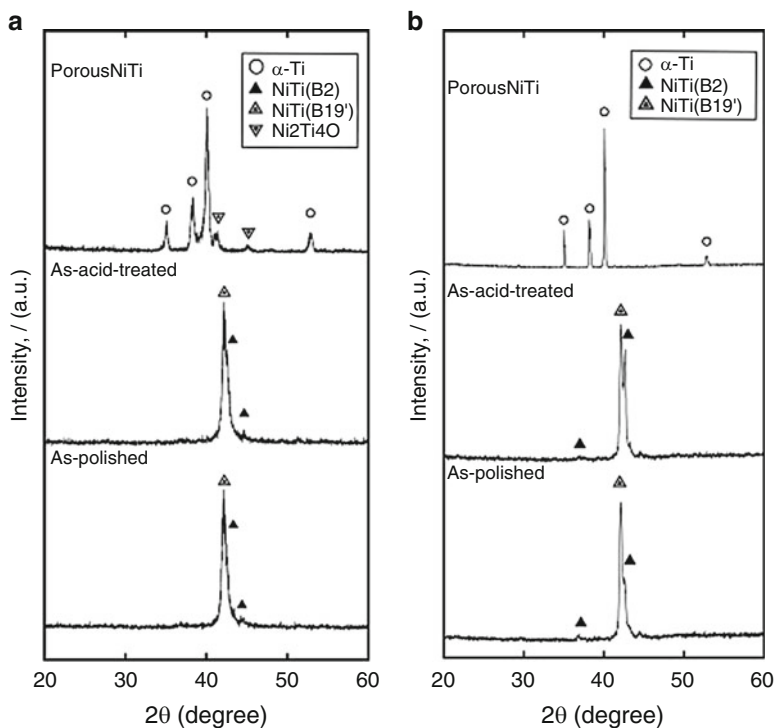
Fig. 8.23 (**a**) α-2θ and (**b**) θ-2θ XRD patterns of As-polished, As-acid-treated, and porous NiTi oxidized in air at 573 K for 86.4 ks (Reprinted from Ref. [24]. Copyright 2010, with permission from Tohoku University, Japan)

water and ethanol for 0.3 ks followed by drying. The holding times were 86.4 ks at 573 K and 0 ks at 873 K (here, "0 ks" means that after reaching 873 K, furnace cooling (FC) began immediately).

8.3.1.3 Phase and Morphology

Figures 8.23 and 8.24 show XRD patterns of the samples oxidized at 573 K for 86.4 ks and 873 K for 0 ks, respectively, under the α-2θ and θ-2θ scanning modes. The titanium oxide phase was not detected from either of the samples oxidized at 573 K for 86.4 ks in air. In the porous NiTi, the Ni_2Ti_4O phase was likely detected. However, because the crystal structure of the Ni_2Ti_4O phase is quite similar to the $NiTi_2$ phase, it was difficult to identify the phase after oxidation treatment by the XRD method. There are some reports of a Ni_2Ti_4O phase forming via the interaction with the oxygen in air [26, 27]. Therefore, we consider that the Ni_2Ti_4O phase formed in the porous NiTi. More detailed investigation is necessary for precise phase identification. Meanwhile, the rutile and Ni_3Ti phases were detected in the
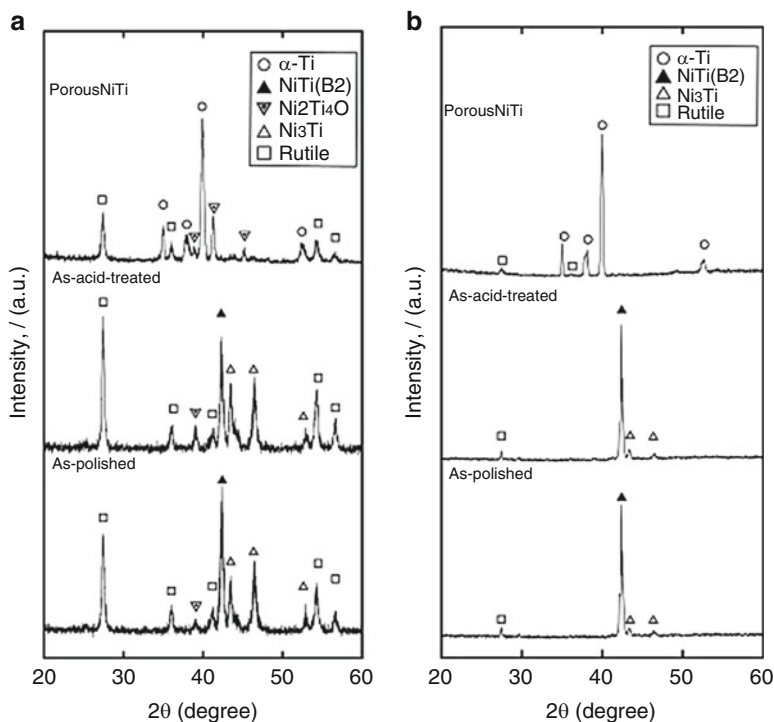
Fig. 8.24 (**a**) α-2θ and (**b**) θ-2θ XRD patterns of As-polished, As-acid-treated, and porous NiTi oxidized in air at 873 K for 0 ks (Reprinted from Ref. [24]. Copyright 2010, with permission from Tohoku University, Japan)

As-polished sample oxidized at 873 K for 0 ks in air. The formation mechanism of the Ni_3Ti phase is considered to be the result of Ti diffusion into the surface oxide layer, wherein the Ti-poor region that formed beneath the oxide layer transformed into a relatively Ni-rich phase, Ni_3Ti. In the porous NiTi, rutile and Ni_2Ti_4O phases were detected. Figures 8.25 and 8.26 show SEM images of the surface features of the samples after oxidation at 573 K for 86.4 ks and 873 K for 0 ks in air, respectively. No obvious change of surface features was observed in the As-polished and As-acid-treated samples before/after oxidation at 573 K for 86.4 ks in air. However, by oxidation at the highest temperature of 873 K for 0 ks in air, oxide particles formed. In the porous NiTi sample, a more strongly interconnected porous structure formed after the oxidation treatment and was more significant for the sample oxidized at 873 K for 0 ks in air. Figure 8.27 shows SEM images of the cross section of the porous NiTi oxidized at the lowest temperature of 573 K for 86.4 ks in air. No obvious change was detected compared to the untreated sample (see Fig. 8.19). Figure 8.28 shows SEM images of the cross section of the porous NiTi oxidized at 873 K for 0 ks in air. After the treatment, the pores in Region II become more significant, and the interface between Regions II and III becomes unclear.
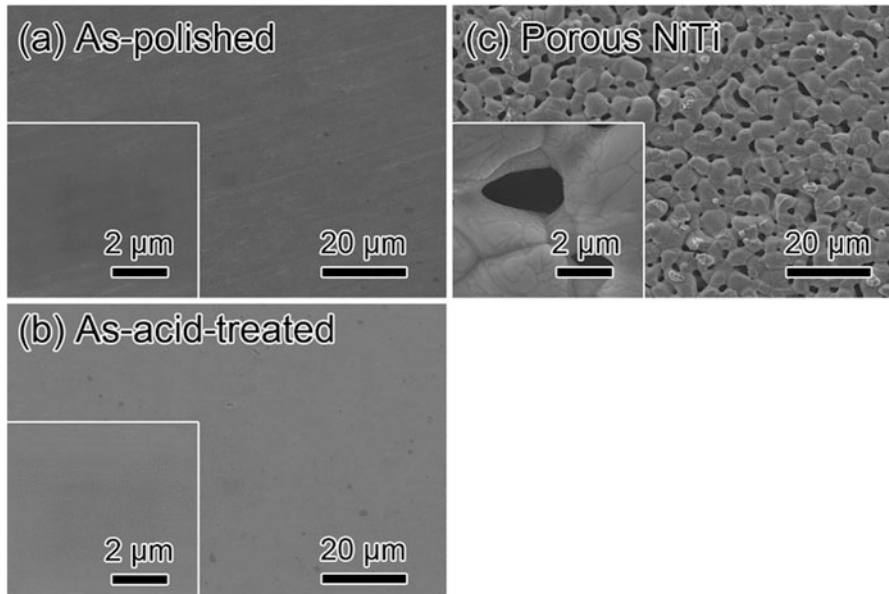
Fig. 8.25 SEM images of the surface of As-polished (**a**), As-acid-treated (**b**), and porous NiTi (**c**) oxidized in air at 573 K for 86.4 ks (Reprinted from ref. [24]. Copyright 2010, with permission from Tohoku University, Japan)

Fig. 8.26 SEM images of the surface of As-polished (**a**), As-acid-treated (**b**), and porous NiTi (**c**) oxidized in air at 873 K for 0 ks (Reprinted from Ref. [24]. Copyright 2010, with permission from Tohoku University, Japan)
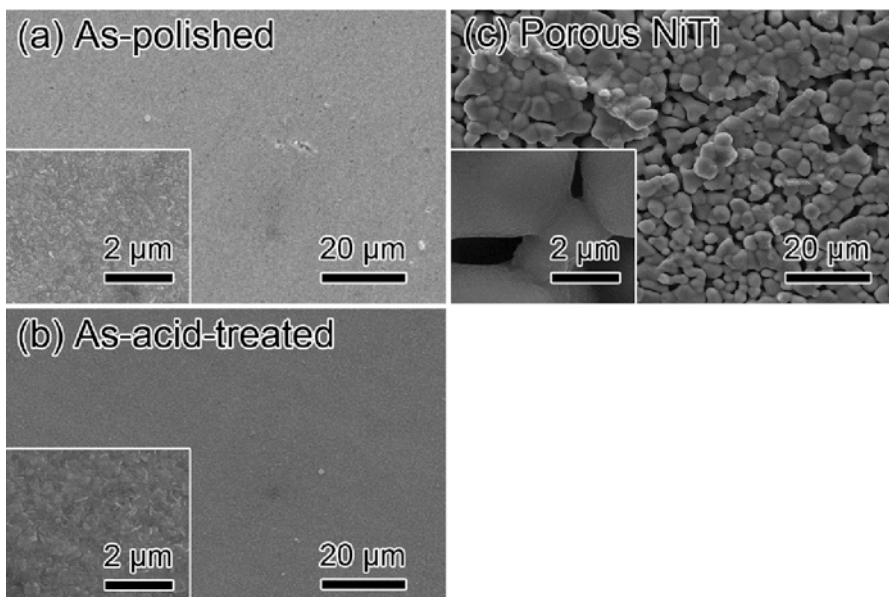
Fig. 8.27 Cross sections of porous NiTi oxidized in air at 573 K for 86.4 ks (Reprinted from ref. [24]. Copyright 2010, with permission from Tohoku University, Japan)

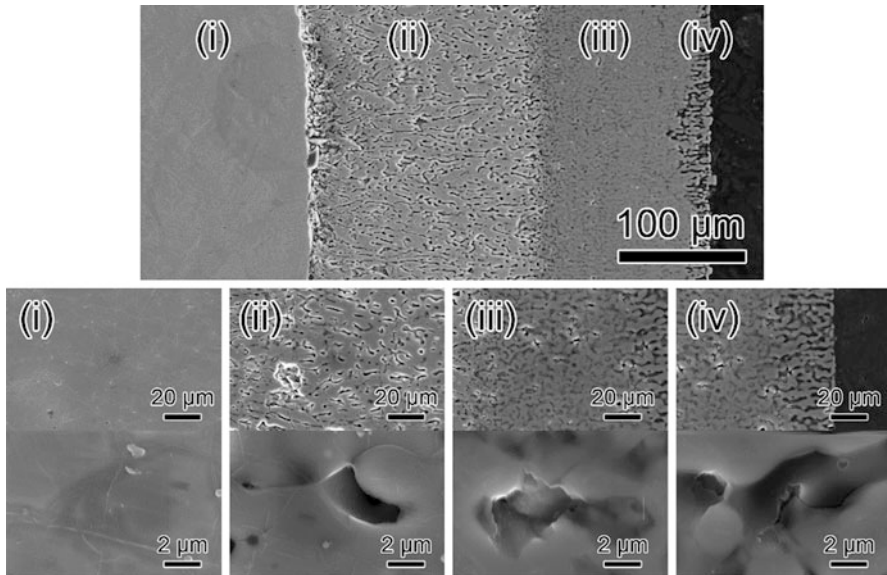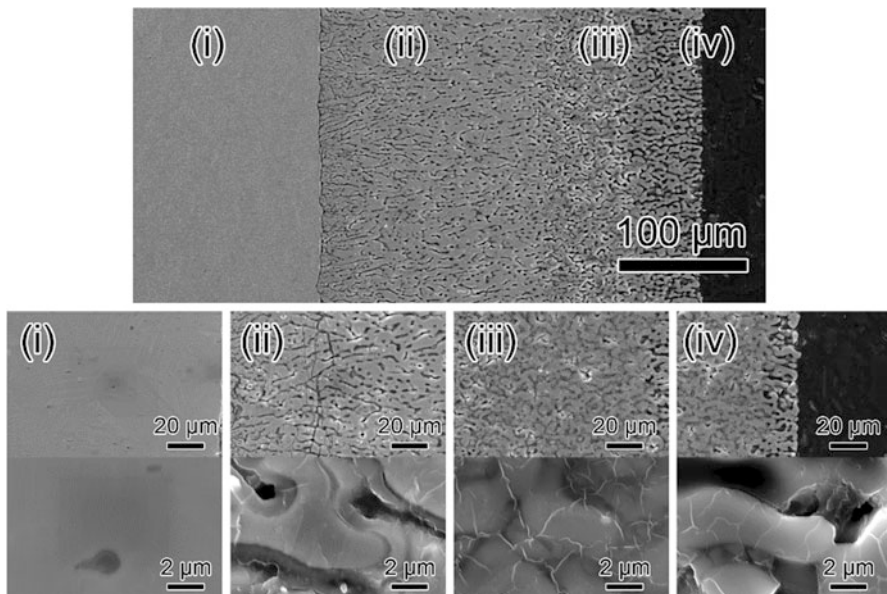**Fig. 8.28** Cross sections of porous NiTi oxidized in air at 873 K for 0 ks (Reprinted from Ref. [24]. Copyright 2010, with permission from Tohoku University, Japan)
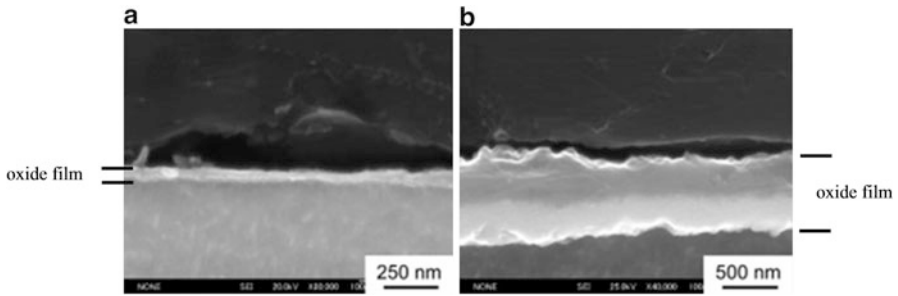
oxide film

oxide film

Fig. 8.29 Cross section of As-polished oxidized in air (**a**) at 573 K for 86.4 ks and (**b**) at 873 K for 0 ks (Reprinted from Ref. [24]. Copyright 2010, with permission from Tohoku University, Japan)

8.3.1.4 Thickness and Composition Profile

Figure 8.29 shows SEM images of the surface region of the cross section of the As-polished sample after oxidation treatment. For oxidization at 573 K for 86.4 ks in air, an oxide film of about 50 nm thickness was formed, which is thinner than the detection limit of the XRD technique. Therefore, no obvious diffraction from the oxide film was detected from the XRD pattern even using the α-2θ scanning mode (Fig. 8.23a). The thickness of the oxide film formed by oxidation at 873 K for 0 ks in air was about 500–700 nm. The As-acid-treated sample exhibits a similar XRD pattern (Fig. 8.24a), indicating that the thickness of the oxide film is very similar to that of the As-polished sample. In the porous NiTi sample, the cross section could not be observed because the mechanical polishing damaged the fragile surface of the porous structure. However, the surface oxide film that formed at the lower oxidation temperature was considered to be thin. Hence, the surface oxide film that developed at 573 K is expected to have good adhesion to the substrate. For microstructural observation of the oxidized porous NiTi sample, the focused ion beam (FIB) technique is useful for fabricating cross sections. Figure 8.30 shows a line analysis of the EDX composition profile of the porous NiTi sample oxidized under various conditions in air from the sample center to the surface. In the sample oxidized at 573 K for 86.4 ks in air, oxygen was detected from Region I to Region III, and its intensity is stronger in Region III, suggesting that oxidation proceeded to this depth. Similarly, in the porous NiTi sample oxidized at 873 K for 0 ks in air, oxygen was detected from Region I to Region III.

8.3.1.5 Evaluation of Ni and Ti Ion Release Behavior in Simulated Body Fluid

Figure 8.31 shows the immersion time dependence of Ni and Ti ion release from the porous NiTi sample in a 1 mass% lactic acid solution after 86.4 ks (1 day), 259.2 ks (3 days), and 604.8 ks (7 days). The Ni and Ti ion release increase with increasing immersion time. Figure 8.32 shows the immersion time dependence of Ni and Ti
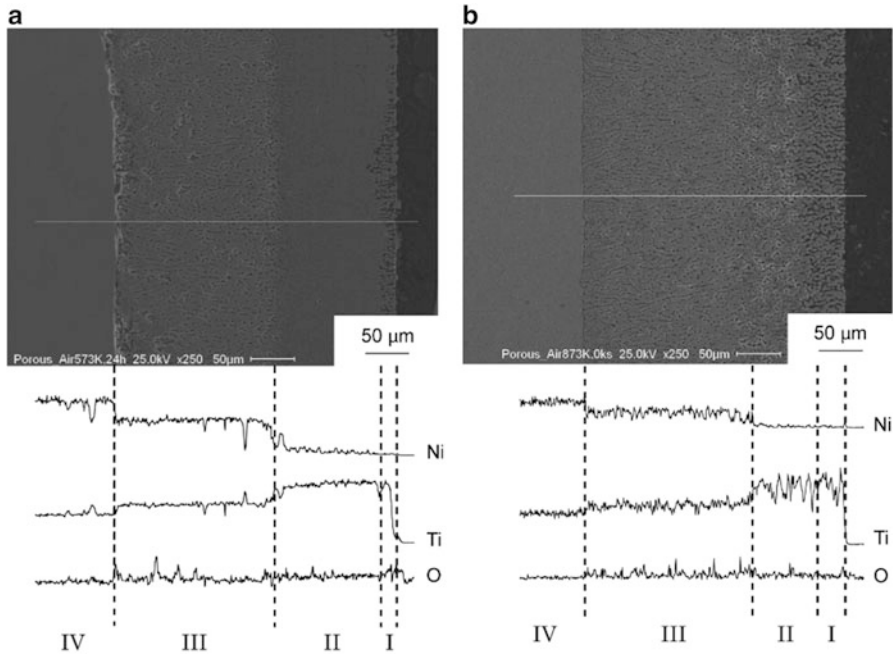
Fig. 8.30 Line analyses of cross sections of porous NiTi oxidized in air at 573 K for 86.4 ks (**a**) and at 873 K for 0 ks (**b**) (Reprinted from Ref. [24]. Copyright 2010, with permission from Tohoku University, Japan)

Fig. 8.31 Concentration of released Ni and Ti ions from porous NiTi into a 1 mass% lactic acid solution after 86.4 ks (1 day), 259.2 ks (3 days), and 604.8 ks (7 days) (Reprinted from ref. [24]. Copyright 2010, with permission from Tohoku University, Japan)
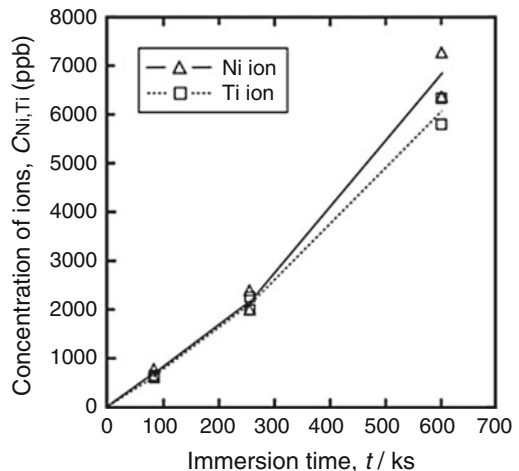
ion release from the As-polished and As-acid-treated samples in a 1 mass% lactic acid solution after 1, 3, and 7 days. For the As-polished sample, the Ni ion release decreases with increasing immersion time, while that of the Ti ion increases linearly

Fig. 8.32 Concentration of released Ni and Ti ions from As-polished and As-acid-treated NiTi into a 1 mass% lactic acid solution after 86.4 ks (1 day), 259.2 ks (3 days), and 604.8 ks (7 days) (Reprinted from Ref. [24]. Copyright 2010, with permission from Tohoku University, Japan)
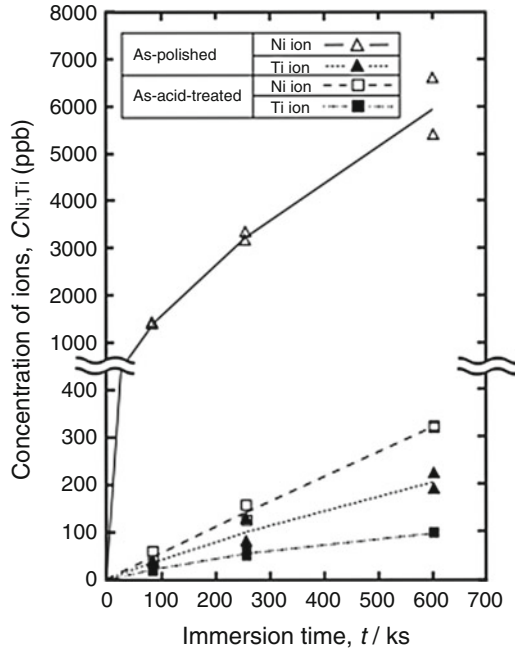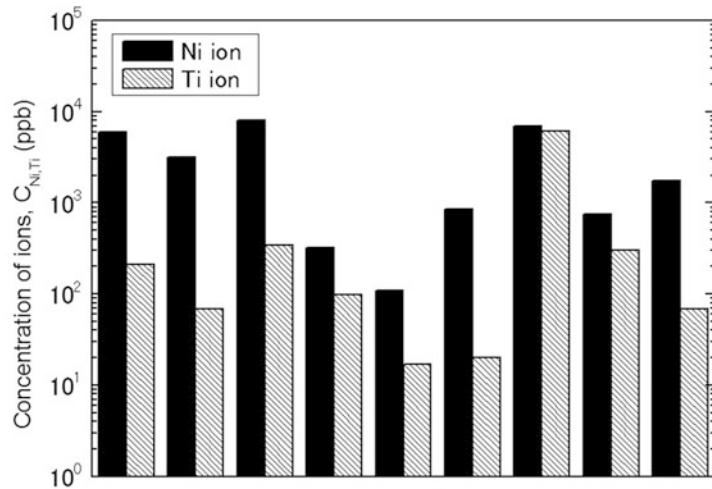

with increasing immersion time. Figure 8.33 shows a comparison of Ni and Ti ion release among all samples in a 1 mass% lactic acid solution after 7 days. The table at the bottom of the figure summarizes the conditions of sample preparation and concentrations of ion release. Concentrations of released Ni and Ti ions are 6,010 ppb and 208 ppb, respectively, from the As-polished and 6,930 ppb and 6,059 ppb, respectively, from the porous NiTi sample. There was no significant difference in the concentration of Ni ion release between these samples. Considering that the porous NiTi sample has a much larger surface area than that of the As-polished sample, it can be concluded that the dealloying treatment in the Ce melt performs well for reducing the extent of Ni ion release. The As-polished sample oxidized at 573 K for 86.4 ks in air showed Ni and Ti ion release concentrations of 3,167 ppb and 69 ppb, respectively, being lower than those of the As-polished sample. On the other hand, the As-polished sample oxidized at 873 K for 0 ks in air shows Ni and Ti ion release concentrations of 8,034 ppb and 343 ppb, respectively, being larger than those of the As-polished sample. The porous NiTi samples oxidized under both conditions resulted in a diminished Ni ion release, and especially, the oxidization treatment at 537 K for 86.4 ks in air was found to be the most effective for reducing Ni ion release, which is the same tendency demonstrated by the As-polished samples. A depth profile by XRD of the porous NiTi suggests that the 1 mass% lactic acid solution penetrated into Region III containing the $NiTi_2$ phase and contacted with Region IV (the substrate). These regions, which are more enriched by Ni, thus released more Ni ions. As a result, the porous NiTi sample released a higher concentration of Ni ions than the As-polished sample. The

Fig. 8.33 Concentration of released Ni and Ti ions from each specimen treated under various conditions into a 1 mass% lactic acid solution after 604.8 ks (7 days) immersion (Reprinted from Ref. [24]. Copyright 2010, with permission from Tohoku University, Japan)

increased Ti ion release from the porous NiTi sample was caused mainly by the greatly increased surface area. The specific surface area of the porous NiTi can be roughly estimated to be the range of 1~10 m^2/g, based upon another dealloying study for porous Nb [11]. By adopting this result, the surface area of the porous NiTi (~0.3 g) was estimated to be 0.3~3 m^2, which is ~$10^{4 \sim 5}$ times larger than that of the As-polished sample (1.25×10^{-4} m^2). Although the increase of surface area caused by the dealloying treatment is very large, the increase of Ni ion release is not so high, indicating that Ni ion release from a unit surface area efficiently decreased. However, when we compare the Ni ion release from samples with the same dimensions, the total amount of Ni ion release is more important than that from the unit surface area. Further optimization on the dealloying conditions for suppressing an increase in the surface area by the dealloying treatment is required to reduce the absolute value of the Ni ion release.

8.3.1.6   Effect of Oxidization on the Ion Release

Oxidation treatment on the As-polished sample at 537 K for 86.4 ks in air resulted in decreased ion release. However, the oxidization treatment at 873 K for 0 ks in air resulted in an increased Ni ion release. Firstov has reported that oxidization treatments at 537–773 K in air formed flat oxide films, while those at 837–1,073 K formed roughened and nanoporous oxide films [28]. Sugawara et al. reported the formation of an amorphous Ti oxide film on the NiTi alloy by oxidization treatment below 773 K in a gas mixture consisting of 80 % N_2 and 20 % O_2 [29]. This suggests that the reduced Ni ion release from the sample oxidized at 573 K for 86.4 ks in air was caused by the formation of a dense amorphous oxide layer by oxidation treatment, which in the present study effectively acted as a barrier against Ni ion release. By the oxidization treatment at 873 K for 0 ks in air, the formation of oxide particles on the titanium oxide surface is observed, as described in the Section of 8.3.1.3, which is in agreement with the phenomena reported by Firstov and Sugawara. Due to roughening of the surface film by oxidation at 873 K for 0 ks in air, a pathway for Ni ion release was formed in the titanium oxide film, resulting in a reduced barrier effect against Ni ion release. In addition, as shown in Fig. 8.23, formation of Ni_3Ti phase on the surface was observed, which also contributed to a greater Ni ion release from the sample.

8.4   Summary

Using the dealloying method in a metallic melt, selective removal of toxic Ni element from the surface of NiTi alloy, which has been used as a biomedical metal, was attempted in order to improve their biocompatibility.

1. By immersing NiTi into a Ce melt, the Ni concentration on the surface of the NiTi alloy was drastically reduced while developing a porous Ti surface layer.
2. Although a drastic decrease of surface Ni concentration was demonstrated, Ni ion release from the dealloyed NiTi in a lactic acid aqueous solution was found to slightly decrease from that of nontreated NiTi. This is considered to be due to the substantially increased surface area, which is ~$10^{4\sim5}$ times larger than that of the original sample, induced by the dealloying treatment, although Ni ion release per unit of surface area of the dealloyed sample was successfully decreased.
3. By surface oxidation treatment of the dealloyed NiTi at 537 K in air, ion release in the lactic acid aqueous solution was found to be suppressed.

More research is required to optimize the dealloying conditions that can realize a reduction of the surface concentration of a toxic element without increasing the surface area. Additionally, more effective surface treatments can be achieved by applying the dealloying method together with a carefully crafted subsequent surface oxidation treatment.

References

1. Wu SK, Lin HC, Lee CY (1999) Gas nitriding of an equiatomic TiNi shape memory alloy. II. Surf Coat Technol 113:13–16
2. Lahann J, Klee D, Pluester W, Hoecker H (2001) Bioactive immobilization of r-hirudin on CVD-coated metallic implant devices. Biomaterials 22:817–826
3. Poon RWY, Yeung KWK, Liu XY, Chu PK, Chung CY, Lu WW (2005) Carbon plasma immersion ion implantation of nickel-titanium shape memory alloys. Biomaterials 26:2265–2272
4. Zhao XK, Cai W, Zhao LC (2002) Corrosion behavior of phosphorus ion-implanted Ni50.6Ti29.4 shape memory alloy. Surf Coat Technol 155:236–238
5. Liu JX, Yang DZ, Shi F, Cai YJ (2003) Sol-gel deposited TiO_2 film on NiTi surgical alloy for biocompatibility. Thin Solid Films 429:225–230
6. Chu CL, Chung CY, Chu PK (2006) Surface oxidation of NiTi shape memory alloy in a boiling aqueous solution containing hydrogen peroxide. Mater Sci Eng A 417:104–109
7. Man HC, Cui ZD, Yue TM (2001) Corrosion properties of laser surface melted NiTi shape memory alloy. Scr Mater 45:1447–1453
8. Wada T, Yubuta K, Inoue A, Kato H (2011) Dealloying by metallic melt. Mater Lett 65:1076–1078
9. Wada T, Setyawan AD, Yubuta K, Kato H (2011) Nano- to submicro-porous beta-Ti alloy prepared from dealloying in a metallic melt. Scr Mater 65:532–535
10. Wada T, Kato H (2013) Three-dimensional open-cell macroporous iron, chromium and ferritic stainless steel. Scr Mater 68:723–726
11. Kim JW, Wada T, Kim SG, Kato H (2014) Sub-micron porous niobium solid electrolytic capacitor prepared by dealloying in a metallic melt. Mater Lett 116:223–226
12. Tsuda M, Wada T, Kato H (2013) Kinetics of formation and coarsening of nanoporous α-titanium dealloyed with Mg melt. J Appl Phys 114(1–8):113503
13. Raney M (1925) Method of preparing catalytic material. US patent 1,563,587, 1 Dec 1925
14. Khaidar M, Allibert C, Driole GP (1982) Composition, structure and crystallite size of Raney catalysts proceeding from several Ni-Al and Fe-Al intermetallic phases. Mater Res Bull 17:329–337
15. Hotta K, Kuromatsu T (1972) Kinetics of liquid-phase hydrogenation of aliphatic α, β-unsaturated aldehyde over Raney cobalt catalyst modified with Co-, Mn-, Ni-, and $PdCl_2$. Bull Chem Soc Jpn 45:3118–3121
16. Forty AJ (1979) Corrosion micromorphology of noble metal alloys and depletion gilding. Nature 282:597–598
17. Erlebacher J, Seshadri R (2009) Hard materials with tunable porosity. MRS Bull 34:561–568
18. Boer FR, Perrifor DG (1988) Cohesion in metals. Elsevier Science Publishers B.V, Amsterdam
19. Takeuchi A, Inoue A (2005) Classification of bulk metallic glasses by atomic size difference, heat of mixing and period of constituent elements and its application to characterization of the main alloying element. Mater Trans 46:2817–2829
20. ASM Alloy Phase Diagram Database (2014) ASM international, Materials Park. http://www1.asminternational.org/AsmEnterprise/APD. Accessed 25 Feb 2014
21. Wada T, Yubuta K, Ichitsubo T, Segawa H, Yoshida H, Kato H (2014) Three-dimensional nanoporous silicon for lithium ion rechargeable battery negative electrode by dealloying with metallic melt (unpublished research)
22. Cheng CH, Hsu HC, Wu SC, Wang HW, Ho WF (2009) Effects of chromium addition on structure and mechanical properties of Ti-10Zr alloy. J Alloys Compd 484:524–528
23. Suzuki T, Tsuda M, Setyawan AD, Wada T, Kato H (2014) (unpublished research)
24. Hirohashi M (2010) Surface modification of NiTi for biomedical applications. Bachelor thesis, Tohoku University Japan
25. Hornbogen E (1999) Ausforming of NiTi. J Mater Sci 34:599–606

26. Chuprima VG, Shalya IM (2002) Reaction of TiNi with oxygen. Powder Metall Met Ceram 41:85–89
27. Khodorenko VN, Soldatova MI, Gyunter VE (2011) Effect of the composition of a titanium nickelide alloy on its structure and on the formation of the grain boundary ensemble. Russ Phys J 53:827–834
28. Firstov GS, Vitchev RG, Kumar H, Blanpain B, Van Humbeeck J (2002) Surface oxidation of NiTi shape memory alloy. Biomaterials 23:4863–4871
29. Sugawara H, Goto H, Komotori J (2006) Effect of thermal oxidation treatment on surface characteristic and corrosion resistance of NiTi shape memory alloy. J Soc Mater Sci Jpn 55:965–970

Chapter 9
Functionally Graded Metallic Biomaterials

Yoshimi Watanabe, Hisashi Sato, and Eri Miura-Fujiwara

Abstract In functionally graded materials (FGMs), the composition and/or microstructure gradually changes over the volume [3–5], resulting in corresponding changes in the properties of the materials. There are many areas of application for FGMs, and one of them is biomedical application. In this chapter, at first, the merits of the metallic biomaterials with graded composition and/or microstructure are described. Then, microstructures and mechanical properties of Ti/biodegradable-polymer FGMs for bone tissue by spark plasma sintering (SPS) method, continuous graded composition in Ti–ZrO_2 bio-FGMs by mixed-powder pouring method, and Al-based FGMs containing TiO_2 nanoparticles with antibacterial activity by a centrifugal mixed-powder method are introduced. Also, our experimental results of white ceramic coating on Ti–29Nb–13Ta–4.6Zr alloy for dental application and magnetic graded materials by inhomogeneous heat treatment of SUS304 stainless steel are given.

9.1 Functionally Graded Materials (FGMs) for Biomedical Applications

Biomaterials should simultaneously satisfy many requirements and possess properties such as nontoxicity, corrosion resistance, thermal conductivity, strength, fatigue durability, biocompatibility, and sometimes esthetics [1]. A single composition with a uniform structure may not satisfy all such requirements. For example, in the case of a dental implantation, the part positioned inside the jaw bone needs more biocompatibility and affinity for bone formation, while the other part

---

Y. Watanabe (✉) • H. Sato

Nagoya Institute of Technology, Gokiso-cho, Showa-ku, Nagoya 466-8555, Japan
e-mail: yoshimi@nitech.ac.jp

E. Miura-Fujiwara
University of Hyogo, Himeji, Japan

positioned outside jaw bone and exposed to intraoral conditions needs the mechanical properties and good fit of shape to adapt to prosthetic appliances [2]. However, although the surface is sometimes modified with a coating layer, currently used implants have mostly uniform composition and structure inside each material layer. To satisfy such requirements and possess properties within one material simultaneously, the concept of functionally graded materials (FGMs) is very useful, where FGMs are the advanced composite materials characterized by spatial variations in composition and/or microstructure that changes over the volume [3–5]. Figure 9.1 illustrates the compositional and functional differences between coated-type or joined-type composite and FGMs. The coated-type or joined-type composite, shown in Fig. 9.1a, is a type of macroscopically inhomogeneous material with *material A* at one end and *material B* at the other. The most serious problem with the coated-type or joined-type composite is a macroscopic interface. Since the functions of this material change discretely from the *material A* part to the *material B* part at the macroscopic interface, cracking and/or delamination should occur near/at the interface during processing or use of the part. This problem can be overcome by eliminating the macroscopic interface, as shown in Fig. 9.1b, where the composition and/or microstructure varies gradually. Thus, the properties should be changed continuously by the absence of a macroscopic interface in the FGMs.

The suitable properties for dental implant are shown in Fig. 9.2. For the case of uniform implant, the properties such as strength and biocompatibility are constant throughout the implant material. On the other hand, the implant with compositional gradient could control the functions of mechanical properties and biocompatibility, depending on the necessity of each part of implant, without the abrupt change due to the formation of discrete boundary [6]. Thus, the so-called trade-off relation can be overcome by the idea of FGMs.

Fig. 9.1 The compositional and functional differences between coated-type or joined-type composite and FGMs
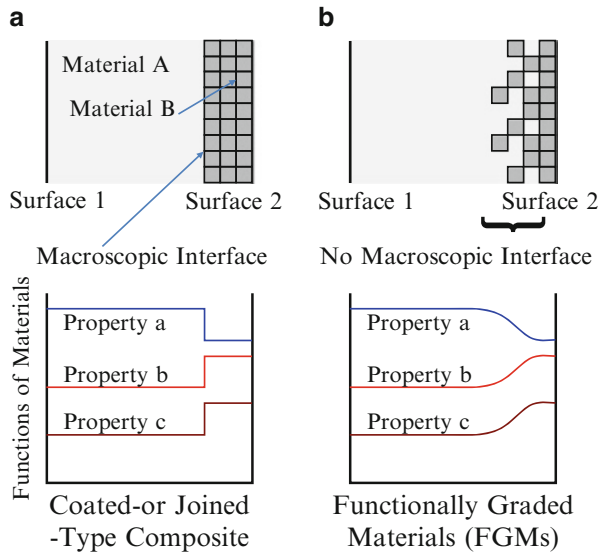
Fig. 9.2 Suitable properties of functionally graded dental implant
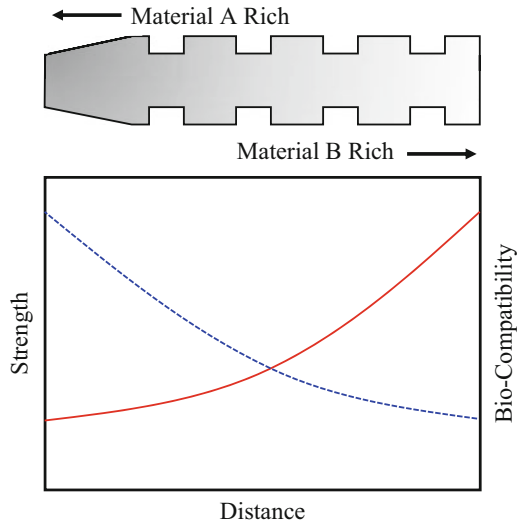
Fig. 9.3 Transversal cross section of bamboo stem
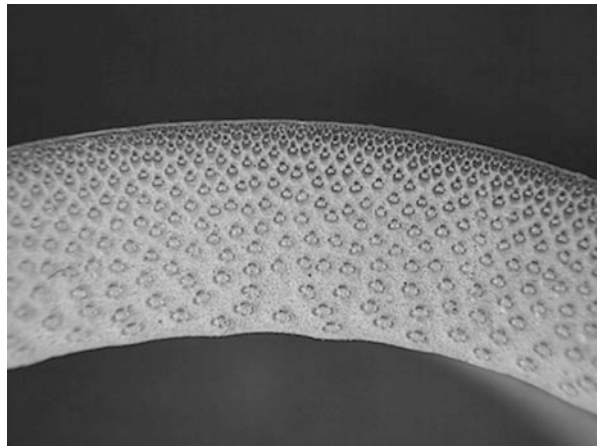
Indeed, we can find many FGMs structures in nature; this is because biological systems such as plant stems and tree stems, animal bones, mollusk shells, and other biological hard tissues tend to be optimized for the loading conditions, to which they are subjected [5]. Human tissues have been also developed and remodeled in such a way to best adapt the function requirements. Consequently, the biological systems are complicated and non-uniform. For example, bamboo and certain other plants have excellent characters based on functionally graded structures [7]. Figure 9.3 shows a cross section of bamboo stem. The matrix of bamboo is filled by soft tissue cells called parenchymatous cells, and that is longitudinally reinforced by strong fibers called the vascular bundle sheath. Graded structure of

the density, size, and shape of the vascular bundle sheath can be found along the radial direction.

A number of FGMs fabrication methods have been proposed and comprehensive reports have been given on the general fabrication methods [3–5]. In general, there are three approaches to fabricate FGMs, as shown in Fig. 9.4. The first one is to eliminate the interface of coated-type or joined-type composite, eliminating discontinuities in the properties at the interface, as shown in Fig. 9.4a. Compositional gradient can be formed by elimination of the sharp interface by diffusion. The second one is to induce non-uniform distributions of dispersoids in a homogeneous particle composite, creating multiple functions within the material, as shown in Fig. 9.4b. One example is centrifugal method. In the centrifugal method, a centrifugal force applied to a homogeneous molten composite assists the formation of the desired gradation. The composition gradient is then achieved primarily due to the difference in the centrifugal force produced by the difference in density between the molten metal and solid particles [8]. The apparatus for the centrifugal method and motion of solid particles under the centrifugal force are shown in Fig. 9.5. The third one is carried out by sequential buildup of layers, as shown in Fig. 9.4c. Powder processing, thermal spray processing, chemical vapor deposition (CVD), and physical vapor deposition (PVD) are the typical examples.

Fabrication of FGMs by the powder processing is schematically illustrated in Fig. 9.6. At first, *material A* and *material B* are weighed and mixed. Then, graded compacts are produced by sequentially layering the powder mixture in the die according to a predesigned spatial distribution of the composition. Finally, the sintering is carried out by hot isostatic pressing (HIP), pressureless sintering after cold isostatic pressing (CIP) compaction, hot press, and spark plasma sintering (SPS).
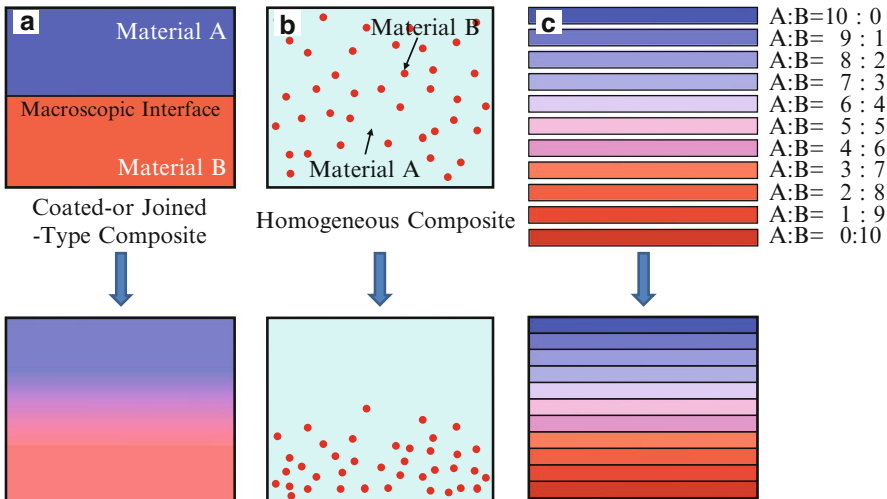

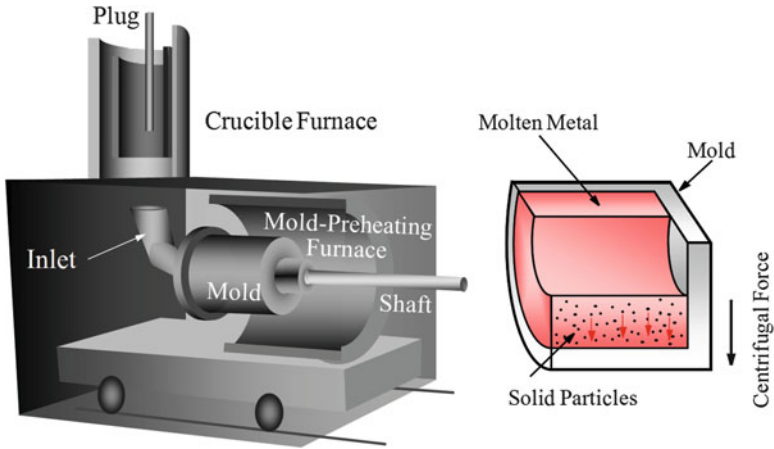**Fig. 9.4** Three approaches to fabricate FGMs

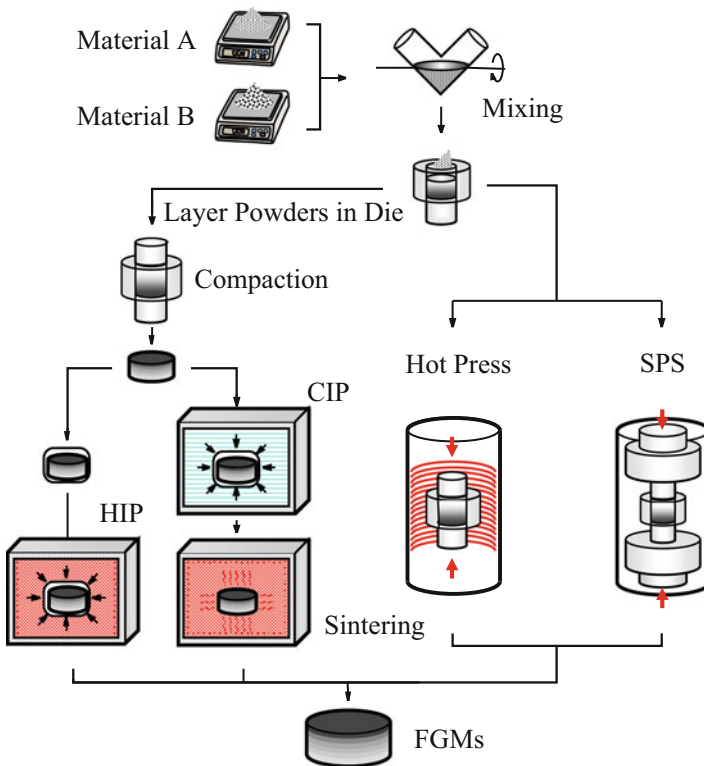**Fig. 9.5** The apparatus for the centrifugal method and motion of solid particles under the centrifugal force

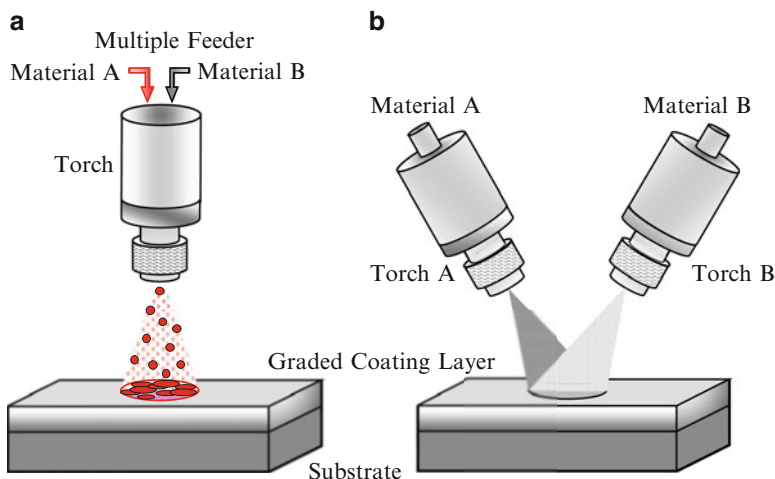**Fig. 9.6** Fabrication process of the FGMs by powder processing

Fig. 9.7 Fabrication of the FGMs by thermal spray processing. (**a**) Multiple feeder method and (**b**) multiple torch method

In thermal spraying, feedstock material (coating precursor) is introduced into a combustion or plasma flame. The molten or semimolten micrometer-sized particles are accelerated toward substrates, and coatings are made by the accumulation of numerous sprayed particles. Since the deposit by the thermal spray processing is formed through the sequential buildup of layers, a number of approaches can be used to produce a graded deposit [9]. Figure 9.7a, b shows multiple feeder method and multiple torch method, respectively. In the case of multiple feeder method, *material A* and *material B* are simultaneously introduced into the plasma jet by changing the mixture ratio. On the other hand, in the case of multiple torch method, *material A* and *material B* are deposited through torch A and torch B, respectively, with optimum spray parameters for each material.

Functionally graded biomaterials are also fabricated by several methods. For example, titanium nitride–apatite functionally graded implants are fabricated by SPS method [10]. It is reported that functionally graded Ti–HAP coatings on Ti–6Al–4V have been fabricated by chemical solution deposition [11]. Ti–TiC–C gradient biomaterial has been prepared by means of plasma source ion implant–ion beam enhanced deposition [12]. Functionally graded (Ca–Ti–O)-(Ca–P–O) bioceramic film is formed by metal organic chemical vapor deposition (MOCVD) method [13]. In this chapter, our recent experimental results, Ti/biodegradable-polymer FGMs for bone tissue fabricated by SPS method, continuous graded composition in Ti–ZrO_2 bio-FGMs fabricated by mixed-powder pouring method, white ceramic coating on Ti–29Nb–13Ta–4.6Zr alloy for dental application, Al-based FGMs containing TiO_2 nanoparticles with antibacterial activity by a centrifugal mixed-powder method, and magnetic graded materials by inhomogeneous heat treatment of SUS304 stainless steel will be introduced.

9.2 Ti/Biodegradable-Polymer FGMs for Bone Tissue Fabricated by SPS Method [14]

Ti and Ti alloys are widely used as metallic implants due to their excellent mechanical properties, corrosion resistance, and nontoxic behavior. However, the Young's modulus of currently used Ti alloys (90–110 GPa) is still not ideal compared with that of human bone (10–20 GPa), which may lead to premature failure of the implant [15, 16]. Therefore, the low Young's modulus Ti alloys are required to decrease the stress-shielding effect in bone implant coupling, enhancing bone regeneration and avoiding resorption process. In order to reduce the apparent elastic modulus of Ti and its alloys, recently, porous Ti and its alloys have been developing. Moreover although they are classified into bioinert materials, a conduction of living bone occurs on the surface of implanted materials that reside in the body for a long period. This can lead to refracture of cured bone in removal operations [17].

Meanwhile, poly-L-lactic acid (PLLA) has attracted much attention, because it is biodegradable, compostable, producible from renewable resources, and nontoxic to the human body and the environment [18]. If Ti-based biocomposites containing PLLA could be fabricated, the PLLA can be gradually decomposed inside the body with progress of time, and then the pore can be generated into the Ti matrix during repairing of the bone. Since the bone can simultaneously penetrate into the pore, the Ti matrix can be tightly bonded with the bone. However, there is a large difference of melting point between Ti and PLLA. Namely, the melting points of Ti and PLLA are 1,670 °C and around 170–180 °C, respectively. Therefore, the process of the Ti-based biocomposite containing PLLA must be done at relative lower temperature; as a result, the strength of the obtained composite becomes lower [19]. Alternatively, the space holder method is applied. Porosity is generated by removing the spacer that was sintered with the base material [20, 21]. Moreover, for the bulk mechanical property, fabricated Ti–PLLA composite must have lower Young's modulus, while wear resistance around the surface must be improved. Such trade-off relation can be overcome by the concept of FGMs.

Prior to fabricating the Ti–PLLA FGMs, the Ti–NaCl composite was fabricated by SPS method using powder mixture of commercially pure (CP) Ti powder (under 56 μm) and NaCl (hexahedron shapes; some of the NaCl particle size was over 500 μm) to complete the sintering of Ti matrix, since the difference in melting points of these materials is relatively small. Volume fractions of NaCl powder were 30 vol%, 50 vol.%, and 70 vol.%. The Ti–NaCl powder mixture was sintered at 700 °C for 5 min under applied stress of 30 MPa. Figure 9.8a, b shows optical microscope (OM) images of Ti–30vol.%NaCl and Ti–70vol.%NaCl composites, respectively [14]. The upper and lower pictures were observed on plane Z_0 and plane R, respectively. As can be seen in Fig. 9.8, oblate NaCl particles are observed on the plane R, whereas there is no anisotropic microstructure on the plane Z_0. That is, NaCl particles are compressed during the SPS process.
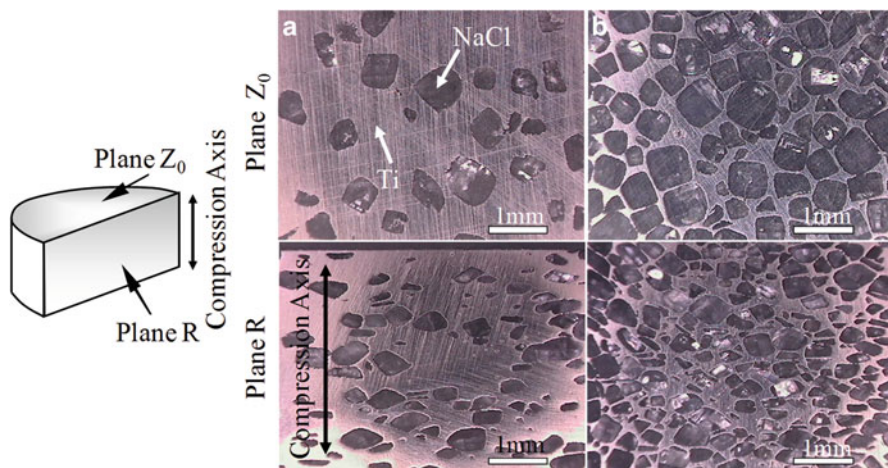
Fig. 9.8 OM images of (**a**) Ti–30 vol.%NaCl and (**b**) Ti–70 vol.%NaCl composites at plane Z_0 and plane R before dissolving NaCl particles (Reprinted from Ref. [14], Copyright 2011, with permission from Elsevier)

The Ti–NaCl composites were put into hot water of 100 °C to obtain porous Ti. Hereafter porous Ti samples obtained from Ti–30vol.%NaCl, Ti–50vol.%NaCl, and Ti–70vol.%NaCl composites by the dissolution process are abbreviated to porous Ti(30), porous Ti(50), and porous Ti(70), respectively. It is found that porous Ti(50) and porous Ti(70) samples have no remained NaCl particles, and porous Ti(50) and porous Ti(70) have open pores. Figure 9.9 shows the pore size distribution in the porous Ti(50) [14]. In these graphs, mean pore size range in the specimen distributes within 200–600 μm. It is reported that the optimal pore size in porous bone substitutes to obtain differentiation and growth of osteoblasts and vascularization is approximately 300–400 μm or 200–500 μm [22]. Thus, the obtained porous Ti is satisfied the basic requirement of biomedical pores of hard tissues.

Relationship between bulk density and porosity was investigated as shown in Fig. 9.10 [14]. As can be seen, the more porosity increased, the more density decreased linearly. Since the density of bone is 1.6–2.0 Mg/m^3, the porous Ti(50) has closed value to the range of bone density. In addition, at least the most of all pores is supposed to be open pore and no residual NaCl remained in the bulk in Ti (50).

Young's modulus and 0.2 % proof stress of pure Ti and porous Ti samples are shown in Fig. 9.11a, b, respectively [14]. Young's modulus and 0.2 % proof stress of samples are decreased with increasing volume fraction of pores (porosity). Moreover, anisotropy of these properties is found for porous Ti samples. Although Young's modulus of pure Ti is close to the required one, 0.2 % proof stress of pure Ti is much larger than the required yield stress. On the other hand, Young's modulus of the porous Ti(30) is smaller than the required modulus, and its 0.2 %
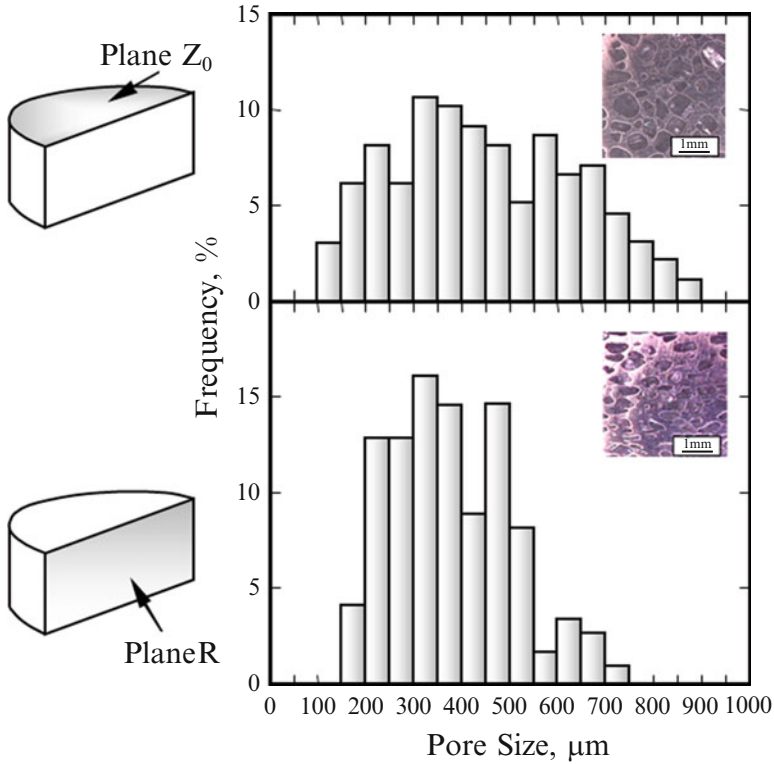
Fig. 9.9 The pore size distributions in the porous Ti(50) at plane Z_0 and plane R (Reprinted from Ref. [14], Copyright 2011, with permission from Elsevier)

Fig. 9.10 Relationship between bulk density and porosity in porous Ti (Reprinted from Ref. [14], Copyright 2011, with permission from Elsevier)
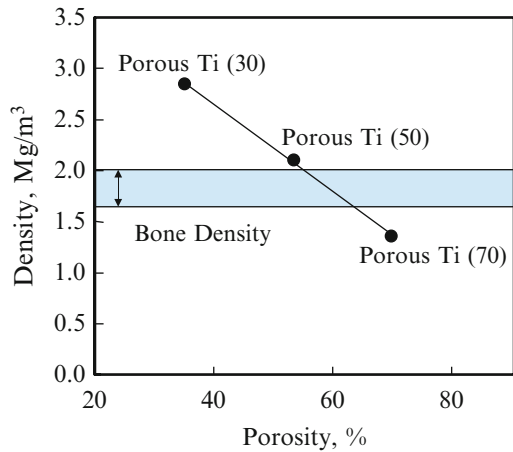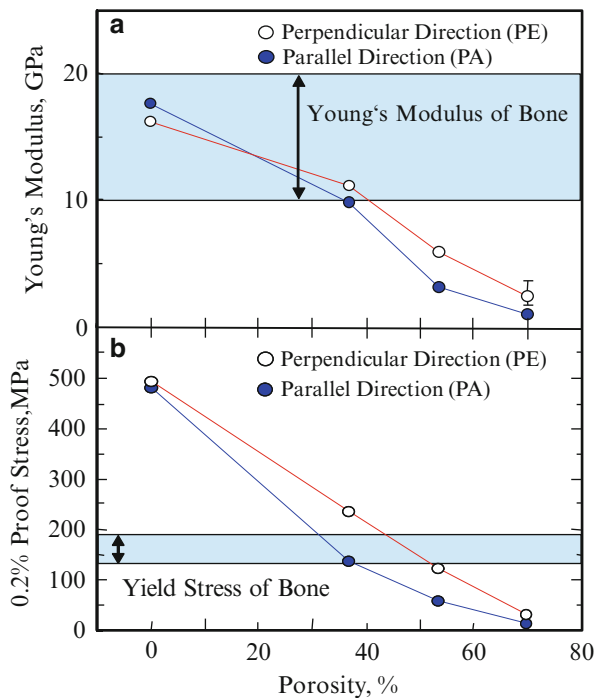
Fig. 9.11 Young's
modulus and 0.2 % proof
stress of pure Ti and porous
Ti samples. Compression
axes are along
perpendicular (PE) and
parallel (PA) direction
(Reprinted from Ref. [14],
Copyright 2011, with
permission from Elsevier)

proof stress is almost the same stress with ideal metallic implant material. From
these results, it is found that porous Ti(30) can satisfy both requirements of Young's
modulus and yield stress as a metallic implant material by means of improving its
Young's modulus, although the porous Ti(30) does not have open pores. In addi-
tion, porous Ti(50) has open pores and it is likely to be able to satisfy the
requirements by means of adding a reinforcement material into pores. Biodegrad-
able material such as PLLA would be one of expectable materials as reinforcement
filler.

To fabricate the Ti–PLLA FGMs, porous Ti sample obtained from Ti–NaCl
composites with 50 vol.% NaCl and PLLA pellets were mixed in recovery flask,
and the flask was heated at about 200 °C to melt PLLA pellets. After porous Ti
samples were covered with melted PLLA, an aspirator vacuumed the samples in the
flask to remove the air in pores. Following the procedures, the flask was reverted to
atmospheric pressure and then melting PLLA was introduced into the pores of
porous Ti samples. Figure 9.12a, b shows OM micrographs showing the Ti–PLLA
FGMs sample fabricated from porous Ti(50) at surface region (Plane Z_0) and
interior region (Plane $Z_{h/3}$), respectively [14]. It seems that PLLA is successfully
introduced into the Ti matrix. It must be noted here that some pores are observed on
the Plane $Z_{h/3}$ as shown in Fig. 9.12b, while there is no pore on Plane Z_0 as shown in
Fig. 9.12a. The amount of pore changes from place to place, and such porosity

Fig. 9.12 OM images at (**a**) plane Z_0 and (**b**) plane $Z_{h/3}$ in Ti–PLLA FGMs sample fabricated from porous Ti (50) (Reprinted from Ref. [14], Copyright 2011, with permission from Elsevier)
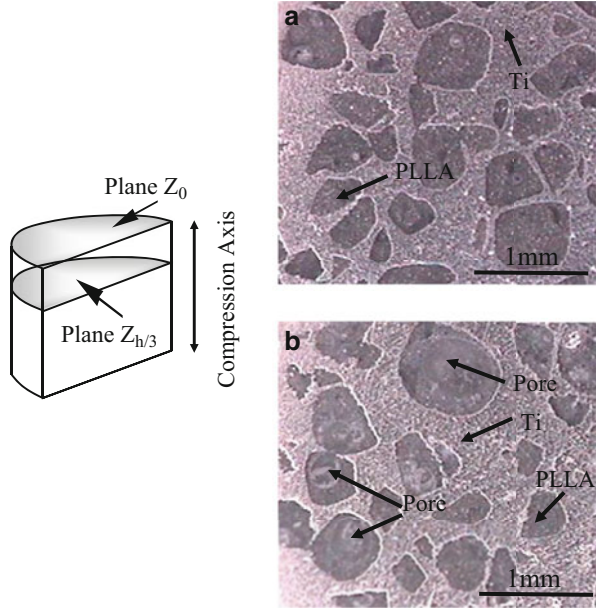
Fig. 9.13 Results of wear tests sliding along three different directions under reciprocal movement (Reprinted from Ref. [14], Copyright 2011, with permission from Elsevier)
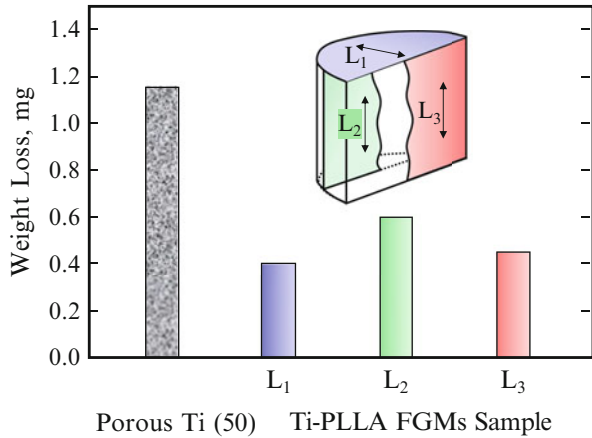
distribution could cause gradients of mechanical properties in the fabricated Ti–PLLA FGMs sample.

Wear tests for fabricated Ti–PLLA FGMs sample were performed using a ball-on-disk-type machine, where the samples were slid along three different directions under reciprocal movement against a stationary counter sphere of stainless steel. The results are shown in Fig. 9.13, as well as that from porous Ti(50) [14]. It is seen that osmotic PLLA into porous Ti enhances its wear resistance. Since PLLA is much softer than Ti matrix, it is supposed that PLLA near worn surface was
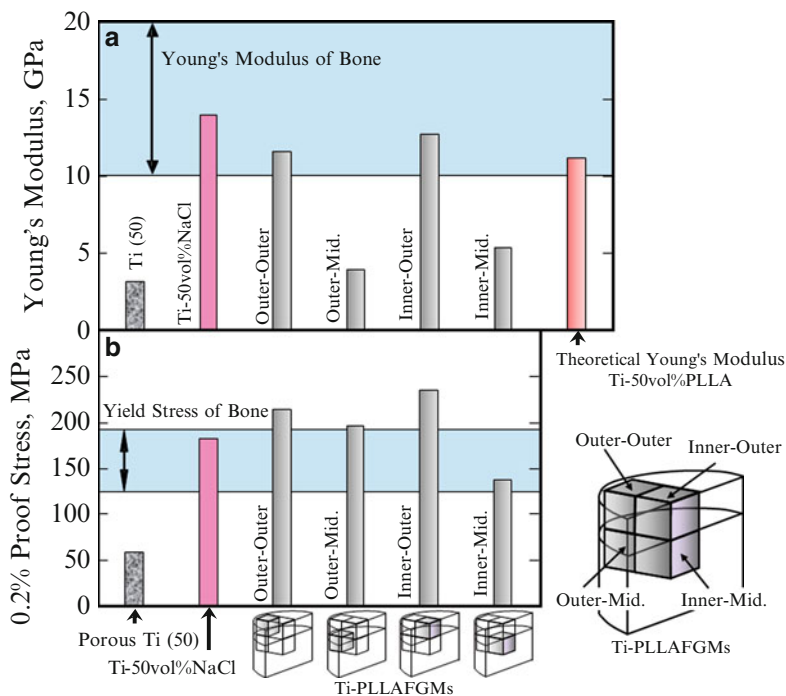
Fig. 9.14 (**a**) Young's modulus and (**b**) 0.2 % proof stress of porous Ti(50), Ti–50 vol.%NaCl composite and Ti–PLLA FGMs with different regions. Theoretical Young's modulus of Ti–50 vol. %PLLA FGMs is also shown in (**a**) (Reprinted from Ref. [14], Copyright 2011, with permission from Elsevier)

preferentially scraped out from the Ti–PLLA FGMs sample and subsequently spreads out and covers on the Ti matrix during friction. It is considered that preferential abrasion and coating of PLLA due to wear protects against wear of Ti matrix and reduces adhesion of counter-face with Ti.

Young's modulus and 0.2 % proof stress of porous Ti, Ti–NaCl composite, and Ti–PLLA FGMs sample with different parts are shown in Fig. 9.14a, b, respectively. As shown in Fig. 9.14a, the porous Ti(50) has the lowest Young's modulus, since it has a porous structure. On the contrary, the highest Young's modulus was observed for the pore-free Ti–NaCl composite, which is within the range of the modulus of the bone. Theoretical Young's modulus of Ti–PLLA FGMs calculated by simple rule of mixture is also shown in this figure. It should be noted that the Young's modulus values of Ti–PLLA FGMs samples from outer–outer and inner–outer positions were in excellent agreement with the theoretical one. 0.2 % proof stress of Ti–PLLA FGMs also changes from place to place. In this way, the mechanical property gradients are observed for Ti–PLLA FGMs, which may be caused by the volume fractional gradient of pores, as shown in Fig. 9.12. Since Young's modulus and 0.2 % proof stress of the Ti–PLLA FGMs sample are close to

the required ones, Ti–PLLA FGMs satisfy the required mechanical properties of metallic implant material by means of PLLA dispersion in porous Ti. It can be expected that optimum performance will be obtained just after implantation of the composite into the bone, and then PLLA will gradually degrade and be absorbed into the body. Although its mechanical properties will become lower as PLLA degrades, osteogenesis will occur in the pore instead.

9.3   Continuous Graded Composition in Ti–ZrO$_2$ Bio-FGMs Fabricated by Mixed-Powder Pouring Method

In session 9.1, it is described that the powder processing has many advantages to fabricate the FGMs. However, the graded structure fabricated by the powder processing becomes stepwise structure, and it is, unfortunately, difficult to produce the FGMs with continuous gradients. By a centrifugal slurry method, this short-coming can be overcome. For centrifugal slurry method, slurry with two types of solid particles will be used, namely, high-velocity particle with larger density and/or larger particle size and low-velocity particle with smaller density and/or smaller particle size, as shown in Fig. 9.15a [8, 23]. Since the motion of solid particles in viscous liquid under centrifugal force can be determined by the Stokes' law, the terminal velocity is reached at a very early stage of the centrifugal casting method [24, 25]. Therefore, the velocity of particles within a liquid under centrifugal force, dx/dt, can be expressed as
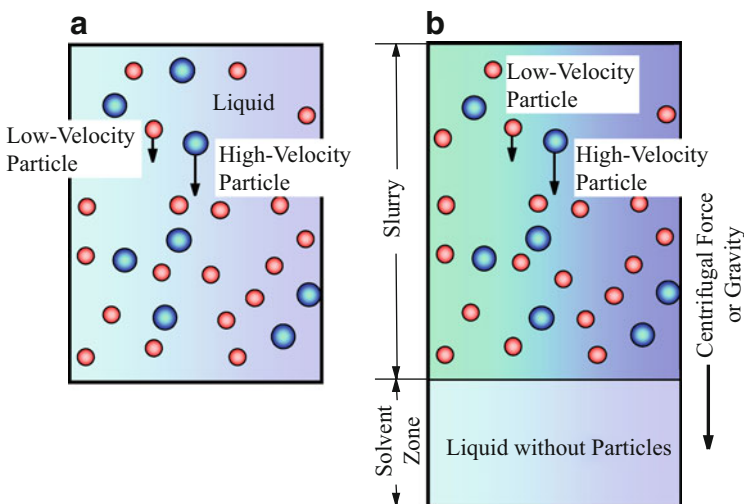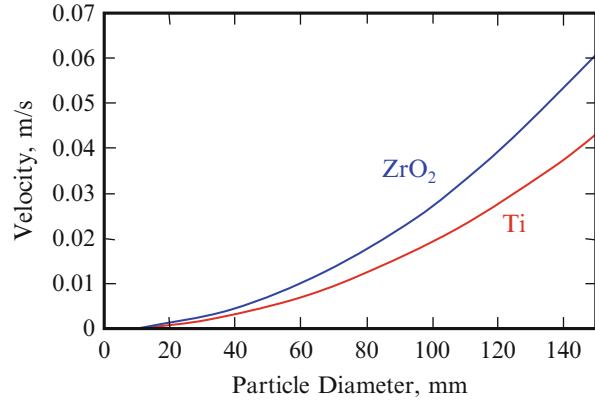

Fig. 9.15 Fabrication process to obtain green body with continuous gradient under a centrifugal force. (**a**) Centrifugal slurry method [8] and (**b**) centrifugal slurry–pouring method [27]

Fig. 9.16 Velocities of Ti and ZrO₂ particles under the centrifugal force [23]

$$\frac{\mathrm{d}x}{\mathrm{d}t} = \frac{|\rho_p - \rho_m| G g D_p^2}{18\eta} \tag{9.1}$$

where ρ_p, ρ_m, D_p, G, g, and η are density of particle, density of liquid, particle diameter, G number showing the level of centrifugal force, gravitational acceleration, and apparent viscosity of liquid, respectively. The continuous gradient can be obtained by the difference of migration rate between the two kinds of particles, i.e., high-velocity particle and low-velocity particle, predicted by Eq. 9.1. After complete sedimentation occurs, the liquid part of the slurry will be removed, and a green body with continuous gradient can be obtained. The green body is, then, subjected to sintering, and finally an FGMs sample with continuous gradient can be fabricated.

In order to verify and confirm the above idea, we shall focus on the Ti–ZrO₂ FGMs. ZrO₂ ceramics have several advantages over other ceramic materials, due to the transformation-toughening mechanisms operating in their microstructure that can give to components made out of them, very interesting mechanical properties [26]. Partially stabilized ZrO₂ (PSZ) and tetragonal ZrO₂ polycrystal (TZP) are common biomaterials used in orthopedic applications. Figure 9.16 shows migration velocities of Ti and ZrO₂ particles under the centrifugal force [8, 23], where the densities of Ti and ZrO₂ are 4.5 Mg/m³ and 5.95 Mg/m³, respectively. When the particle size is the same, the velocity of ZrO₂ particle is higher than that of Ti particle, due to its larger density. On the other hand, if the slurry contains the smaller ZrO₂ particles and larger Ti particles, the Ti particles can have high velocity in a specific condition.

Compositional gradient of the FGMs sample fabricated by the centrifugal slurry method is simulated for the Ti–ZrO₂ system with particle sizes of 63 ~ 90 μm for Ti particle and 75 ~ 106 μm for ZrO₂ particle. In this case, Ti particle becomes low-velocity particle and ZrO₂ particle becomes high-velocity particle. Results are shown in Fig. 9.17a [27]. In this figure, the horizontal axis is the normalized position of the green body, and 0.0 and 1.0 correspond to the top and bottom

Fig. 9.17 Distributions of Ti and ZrO_2 particles within the FGMs fabricated by (**a**) the centrifugal slurry method and (**b**) the centrifugal slurry-pouring method (computer simulation) [27]. In (**b**), width of solvent zone is 100 mm
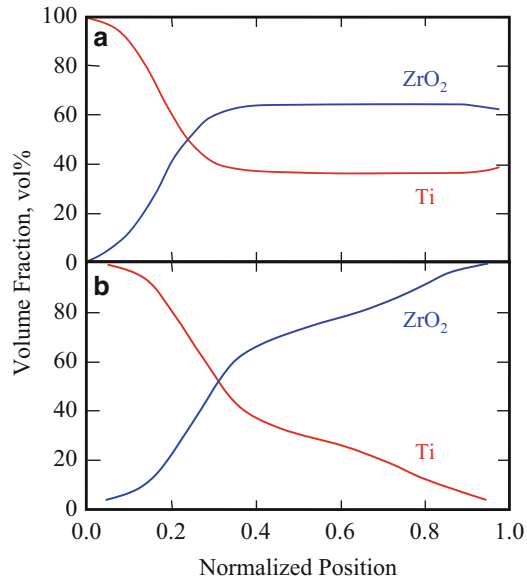
surfaces of the settled green body, respectively. This result clearly indicates that continuous gradient can be obtained by the centrifugal slurry method. However, large compositional gradient (from 0 vol.% at one end to 100 vol.% at another end of the FGMs sample for specific component) cannot be achieved, since the low-velocity Ti particles placed at the bottom region before the sedimentation still may remain around the same region after the complete sedimentation.

To solve the above shortcoming, a slurry-pouring method has been proposed to fabricate the FGMs with large compositional gradient [8, 23]. The slurry with high-velocity particle and low-velocity particle was poured into the spinning mold with solvent zone, as shown in Fig. 9.15b. The existence of solvent zone increases the sedimentation period. As a result, large compositional gradient, for example, from 0 vol.% at one end to 100 vol.% at another end, can be fabricated. The computer simulation is conducted for the slurry-pouring method, and results are shown in Fig. 9.17b; here the width of solvent zone is 100 mm [8, 23]. It must be noted here that the FGMs sample has a continuous gradient, and the volume fraction of Ti at the normalized position of 0.0 is 0 vol.%, while 100 vol.% at 1.0 position. Thus, a large compositional gradient can be achieved by the slurry-pouring method.

An experimental study of the slurry-pouring method was conducted where crushed ice is used as the particle suspension medium to control the particle sediment from the initiation to the end [28]. The hollow tube was filled with the crushed ice of 78.5×10^{-6} m^3, prepared using the ice crusher, as shown in Fig. 9.18a [28]. A hollow tube with a length of 220 mm made of plastic was fitted and sealed to another end of the graphite die. The height of the total suspension, i.e., the length of the hollow tube along with the graphite die is 250 mm. Homogeneously mixed powders of Ti and ZrO_2 with a volume ratio 1:1 were poured from
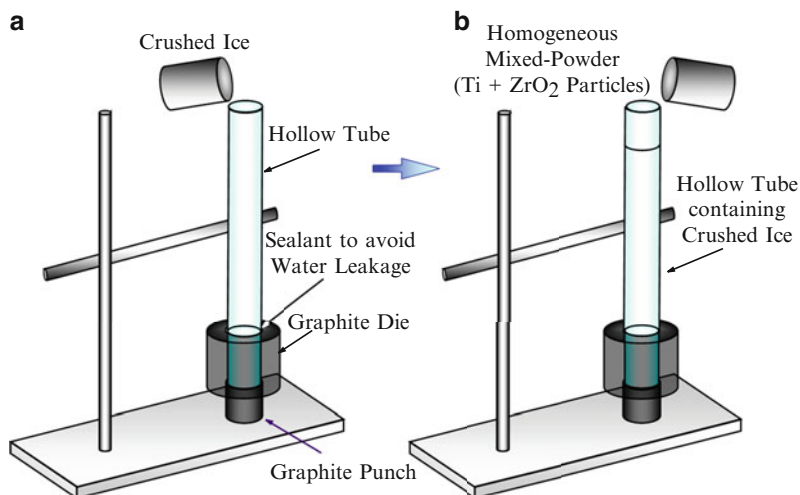
Fig. 9.18 Experimental setup of the slurry-pouring method. (**a**) Pouring crushed ice into a hollow tube and (**b**) pouring homogeneous Ti–ZrO$_2$ mixed powder into a hollow tube containing crushed ice [28]

the top of the crushed ice, as shown in Fig. 9.18b [28]. The crushed ice was allowed to melt gradually under isothermal conditions at 40 °C. Sedimentation of Ti and ZrO$_2$ particles proceeded along longitudinal direction of the hollow tube at the uniform temperature. The homogeneously mixed powders poured on the top of crushed ice will move down to the bottom of the graphite die. Sedimentation of the mixed powders depends on the densities and/or sizes of the particles. After settlement, a green body with compositional gradient was obtained.

The concentrations of Ti and ZrO$_2$ at each region were analyzed by energy-dispersive X-ray spectrometry (EDX), and the volume fraction distributions of Ti and ZrO$_2$ in FGMs were obtained as shown in Fig. 9.19 [28]. The particle size ranges of Ti particle and ZrO$_2$ particle are 63–90 μm and 75–106 μm for Fig. 9.19a, 45 μm pass and 38–75 μm for Fig. 9.19b, and 90–150 μm and 106–150 μm for Fig. 9.19c, respectively. The results of computer simulation are also shown in these figures [28]. It can be seen from these figures that the volume fraction of Ti is close to 100 vol.% between the normalized positions of 0 and 0.2 in all the samples. The composition of Ti decreases and that of ZrO$_2$ increases continuously and gradually, to become nearly homogeneous between normalized positions of 0.6 and 0.65. The volume fraction of ZrO$_2$ reaches close to 100 vol.% between the normalized positions 0.8 and 1, as shown in Fig. 9.19a, b. Therefore, it is found that the proposed method is an effective fabrication technique for FGMs with large and continuous compositional gradient. The hardness values in Ti–ZrO$_2$ FGMs samples are also shown in these figures. The hardness inside the fabricated FGMs increases
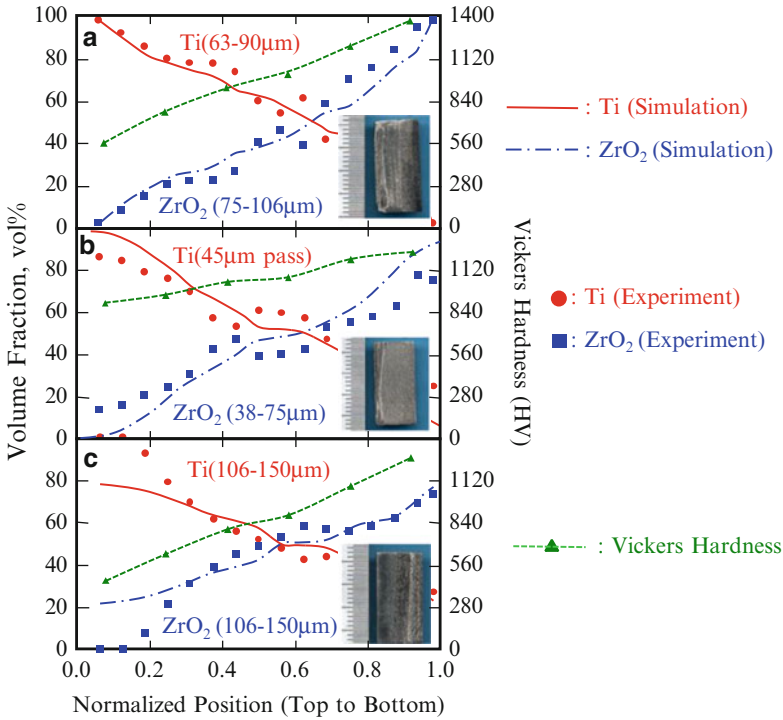
Fig. 9.19 Comparison of experimental volume fraction results with simulation results and effects of hardness number in Ti–ZrO$_2$ FGMs fabricated from different particle sizes [28]

with the increase in normalized position 0–1, thereby confirming the increasing ZrO$_2$ content across the normalized position. In this way, bio-FGMs with hardness gradient can be obtained.

9.4 White Ceramic Coating on Ti–29Nb–13Ta–4.6Zr Alloy for Dental Application

Although ceramic materials are becoming popular and starting to substitute for metallic parts of dental devices, such as dental implant, crown, denture, bracket, wire, and so on, metals are superior to in terms of ductility. Presently, a ceramic fused metallic core crown is commonly used, not only by the biological and mechanical requirements but also the esthetic requirement. However, exfoliation between metallic core and ceramic surface is one of the most serious clinical problems [29]. If one can obtain white-colored metallic materials, which own high ductility, high strength, and excellent esthetic properties, this problem is overcome. Not only Pt group or Au group alloys but also Ti alloys have been
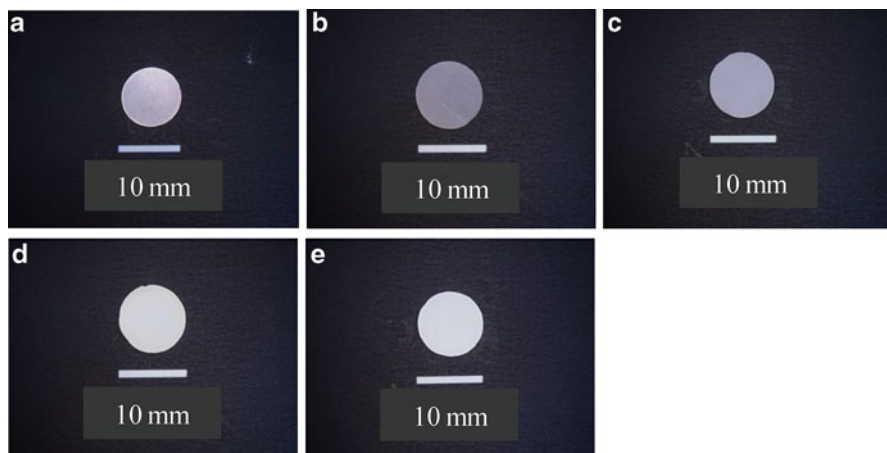
Fig. 9.20 Appearances of TNTZ sample surfaces. (**a**) Before oxidation treatment. (**b**) Oxidation treated at 900 °C for 1.8 ks, (**c**) at 900 °C for 3.6 ks, (**d**) at 1,000 °C for 1.8 ks, and (**e**) at 1,000 °C for 3.6 ks [34]

used for dental materials because of their high corrosion resistance and excellent mechanical properties. Since it is known that a white-colored TiO_2 layer is formed by high-temperature oxidation of pure Ti, it is expected that a white oxide film can be also formed by heat treatment on Ti alloys. Ti–29Nb–13Ta–4.6Zr (TNTZ) alloy is a β-type Ti alloy with excellent mechanical properties as a biomedical load-bearing material developed by Niinomi et al. [30, 31]. The ideal metallic white materials could be realized when esthetically and mechanically excellent oxide coating having durability against exfoliation of TNTZ can be made. As described in session 9.1, compositional gradient can be formed by elimination of the sharp interface by diffusion. White ceramic coating on TNTZ and Ti with graded microstructure for dental applications is, thus, carried out by oxidation treatment [32–34].

Hot-rolled TNTZ and pure Ti bars with a diameter of φ10 mm were used as a substrate material. After annealing at 800 °C, the bar was sliced with a thickness of about 1 mm. The slices were polished with emery paper up to #1,500. The polished samples were oxidized in air furnace at 800 °C, 900 °C, 1,000 °C, and 1,200 °C from 0.6 ks to 10.8 ks. The samples were air-cooled after heat treatment. Macroscopic appearance of TNTZ sample before and after oxidation treatment is shown in Fig. 9.20 [34]. It is obvious that matte and bright oxide film was formed on the metallic TNTZ surface after oxidation. Brightness visually increased with increasing holding time or oxidized temperature; however, the oxidation film peeled off after long-time and/or high-temperature treatment. Although the figure is not presented here, the oxidation film of the TNTZ substrate oxidized at 1,000 °C for 7.2 ks exfoliated from the substrate completely after oxidation. This is because of the difference of thermal expansion between the oxide and metal substrate. To solve this problem, slow cooling and oxidation at minimum temperature were examined.

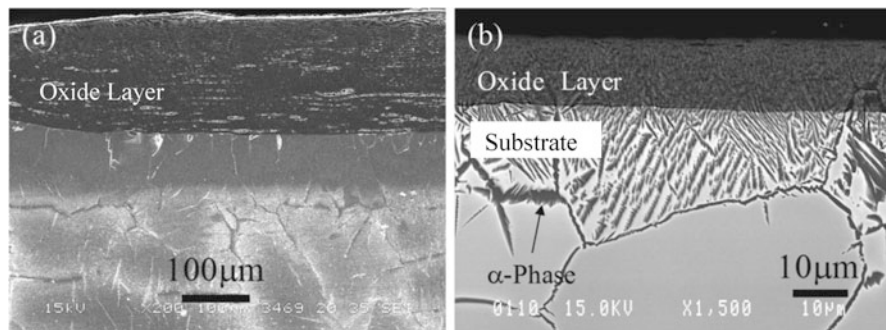**Fig. 9.21** SEM cross-sectional images around surface of oxidized (**a**) Ti and (**b**) TNTZ samples. The oxidation treatment was carried out at 1,000 °C for 3.6 ks and furnace cooling for Ti sample and 1,000 °C for 1.8 ks and air cooling for TNTZ sample (Reprinted from Ref. [33], with permission from TMS)

From our results, oxidation at 1,000 °C for 3.6 ks for Ti and 1,000 °C for 1.8 ks was the best heat treatment condition in terms of avoiding exfoliation during oxidation.

Cross-sectional microstructures of Ti and TNTZ after oxidation treatment were investigated by SEM, and results are shown in Fig. 9.21a, b, respectively [33]. In Fig. 9.21a, the oxide layer of Ti exhibited unique microstructure with a stratified formation, which means an oxide particle layer and a gap stacked one by one. On the other hand, dense oxide layer was formed on TNTZ substrate as shown in Fig. 9.21b. Regarding substrate microstructure in Fig. 9.21b, grain growth during oxidation was observed in substrate beneath the oxide layer; in addition, lamellar structure was observed in the grain of TNTZ. This lamellar structure consisted of the $\alpha + \beta$-phase. The α-phase was precipitated owing to O diffusion during oxidation since O acts as an α-phase stabilizer. The α-phase close to the interface contained about 20 mol% of O, whereas the matrix had less than 10 mol% of O. Concurrently, Nb and Ta concentrations at the α-phase were lower than in the matrix.

In order to obtain detailed information about oxide/substrate interface, depth profile of chemical composition was studied by X-ray photoelectron spectroscopy (XPS) for TNTZ sample oxidized at 1,000 °C for 1.8 ks. The obtained results are shown in Fig. 9.22 [32]. In this figure, it seems both O and Ti contents were homogeneous in the oxide layer, and O rapidly decreased at the lamellar structure layer. After that, O gradually decreased in substrate. On the other hand, Ti content was uniform in the substrate and decreased rapidly at the lamellar structure and then Ti content became uniform at the oxide layer. Content ratio Ti/O was close to 1:2; thus, TiO_2 was considered to be a major oxide. In addition, depth profile of other elements, Nb, Ta, and Zr, seemed to have a similar tendency to that of Ti. These elements are supposed to form oxide. According to XRD measurements, although which is not shown here, not only TiO_2 but also $Ti(Nb, Ta)_2O_7$ and/or $Ti(Nb, Ta)O_4$ were detected in the oxide layer.
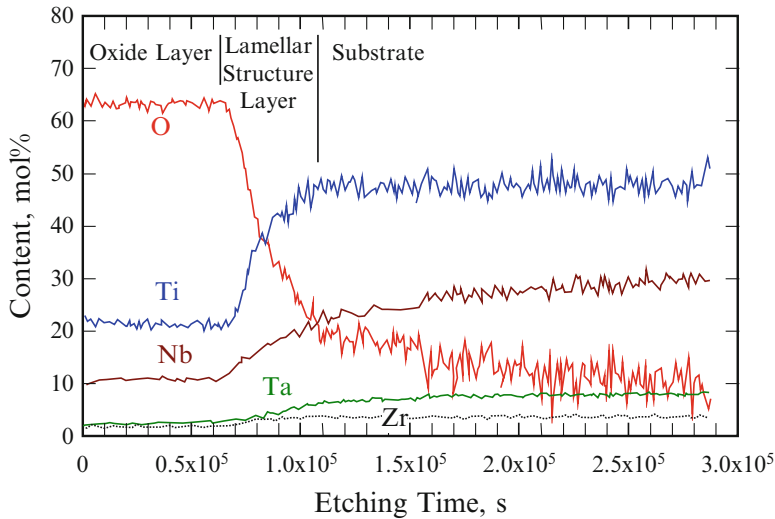
Fig. 9.22 XPS depth profile of TNTZ oxidized at 1,000 °C for 1.8 ks [32]

Fig. 9.23 Relationship between oxide layer thickness and holding time of TNTZ and Ti (Reprinted from Ref. [33], with permission from TMS)
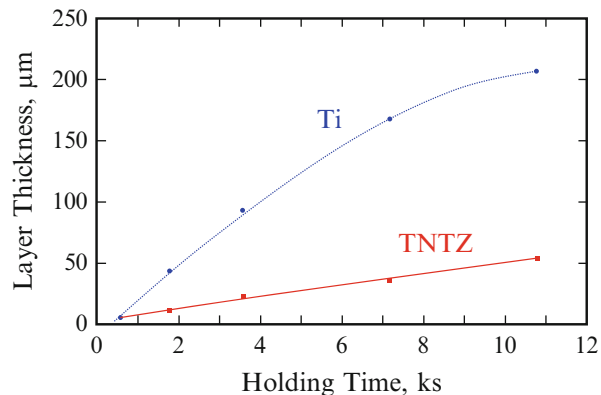
Figure 9.23 shows the relationship between thickness of the oxide layer and holding time [33]. Thickness of the oxide layer was measured from a cross-sectional image taken by SEM. It is seen that thickness of the oxide layer increased with increasing holding time in both TNTZ and Ti samples. Moreover, the oxide layer thickness of Ti at each oxidation time in this figure is bulk thickness; thus, true oxide thickness should be thinner than the appearance.

The color of the oxidized surface was measured using a spectrophotometric colorimeter. Color was expressed in terms of L*a*b* color system (CIE1976) [35]. In this color system, color space was expressed by the parameter of brightness L* and chromaticity coordinates a* and b*. L* indicates brightness, and a* and b* express redness (+) ~ greenness (−) and blueness (+) ~ yellowness (−), respectively, as shown in Fig. 9.24.

Fig. 9.24 L*a*b* color space in a 3-dimensional display showing CIELab color system [35]. Copyright (2014)The Japan Society of Applied Physics
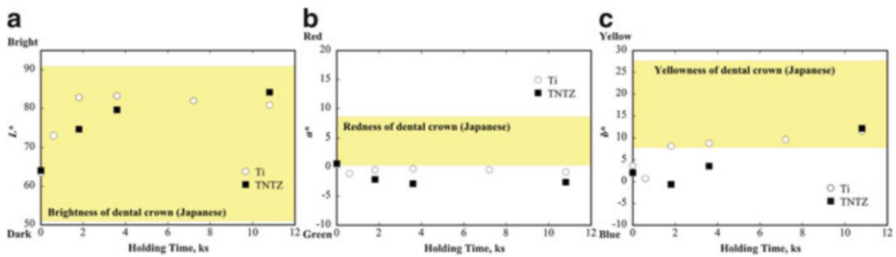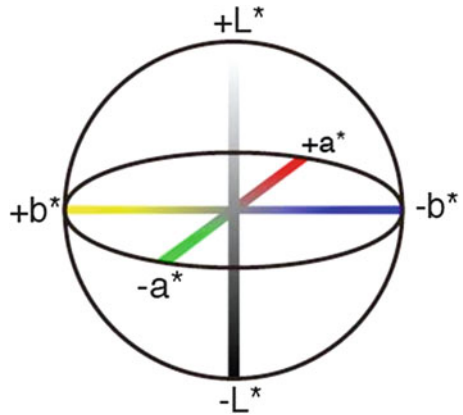
Fig. 9.25 Relationships between holding time and (a) L*, (b) a*, and (c) b* parameters (Reprinted from Ref. [33], with permission from TMS)

The color of the samples oxidized at 1,000 °C was measured using the spectro-photometric colorimeter. Figure 9.25 shows relationships between holding time and L*a*b* parameters. Color range of the crown of Japanese's natural tooth reported elsewhere [36] was also shown in these figures. In Fig. 9.25a, L* (bright–dark) of both Ti and TNTZ samples parabolically increased with increasing holding time at the initial stage of oxidation treatment, and then plateau appeared. Plateau region began from about 2 ks to 3.6 ks in Ti and TNTZ samples, respectively. It is noteworthy that L* of both Ti and TNTZ samples was in the range of Japanese's tooth color. Regarding b* (blue–yellow) shown in Fig. 9.25c, parabolic oxidation time dependence was observed as well as L*. It is considered from these results that L* and b* change depending on the thickness of the oxide layer. At short holding time, observed b* was out of the range in either Ti or TNTZ sample, and then b* also increased with increasing holding time. Thus, b* eventually reached within the range of tooth color. On the other hand, in Fig. 9.25b, a* (green–red) of both samples was below the range regardless of holding time, and time dependence on a* seemed to be negligible in the Ti sample and to be small but negative in the TNTZ sample. From these results, L* and b* increased with increasing holding time; thus, these parameters can be controlled by oxidation condition while exfoliation should
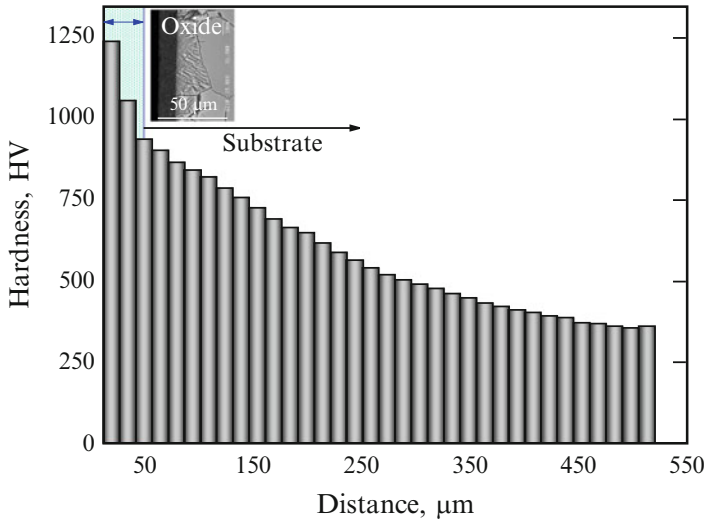
Fig. 9.26 Hardness distributions in oxidized TNTZ sample measured by nano-indentation hardness tester

be taken into account. It is reported that maximum brightness as an opaque resin for a facing metal crown is $L^* \leqq 80$ [37]; therefore, brightness of the oxide film obtained in this study is sufficient for opaque material for artificial tooth.

Nano-indentation hardness tests of TNTZ sample were carried out and results are shown in Fig. 9.26. As can be seen, hardness of the oxide layer was higher than the substrate close to the oxide layer. Moreover, hardness is changed from place to place. This graded hardness in the oxide layer would come from microstructural difference inside the layer. However, details of microstructure inside the oxide layer are our future work. Formation of oxide layer with graded hardness may be one reason of the high exfoliation resistance of oxide/TNTZ.

9.5 Al-Based FGMs Containing TiO$_2$ Nanoparticles with Antibacterial Activity by a Centrifugal Mixed-Powder Method

Medical devices are highly susceptible to bacterial contamination. Various methods have been proposed to confer the biomaterials' antibacterial activity [38]. An anatase-type TiO$_2$ is well known as the most effective photocatalyst, and it shows useful self-cleaning, deodorizing, and antibacterial functions, even under weak UV light. For these applications, TiO$_2$ is prepared as nanosized crystals to bring out its full abilities [39]. With the above in mind, Al-based FGMs containing antibacterial TiO$_2$ particles have been developed. Since the photocatalytic and antibacterial TiO$_2$ particle has a nanosized diameter, the motion of TiO$_2$ particles with different
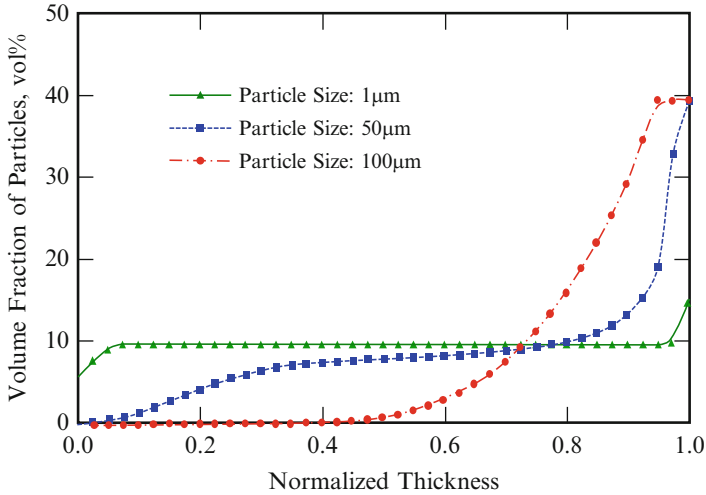
Fig. 9.27 Simulated particle distributions of TiO_2 in Al–TiO_2 FGMs fabricated by centrifugal method [40]

particle sizes in a molten Al under a centrifugal force is numerically modeled based on the Stokes' law (Eq. 9.1). Figure 9.27 shows the effect of particle size on the compositional gradient in the Al–TiO_2 FGMs fabricated by the centrifugal method shown in Fig. 9.5 [40]. These distributions of TiO_2 particles shown in Fig. 9.27 are obtained by calculation basing on Stokes' law. The volume fraction of TiO_2 and centrifugal force were fixed to be 10 vol.% and $G = 50$, respectively. The abscissa represents the position of normalized thickness of the ring, i.e., 0.0 is the inner surface and 1.0 is the outer surface. As can be seen, TiO_2 particles with 100 μm in diameter are gradually distributed in Al–TiO_2 FGMs sample; however, TiO_2 particles with 1 μm in diameter were almost homogeneously distributed in the sample. Therefore, it is concluded that the compositional gradient of nanoparticles in the FGMs fabricated by the centrifugal method is very small.

Alternatively, a centrifugal mixed-powder method is proposed as a novel processing technique to fabricate nanoparticle distributed FGMs. The experimental procedure of the centrifugal mixed-powder method is shown in Fig. 9.28 [40]. As a first step, a powder mixture of nanoparticles and metal matrix particles is inserted into a spinning mold, as shown in Fig. 9.28a. Then, molten metal matrix is poured into the spinning mold with the powder mixture, as shown in Fig. 9.28b. As a result, the molten metal matrix penetrates into the space between the particles due to the pressure exerted by the centrifugal force, as shown in Fig. 9.28c. At the same time, the metal matrix powder is melted by the heat from molten matrix poured from the crucible, as show in Fig. 9.28d. Finally, an FGMs ring with nanoparticles distributed on its surface can be obtained, as show in Fig. 9.28e. Using this processing method, Al–TiO_2 FGMs were fabricated.

Figure 9.29 shows the Ti concentration of Al–TiO_2 FGMs rings as a function of normalized thickness [40]. As can be seen, Ti concentration in both Al–TiO_2 FGMs
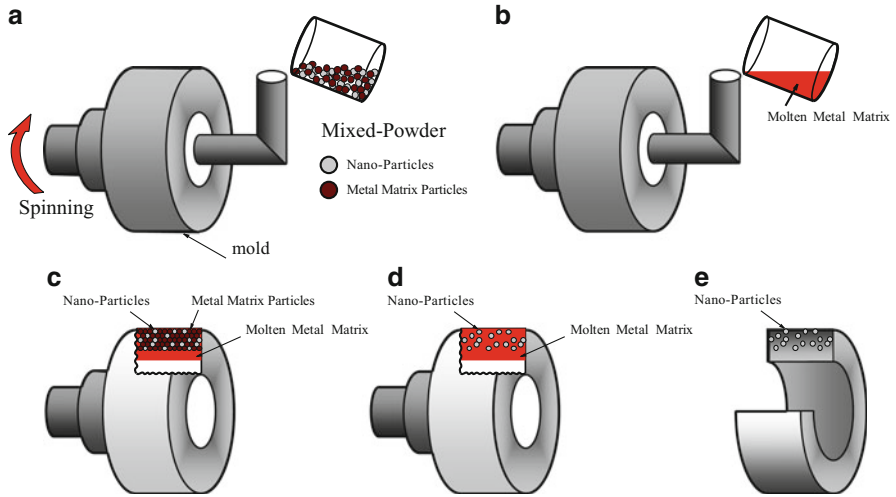
Fig. 9.28 The schematic illustration showing the process of the centrifugal mixed-powder method [40]
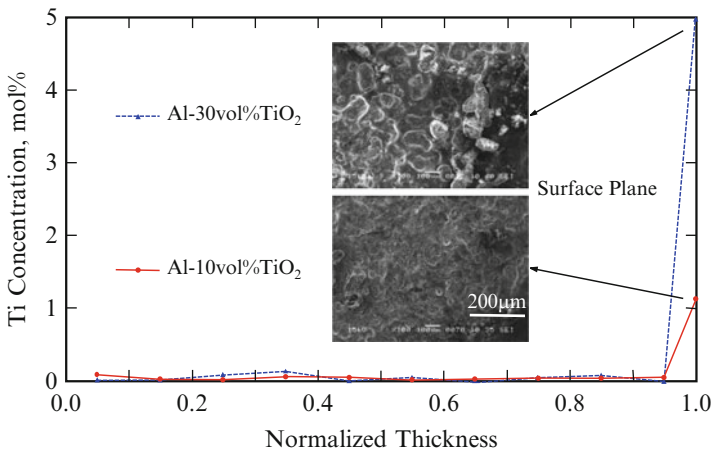
Fig. 9.29 Distributions of Ti concentration in Al–TiO$_2$ FGMs rings [40]

rings is almost constant from the normalized thickness of 0–0.95, and Ti is not detected inside the Al–TiO$_2$ FGMs. However, on the surface of the FGMs rings, Ti is detected. It is found that TiO$_2$ nanoparticles are distributed only on the outer surface of Al–TiO$_2$ FGMs rings. It is also found that TiO$_2$ nanoparticle distribution on the surface of the ring may be controlled by the volume fraction of TiO$_2$ nanoparticle in powder mixture.

Fig. 9.30 The change in the saturation magnetization with heating temperature. The starting temperature of the reverse transformation, A_s, and the finishing temperature, A_f, are determined to be about 500 °C and 700 °C, respectively
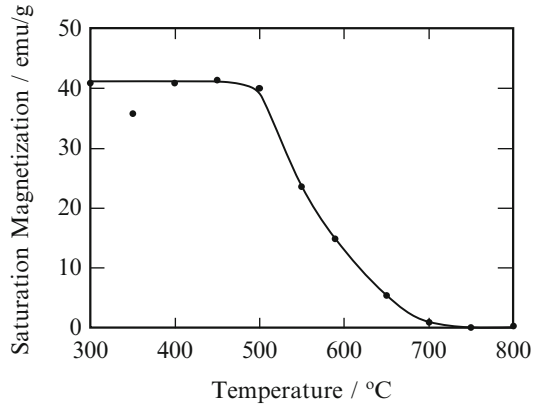
9.6 Magnetic Graded Materials by Inhomogeneous Heat Treatment of SUS304 Stainless Steel

Stainless steel is a major material to produce medical devices due to the superior machinability and corrosion resistance in a biological environment. Development of medical devices, such as stent, catheter, or coil anchor implanted in the human body, has played a key role in the recent progress on medical treatments [41].

Meanwhile, it is well known that plastic deformation of type 304 stainless steel (Fe–18mass%Cr–8mass%Ni) in the austenite (γ) phase can induce formation of the martensite (α') phase [42]. Martensite and austenite phases are ferromagnetic and paramagnetic at room temperature, respectively. Since the amount of deformation-induced martensite increases with an increase in the local strain, the saturation magnetization of the deformed austenitic stainless steel should also increase with increasing strain. Using this phenomenon, a magnetically graded material can be fabricated by inhomogeneous tensile deformation [43] or inhomogeneous rolling deformation [44] of wedge-shaped 304 austenitic stainless steel specimens. This FGMs fabrication method is termed the martensitic transformation technique.

It is also known that the α'-phase can transform into the γ-phase when the alloy is heated. This reverse transformation is accompanied by a ferromagnetic to paramagnetic transition. Along the temperature gradient from the starting temperature of the reverse transformation to the finishing temperature, the magnitude of saturation magnetization decreases. This phenomenon has also been used to produce a magnetically graded material by inhomogeneous heat treatment of deformed 304 stainless steel [45].

The initial α'-martensite phase in SUS304 stainless steel fiber was introduced by cooling down to the liquid nitrogen temperature (-196 °C). After the cooling, the fiber specimen was annealed within a temperature gradient to introduce the reverse transformation in controlled manner. Figure 9.30 shows the saturation magnetization of heat-treated SUS304 stainless steel fiber plotted as a function of the heating temperature. It is clear that the saturation magnetization decreases with increasing

Fig. 9.31 The change of the local temperature of the furnace during the thermal gradient heat treatment of the specimen and the saturation magnetization distribution in the specimen
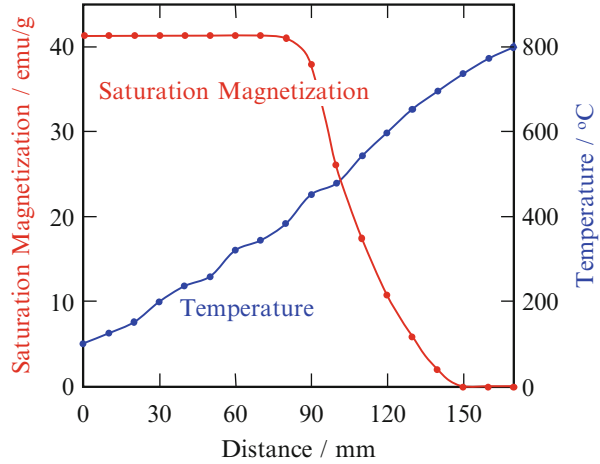
heating temperature above around 500 °C. This is because the ferromagnetic martensite phase transforms into the paramagnetic γ-austenite phase by the heating process. The saturation magnetization is almost zero in the specimen heated above 700 °C. Therefore, the starting temperature of the reverse transformation, A_s, and the finishing temperature, A_f, are determined to be about 500 °C and 700 °C, respectively.

Figure 9.31 shows the change of the local temperature of the furnace during the thermal gradient heat. Corresponding distribution of the saturation magnetization in the specimen is also shown in Fig. 9.31. As can be seen, the saturation magnetization in the specimen is graded. In this way, a magnetic graded fiber can be successfully fabricated by using the α′ to γ reverse transformation in SUS304 stainless steel.

Magnetically graded SUS304 stainless steel can be used as a magnetic attachment for a dental material. The fabricated material has both magnetic and mechanical gradients. Moreover, it is known that the corrosion resistance of the austenitic phase is better than that of the martensitic phase. Therefore, we can simultaneously fabricate three different gradient properties in one sample.

9.7   Conclusions

In this chapter, the merit of the metallic biomaterials with graded composition and/ or microstructure and our recent results, namely, Ti/biodegradable-polymer functionally graded materials (FGMs) for bone tissue fabricated by spark plasma sintering (SPS) method, continuous graded composition in Ti–ZrO_2 bio-FGMs fabricated by mixed-powder pouring method, white ceramic coating on Ti–29Nb–13Ta–4.6Zr (TNTZ) alloy for dental application, Al-based FGMs containing

TiO_2 nanoparticles with antibacterial activity by a centrifugal mixed-powder method, and magnetic graded materials by inhomogeneous heat treatment of SUS304 stainless steel, were described. The materials used for implants need to satisfy the all-round properties of biocompatibility, strength, corrosion resistance, and so on. The concept of FGMs is very useful to satisfy such requirements, and they possess properties within one material, simultaneously.

References

1. Sadollah A, Bahreininejad A (2012) Optimum functionally gradient materials for dental implant using simulated annealing. In: Tsuzuki MSG (ed) Simulated annealing – single and multiple objective problems. InTech, New York, Croatia. doi:10.5772/45640
2. Watari F, Yokoyama A, Matsuo H, Miyao R, Uo M, Kawasaki T, Omori M, Hirai T (2001) Biocompatibility of functionally graded implants. In: Ichikawa K (ed) Functionally graded materials in the 21st century. Kluwer Academic Publishers, Boston, pp 187–190
3. Hirai T (1996) Functional gradient materials. In: Cahan RW, Hassen P, Kramer EJ (eds) Processing of ceramics, Part 2, Materials science and technology, vol 17B. VCH Publishers, Weinheim, pp 293–341
4. Suresh S, Mortensen A (1998) Fundamentals of functionally graded materials, processing and thermomechanical behaviour of graded metals and metal-ceramic composites. IOM Communications Ltd., London
5. Miyamoto Y, Kaysser WA, Rabin BH, Kawasaki A, Ford RG (eds) (1999) Functionally graded materials: design, processing and applications. Kluwer Academic Publishers, Boston
6. Wataria F, Yokoyama A, Omori M, Hirai T, Kondo H, Uo M, Kawasaki T (2004) Biocompatibility of materials and development to functionally graded implant for bio-medical application. Comput Sci Technol 64:893–908
7. Amada S (1995) Hierarchical functionally gradient structures of bamboo, barley, and corn. MRS Bull 20:35–36
8. Watanabe Y, Sato H (2011) Review fabrication of functionally graded materials under a centrifugal force. In: Cuppoletti J (ed) Nanocomposites with unique properties and applications in medicine and industry. InTech, New York, Croatia, pp 133–150
9. Sampath S, Herman H, Shimoda N, Saito T (1995) Thermal spray processing of FGMs. MRS Bull 20:27–31
10. Kondo H, Yokoyama A, Omori M, Ohkubo A, Hirai T, Watari F, Uo M, Kawasaki T (2004) Fabrication of titanium nitride/apatite functionally graded implants by spark plasma sintering. Mater Trans 45:3156–3162
11. Lim Y-M, Park Y-J, Yun Y-H, Hwang K-S (2002) Functionally graded Ti/HAP coatings on Ti–6Al–4 V obtained by chemical solution deposition. Ceram Int 28:37–41
12. Yin GF, Luo JM, Zheng CQ, Tong HH, Huo YF, Mu LL (1999) Preparation of DLC gradient biomaterials by means of plasma source ion implant-ion beam enhanced deposition. Thin Solid Films 345:67–70
13. Sato M, Tu R, Goto T, Ueda K, Narushima T (2009) Preparation of functionally graded Bioceramic film by MOCVD. Mater Sci Forum 631–632:193–198
14. Watanabe Y, Iwasa Y, Sato H, Teramoto A, Abe K, Miura-Fujiwara E (2011) Microstructures and mechanical properties of titanium / biodegradable-polymer FGMs for bone tissue fabricated by spark plasma sintering method. J Mater Process Technol 211:1919–1926
15. Reilly DT, Burstein AH (1975) The elastic and ultimate properties of compact bone tissue. J Biomech 8:393–396
16. Narushima T (2005) Titanium and its alloys as biomaterials. J Jpn Inst Light Met 55:561–565

17. Ueda M, Sasaki Y, Ikeda M, Ogawa M (2009) Chemical-hydrothermal synthesis of bioinert ZrO_2-TiO_2 film on Ti substrates. Mater Trans 50:2104–2107
18. Tsuji H, Tezuka Y, Saha SK, Suzuki M, Itsuno S (2005) Spherulite growth of L-lactide copolymers: effects of tacticity and comonomers. Polymer 46:4917–4927
19. Sato H, Umaoka S-i, Watanabe Y, Kim I-S, Kawahara M, Tokita M (2007) Biodegradable fiber reinforced Ti composite fabricated by spark plasma sintering method. Mater Sci Forum 539–543:3201–3206
20. Miura-Fujiwara E, Teramoto T, Sato H, Kobayashi E, Watanabe Y (2010) Fabrication of Ti-based biodegradable material composites prepared by spark plasma sintering method. Mater Sci Forum 654–656:2158–2161
21. Hasebe T, Kobayashi E, Tezuka H, Sato T (2013) Effects of sintering conditions on mechanical properties of biomedical porous Ti produced by spark plasma sintering. Jpn J Appl Phys 52:01AE03 (4 pages)
22. Wen CE, Mabuchi M, Yamada Y, Shimojima K, Chino Y, Asahina T (2001) Processing of biocompatible porous Ti and Mg. Scr Mater 45:1147–1153
23. Watanabe Y, Miura-Fujiwara E, Sato H (2010) Fabrication of functionally graded materials by centrifugal slurry-pouring method and centrifugal mixed-powder method. J Jpn Soc Powder Powder Metall 57:321–326
24. Kang CG, Rohatgi PK (1996) Transient thermal analysis of solidification in a centrifugal casting for composite materials containing particle segregation. Metall Mater Trans B 27:277–285
25. Watanabe Y, Yamanaka N, Fukui Y (1998) Control of composition gradient in a metal-ceramic functionally graded material manufactured by the centrifugal method. Compos Part A 29A:595–601
26. Piconi C, Maccauro G (1999) Review Zirconia as a ceramic biomaterial. Biogeosciences 20:1–25
27. Watanabe Y, Miura-Fujiwara E, Sato H (2011) Fabrication of functionally graded materials by combination of centrifugal force and sintering method. J Jpn Soc Powder Powder Metall 58:11–17
28. Jayachandran M, Tsukamoto H, Sato H, Watanabe Y (2013) Formation behavior of continuous graded composition in Ti-ZrO_2 functionally graded material fabricated by mixed-powder pouring method. J Nanomater 2013:504631 (8 pages)
29. Miura E, Tabaru T, Liu J, Tanaka Y, Shiraishi T, Hisatsune K (2004) Effect of gold coating on interfacial reaction between dental porcelain and titanium. Mater Trans 45:3044–3049
30. Kuroda D, Niinomi M, Morinaga M, Kato Y, Yashiro T (1998) Design and mechanical properties of New β type titanium alloys for implant materials. Mater Sci Eng A243:244–249
31. Niinomi M, Hattori T, Morikawa K, Kasuga T, Suzuki A, Fukui H, Niwa S (2002) Development of low rigidity β-type titanium alloy for biomedical applications. Mater Trans 43:2970–2977
32. Miura-Fujiwara E, Yamada S, Obata A, Sato H, Watanabe Y, Kasuga T, Niinomi M (2012) Oxidation behavior and effect of layer thickness on whiteness and exfoliation behavior of Oxide Film Formed on Ti-Nb-Ta-Zr Alloy. In: Proceedings of the Ti-2011 conference, III, China National Convention Center, Beijing, China, pp 2116–2120
33. Miura-Fujiwara E, Mizushima K, Yamada S, Watanabe Y, Kasuga T, Niinomi M, Yamasaki T (2013) Aesthetic and mechanical properties of oxide coated Ti-Nb-Ta-Zr alloys as a dental material. In: Proceedings of the 8th pacific rim international conference on advanced materials and processing, TMS (The Minerals, Metals & Materials Society), Hilton Waikoloa Village, Waikoloa, HI, USA, pp 1543–1550
34. Obata A, Miura-Fujiwara E, Shimizu A, Maeda H, Nakai M, Watanabe Y, Niinomi M, Kasuga T (2013) White-ceramic conversion on Ti-29Nb-13Ta-4.6Zr surface for dental applications. Adv Mater Sci Eng 2013:501621 (9 pages)

35. Miura-Fujiwara E, Mizushima K, Watanabe Y, Kasuga T, Niinomi M (2014) Color tone and interfacial microstructure of white oxide layer on CP Ti and Ti-Nb-Ta-Zr alloys. Jpn J Appl Phys 53:11RD02
36. Hasegawa A, Motonomi A, Ikeda I, Kawaguchi S (2000) Color of natural tooth crown in Japanese people. Color Res Appl 25:43–48
37. Shiba W, Uno M, Ishigami H, Kurachi M (2009) Means for reproducing shade guide color with laboratory-cured prosthetic composite. J Gifu Dent Soc 35:149–159
38. Yuan W, Ji J, Fu J, Shen J (2008) A facile method to construct hybrid multilayered films as a strong and multifunctional antibacterial coating. J Biomed Mater Res Part B 85B:556–563
39. Tang W, Chen Z, Katoh S (2004) Preparation of a nanocrystalline TiO_2 photocatalyst using a dry-process with acetylene black. Chem Lett 33:1200–1201
40. Watanabe Y, Inaguma Y, Sato H, Miura-Fujiwara E (2009) A novel fabrication method for functionally graded materials under centrifugal force: the centrifugal mixed-powder method. Materials 2:2510–2525
41. Uenishi K, Seki M, Takatsugu M, Kunimasa T, Kobayashi KF, Ikeda T, Tsuboi A (2002) Microstructure and tensile strength of stainless steel wires micro spot melted by YAG laser. Mater Trans 43:3083–3087
42. Mangonon PL, Thomas G (1970) Structure and properties of thermal-mechanically treated 304 stainless steel. Metall Trans 1:1587–1594
43. Watanabe Y, Nakamura Y, Fukui Y, Nakanishi K (1993) A magnetic-functionally graded material manufactured with deformation-induced martensitic transformation. J Mater Sci Lett 12:326–328
44. Watanabe Y, Kang SH, Chan JW, Morris JW Jr (1999) Fabrication of magnetically graded material by rolling deformation of wedge-shaped 304 stainless steel. Mater Trans JIM 40:961–966
45. Watanabe Y, Momose I (2004) Magnetically graded materials fabricated by inhomogeneous heat treatment of deformed stainless steel. Ironmak Steelmak 31:265–268

Part III
Applications

Chapter 10
Metallic Biomaterials in Orthopedic Surgery

Manabu Ito, Tomohiro Onodera, and Tadanao Funakoshi

Abstract Metals have the longest history in the field of orthopedic surgery among numerous biomaterials. Metallic implants were used for the first time to fix spine fractures more than 100 years ago. Since then, metallic orthopedic implants were used routinely for fixation of bone fractures and deformity correction of the spine and long bones. The advantages of metals are excellent mechanical stiffness and fracture toughness to provide unstable fracture sites with sufficient stability to achieve biological bony union. Clinically used metals are stainless steel, Co-Cr (cobalt-chrome), and titanium alloys. The common indications of metallic implants for orthopedic surgery are fixation of bony fractures at different parts of the body, joint replacement, and deformity correction of long bones and the spinal column. Metallic implants are often removed at postoperative 1 or 2 years, after complete bony union is obtained, in order to prevent osteopenia or osteoporosis related to a stress-shielding effect around the location of the metallic implant. Future modification of the mechanical stiffness of metals may reduce the risk of stress-shielding effect. Also, biocompatible or osteoconductive metallic implants would be of significant clinical value with a longer survival of the artificial joint prosthesis. Many new technologies of surface modifications for metallic joint prosthesis have been invented to obtain direct bonding between the bone and metallic prosthesis for longer survival of prostheses. As the elderly population shows a significant increase around the globe, the demand for metallic orthopedic implants to maintain their quality of life has been expanding in recent years.

Keywords Orthopedic surgery • Fracture fixation • Joint replacement • Spinal reconstruction • Bone ingrowth • Stress shielding • Implant loosening • Biocompatibility • Bone union

M. Ito (✉)
Department of Spine and Spinal Cord Disorders, National Hospital Organization Hokkaido Medical Center, 5-7-1-1 Yamanote, Nishi-ku, Sapporo 063-0005, Japan
e-mail: manabuito98@nifty.com

T. Onodera • T. Funakoshi
Department of Orthopaedic Surgery, Hokkaido University Graduate School of Medicine, Sapporo, Japan

10.1   Introduction

The use of metallic implants to fix bone fractures started more than 100 years ago. The first clinical report was in 1891 that silver wires were used for a young patient with spinal fracture at the thoracic spine [1]. The first metal plate to fix bone fracture was reported in 1895 [2]. Since then, stainless steel, cobalt-chrome (Co-Cr), and titanium alloys have been developed and used for treatment of a large variety of orthopedic disorders in humans [3–5]. Metal implants such as screws and plates for fracture fixation showed a dramatic improvement by the end of the Second World War. In recent years, metals have been used extensively for all kinds of artificial joints and internal fixators of the spine to correct spinal deformities, tumors, and degenerative disorders. The majority of current orthopedic implants are made of metals [6].

At present, many developed countries are facing a rapid increase in the elderly population. Along with this increase, the main clinical targets are switching from fractures of the extremities to degenerative diseases such as joint arthritis and osteoporosis. Orthopedic implants are increasingly contributing to allow elderly people to ambulate with healthy conditions and to improve their quality of life. Under these circumstances, there is increasing demand for artificial joints in the upper and lower extremities and spinal instrumentation surgery for osteoporotic spinal fractures and spinal deformities in the elderly.

10.2   Fracture Fixation

10.2.1   Mechanical Stiffness of Metal Implants for Bony Fusion

Metal implants are frequently used for treatment of bony fractures to stabilize the fracture sites to obtain biological bony union. The most common surgical technique to fix fractured bone is to place a metal plate over the cortex bone at the fracture site with several metallic cortical screws above and below the fracture site (Fig. 10.1).

For transverse or oblique types of fracture of long bones such as femur and humerus, an intramedullary nail or rod is inserted into the medullary canal of the fractured long bone to stabilize the fracture site (Fig. 10.2) [7–9].

For open fractures which are exposed to the air outside the body by severe soft tissue injuries over the fractures, external fixators are best indicated not only to stabilize the comminuted fracture but also to handle the risk of postoperative infection (Fig. 10.3) [10].

Another indication of an external fixator is leg length discrepancy or severe deformity of the extremities due to malunion after fractures and prolonged infection [11]. Gradual lengthening by distraction is possible by using external fixators until the final goal of lengthening is achieved.

Fig. 10.1 (**a**) Preoperative radiograph of ankle fracture. (**b**) Postoperative radiograph of plate fixation for ankle fracture

To obtain complete biological bony union, rigid stabilization at the site of the fracture should be maintained for several months. The excellent mechanical stiffness of metallic implants is beneficial to obtain biological solid union at the fracture site by providing better stability. The bony healing process at the fracture sites starts by the formation of soft immature woven bone between the gaps, which is followed by the remodeling phase with formation of rigid mature bone in which collagen fibers are perfectly aligned to provide mechanical strength to the fracture sites. Physiological mechanical stress may lead immature soft bone to develop more rigid cortical bone to sustain the load at the fracture site.

10.2.2   Stress-Shielding Effect

Since metallic implants have significantly higher mechanical properties than human cortical bones, long-term fixation by rigid metallic implants over the fracture sites would decrease mechanical stress and end up enhancing bone resorption at the bone under the metallic implants [12, 13]. This effect is called device-related osteopenia or osteoporosis by activating osteoclasts by stress-shielding effect. This stress-shielding effect should be avoided to maintain the bone quality, so the removal of

Fig. 10.2 (**a**) Preoperative radiograph of tibial shaft fracture. (**b**) Postoperative radiograph of intramedullary nail for the tibia

metallic implants is recommended especially in the weight-bearing bones after solid bony fusion is obtained at the fracture site after a certain period of time. In clinical situations, removal of metallic implants such as screws and plates over fracture sites in the upper or lower extremities is commonly performed later than postoperative 1 year. Removal of metallic implants in the extremities is pretty simple and does not require difficult surgical interventions. Many orthopedic surgeons, therefore, recommend patients for removal of metallic implants overt the fracture sites to enhance bone remodeling and solid biological fusion. Stress-shielding effect occurs not only at the extremities but also at the spinal column. Removal of metallic implants from the spine, however, often requires invasive surgical procedures for back muscles so that many spine surgeons ask patients for removal of spinal implants only when serious implant-related problems are seen.

Fig. 10.3 External fixator for fusion at the ankle joint
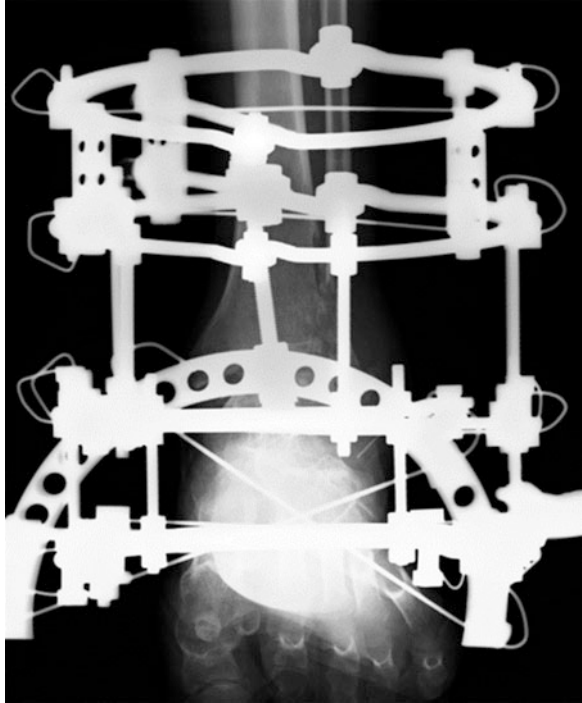
10.2.3 Biocompatibility

Though stainless steel had been the most commonly used in clinics for fracture fixation, fracture fixation devices made of titanium alloys have become most popular in recent years. Since titanium alloys have excellent biocompatibility, new bone formation can be observed over the titanium fixation devices, which makes removal of implants difficult in some patients when abundant new bone formation occurs over the implants [14]. New bone formation over stainless steel is much less than that of titanium alloys so that stainless steel devices are preferable in some patients who need removal of metallic implants long after surgery. Absorbable screws and plates made of absorbable PLLA are now clinically available to prevent stress-shielding effect in order to avoid implant removal after the initial surgery [15, 16].

10.2.4 Artifacts and Heat Production in MRI (Magnetic Resonance Image) Scan

One of the demerits of using metallic implants for orthopedic surgery is a formation of artifacts around the metallic implants on MR images, which disturb clinical assessment at the surrounding tissues (Fig. 10.4) [17].

When metal implants are placed in the spine, device-related artifacts interfere with the ability of clinicians to assess further neural disorders next to the implants. Another concern is that metallic implants may impart heat to the surrounding tissues while taking MR images (Fig. 10.5) [18].

Higher magnetic fields have a higher risk of producing significant heat affecting the surrounding soft tissue, so radiologists should be aware of this effect in patients with orthopedic metal implants.

Fig. 10.4 Metal artifact on MR image in the thoracic spine
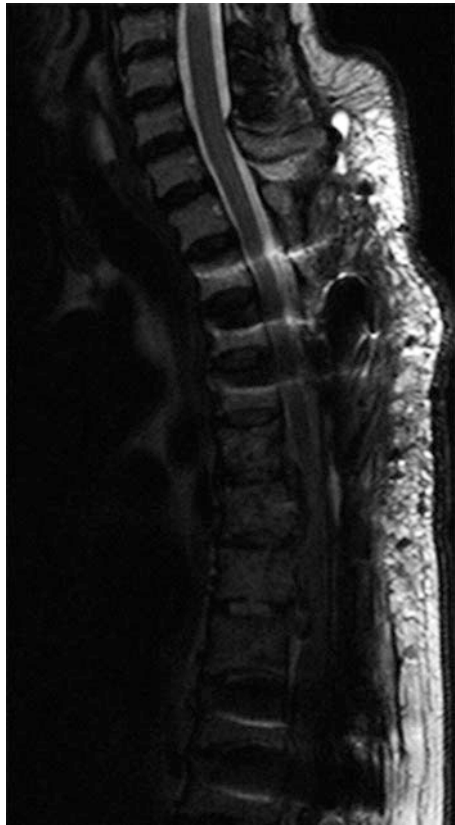
Fig. 10.5 A patient with heat production around a metallic implant during MRI scan
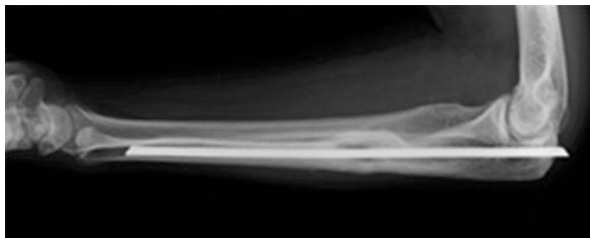
10.3 Artificial Joints

10.3.1 Indications of Joint Replacement

Artificial joints are indicated for patients with severe destruction of any joints from small finger joints to large weight-bearing joints due to trauma, osteoarthritis, or tumors. The biggest role of artificial joints is to restore the damaged joint functions to maintain the ambulatory functions of those who became unable to stand or walk with severely damaged joints. Artificial joints are now available for hip (Fig. 10.6), knee (Fig. 10.7) shoulder (Fig. 10.8), elbow, ankle (Fig. 10.9), wrist, and even fingers (Fig. 10.10).

The major sales of artificial joints in the whole world were hip and knee joints, and the value of the market in 2011 was worth $12.8 billion [19]. Due to a rapid and steady increase in the aged population, the demand for artificial joints is increasing to treat degenerative joint disorders in the elderly.

10.3.2 Total Hip Arthroplasty

The first total hip arthroplasty (THA) was invented and introduced in the 1960s by Sir Charnley, and the Charnley system is still widely used in the present orthopedic field [20, 21]. Artificial hip joints are formed by two components, corresponding to the femoral side and acetabular side. The acetabular component consists of cup and liner. The femoral component of the Charnley THA consists of a stem and head made of stainless steel and Co-Cr-Mo or Ti alloys. The acetabular component is a socket made of ultrahigh molecular weight polyethylene (UHMWPE) which is fixed to the pelvis with bone cement (polymethylmethacrylate, PMMA). Due to the friction between the cup (polymer) and femoral head (metal) under repetitive motion of the hip joints, wear debris produced at the contact area of polymer and metal would lead to osteolysis around the components and end up with loosening of the artificial joints long after the initial surgery (Fig. 10.11) [22–29].

The survival rate of the Charnley THA at postoperative 25 years was 90 % with the femoral component and 75 % of the acetabular component [29, 30]. Since many patients who underwent THA would live longer than 25 years after the first surgery,

Fig. 10.6 Postoperative
radiograph of total hip
replacement

there are increasing numbers of patients who need revision surgery due to the loosening of the prostheses in recent years. Longer survival of prosthesis function is a major clinical goal for the manufacturers of artificial joints.

10.3.3 Prosthetic Loosening

The predisposing factors of prosthesis loosening in THA are not only debris due to the friction between the acetabular and femoral components but also the dysfunction of lubrication between the two components. The amount of debris formed at the joint surface depends on the combination of the materials used for the acetabular and femoral components. The worst combination of the two components is that of a metal head and a polyethylene cup [23, 24]. Recently, combination of ceramics on ceramics and metal on metal is under investigation to establish artificial joints with less debris formation. Ceramics, however, do not have sufficient fracture toughness and may easily break under physiological loading conditions. Metal on metal would be acceptable from the mechanical point of view, but may produce metal debris in the joints. Co-Cr-Mo is now used for acetabular components and has gained

Fig. 10.7 Postoperative
radiograph of total knee
replacement

Fig. 10.8 Postoperative
radiograph of total shoulder
replacement

Fig. 10.9 Postoperative radiograph of total elbow replacement

Fig. 10.10 Pre- and postoperative radiograph of total finger joint replacement

popularity in European countries due to its wear resistance. Another attempt to improve the wear resistance of UHMWPE is gamma ray exposure followed by heat treatment, which needs further investigation to prove its long-term clinical efficacy and safety [31].

Fig. 10.11 Loosening of the acetabular component of artificial hip joint

10.3.4 PMMA and Surface Modifications

PMMA cement has been extensively used for attachment between the host bone and the femoral or acetabular components. PMMA cement has benefits to fix bone and both components within a very short period of time, but PMMA creates heat over 60° which can damage the surrounding tissues, and toxic residual monomers of PMMA are of significant clinical concern. PMMA injection to the intramedullary channel in the long bones has a great potential risk of lung or brain embolism which could cause serious life-threatening complications in the patients. In order to prevent such catastrophic complications, surface modifications of the metal and more osteoconductive materials have gained their popularity to achieve direct bonding between the host bone and the components without PMMA cement. Artificial joints without PMMA cement are called cementless systems, and those requiring very small amount of PMMA are hybrid systems [32]. One of the surface modifications to obtain better bone ingrowth into the surface of the component is plasma spray coating on Ti to create an irregular surface on the component and fine grooves for bony ingrowth to have a strong bone and metal attachment (Fig. 10.12) [33, 34].

Another attempt is to cover the metal surface with osteoconductive materials such as hydroxyapatite (HA) or apatite-wollastonite bioactive glass ceramic

Fig. 10.12 Surface
modification of the femoral
component of artificial hip
joint

(AWGC) [35, 36]. These attempts can improve the biocompatibility of metal implant to the bone, which will provide artificial joints with longer survival periods. PMMA cement is difficult to remove completely during revision surgery so that cementless or hybrid artificial joints are also beneficial to both surgeons and patients.

10.3.5 *Minimally Invasive Surgery (MIS)*

By development of surgical equipment in recent years, minimally invasive surgery (MIS) which does not require a conventional large skin incision and muscle release has become widespread in the field of orthopedic surgery. MIS enables short hospital stay and early return of patients to sport activities due to minimal damage to the muscles [37]. There will be further development of MIS for all types of joint arthroplasty in the future.

10.4 Spinal Reconstruction

10.4.1 Spinal Instrumentation Surgery

The first application of metallic implant to the spinal column was reported by Hadra in 1891 [1]. Ag wires were placed in the thoracic spine for treatment of spinal fracture. The most important historical event in the spinal reconstruction surgery was the invention of the Harrington instrumentation in 1962 [38]. Professor Paul Harrington started to use his spinal implants consisting of hooks and rods made of stainless steel for treatment of severe spinal deformity and fracture dislocations of the spine (Fig. 10.13).

Since the introduction of his device, surgeries to correct and stabilize the spine with metallic implants have shown a dramatic development, and surgeries using metal implants to correct and stabilize the spine were named spinal instrumentation surgery. The Harrington instrumentation surgery was modified by his followers by adding sublaminar wires, tapes, and pedicle screws [39]. Titanium alloys are the most popular material for recent spinal implants due to their biocompatibility and fewer metal-related artifacts in MR (magnetic resonance) images [40]. Spinal

Fig. 10.13 Pre- and postoperative radiograph of Harrington instrument for adolescent idiopathic scoliosis
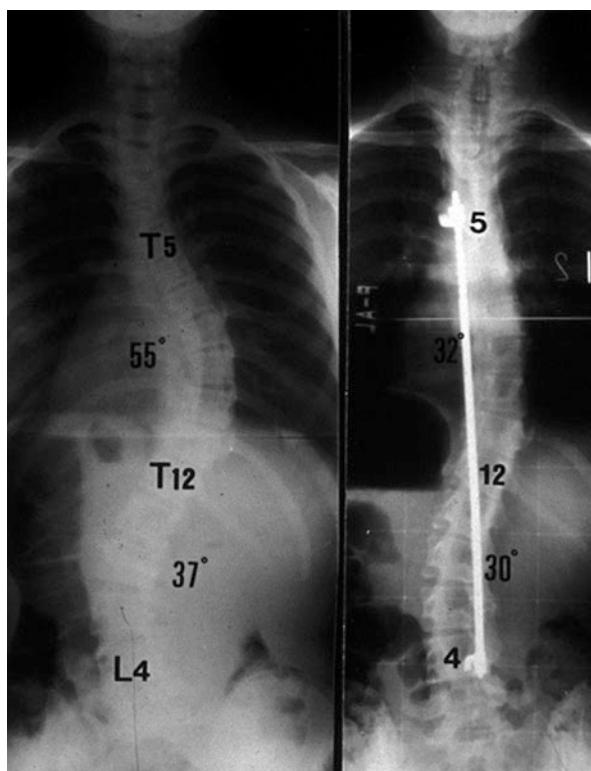
implants made of stainless steel or Co-Cr are still used especially for correction of rigid spinal deformities such as severe scoliosis and rigid kyphosis due to their superior mechanical stiffness to obtain better correction and maintain the spinal stability after surgery.

In the field of orthopedic surgery, spinal metallic implants are indispensable to correct spinal deformity and to stabilize the damaged unstable spine (spinal instability) caused by trauma, degenerative changes, and tumors. The implants maintain the stability at the site of instability until complete bony fusion is obtained. Spinal implants may be accompanied by any type of bone grafts to achieve biological bony fusion. In the early years of spinal instrumentation surgery, since spinal implants were too simple in their structures to provide the spine with sufficient stability, patients had to be bed bound for several months until complete bony fusion was established. With the development of modern spinal implants with excellent mechanical stability, patients are now able to ambulate immediately after surgery. The recent development of metallic implants for the spine has contributed to enhance the QOL (quality of life) of patients who suffer from destructive disorders of the spine and require spinal instrumentation surgery to restore and restabilize the spine. Unless biological bony fusion was obtained, fatigue failures of the metallic implants would occur at the end so that solid biological bony fusion has to be obtained at the site of metallic implants.

10.4.2   Pedicle Screw System

The most popular spinal implant is a pedicle screw system consisting of bilateral screws at the bilateral pedicles, which are connected to screws above and below with metal rods or plates (Fig. 10.14).

This system is the mechanically strongest among numerous spinal fixation systems [41]. This system can be applied from the occiput to the sacrum to correct sagittal, coronal, and rotational deformity of the spine [42–45]. Since there are large personal variations in the three-dimensional alignment of the spine, surgeons often bend rods or plates to fit the individual spinal alignment of the spine during surgery. Titanium alloys are now most commonly used for spinal implants because of their easiness to bend during surgery by surgeons' hands. However, bending a metallic rod or plate at multiple times may lead the material to plastic deformation which makes them significantly weaker mechanically. Surgeons should be familiar with the mechanical characteristics of each material used for surgery and refrain from excessive manual bending of the rods or plates to maintain the original mechanical property of each metal.
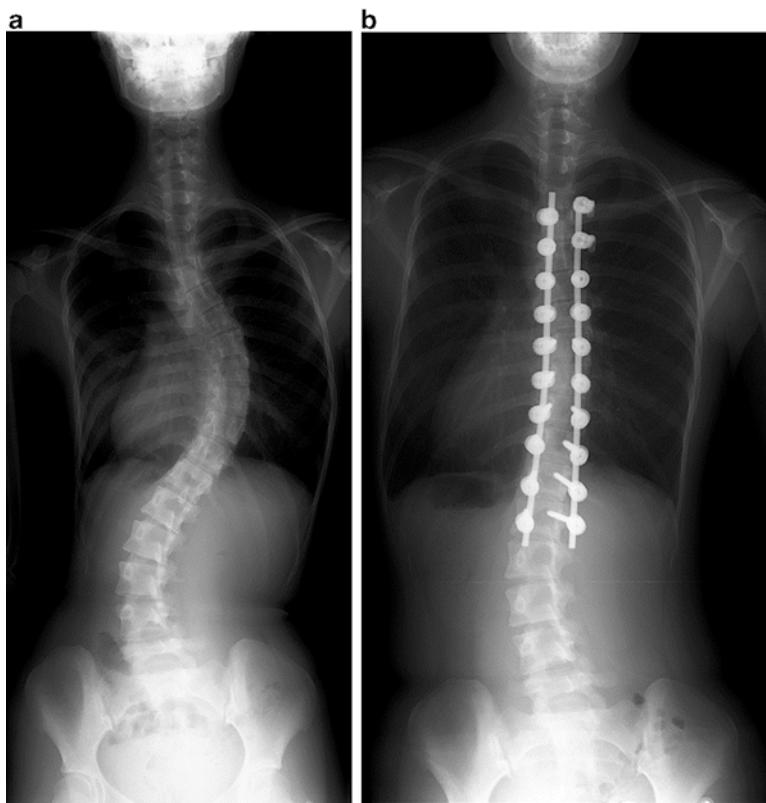
Fig. 10.14 (**a**) Preoperative radiograph of adolescent idiopathic scoliosis. (**b**) Postoperative radiograph of pedicle screw system for adolescent idiopathic scoliosis

10.4.3   Vertebral Spacers and Intervertebral Cages

Besides pedicle screws, rods, and plates, there are many other metallic implants used for spinal reconstruction surgeries. Intervertebral cages or spacers are used after resection of intervertebral disks in degenerative spinal disorders with spinal instability (Fig. 10.15).

Vertebral spacers or cages are indicated after resection of vertebral bodies in patients with severe burst fractures and spinal tumors. Autogenous, allogenic, or synthetic bone grafts are packed into the cages or spacers to obtain solid biological fusion to the adjacent vertebrae. The use of spinal cages or spacers was able to reduce the need for taking structural bone grafts from the patient's iliac bone or fibula, which significantly reduced complications related to bone graft harvest. Other materials used for cages or spacers besides metals are hydroxyapatite, PEEK, carbon fibers, and absorbable materials such as PLLA [46–48].
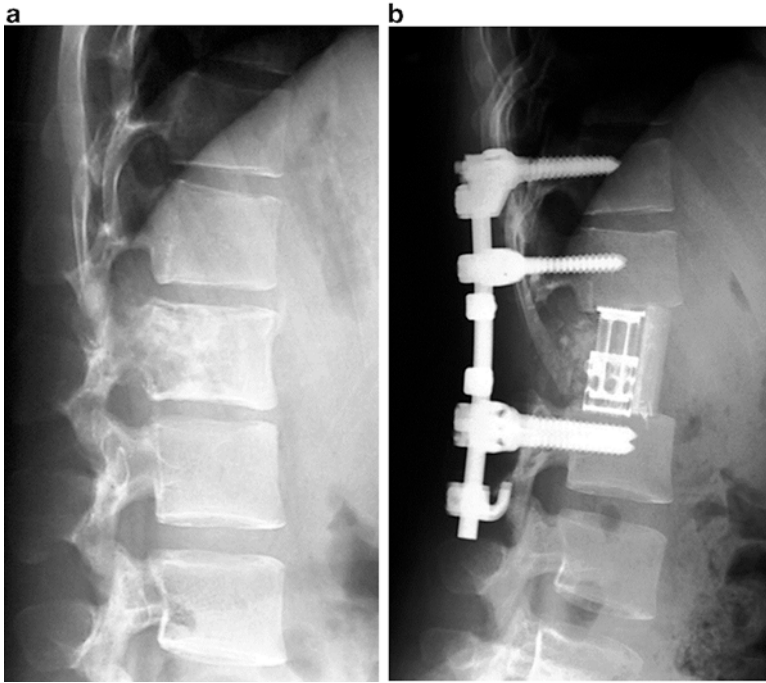
Fig. 10.15 (**a**) Preoperative radiograph of a patient with primary spinal tumor (giant cell tumor). (**b**) Postoperative radiograph of spinal reconstruction with pedicle screws and a vertebral spacer with bone grafts

Along with the increase of the aged population with osteoporosis and degenerative scoliosis with neurological complications, the clinical demand for metallic implants in spinal reconstruction surgery is increasing. Carbon or PEEK cages are becoming more popular in spinal reconstruction surgery due to their material characteristics and because they do not create artifacts on MR images, which often impede further clinical assessment.

10.4.4 Innovative Technology

Motion preservation technology including artificial intervertebral disks, artificial facet joint, and flexible rods is one of the recent trends in spinal reconstruction surgery, but the use of lumbar artificial disks are decreasing due to an increasing number of loosening or displacement of lumbar artificial disks which require revision surgery [49]. Revision surgery of lumbar artificial disks is difficult and often associated with intra- and postoperative complications. Long-term clinical studies of motion preservation technologies for treatment of various spinal disorders are needed to verify the clinical benefits of motion preservation technology.

Spinal deformity correction surgery for juvenile spinal deformity patients using expandable metallic rods is now under way to seek the best material and treatment for difficult spinal deformities in patients who are still growing [50].

10.5   Conclusions

Metallic implants have been used extensively in the field of orthopedic surgery for more than a century. Fracture fixation, joint replacement, and spinal deformity correction are the main clinical indications of using metallic implants. Due to the excellent mechanical stiffness and fatigue toughness of metals, metallic implants have made possible early ambulation and shorter hospital stay of patients. At the present time, metallic implants are indispensable for treatment of all kinds of orthopedic diseases and injuries.

In spite of their benefits of metallic implants, there are some clinical problems related to them. One is a stress-shielding effect leading to osteopenia or osteoporosis under the area of rigid metallic implants. Modification of the stiffness of metallic implants to that of human cortical bone is needed to solve this problem. Another improvement should be made in surface modifications over the metallic surface or porous metals to achieve direct bonding between the metallic implant and the host bone.

References

1. Hadra BE (1891) Wiring of the vertebrae as a means of immobilization in fracture and Pott's disease. The times and register. Medical Press, Philadelphia, pp 1–8
2. Lane WA (1895) Some remarks on the treatment of fractures. BMJ 1:861–863
3. Sherman WO (1912) Vanadium steel bone plates and screws. Surg Gynecol Obstet 14:629–634
4. Uhthoff HK et al (1981) The advantages of titanium alloy over stainless steel plates for the internal fixation of fractures: an experimental study in dogs. J Bone Joint Surg (Br) 63:427–434
5. Uhthoff HK et al (2006) Internal plate fixation of fractures. Short history and recent development. J Orthop Sci 11:118–126
6. Global Biomedical Metal Market (2013) Acmite market intelligence, Ratingen, Germany
7. Hartin NL et al (2006) Retrograde nailing versus fixed-angle blade plating for supracondylar femoral fractures. A randomized controlled trial. ANZ J Surg 76:290–294
8. Shelbourne KD, Bruckmann FR (1982) Rush-pin fixation of supracondylar and intercondylar fractures of the femur. J Bone Joint Surg Am 64:161–169
9. Sanders R et al (1989) Treatment of supracondylar-intracondylar fractures of the femur using the dynamic condylar screw. J Orthop Trauma 3:214–222
10. Arazi M et al (2001) Ilizarov external fixation for severely comminuted supracondylar and intercondylar fractures of the distal femur. J Bone Joint Surg (Br) 83:663–667

11. Paley D (1990) Problems, obstacles, and complications of limb lengthening by the Ilizarov technique. Clin Orthop 250:81–104
12. Uhthoff HK, Dubuc FL (1971) Bone structure changes in the dog under rigid internal fixation. Clin Orthop 81:165–170
13. Akeson WH et al (1976) The effects of rigidity of internal fixation plates on long bone remodeling. Acta Orthop Scand 47:241–249
14. Niinomi M (2008) Biologically and mechanically biocompatible titanium alloys. Mater Trans 49:2170–2178
15. Majola A et al (1992) Absorbable self-reinforced polylactide (SR-PLA) composite rods for fracture fixation: strength and strength retention in the bone and subcutaneous tissue of rabbits. J Mater Sci Mater Med 3:43–47
16. Van der Elst M et al (1995) Tissue reaction on PLLA versus stainless steel interlocking nails for fracture fixation: an animal study. Biomaterials 16:103–106
17. Hargreaves BA et al (2011) Metal-induced artifacts in MRI. Am J Roentgenol 197:547–555
18. MRI Safety. com. http://www.mrisafety.com/safety_article.asp?subject=44
19. Pharma report. Large joint reconstruction: global market prospects 2012–2022. http://www.visiongain.com/Report/910/Large-Joint-Reconstruction-Global-Market-Prospects-2012-2022
20. Charnley J (1961) Arthroplasty of the hip: a new operation. Lancet 1:1129
21. Charnley J (1970) Total hip replacement by low-friction arthroplasty. Clin Orthop 72:7–21
22. Tsao A et al (1993) Failure of the porous-coated anatomic prosthesis in total knee arthroplasty due to severe polyethylene wear. J Bone Joint Surg Am 75:19–26
23. Hirakawa K et al (1996) Characterization of debris adjacent to failed knee implants of 3 different designs. Clin Orthop 331:151–158
24. Sychterz CJ et al (2000) Comparison of in vivo wear between polyethylene liners articulating with ceramic and cobalt-chrome femoral heads. J Bone Joint Surg (Br) 82:948–951
25. Amstutz AC et al (1973) Knee joint replacement-development and evaluation. Clin Orthop 94:24–41
26. Parrish EF (1966) Treatment of bone tumors by total excision and replacement with massive autologous and homologous grafts. J Bone Joint Surg Am 48:969–990
27. Walldius B (1953) Arthroplasty of the knee using an acrylic prosthesis. Acta Orthop Scand 24:1
28. Long M, Rack HJ (1998) Titanium alloys in total joint replacement -a materials science perspective. Biomaterials 19:1621–1639
29. Bozic KJ et al (2005) Implant survivorship and complication rates after total knee arthroplasty with a third generation cemented system. Clin Orthop 430:117–124
30. Morgan CG et al (1991) Survivorship analysis of the uncemented porous-coated anatomic knee replacement. J Bone Joint Surg Am 73:848–857
31. Sutula LC et al (1995) The Otto Aufranc Award. Impact of gamma sterilization on clinical performance of polyethylene in the hip. Clin Orthop 319:28–40
32. Duffy GP et al (1998) Cement versus cementless fixation in total knee arthroplasty. Clin Orthop 356:66–72
33. McKellop HA et al (1999) Development of an extremely wear-resistant ultra high molecular weight polyethylene for total hip replacements. J Orthop Res 17:157–167
34. Park MS et al (2003) Plasma spray-coated Ti femoral component for cementless total hip arthroplasty. J Arthroplasty 18:626–630
35. Akizuki S et al (2003) Fixation of a hydroxyapatite-tricalcium phosphate-coated cementless knee prosthesis. Clinical and radiographic evaluation seven years after surgery. J Bone Joint Surg Br 85:1123–1127
36. Fujita H et al (2000) Evaluation of bioactive bone cement in canine total hip arthroplasty. J Biomed Mater Res 49:273–288
37. Meneghini RM et al (2006) Muscle damage during MIS total hip arthroplasty: Smith-Peterson versus posterior approach. Clin Orthop 453:293–298

38. Harrington PR (1962) Treatment of scoliosis correction and internal fixation by spinal instrumentation. J Bone Joint Surg Am 44:591
39. Takahata M et al (2007) Comparison of novel ultra-high molecular weight polyethylene tape versus conventional metal wire for sublaminar segmental fixation in the treatment of adolescent idiopathic scoliosis. J Spinal Disord Tech 20:449–455
40. Stradiotti P et al (2009) Metal-related artifacts in instrumented spine. Techniques for reducing artifacts in CT and MRI: state of the art. Eur Spine J 18(Suppl 1):102–108
41. Kothe R et al (2004) Biomechanical analysis of transpedicular screw fixation in the subaxial cervical spine. Spine 29:1969–1975
42. Suk SI et al (1995) Segmental pedicle screw fixation in the treatment of thoracic idiopathic scoliosis. Spine 20:1399–1405
43. Abumi K et al (1994) Transpedicular screw fixation for traumatic lesions of the middle and lower cervical spine. Description of the techniques and preliminary report. J Spinal Disord 7:19–28
44. Ito M et al (2010) Simultaneous double rod rotation technique in posterior instrumentation surgery for correction of adolescent idiopathic scoliosis. Technical note. J Neurosurg Spine 12:293–300
45. Salmingo R et al (2012) Corrective force analysis for scoliosis from implant rod deformation. Clin Biomech 27:545–550
46. Hojo Y et al (2005) A biomechanical and histological evaluation of a bioresorbable lumbar interbody fusion cage. Biomaterials 26:2643–2651
47. Takemoto M et al (2007) A porous bioactive titanium implant for spinal interbody fusion: an experimental study using a canine model. J Neurosurg Spine 7:435–443
48. Kato K et al (2013) Novel multilayer Ti foam with cortical bone strength and cytocompatibility. Acta Biomater 9:5802–5809
49. Tripiano P et al (2006) Lumbar total disc replacement. Surgical technique. J Bone Joint Surg Am 88(Suppl 1):50–64
50. Cheung KM et al (2012) Magnetically controlled growing rods for severe spinal curvature in young children: a prospective case series. Lancet 379:1967–1974

Chapter 11
Stents: Functions, Characteristics, and Materials

Koichi Tsuchiya and Akiko Yamamoto

Abstract In the last few decades, there has been a remarkable progress in the field of minimally invasive surgery. Such progress has been supported by the invention and development of novel medical devices, such as stents, guide wires, and filters. Stents may be one of the most important devices used for various lesions including coronary, carotid, biliary, etc. Materials used for these devices are divers, ranging from metallic materials (e.g., stainless steels, cobalt-chromium alloys, nitinol, magnesium alloys, etc.) to biodegradable polymers. This chapter introduces the functions of stents and the currently used materials, and also gives some prospect for future materials and device development.

11.1 Introduction

Over the past few decades, minimally invasive surgery has rapidly gained its popularity. Such progress has been supported by the invention and development of novel devices, such as catheters, stents, guide wires, filters, etc. Of particular importance is percutaneous transluminal coronary angioplasty (PTCA) or percutaneous coronary intervention (PCI). As compared to standard open up surgery, PCI has several advantages: minimal physical burden, shorter hospitalized period, fewer number of staffs required for an operation, and lower cost.

The pioneer of the PCI may be Werner Forssmann, who inserted a 65 cm ureteral catheter into a vein of his own arm in 1929. He then walked to X-ray room to film his body and prove that the catheter reached his right ventricle.

K. Tsuchiya (✉)
Research Center for Strategic Materials, National Institute for Materials Science,
Sengen 1-2-1, Tsukuba 305-0047, Japan
e-mail: tsuchiya.koichi@nims.go.jp

A. Yamamoto
International Center for Materials Nanoarchitectonics, National Institute for Materials Science,
Namiki 1-1, Tsukuba 305-0044, Japan
e-mail: yamamoto.akiko@nims.go.jp

The first PTCA was done by a German cardiologist Andreas Gruentzig. He succeeded to expand the lumens of narrowed arteries by balloon angioplasty in 1977. By 1990, lumen stenosis of the coronary arteries was more commonly treated by the angioplasty technique using a balloon catheter than by standard bypass surgery. But it was also recognized that about 50 % of patients suffered from recurrence of arterial clogging (restenosis) after removal of the balloon. After listening to a talk by Gruentzig in a conference, Julio Palmaz came up with an idea to put a scaffold into a vessel to hold it open and to prevent the restenosis. He co-developed a "stent" with Richard Schatz, and the developed stent was approved for a use in peripheral arteries in 1991 and for coronary in 1994 by the FDA.

After the Palmaz-Schatz stent, numerous types of stents were developed and clinically used in treatment for various lesions. In this chapter, features and characteristics of stents and material aspects of the stents are overviewed.

11.2   Structures and Functions of Stents

A stent is a mesh tube used to prevent the lumen from occlusion (blockage) or stenosis (narrowing) by various disease-induced reasons. An example of a stent and its delivery system is shown in Fig. 11.1. The delivery system is composed of a handle, a catheter, and a sheath, in which a stent is encapsulated. Stents are usually cut out from a metallic tube by precision laser cutting. The diameter of stents is typically 2–5 mm and the length is in the range of 6–30 mm for coronary. For biliary, the diameter is about 6–14 mm and the length 20–150 mm. The stent is composed of struts (frames) and markers, if necessary. Markers are made of radiopaque materials and welded on the both ends of stents.

The stents for the esophagus have a larger dimensions, 16–20 mm diameter, and are woven mesh tubes made of nitinol wires. Grafted stents, or covered stents, are also used for the esophagus.

Stents can be classified into two types depending on how they are deployed: *balloon expandable* and s*elf-expandable*. Balloon-expandable stents are most commonly used for coronary. Procedure of stenting is illustrated in Fig. 11.2. A doctor inserts a catheter through an artery from the groin, leg, or arm. X-ray angiography is used to know the location of the closure and the catheter. Contrast medium, a dye or other substances, is injected into a vein through the catheter near the area of blockage, so the blood flow through the arteries can be visualized on the monitors. The visibility of the stent under X-ray angiography is an important factor for the operation. After placing the stent, the vessel is checked with intravascular ultrasound (IVUS) or by optical coherence tomography (OCT). These devices can image the cross section of the stented vessel and are useful to check the status of the lesion area, e.g., cohesiveness of the stent to the vessel wall.

The design of stent strut varies largely depending on the producer as shown in Fig. 11.3. The complex shape of the stent is designed considering many factors, such as high hoop rigidity, ease of deployment, minimization of recoil,

Fig. 11.1 Stent for the femoral artery (Terumo, "Misago^{TM}", Reprinted from [1] under special permission from Terumo Corporation)
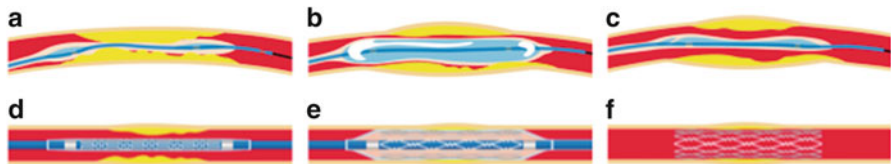
Fig. 11.2 Typical procedure for stenting. (**a**) Balloon catheter is inserted into the vessel to the site of the blockage. (**b**) Balloon is inflated to open the closed vessel. (**c**) Balloon is deflated and balloon catheter is retracted. (**d**) Catheter with a stent and balloon is inserted. (**e**) Balloon is inflated to open the stent. (**f**) Stent keeps the vessel open after the retraction of balloon and catheter

Fig. 11.3 Various designs of stent struts [2]

minimization of axial length change on deployment, uniform application of stress to the vessel wall, flexibility, conformability, and crossability. Stress concentration at both ends of the stent often causes restenosis.

Most of metallic stents are cut from a metallic tube by precision laser cutting. To minimize the internal stress introduced, annealing is applied to improve the fatigue life. In the case of self-expandable stent made of nitinol, shape-setting treatment is applied. Surface finishing of the stents is also very important. Various methods, such as mechanical polishing, blasting, horning, etching, and electropolishing, are used. Most of the stents have markers made of materials with high opacity for X-ray, e.g., platinum, gold, and tantalum, to ensure the visibility of stent position by X-ray angiography. These markers are welded to the struts near the ends of the stents. The possibility of galvanic corrosion has to be taken into consideration.

11.3   Balloon-Expandable Stents

Balloon-expandable stents are manufactured in the diameter that fits in the catheter sheath and expanded to the diameter of the blood vessel by inflating a balloon. Thus, the stents are plastically deformed. Figure 11.4 shows how the hoop stress in stents (lower part of the diagram) and in the vessel (upper part of the diagram) changes on deployment. As it is expanded from the initial diameter (4 mm in the figure), the stents experience the tensile hoop stress up to point b. As the stent touches the vessel of 7 mm diameter at point a, the vessel now experiences the tensile hoop stress which increases to point b. After deflating the balloon, the compressive hoop stress is applied to stents, and the stents recoil to the diameter of 8.25 mm, which corresponds to the diameter at which the stress on the blood vessel and that on the stent balance (point c).

A variety of metallic materials have been used for balloon-expandable stents as summarized in Table 11.1. Most widely used materials for balloon-expandable stents are 316L stainless steel and Co-Cr alloy. SUS316L is the most commonly used metallic material in the biomedical field. The formation of stable Cr_2O_3 passive film leads to better corrosion resistance. The tensile properties can be varied widely by processing conditions.

In the early 2000s, there are a number of reports on the relation between the restenosis and strut thickness of a stent. Several clinical reports [4, 5] indicated that a reduced strut thickness lowers the restenosis rates as shown in Fig. 11.5. These reports drove the demands for stronger and more rigid materials. Co-Cr alloy has a higher strength and better radiopacity than 316L. It also has good corrosion resistance, has good fatigue resistance, and is nonmagnetic. The alloy has been used for medical implants since 1937. The first stent using Co-20Cr-35Ni-10Mo was developed by Medtronic as "Driver[TM]" in 2003. This alloy was originally developed as a heat-resistant alloy known as Elgiloy[TM]. The strut thickness was reduced to 80–90 μm compared to 130–140 μm of earlier SUS316L stents.
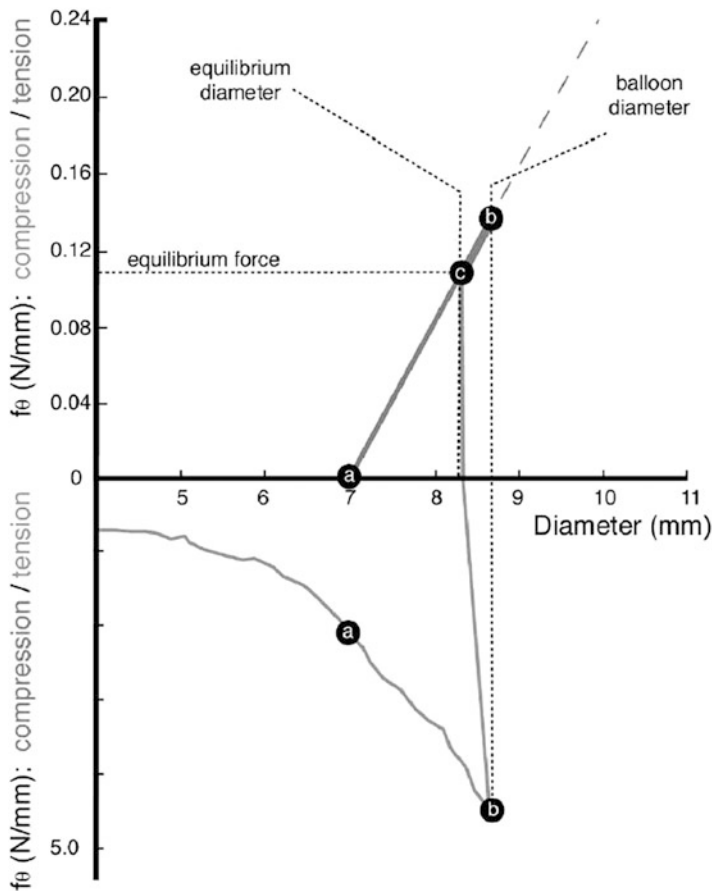
Fig. 11.4 Hoop stress of stent and vessel (Reprinted from [3], Copyright 2002, with permission from Elsevier)

Table 11.1 Metallic materials used for stents

Material	SUS316L	Ta	Co-Cr	Ti	Pt-Cr steels	Nitinol
Young's modulus (GPa)	192	61	200	100–120	191–203	50*
Yield stress (MPa)	175	200	550	310–490	460–480	~200
Tensile stress (MPa)	480	500	720	380–640	824–834	~1,000
Tensile elongation (%)	>40	>60	3	10–20	43.0–44.8	~10
Radiopacity	Normal	Very good	Good	Poor	Very good	Good

Strong demands for materials with a higher strength, rigidity, and radiopacity led to a new alloy specifically designed for coronary stents. Boston Scientific developed Pt-Cr steel, Fe – (32.5–33.5 wt%)Pt – (17.5–18.5 wt%)Cr – (2.43–2.83 wt%) Ni [6, 7]. To attain higher radiopacity, a part of Fe and Ni was substituted by Pt.
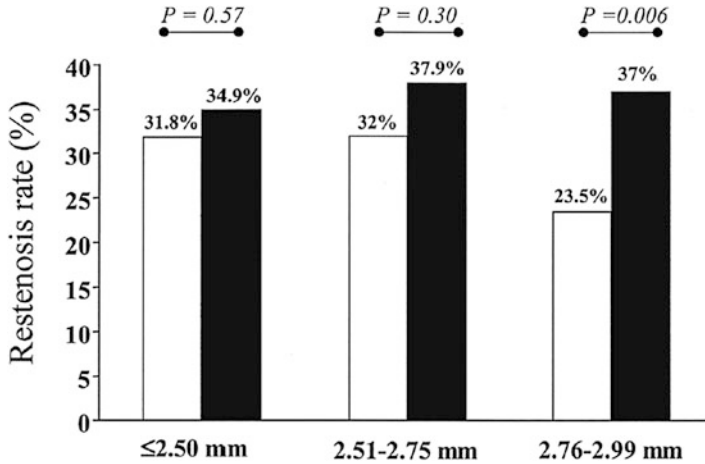
Fig. 11.5 Restenosis rates in lesions treated with a stent with a strut thickness of < 0.10 mm (thin group; open bars) and a stent with a strut thickness ≥ 0.10 mm (thick group; solid bars), according to the reference vessel diameter (≤ 2.50, 2.51–2.75 and 2.76–2.99 mm) (Reprinted from [4], Copyright 2002, with permission from Elsevier)

The amount of Pt was designed to give a good balance between strength, ductility, and radiopacity. The alloy was used for OMEGA^{TM} stents which have a strut thickness of 81 μm and width of 91 μm.

11.4 Self-Expandable Stents

Self-expandable stents are manufactured to be the size of vessel diameter, or slightly larger, and are crimped and constrained in a sheath on a tip of catheter. When it is delivered to the intended site, the sheath is retracted and the stent deploys by itself. Most often, this self-deployment is achieved by superelasticity of shape memory alloy as shown in Fig. 11.6 [8]. Nitinol (TiNi alloy) is almost the only material used for self-expandable stents, due to its superior superelastic properties, good corrosion resistance, and biocompatibility. The basic aspect of nitinol and superelasticity can be found in Chap. 10 or elsewhere [9]. Superelasticity is a kind of pseudoelasticity induced by stress-induced martensitic transformation. As shown in Fig. 11.6, the stress-strain curve is characterized by a stress plateau and large hysteresis. A superelastic stent is in the parent phase when in an unconstrained condition and in the martensite phase when constrained, i.e., inside the sheath. A nitinol stent takes an advantage of the stress plateau and hysteresis. The stents can apply relatively gentle force corresponding to a lower stress plateau to the vessel wall for an extended range of strain. Meanwhile, when an external force is applied to deform or buckle the deployed stent, it resists with the higher stress corresponding to the upper plateau stress. This can be an advantage for the stent
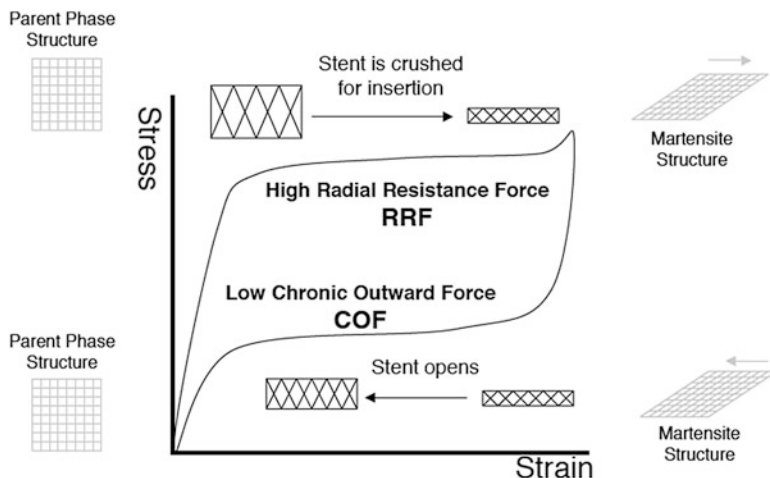
Fig. 11.6 The radial resistive force and chronic outward force as a function of the superelastic hysteresis loop (Reprinted from [8], Copyright 2004, with permission from Elsevier)

which often experiences severe bending or flattering, and thus, the self-expanding stents are most widely used in peripheral as well as biliary arteries. Biliary stents require maneuverability through loops, curvatures, and angulated anatomies and thus high flexibility. A self-expandable stent is also important for carotid and neurovascular vessels since a balloon-expandable stent cannot be used because of a high pressure required for the expansion, which may damage the thin wall of the brain vessels.

11.5 Drug-Eluting Stents (DES)

For bare-metal coronary stents, a clinical report indicated about 20 % of cases ended in restenosis and thrombosis that arise most typically ~30 days after stenting [10]. To minimize this reaction, most of the current coronary stents are drug-eluting stents (DES). The surface of a metallic stent is coated with non-degradable/degradable polymers containing an immunosuppressant or anticancer drug. The first-generation DESs were "Cypher" by Johnson & Johnson and "Taxus" by Boston Scientific. Both used 316L stent as a platform. Most of the second-generation DESs use Co-Cr (Abbott "Xience," Medtronic "Resolute Integrity") or Pt-Cr (Boston Scientific "Promus") stents as the platform. The use of thin strut stents leads to early reendothelialization and is an advantage also for DES [10].

11.6   Bioabsorbable Stents

11.6.1   Emergence of the Research and Development
for Bioabsorbable Stents

As described in the previous sections, metallic stents were incorporated into the cardiovascular intervention to give a mechanical support for vessel wall dissections, elastic recoil, and constrictive remodeling of the target lesion after the dilatation of a narrowed artery by a balloon catheter. However, there is still the problem of an in-stent restenosis by neointimal hyperplasia, which is an overgrowth of endothelial and/or smooth muscle cells. The causes of this overgrowth are considered as a physical damage of dilatation, a foreign-body reaction against a metallic stent, and a mechanical stimulation by the stent due to the difference in mechanical properties between the stent and the artery. To solve this problem pharmaceutically, a drug-eluting stent is introduced, which successfully reduced the ratio of in-stent restenosis as between 4 and 15 % [11], but it also caused late and very late stent thrombosis since the stent strut is not covered by the neointima which possibly causes strut malapposition. Therefore, patients should keep taking an antiplatelet drug for a long time such as over a year, which leads to a high risk of hemorrhage and precludes any kind of operation to treat other symptoms. This lack of endothelialization is not observed on the previous bare-metal stents and severely influences the patient's remaining time and quality of life.

As the next generation of cardiovascular intervention, the research and development of bioabsorbable stents, or bioresorbable scaffolds, was started at the end of the twentieth century; the first clinical study of a biodegradable polymer stent was performed in Japan in 1998 [12]. After that, various attempts were made to satisfy the requirement for a bioabsorbable stent, which can dilate the narrowed artery; can support vascular dissections; can prevent elastic recoil, constructive remodeling, and neointimal overgrowth; and, finally, can disappear after a certain period of time, that is, when the physiological remodeling of the target lesion is achieved. The disappearance of the stent will be beneficial not only to avoid the prolonged inflammation at the implanted site causing neointimal hyperplasia but also to enable easy access to the downstream of the artery for another catheter intervention. Another benefit of bioabsorbable stents is the application to infants or children with rapid growth changing the size of organs and blood vessels.

As materials for bioabsorbable stents, not only biodegradable polymers such as poly-L-lactic acids and its copolymers but also metals such as magnesium alloys, iron-based alloys, and pure zinc are now under investigation. Some of them are under clinical studies (see Table 11.2), and no metallic stents but only two types of polymeric stents are available in the market [13]. In the rest of this section, the recent development of these metallic and polymeric stents will be briefly introduced.

Table 11.2 Clinical results of bioabsorbable stents [13, 43]

Name	Material	Drug elution	Total strut thickness (μm)[a]	Stent coverage (%)	LLL at 6 months (mm)	TLR rate at 1 year (%)
AMS®-1	WE43	−	165	10	1.08 ± 0.49 (at 4 months)	45 %
DREAMS®1	WE43	+	125		0.64 ± 0.50	9.1 % (at 6 months)
Igaki-Tamai®	PLLA	−	170	24	0.91 ± 0.69	
Absorb®1.0	PLLA	−	156	25	0.43 ± 0.37	0 %
Absorb®1.1	PLLA	+	156	25	0.19 ± 0.18	3.6 %
REVA®	Polymer[b]	−	200	55	1.46 ± 0.71	67 %
DESolve®	Polymer[c]	+	200	65	0.21 ± 0.34 or 0.19 ± 0.19[d]	

[a]Including coating
[b]Poly-tyrosine-derived polycarbonate
[c]Salicylate-derived polymer
[d]Two types of drugs are coated separately

11.6.2 Magnesium Alloy

Magnesium and its alloys are one of the candidates for bioabsorbable metals since magnesium is easily corroded by reacting with water in the body fluid. Furthermore, magnesium is an essential element for the human being, and its concentration in an adult human is the fourth highest among all metallic elements, following sodium, potassium, and calcium. Therefore, the acceptable upper limit of released ion concentration is expected to be high, suggesting low possibility of toxic reaction due to the released Mg^{2+} ions. Because of its high specific strength and Young's modulus, which is closer to that of human cortical bone, Mg alloys first applied to the orthopedic field. In 2003, however, a first magnesium stent made with AE21 (Mg-2wt.%Al-1wt.%RE, RE: mixture of rare earth element) was implanted into a porcine artery, and its endothelialization was confirmed at day 35 [14]. Further investigation with swine or minipig models revealed less neointimal formation of magnesium alloy stents made with WE43(Mg-4wt%Y-3wt%RE)-based alloy than that of 316L stainless steel bare-metal stents [15, 16]. After 3 months of implantation into swine arteries, the disappearance of the WE43-based alloy stent was confirmed (see Fig. 11.7) [17]. A preclinical study of AZ31(Mg-3wt.%Al-1wt.% Zn) alloy stent was also performed with rabbit aorta model, reporting that the non-polymer-coated, phosphorized AZ31 stent disappeared around 105 days[18].

Several clinical studies were already reported for the WE43-based alloy stent. At the first clinical study performed in 2004, 23 stents were implanted into the ischemic lower limb of 20 patients [19–21], reporting no acute toxic reaction due to the magnesium stent implantation, and the stents degraded within 6 weeks [19–21]. The safety of the WE43-based stent was also confirmed by the clinical cases with preterm and newborn infants [22, 23]. Further investigation to the coronary arteries was carried out for 63 patients with 71 stents and resulted in 45 % of target lesion revascularization (TLR) at 12 months after operation, which is higher than those of current bare-metal stents (28 %) or DES (6 %) [24]. The implanted WE43-based stents were considered to be degraded within 4 months [24]. These studies suggested the lack of the duration maintaining stent integrity; in other words, the degradation rate of employed stents is too fast for this application. Supposing the cross section of a stent strut as $150 \times 150 \ \mu m^2$ and the degradation period as 1 year, the estimated corrosion rate is about 75 μm/year. This is not the easy value to achieve by conventional magnesium alloys. These clinical studies also revealed lower risk of late thrombosis which is an issue for recent drug-eluting stents.

Aiming to improve the duration of maintaining mechanical integrity at the coronary artery and to reduce the ratio of the patients with revascularization, a polymer-coating drug-eluting WE43-based stent is prepared and investigated with a porcine coronary model. In this study, the degradation rate of the stent after 28 days of implantation is 0.036–0.072 mg/cm$^2 \cdot$d (=72–144 μm/year) and the stent disappeared within 6 months [25]. The clinical study of this drug-eluting magnesium stent found that the late lumen loss (LLL) at 12 months postoperation successfully reduced to 0.52 ± 0.39 mm from 1.08 ± 0.49 mm of the non-coated
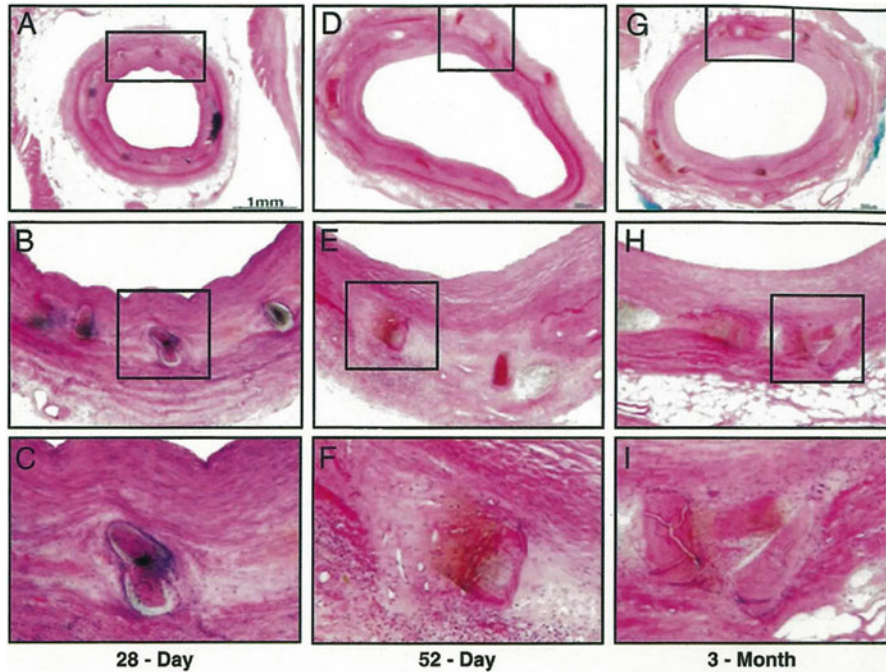
Fig. 11.7 Histology of porcine coronary arteries implanted with WE43-based stents (AMS-1) for 28 days (A, B, C), 52 days (D, E, F), and 3 months (G, H, I) (Reprinted from Ref. [17], Copyright 2008 with permission from Elsevier)

magnesium stent [26, 27]. However, this value is not close to that of a biodegradable polymer stent, Absorb1.1, that is, 0.27 ± 0.32 mm at 12 months postoperation [13]. Therefore, modification of WE43-based magnesium drug-eluting stent is attempted on the following points: increasing the strut thickness to 150 µm, attaching tantalum radiopaque markers at both ends, increasing the number of strut crowns per stent length, changing the drug and the biodegradable polymer, and increasing the coating thickness (see Fig. 11.8) [27]. This new version of biodegradable WE43-based magnesium stent is now under clinical study as the BIOSOLVE-II trial.

To satisfy the requirement in the degradation rate of magnesium alloy stents, development of new magnesium alloys, microstructure controlling processes, and coating/surface modification technologies are carried out by various research groups, which are well described in other review articles [28–30]. Most of these researches are still at a laboratory level, not at clinical nor preclinical level yet.

Since magnesium alloys generally take a hexagonal closed-packed system having a few slip planes available at room temperature, plastic working of magnesium alloys requires heating around 573 K (=300 °C). The melting point of pure magnesium is relatively low at 923 K (=650 °C), suggesting heating susceptibility of the microstructure. A laser cutting process of a stent strut from a thin tube may
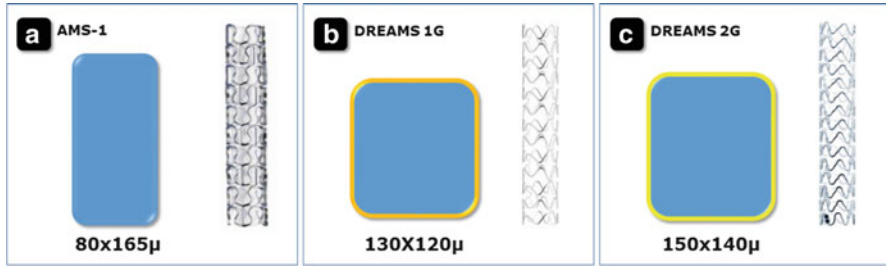
Fig. 11.8 Schematic cross-sectional profiles of WE43-based stent struts of AMS-1 (**a**), drug-eluting absorbable metal scaffold, DREAMS 1st generation (**b**), and DREAMS 2nd generation (**c**). The poly(lactide-co-glycolide) coating with paclitaxel is shown as a thin orange layer in (**b**), whereas the polylactide coating with sirolimus is shown in thin yellow layer in (**c**) [27]

locally influence alloy microstructure. Technological development of fabrication processes is also important for the success of magnesium alloy stents.

11.6.3 Iron and Its alloy

Iron is another candidate for bioabsorbable metals since it is an essential element for the human being, expecting relatively low toxicity, and it also has relatively low corrosion resistance in the biological environment. Because of the relatively low mechanical properties and too fast degradation of magnesium alloys, stent application of pure iron and iron-based alloys attracted several groups of researchers, but no clinical study is reported yet.

First preclinical investigation of pure iron stent was carried out by a rabbit aorta model in 2001 [31], followed by a porcine artery model [32, 33]. At 18 months postoperation in a rabbit model, the exact degradation rate of iron stent was too difficult to assess even though brownish corrosion products were observed surrounding the stent strut with macrophages as a sign of mild local inflammation [31]. The colorization of the tissue surrounding stent struts was also observed in porcine cases, starting at 14 days of implantation and longer (see Fig. 11.9) [32, 33]. The excretion of the corrosion products by the reticuloendothelial system was observed after 1 month postoperation, showing small amounts of macrophages containing corrosion products in the lymph nodes near the implantation site [33]. After 3-month implantation, focal accumulation of the corrosion products was observed in the spleen, as well as macrophages containing irons in the lymphatic pathways along the aorta [33]. However, no sign of significant iron overload was reported [31, 33], since the implanted amount of iron is small as several tens of micrograms, which is much lower than the overload level for a whole animal.

Stent integrity was maintained to the end of the follow-up period as it was hardly degraded during 12–18 months [31, 33]. Complete endothelialization was
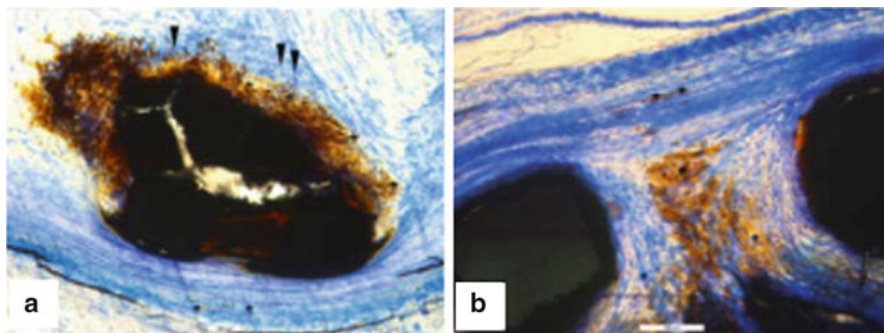
Fig. 11.9 Histology of iron stent struts after implantation of 180 (**a**) and 360 (**b**) days into porcine aorta (Reprinted from Ref. [33], Copyright 2006, with permission from Elsevier)

observed, resulting in no obvious thrombogenesis [31–33]. The angiographic results revealed no significant difference between the 316L and Co-Cr alloy control stents [31–33]. These studies suggests that the excretion of corrosion products around the struts may cause a local, prolonged inflammation even though the amount of corrosion products is very low to cause any overdose reaction at a specific organ. It is also suggested that the degradation rate of pure iron stent is too low for a coronary stent, which is ideal to disappear in 12–24 months after implantation even though there is still a discussion about an optimal degradation period and mechanical integrity duration among researchers [29].

To shorten the degradation period of the iron stent, vacuum plasma nitriding was employed to prepare a stent with thinner (70 μm) strut [34]. Implantation into mini-pig up to 28 days reported no significant difference in the endothelialization ratio, vascular histomorphometry, and other histological observations [34] as similar to the previous in vivo studies. However, no information about the degradation of the iron stent was reported due to the short (28 days) follow-up period.

Other approaches to reduce the degradation period of iron stent are microstructure control such as equal channel angular pressure (ECAP) technique [35] or electroforming [36] and alloying. Fe-Mn alloys are mainly investigated [37–39].

11.6.4 Zinc

To achieve an ideal degradation rate for a bioabsorbable coronary stent that is lower than magnesium alloys but higher than pure iron, application of pure zinc is attempted. Zinc is also an essential element for the human being, but the concentration of zinc in the human blood plasma is 12–18 μM (=0.8–1.2 mg/L), which is much smaller than that of magnesium (0.5–1 mM = 12–24 mg/L) [40]. The concentration of zinc in blood plasma of a patient with zinc overdose symptom is reported as 31.5–640 μM (=2.1–42 mg/L), whose lower value is much smaller than

that of magnesium as > 2.5 mM (>60.8 mg/L) as well [41]. These data indicate that the acceptable range of the zinc concentration in blood plasma is not so wide, suggesting that the implantation of zinc as a larger device is probably not recommended. Since a coronary stent prepared from pure zinc probably has a weight of only around 50 mg, an assumption of degrading by 12 months gives the daily release about 0.14 mg/day, which is below the plasma concentration in the overdose case.

An in vivo study implanting a pure zinc wire into a rat abdominal aorta reported that the initial degradation rate at 1.5 months was less than 20 μm/year [42]. After 4 months of implantation, the cross-sectional area of the implanted wire reduced to about 70 % of that of the initial condition, with no obvious sign of tissue necrosis or repulsion [42]. However, the tensile strength of pure zinc is ~120 MPa [42], suggesting the necessity of alloying and microstructure modification to improve the mechanical properties while maintaining its "favorable" degradation rate.

11.6.5 Biodegradable Polymers

To date, the most successful bioabsorbable stent is prepared with semi-crystalline poly-L-lactic acid (PLLA) coated with poly(D,L-lactic acid) containing an antiproliferative drug (everolimus) [13]. The stent design is in-phase hoops with straight links to each other with platinum markers, maintaining radial support for 6 months and disappearing within 2 years [33]. Clinical studies of the latest version of this stent reported LLL at 6 and 12 months postoperation as 0.19 ± 0.18 mm and 0.27 ± 0.32 mm, respectively [13]. Other clinical parameters such as TLR rate are also comparable to those of the latest, most popular drug-eluting stents [13]. However, the lower mechanical properties of bioabsorbable polymer stents than those of conventional metallic stents restrict their stent design, especially strut thickness, and thus reduce their deliverability and applicable clinical conditions. Therefore, clinical studies in a larger scale and wider application are in progress as the ABSORB II and the ABSORB EXTEND, as well as worldwide evaluation programs in Asia, Africa, and Australia.

Another stent available in the market has a similar structure, a PLLA-based stent containing two novel antiproliferative drugs (Novolimus and Myolimus), designed to have out-of-phase hoops with straight links and to disappear within 2–3 years [13]. Small-scale clinical studies also reported LLL at 6 months as 0.19 ± 0.19 mm for Novolimus and 0.21 ± 0.34 mm for Myolimus [13]. The endothelialization ratio at 6 months is 98.7~98.8 % for both drugs [13].

Among several developments of a polymer-based bioabsorbable stent in progress, a few have unique strategies to conquer some drawbacks of PLLA-based bioabsorbable stents. One of them employs poly-tyrosine-derived polycarbonate polymer containing iodine to be radiopaque with a tubular "slide-and-lock" design [43]. Another uses poly(anhydride-ester) based on salicylic acid and adipic acid anhydride, having a tubular design with laser-cut voids [13]. The features of these

stent designs are relatively high coverage of artery as 55–65 %, whereas those of conventional metallic stents and successful PLLA ones are about 10 % and 25 %, respectively [33]. This high coverage enables to increase the mechanical integrity and drug dose, as well as to reduce dissected area of artery and penetration of loose plaque. However, small-scale clinical studies for these stents resulted in high TLR rate at 12 months of about 67 % for the poly-tyrosine-based stent [43] or increased neointimal formation for the poly-salicylate-based stent [13], forcing redesigning of both stents.

11.7 Summary and Perspective

In this chapter, functions and characteristics of stents and materials used for the stents were overviewed. The current status of research and development on biodegradable stents, the next generation of vascular intervention, was also reviewed. A key issue for the success of metal-based bioabsorbable stents is to achieve a clinical result comparable to the polymer-based stents with a similar level of mechanical support to conventional metallic stents. The trend of miniaturization of the stents, i.e., thinner struts, smaller area, and smaller diameter in a crimped state, will continue in the future since it is beneficial for faster remodeling of vessel walls and better maneuverability on delivery. This trend requires materials with even higher strength, higher rigidity, and higher radiopacity. One possible method to achieve higher strength may be microstructure refinement by severe plastic deformation. There are extensive researches going on about this subject, and a number of results were reported in the application to artificial joints or orthodontic wires, but applications to vascular indwelling devices are scarcely seen [44]. Ultrafine grains or nanograins may also be beneficial to improve the corrosion resistance. Microstructure control can influence cellular response to metal surface via protein adsorption behavior [45, 46]. Rigidity or elastic modulus as well as radioopacity is an "element-dependent" property, and it is difficult to control by microstructures. One interesting exemption is nitinol, in which nanograins or even amorphous phase can be easily obtained by plastic deformation. Increase in Young's modulus was reported in severely cold-drawn wires [47] or SMAT (surface mechanical attrition)-treated samples [48]. But this is a special case; composite or hybrid materials approach may be necessary to obtain high-modulus materials.

References

1. http://www.terumo.co.jp/medical/equipment/me240.html
2. Baskot BG (ed) (2013) What should we know about prevented, diagnostic, and interventional therapy in coronary artery disease. Intech (Open access book available at http://www.intechopen.com/books/)

3. Duerig TW, Wholey MA (2002) Comparison of balloon- and self-expanding stents. Minim Invas Ther Allied Technol 11:173–178

4. Briguori C, Sarais C, PagnottaP LF, Montorfano M, Chieffo A, Sgura F, Corvaja N, Albiero R, Stankovic G, Toutoutzas C, Bonizzoni E, Di Mario C, Colombo A (2002) In-stent restenosis in small coronary arteries. J Am Coll Cardiol 40:403–409

5. Pache J, Kastrati A, Mehilli J, Schuhlen H, Dotzer F, Hausleiter J, Fleckenstein M, Neumann F-J, Sattelberger U, Schmitt C, Muller M, Dirschinger J, Shomig A (2003) Intracoronary stenting and angiographic results: strut thickness effect on restenosis outcome (ISAR-STE-REO-2) trial. J Am Coll Cardiol 41:1283–1288

6. O'Brien BJ, Stinson JS, Larsen SR, Eppihimer MJ, Carroll WM (2010) A platinum-chromium steel for cardiovascular stents. Biomaterials 31:3755–3761

7. Allocco DJ, Jacoski MV, Huibregste B, Mickley T, Dawkins KD (2011) Platinum chromium stent series. Interv Cardiol 6:134–141

8. Morgan NB (2004) Medical shape memory alloy applications – the market and its products. Mater Sci Eng A378:16–23

9. Yamauchi K, Ohkata I, Tsuchiya K, Miyazaki S (2011) Shape memory and superelastic alloys. Woodhead Publishing, Cambridge

10. Suzuki T (2014) Present and future requirements for materials in cardiovascular intervention. Materia Jpn 53:148–152

11. Erne P, Svhirt M, Resink TJ (2006) The road to bioabsorbable stents: reaching clinical reality? Cardiovasc Interv Radiol 29:11–16

12. Tamai H, Igaki K, Kyo E, Kosuga K, Kawashima A, Matsui S, Komori H, Tsuji T, Motohara S, Uehata H (2000) Initial and 6-month results of biodegradable poly-l-lactic acid coronary stents in humans. Circulation 102:399–404

13. Campos CAM, Zhang YJ, Bourantas CV, Muramatsu T, Garcia-Garcia HM, Lemos PA, Iqbal J, Onuma Y, Serruys PW (2013) Bioresorbable vascular scaffolds in the clinical setting. Interv Cardiol 5:639–646

14. Heublein B, Rohde R, Kaese V, Niemeyer M, Hartung W, Haverich A (2003) Biocorrosion of magnesium alloys: a new principle in cardiovascular implant technology? Heart 89:651–656

15. Waksman R, Pakala R, Kuchulakanti PK, Baffour R, Hellinga D, Seabron R, Tio FO, Wittchow E, Hartwig S, Harder C, Rohde R, Heublein B, Andreae A, Waldmann KH, Haverich A (2006) Safety and efficacy of bioabsorbable magnesium alloy stents in porcine coronary arteries. Catheter Cardiovasc Interv 68:607–617

16. Loos A, Rohde R, Haverich A, Barlach S (2007) In vitro and in vivo biocompatibility testing of absorbable metal stents. Macromol Symp 253:103–108

17. Slottow TLP, Pakala R, Okabe T, Hellinga D, Lovec RJ, Tio FO, Bui AB, Waksman R (2008) Optical coherence tomography and intravascular ultrasound imaging of bioabsorbable magnesium stent degradation in porcine coronary arteries. Cardiovasc Revasc Med 9:248–254

18. Li H, Zhong H, Xu K, Yang K, Liu J, Zhang B, Zheng F, Xia Y, Tan L, Hong D (2011) Enhanced efficacy of sirolimus-eluting bioabsorbable magnesium alloy stents in the prevention of restenosis. J Endovasc Ther 18:407–415

19. Mario H, Griffiths CD, Goktekin O, Peeters N, Verbist J, Bosiers M, Deloose K, Heublein B, Rohde R, Kasese V, Ilsley C, Erbel R (2004) Drug-eluting bioabsorbable magnesium stent. J Interv Cardiol 17:391–395

20. Peeters P, Bosiers M, Verbis J, Deloose K, Heublein B (2005) Preliminary results after application of absorbable metal stents in patients with critical limb ischemia. J Endovasc Ther 12:1–5

21. Bosiers M, Deloose K, Verbist J, Peeters P (2006) Will absorbable metal stent technology change our practice? J Cardiovasc Surg 47:393–397

22. Zartner P, Cesnjevar R, Singer H, Weyand M (2005) First successful implantation of a biodegradable metal stent into the left pulmonary artery of a preterm baby. Catheter Cardiovasc Interv 66:590–594

23. Schranz D, Zartner P, Michel-Behnke I, Akintürk H (2006) Bioabsorbable metal stents for percutaneous treatment of critical recoarctation of the aorta in a newborn. Catheter Cardiovasc Interv 67:671–673
24. Erbel R, Mario CD, Bartunek J, Bonnier J, de Bruyne B, Eberli FR, Erne P, Haude M, Heublein B, Horrigan M, Ilsley C, Böse D, Koolen J, Lüscher TF, Weissman N, Waksman R (2007) Temporary scaffolding of coronary arteries with bioabsorbable magnesium stents: a prospective, non-randomized multicentre trial. Lancet 369:1869–1875
25. Wittchow E, Adden N, Riedmüller J, Savard C, Waksman R, Braune M (2013) Bioresorbable drug-eluting magnesium alloy scaffold: design and feasibility in a porcine coronary model. Eurointervention 8:1441–1450
26. Haude M, Erbel R, Erne P, Verheye S, Degen H, Böse D, Vermeersch P, Wijnbergen I, Weissman N, Prati F, Waksman R, Koolen J (2013) Safety and performance of the drug-eluting absorbable metal scaffold (DREAMS) in patients with de-novo coronary lesions: 12 month results of the prospective, multicentre, fist-in-man BIOSOLVE-I trial. Lancet 381:836–844
27. Campos CM, Muramatsu T, Iqbal J, Zhang YJ, Onuma Y, Garcia-Garcia HM, Haude M, Lemos PA, Warnack B, Serruys PW (2013) Bioresorbable drug-eluting magnesium-alloy scaffold for treatment of coronary artery disease. Int J Mol Sci 14:24492–24500
28. Li N, Zheng Y (2013) Novel magnesium alloys developed for biomedical application: a review. J Mater Sci Technol 29:489–502
29. Moravej M, Mantovani D (2011) Biodegradable metals for cardiovascular stent application: interests and new opportunities. Int J Mol Sci 12:4250–4270
30. Wang J, Tang J, Zhang P, Li Y, Wang J, Lai Y, Qin L (2012) Surface modification of magnesium alloys developed for bioabsorbable orthopedic implants: a general review. J Biomed Mater Res 100B:1691–1701
31. Peuster M, Wohlsein P, Brügmann M, Ehlerding M, Seidler K, Fink C, Brauer H, Fischer A, Hausdorf G (2001) A novel approach to temporary stenting: degradable cardiovascular stents produced from corrodible metal–results 6–18 months after implantation into New Zealand white rabbits. Heart 86:563–569
32. Waskman R, Pakala R, Baffour R, Seabron R, Hellinga D, Tio FO (2008) Short-term effect of biocorrodible iron stents in porcine coronary arteries. J Interv Cardiol 21:15–20
33. Peuster M, Hesse C, Schloo T, Fink C, Beerbaum P, von Schnakenburg C (2006) Long-term biocompatibility of a corrodible peripheral iron stent in the porcine descending aorta. Biomaterials 27:4955–4962
34. Wu C, Qiu H, Hu X, Ruan Y, Tian Y, Chu Y, Xu X, Xu L, Tang Y, Gao R (2013) Short-term safety and efficacy of the biodegradable ion stent in mini-swine coronary arteries. Chin Med J 126:4752–4757
35. Nie F, Zheng Y, Wei S, Hu C, Yang G (2010) In vitro corrosion, cytotoxicity and hemocompatibility of bulk nanocrystalline pure iron. Biomed Mater 5:065015
36. Moravej M, Purnama A, Fiset M, Couet J, Mantovani D (2010) Electroformed pure iron as a new biomaterial for degradable stents: in vitro degradation and preliminary cell viability studies. Acta Biomater 6:1843–1851
37. Hermawan H, Dube D, Mantovani D (2010) Degradable metallic biomaterials: design and development of Fe-Mn alloys for stents. J Biomed Mater Res 93A:1–11
38. Schinhammer M, Hanzi AC, Loffler JF, Uggowitzer PJ (2010) Design strategy for biodegradable Fe-based alloys for medical applications. Acta Biomater 6:1705–1713
39. Liu B, Zheng Y, Ruan L (2010) In vitro investigation of Fe30Mn6Si shape memory alloy as potential biodegradable metallic material. Mater Lett 65:504–543
40. Haraguchi H (2005) Seimei to kinzoku no sekai (The world of life and metals), Foundation for the Promotion of the Open University of Japan, Tokyo, p 273 (in Japanese)
41. Suzuki T, Wada O (eds) (1994) Mineral, biryo-genso no eiyougaku (Nutritional Science of minerals and trace elements). Dai-ichi shuppan, Tokyo

42. Bowen PK, Drelich J, Goldman J (2013) Zinc exhibits ideal physiological corrosion behavior for bioabsorbable stents. Adv Mater 25:2577–2582
43. Serruys PW, Garcia-Garcia HM, Onuma Y (2012) From metallic cages to transient bioresorbable scaffolds: change in paradigm of coronary revascularization in the upcoming decade? Eur Heart J 33:16–25
44. Ge Q, Dellasega D, Demir AG, Vedani M (2013) The procession of ultrafine-grained Mg tubes for biodegradable stents. Acta Biomater 9:8604–8610
45. Shri DNA, Tsuchiya K, Yamamoto A (2014) Effect of high-pressure torsion deformation on surface properties and biocompatibility of Ti-50.0 mol.%Ni alloys. Biointerphases 9:029007
46. Shri DNA, Tsuchiya K, Yamamoto A (2014) Cytocompatibility evaluation and surface characterization of TiNi deformed by high-pressure torsion. Mater Sci Eng C 43(2014):411–417
47. Tsuchiya K, Hada Y, Ohnuma M, Namajima K, Koike T, Todaka Y, Umemoto M (2009) Production of TiNi amorphous/nanocrystalline wires with high strength and elastic modulus by severe cold drawing. Scr Mater 60:749–752
48. Mei QS, Zhang L, Tsuchiya K, Gao H, Ohmura T, Tsuzaki K (2010) Grain size dependence of elastic modulus in nanostructured NiTi. Scr Mater 63:977–980

Chapter 12
Dental Metallic Materials

Masaaki Nakai and Mitsuo Niinomi

Abstract In dental treatment, treatment for restoring teeth (crown restorations) and for compensating for missing teeth (prosthetic treatments for missing teeth) involves the appropriate selection of metallic, ceramic, polymer materials or a combination of these materials as necessary for each individual patient. These devices are often tailor-made by dental technicians. Metallic materials also play an important role in dental implants and orthodontic treatments. In this chapter, various types of treatment in clinical dentistry under the intraoral environment are introduced, and then an outline of the types and characteristics of metallic materials used in the dental devices required by the aforementioned treatments is provided. Further, a recent progress of research about Ag-Pd-Cu-Au alloys that are the most important dental metallic materials in Japan is reviewed.

Keywords Crown restoration • Prosthetic treatment • Dental implant • Orthodontic treatment • Precious metals • Gold alloys • Silver alloys

12.1 Introduction

Throughout human history, mankind has suffered from various disorders and diseases and has made efforts to remediate such problems. Such efforts have also been made in the field of dentistry, namely, the development and improvement of dental treatment. Unlike bone and soft tissue diseases, dental disease is expected to have less possibility of natural healing because of low metabolic function of the teeth. Therefore, the recovery of function lost by dental caries and periodontal disease has relied on artificial materials.

In dental treatment, partial damage to teeth or loss of entire teeth is common, and the materials used to compensate for the missing parts play an important role in such cases. Treatment for restoring teeth (crown restorations) and for compensating for missing teeth (prosthetic treatments for missing teeth) involves the appropriate selection of metallic, ceramic, polymer materials, or a combination of these

M. Nakai (✉) • M. Niinomi
Institute for Materials Research, Tohoku University, 2-1-1 Katahira, Aoba-ku,
Sendai 980-8577, Japan
e-mail: nakai@imr.tohoku.ac.jp; niinomi@imr.tohoku.ac

materials as necessary for each individual patient. These devices are often tailor-made by dental technicians. Metallic materials also play an important role in dental implants and orthodontic treatments.

In this section, we will first discuss the intraoral environment and then different types of treatment in clinical dentistry before providing an outline of the types and characteristics of metallic materials used in the dental devices required by the aforementioned treatments.

12.2 Intraoral Environment [1]

Intraoral saliva has a pH of 6.2–7.6 and is 99.5 % water. It is an electrolytic solution that, other than mineral elements, contains organic components including protein and amino acids. At first, saliva appears unlikely to be a prime environment for corrosion. However, the pH drops and temperature fluctuations (273–333 K) are regularly caused by food intake. The pieces of food left inside the mouth are absorbed into bacterial cells such as plaque bacteria, and then the organic acids that are primarily lactic acid are produced by mainly anaerobic glycolysis. When sulfoprotein is broken down by the bacteria in protease, hydrogen sulfide that encourages silver alloy tarnishing is produced (Fig. 12.1). Thus, some types of acid are released from the plaque and neutralized; however, many permeate toward the enamel, leading to decreased pH. Within plaque, which contains anaerobic bacteria, organic acid is produced, and an environment deficient in dissolved oxygen is formed; thus, when plaque is adhered to

Fig. 12.1 Silver alloy tarnishing (Reprinted from Ref. [1], Copyright 2010, with permission from the Japan Institute of Metals)

Fig. 12.2 Fretting
corrosion (Reprinted from
Ref. [1], Copyright 2010,
with permission from the
Japan Institute of Metals)
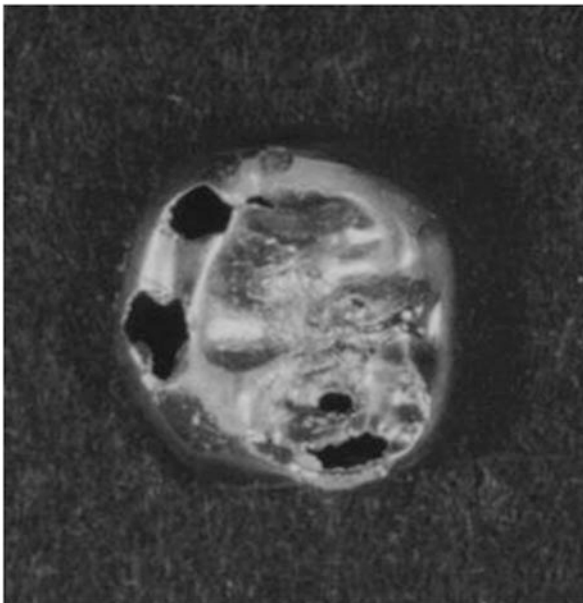
the surface of metallic prosthetic devices, this results in the formation of dissolved acid concentration cells and may cause local corrosion. In particular, because teeth have an anatomically complex shape and are covered in sticky saliva, areas such as spaces between teeth can easily become hotbeds for microorganisms, easily leading to crevice corrosion.

Mastication applies periodic stress to dental devices and causes friction between devices. As maximum biting force in the molar region is generally known to be equivalent to the static load of one's body weight, dental devices may be damaged by stress corrosion and/or fretting corrosion (Fig. 12.2).

Therefore, when dental alloys are worn intraorally for long periods of time as dental devices, multiple factors that deteriorate corrosion resistance accumulate in addition to the formation of a corrosive intraoral environment. Thus, when considering the corrosion resistance of dental metallic materials to be used intraorally, it is important to consider the corrosion resistance of dental devices as a whole rather than the corrosion resistance properties of each individual material.

12.3 Treatment Methods [1]

12.3.1 Crown Restorations

When the shape or function of a tooth crown (part of the tooth exposed within the oral cavity) is partially lost due to dental caries (tooth decay) or external trauma, restoration with artificial materials is conducted.

When the range of damage is restricted to a relatively small area such as the molar occlusal surface (surface on which the back teeth clench) or the adjacent surface to the anterior teeth, restoration is performed by filling the cavity (missing portion left over after the lesion has been removed and the area has been appropriately shaped) with plastic materials that are hardened after they have been shaped. Although gold foil has been used as a filling material, the most common type of metallic plastic filling material is dental amalgam. Restorations using dental amalgam involve filling the cavity with plastic wet amalgam that is a mixture of mercury and amalgam alloy powder containing the main components of silver, tin, and copper. After the amalgam hardens, the filling is polished. Because amalgam filling restorations offer excellent treatment outcomes and operability, they have long been widely clinically applied. However, there are concerns that amalgam is harmful to the human body, and it also has the disadvantages of tarnishing and tooth fractures. Thus, the development of composite resin (composite materials containing ceramic particles as a filler in a high polymer matrix), which adheres to the tooth and offers excellent esthetic properties, has meant that composite resin is now becoming more widely used.

Crown restorations performed by luting dental cement onto a metal casting manufactured outside of the oral cavity are called cast restorations. Inlays (Fig. 12.3) refer to restorations that are shaped to the tooth and fitted to the inside (surrounded by dentin) of the cavity, and crowns (Fig. 12.4) refer to restorations used to cover the cusp when the cavity area is relatively large. Abutment construction to compensate for the area of missing tooth is also frequently used to make crown restorations possible. When the missing area is relatively small, plastic

Fig. 12.3 Inlay (Reprinted from Ref. [1], Copyright 2010, with permission from the Japan Institute of Metals)

Fig. 12.4 Crown (Reprinted from Ref. [1], Copyright 2010, with permission from the Japan Institute of Metals)

filling materials are used, but when the missing area extends to the root canal, prefabricated posts or a metal core comprising a metal casting is used.

Cast restorations involve first removing the caries and then filing down (shaping) and filling in (cavity base, construction) the remaining tooth to make it into a suitable shape for the restoration. Next, dies (impressions) of the row of teeth that will hold the restoration and opposing teeth are taken, and the occlusal relationship is registered (interocclusal registration). The impressions and interocclusal registration results are then used to create a plaster cast, upon which a wax pattern is fabricated. This wax pattern is embedded in heat-resistant investment materials and fired to create a mold. Molten aluminum alloy is then cast in the mold. Dental casting is a type of lost wax process that has been industrialized for precision casting. Finally, the casting is adjusted on the die and in the patient's mouth, before being polished and luted with dental cement. When luting crown restorations onto teeth, dental castings must be extremely precise, and cement layer thickness is ordered per 10 μm. If the cement is too thick, the structure may start to collapse from the exposed cement layer, and the entry of bacteria from food, drink, and saliva may lead to secondary caries, which can cause the casting to fall out. Quartz and silica (SiO_2) cristobalite are used as base investing materials to achieve high casting precision. The setting expansion and thermal expansion of the die materials compensate for alloy casting shrinkage.

Rather than being completely made of metal, crowns are often partially made from hard resin or porcelain the same color as the tooth crown (facing crowns) to enhance esthetics. Strength of adhesive bonding is an important factor for both of the above types of facing crowns, which have complex structures. For the former type, hard resin facing crowns (Fig. 12.5), adhesive primers (pretreatment agents),

Fig. 12.5 Hard resin facing crown (Reprinted from Ref. [1], Copyright 2010, with permission from the Japan Institute of Metals)

have been developed for each type of alloy. The latter, porcelain fused to metal (PFM) crowns, is formed by fusing porcelain onto the alloy surface, as the name suggests. Elements are added to the alloy so that it forms an oxide film that increases the strength of porcelain fusion to metal while also increasing the melting point. Firing temperature is lowered on the porcelain side as well so that the alloy does not change shape and the thermal expansion coefficient of the porcelain is set slightly higher than that of the alloy so that contraction due to cooling after firing does not cause cracks on the interface. Recently, porcelain inlays and crowns (all-ceramic crowns) that use no metal at all are also becoming more commonly used.

12.3.2 Prosthodontic Treatments for Missing Teeth

When teeth are lost due to periodontal disease, caries, or external trauma, prosthodontic treatments using artificial materials to recover form and function are performed.

When one or multiple teeth are missing, two or more teeth are joined as abutment teeth (teeth used to support and maintain dentures), and a bridge (Fig. 12.6) is constructed to recover the lost shape and function of missing teeth. When the bridge is relatively small, a one-piece cast may be used. However, when multiple teeth are missing, parts of the bridge may be cast separately before being

Fig. 12.6 Bridge (Reprinted from Ref. [1], Copyright 2010, with permission from the Japan Institute of Metals)

joined with a soldering alloy or welded with a laser. The area of the missing tooth is covered with an artificial tooth called a pontic, which is shaped taking hygiene, functionality, and esthetics into consideration, depending on its location. Hard resin facing crowns and PFM crowns are used for anterior teeth because esthetic properties are important elements in this area. Furthermore, because the use of adhesive resin increases the bonding strength of luting cement, bridges that require little filing down of the remaining tooth are now a possibility.

Another treatment option is dentures, which morphologically compensate for the missing tooth and accompanying retraction of surrounding tissue and aim for functional and esthetic recovery. Types of dentures include removable dentures, partial dentures (Fig. 12.7) for use with remaining teeth, and full dentures. Partial denture design is diverse, taking into account the number and position of remaining teeth and type of retainer. Metal base dentures contain metal in the frame of the base, which constitutes the body of plate dentures, with the aim of increasing strength and sense of fit. In general, metal base dentures are fabricated via precision casting. Types of retainers used to prevent dentures from falling out include clasps that comprise wires wrapping around the abutment teeth and attachments that exhibit retentive force by joining parts attached to the abutment teeth to parts in the denture. Wire clasps made by bending alloy wires or cast clasps fabricated by casting may be used. Recently, magnetic attachments that utilize the suction force of magnets for retentive force have been developed. Magnets used include samarium-cobalt alloy and neodymium-iron-boron alloy. Ferrite magnetic stainless steel (SUS444, SUSXM27, SUS47J1), which has excellent corrosion resistance, is used for the keeper (side pulled by magnetic force within the dentures) and yoke (magnet cover).

Fig. 12.7 Partial denture (Reprinted from Ref. [1], Copyright 2010, with permission from the Japan Institute of Metals)

12.3.3 Dental Implants

Dental implants are artificial objects embedded into intraoral tissue to compensate for missing teeth. Implants are classified according to the site of insertion into intramucosal, sub-membrane, endodontic, and endosseous implants. Currently, endosseous implants (Fig. 12.8) inserted into the jawbone are the most common and are widely applied clinically. Materials implanted in the root portion in alveolar bone (fixtures) are mainly made of titanium, which has excellent biocompatibility. Good clinical outcomes are achieved with fixtures, as they offer osseointegration with no soft tissue separating them from bony tissue. Furthermore, some have a shape that promotes invasion of bony tissue or are coated with bioceramics such as hydroxyapatite, which offers osseoinduction and osseoconduction. In dental implant treatments, a fixture implanted within the bone is used as the foundation, and the abutment is placed. Then, the "superstructure" comprising a crown, bridge, or prosthesis with base is fixated.

12.3.4 Orthodontic Treatments

Orthodontic treatments use mainly metal wire elasticity or superelasticity as orthodontic force to move teeth into target positions. Orthodontic wires may be made of materials such as stainless steel, cobalt-chromium (Co-Cr) alloy, titanium-nickel
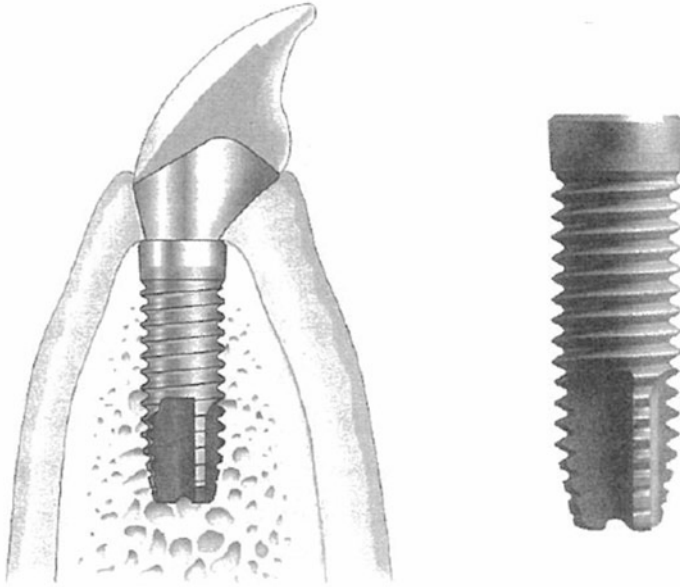
Fig. 12.8 Dental implant (Reprinted from Ref. [1], Copyright 2010, with permission from the Japan Institute of Metals)

(Ti-Ni) alloy, or titanium-molybdenum alloy. Ti-Ni alloy wires that apply superelasticity in particular are widely used clinically due to their persistent exertion of orthodontic force appropriate for moving teeth. Arch fixtures suited to the tooth dentition may be twisted into circular, square cross-sectional shapes or bundle shapes and are fixated in brackets fitted to the labial buccal surfaces of teeth. Various other types of devices are also used in orthodontic treatments to move individual teeth and rows of teeth. These include, for example, expansion appliances for widening narrowed maxillary dentition with screws and thick wires, arch appliances composed of a main wire fixated to the dentition and springs and hooks soldered to this, and orthodontic plates combining labial side guide wires, clasps, and springs with a resin base. Retainers used to prevent recurrence after teeth have been moved to the correct position also come in various shapes. In general, all types of orthodontic devices use Co-Cr alloy or stainless steel wires that have been bent.

12.3.5   Other Treatments

As the extent of dental caries progresses and bacteria reach the dental pulp (soft tissue containing nerves and blood vessels) inside the tooth, the infected pulp must be removed, and the walls of the root canal that held the pulp must be mechanically and chemically expanded and cleaned to make it possible to conserve the tooth. In

this type of endodontic procedure, a stainless steel dental reamer and file are usually used manually for mechanical root canal enlargement. In recent years, motorized root canal preparation using a superelastic Ti-Ni alloy file required for good results even in the case of bent root canals is being clinically applied and is garnering attention.

Because jaw fracture and orthognathic surgery involve fixation of bone fragments, the same osteosynthesis plates used for orthopedic surgery are employed. The plates used in oral surgery, however, are often smaller "mini-plates." Previously, stainless steel plates had been used, but titanium plates have now become mainstream. The plate is bent to follow the bone surface and fixated to the bone fragment with screws. For reconstructive maxillofacial surgery, dental implants and different types of reconstructive plates are used.

12.4 Types and Features of Dental Metallic Materials

12.4.1 Dental Casting Alloys

Dental casting alloys are commonly used in dental treatments such as crown restorations and prosthodontic treatments for missing teeth. These alloys must have sufficient mechanical properties (strength, ductility, etc.) that suit the purpose of their use, offer excellent corrosion resistance, cause no toxicity or irritation, and have superior casting performance. Previously, there were separate standards for each type of alloy, but in 2006, internationally unified standards, "ISO22674: Dentistry—Metallic materials for fixed and removable restorations and appliances" [2], were determined by the International Organization for Standardization (ISO). These standards divide dental metallic materials into six types depending on their mechanical properties and specify the uses for each type (Table 12.1).

12.4.1.1 Dental Casting Gold Alloys

Dental casting gold alloys must offer mechanical properties suitable for their use and superior casting performance while still maintaining the excellent corrosion resistance and chemical stability of gold. The additional elements mainly used to create gold alloys are selected for their ability to improve mechanical properties and lower the melting point. Table 12.2 shows typical elements and their effects [1]. Silver and copper are the main elements that constitute the elemental composition of gold alloys. The hardness and strength are improved by making the copper into a proportional solid solution with gold. When more than approximately 10mass% of copper is added, it undergoes solid phase transformation to Au_3Cu or $AuCu$ superlattice below 680 K; thus, improved mechanical properties due to age hardening can also be anticipated. Copper is also greatly involved in lowering melting

Table 12.1 Mechanical properties and uses of dental restorations and metallic materials for prostheses by type

Type	0.2 % proof stress (MPa) minimum	Elongation (%) minimum	Elastic modulus (GPa) minimum	Uses
0	–	–	–	Fixed restorations with low stress loading (e.g., small, one-sided veneer inlays and veneer crowns, metal frames for porcelain bonding made via electroforming or sintering)
1	80	18	–	Fixed restorations with low stress loading (e.g., one-sided inlays, veneer crowns)
2	180	10	–	Fixed restorations (e.g., inlays, crowns)
3	270	5	–	Fixed restorations and prostheses for multiple teeth (e.g., bridges)
4	360	2	–	Devices with high stress loading (e.g., removable partial dentures, clasps, thin crowns, long span bridges, bridges with small section surfaces, burrs, attachments, implant superstructures)
5	500	2	150	Devices that require high rigidity and strength (e.g., thin removable partial dentures, parts with thin section surfaces, clasps)

Table 12.2 The effects of additional elements in gold alloys

Additional elements	Effects	
	Advantages	Disadvantages
Ag	Reduces redness	Decreases resistance to corrosion
Cu	Lowers melting point, improves mechanical properties	Decreases resistance to corrosion, causes redness
Pt	Improves strength and elasticity	Raises melting point, segregation
Pd	Same as Pt	Raises melting point, decreases resistance to corrosion
Zn	Prevents oxidation	Decreases resistance to corrosion
Ir	Crystal grain refinement	–

point, but when it is added in large amounts, it leads to reddening and decreased corrosion resistance of the alloy. Silver becomes a proportional solid solution with gold but can form an alloy without changing any mechanical properties. Decreasing the amount of gold contained in the alloy and adding copper can prevent reddening. Platinum and palladium are harder than gold and have a higher elastic modulus. They increase the elastic modulus and strength of gold alloys. Therefore, they are
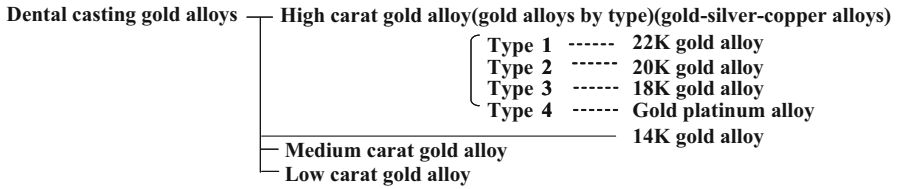
Dental casting gold alloys ─── **High carat gold alloy(gold alloys by type)(gold-silver-copper alloys)**

                                        Type 1 ------ **22K gold alloy**
                                        Type 2 ------ **20K gold alloy**
                                        Type 3 ------ **18K gold alloy**
                                        Type 4 ------ **Gold platinum alloy**
                                                          14K gold alloy

         ├─ **Medium carat gold alloy**
        └─ **Low carat gold alloy**

Fig. 12.9 Types of dental casting gold alloys

added to gold alloys used in large prosthodontic appliances. Like silver, platinum and palladium prevent the reddening effects of adding copper, but, because they markedly increase the melting point, they cannot be added in large amounts to dental casting gold alloys. Although these elements exhibit the same effects on gold alloys, platinum is used with palladium because platinum is prone to segregation. Small amounts of zinc and iridium are also sometimes used as additional elements. Zinc is added to precious alloys for casting as a deoxidizing agent. Iridium cannot be melted easily as it has an extremely high melting point. When a small amount of fine powder iridium is added to a gold alloy, the iridium becomes a crystalline nucleus, promoting the refinement of crystal grains, inhibiting segregation, and improving corrosion resistance and mechanical properties. Dental casting gold alloys (gold-silver-copper alloys) contain at least 60 % gold, and gold + platinum group metals (Pt, Pd) contain at least 75 %. They are classified according to the amount of precious metals contained and their mechanical properties. Figure 12.9 shows the main types of dental casting gold alloys. The American Dental Association Standards (ADAS) and Japanese Industrial Standards (JIS) classify gold alloys into four types based on strength and elongation and define each gold alloy according to type. Standards for dental alloys have also been compiled in "ISO22674: Dentistry—Metallic materials for fixed and removable restorations and appliances." For each of these types, there are gold-silver-copper alloys and gold-platinum alloys with the gold content shown in carats (K). For each composition or use, 22 to 18 K gold alloys are classified into gold alloy types 1, 2, or 3, and gold-platinum alloys for casting are classified as a type 4 gold alloy. All of these alloys are high-carat gold alloys for dental treatment. Some gold-platinum alloys are used for purposes other than casting.

Within Japan, dental treatment is covered by health insurance. JIS T6113 [3] defines dental casting 14 K gold alloys as being suitable for coverage by health insurance. Under JIS, excluding types 1 to 4 and 14 K gold alloys, these are defined as medium-carat dental casting gold alloys with a gold content of 55mass% or greater and low-carat dental casting gold alloys containing a total amount of precious metals (gold and platinum group metals as additional elements) of 35mass% or greater.

Gold alloys separated according to type include gold-silver-copper-platinum-palladium-zinc-type alloys that contain gold, silver, and copper as the main components. As you can see in Table 12.3, which shows the composition of each type of gold alloy, the amount of copper increases from type 1 to type 4, whereas the

Table 12.3   Composition of gold alloys by type

Gold alloy	Composition range (mass%)					
	Au	Ag	Cu	Pt	Pd	Zn
Type 1	80.2–95.8	2.4–12.0	1.6–6.2	0–1.0	0–3.6	0–1.2
Type 2	73.0–83.0	6.9–14.5	5.8–10.5	0–4.2	0–5.6	0–1.4
Type 3	71.0–79.8	5.2–13.4	7.1–12.6	0–7.5	0–6.5	0–2.0
Type 4	62.4–71.9	8.0–17.4	8.6–15.4	0.2–8.2	0–10.1	0–2.7

Table 12.4   Mechanical properties and uses of gold alloys by type

Gold alloy	Properties	Heat treatment	Proof stress (MPa)	Elongation (%)	Main uses
Type 1	Soft	Softening	80–180	>18	Inlays
Type 2	Medium hard	Softening	180–240	>12	Crowns
Type 3	Hard	Softening	240	>12	Crowns, bridges
Type 4	Super hard	Softening	300	>10	Bases, clasps, large prostho-
		Softening	450	>3	dontic devices

Below 1,323 K (1,050°C)

amount of gold decreases. Platinum and palladium are mainly added to types 3 and 4. Copper lowers the melting point and improves hardness and strength. Platinum and palladium are mainly added to improve strength and elastic modulus. These alloys exhibit mechanical properties appropriate for the intended use. The more copper contained, the lower the melting point; however, the melting point rises when more platinum and palladium are added. Thus, JIS T6116 [4] dictates that the sum of these added elements cannot exceed 10mass% and the liquid phase points of gold alloy types 1 through 4 are each below 1,323 K.

Table 12.4 shows the mechanical properties and main uses of the gold alloys by type. Gold alloy types 1 through 4 are defined as soft, medium hard, hard, and super hard in that order. In accordance with an increasing amount of added copper, hardness and strength increase, but elongation decreases. There are no stipulations regarding heat treatment for gold alloys other than type 4. However, types 3 and 4 can undergo hardening heat treatment (regular age hardening) using Au_3Cu or AuCu superlattice and be used in large prosthodontic appliances that require strength.

The prosthodontic appliances in which each type of gold alloy is mainly used include inlays, crowns, bridges, and clasps. Inlays (Fig. 12.3) require border sealing rather than strength, so type 1 gold alloys, which are soft and have high elongation, are used. For crowns (Fig. 12.4), which must withstand occlusal stress, types 2 and 3 are used. For bridges (Fig. 12.6), which are subject to occlusal pressure that bends to become stress, type 3 is used. The metal bases (Fig. 12.7) of large prosthodontic appliances and clasps, which require high elastic modulus, are subject to even greater stress. Therefore, type 4 is used, and hardening heat treatment may be
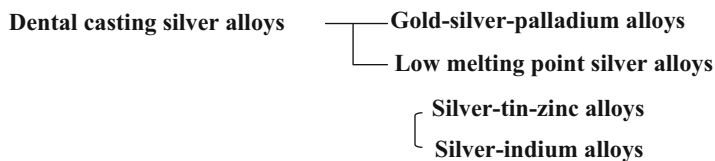
Dental casting silver alloys ———— **Gold-silver-palladium alloys**

└—— **Low melting point silver alloys**

┌ **Silver-tin-zinc alloys**

└ **Silver-indium alloys**

Fig. 12.10 Types of dental casting silver alloys

Table 12.5 The effects of additional elements in silver alloys

Additional elements	Effects	
	Advantages	Disadvantages
Au	Improves resistance to corrosion	Expensive
Cu	Lowers melting point, improves mechanical properties	Decreases resistance to corrosion, causes redness
Pd	Improves sulfur resistance (prevents tarnishing)	Raises melting point
Zn	Prevents oxidation	Decreases resistance to corrosion

applied depending on the circumstances. As each type of gold alloy forms a single-phase solid solution containing at least 50 at.% precious metal (gold and platinum group metals), its high corrosion resistance inhibits, the extent of dental caries progresses and bacteria reach the dental pulp.

12.4.1.2 Dental Casting Silver Alloys

In Japan, gold-silver-palladium alloys (Ag-Pd-Cu-Au alloys) are commonly used dental casting silver alloys, as they are eligible for health insurance coverage. The mechanical properties of these alloys are equivalent to gold alloy types 3–4. Because silver sulfurizes within the mouth and blackens, it is made into an alloy with palladium or gold, which prevents sulfurization and improves corrosion resistance. As the main component is silver, low-melting point silver alloys containing elements such as tin, indium, and zinc are economical but have poor mechanical properties and inferior corrosion resistance. Figure 12.10 shows the main types of dental casting silver alloys.

Like gold, silver is extremely soft and very ductile. It is relatively stable even against acid and alkaline, and its melting point presents no problems for dental casting. However, it has high oxygen solubility during melting, easily absorbs gas, offers poor strength, and tends to sulfurize and blacken. Thus, the added elements shown in Table 12.5 are used to improve these characteristics. Copper contributes to improving mechanical properties and lowering the melting point, whereas zinc works as a deoxidizing agent. Palladium not only improves mechanical properties but also improves corrosion resistance and sulfur resistance and prevents

Table 12.6 Mechanical properties and main uses of gold-silver-palladium alloys

Type	Heat treatment	Hardness (Hv)	Tensile strength (MPa)	Elongation (%)	Main uses
Type 1	Softening	90–160	390–590	10–40	Inlays, crowns
Type 2	Hardening	200–320	640–980	2–15	Bridges, clasps, bases

blackening. However, it also markedly increases the melting point of silver alloys. Gold contributes to improving corrosion resistance.

Gold-silver-palladium alloys contain silver, palladium, copper, and gold as the main components. Adding copper to silver improves mechanical properties and lowers the melting point, while palladium increases sulfur resistance and inhibits tarnishing. A large amount of palladium must be added to achieve sufficient corrosion and sulfur resistance. However, because palladium markedly raises the melting point of silver alloys, gold—which does not raise melting point to the same extent—is added to solve this issue. Like gold-platinum alloys, gold-silver-palladium alloys may be for casting use or non-casting use. Standards for the amount of precious metals (Au, Pd, Ag) contained in each have been stipulated by JIS. JIS T6106 [5] specifies the composition of gold-silver-palladium alloys for casting use. There must be at least 12mass% gold, 20mass% palladium, and 40mass% silver. The restriction stipulating a small amount of palladium differs from the standards for non-casting use (JIS T6105 [6]), which does not require melting. Gold-silver-palladium alloys for casting may undergo hardening heat treatment and, as is shown in Table 12.6, may exhibit the mechanical properties of type 3 and type 4 gold alloys. From inlays to metal bases including clasps, these alloys can be used in prosthodontic devices except those that involve porcelain bonding. Corrosion resistance is excellent in silver alloys, but compared with dental casting gold alloys, the quantity of released ions is somewhat greater, and brownish tarnishing may occur.

JIS T6108 [7] stipulates that type 1 low-melting point silver alloys comprise silver-tin-zinc alloys and type 2 comprise silver-indium alloys. Both contain at least 60mass% of silver and have a melting point of below 1,273 K. The main additional elements of these alloys (zinc, tin, and indium) are non-precious metal elements that contribute to the sulfur resistance of silver. However, sulfurization cannot be prevented unless fairly large amounts of these elements are added. Zinc works as a deoxidizing agent. The addition of large amounts of tin causes decreased elongation and greatly reduces mechanical properties. Indium is effective for tarnishing resistance and causes little loss of malleability. Table 12.7 shows the composition and mechanical properties of silver-tin-zinc alloys and silver-indium alloys. Silver-tin-zinc alloys, which contain less than 5mass% indium and do not contain platinum group metals, are used for inlays. Meanwhile, silver-indium alloys contain at least 5mass% indium and less than 10mass% of platinum group metals. They are used for burrs, posts, and crowns.

Table 12.7 Types and compositions of low melting point silver alloys

Silver alloy	Composition (mass%)					Hardness	Tensile strength (MPa)	Elongation (%)
	Ag	Sn	Zn	In	Other			
Silver-tin-zinc alloys (JIS type 1)	73	9	16	–	–	HB 133	470	3
	65	20	15	–	–	HB 135	314	–
Silver-indium alloys (JIS type 2)	70	–	6	23	Trace amounts of Pd, Pt	Hv 130	372	14
	67	–	5	20	Pd	Hv 196	265	3

Below 1,273 K (1,000 t)

12.4.1.3 Other Dental Casting Alloys

Other dental casting alloys include non-precious alloys such as cobalt-chromium alloys and titanium and titanium alloys.

Dental casting cobalt-chromium alloys (Co-Cr alloys) are composed of 40–70 % cobalt, 20–30 % chromium, 0–20 % nickel, and 0–10 % molybdenum and have mechanical properties equivalent to ISO22674 type 5. These alloys are indicated when heavy loads are applied and strong rigidity is required such as for plate denture metal frames and clasps.

Titanium and titanium alloys have a stable passive film and offer properties that make them suitable metallic materials for use in living organisms. These properties include excellent corrosion resistance and histocompatibility, low specific gravity, and lightness. Previously, it had been difficult to apply these metals to dental casting use due to their high melting point and high reactivity to the atmosphere during melting and die material oxygen. However, research into dental casting technology brought about the development of specialized casting machines and investing materials, making it possible to use titanium and titanium alloys. Titanium (CP Ti) has a wide range of mechanical properties from soft to fairly hard (types 1 through 4), depending on the purity. It is used in denture bases, crowns, and bridges. Titanium alloys (Ti-6Al-7Nb alloys), which offer excellent biological safety in addition to high strength and good operability, have also come to be used in clinical settings (Fig. 12.11).

12.4.2 Alloys for Porcelain Bonding

Porcelain bonding involves welding multiple layers of porcelain to a metal surface to create coloration and texture similar to that of natural teeth (Fig. 12.12). Figure 12.13 shows a section image of a PFM crown. In general, dentin porcelain, which brings out the color of dentin, is applied onto a base of opaque porcelain that is strongly welded to the metal frame. Layers of translucent enamel porcelain are

Fig. 12.11 Metal frame of partial denture made from Ti-6Al-7Nb alloy (Reprinted from Ref. [1], Copyright 2010, with permission from the Japan Institute of Metals)

Fig. 12.12 Porcelain fused to metal crown appearance (Reprinted from Ref. [1], Copyright 2010, with permission from the Japan Institute of Metals)
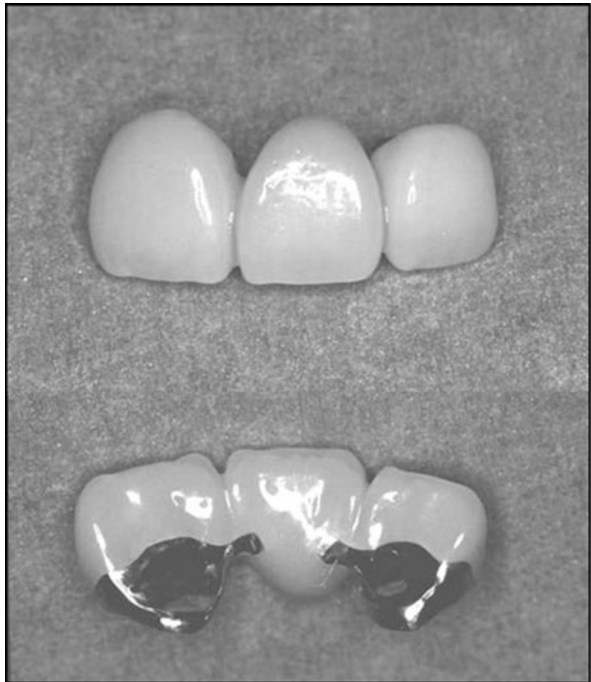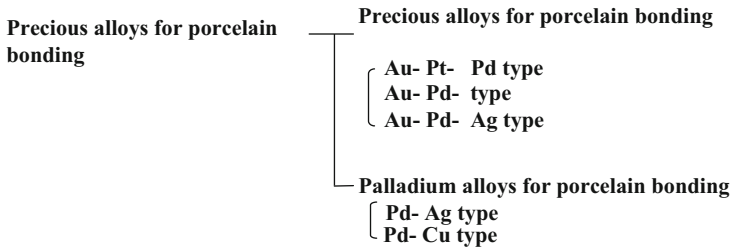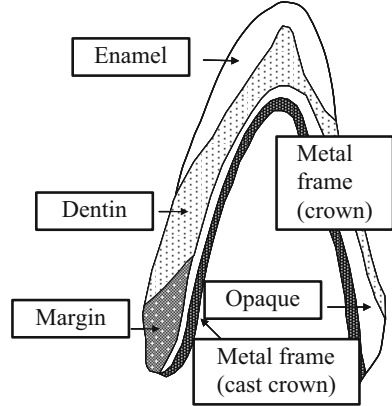
Fig. 12.13 Porcelain fused
to metal crown section
(Reprinted from Ref. [1],
Copyright 2010, with
permission from the Japan
Institute of Metals)

Fig. 12.14 Types of precious alloys for porcelain bonding

then fused onto this. Thus, alloys that are welded onto porcelain are called alloys for porcelain bonding and may be composed of precious or non-precious metals. Porcelain has a greater elastic modulus and a lower coefficient of thermal expansion than metal. During heating and cooling during welding, a high coefficient of thermal expansion than metal causes thermal stress to be applied to the interface between the metal and porcelain. To prevent the porcelain from easily peeling away from the metal or alloy, it is important to make its elastic modulus and coefficient of thermal expansion close to that of porcelain.

In particular, when gold alloys for porcelain bonding commonly used in anterior tooth restorations are used, the porcelain is fired on top of the casting, so very small amounts of the non-precious metals of indium and tin are added. The addition of copper and silver to alloys may cause discoloration to porcelain, so copper is not added and only a very small amount of silver is added.

Precious alloys for porcelain bonding are divided into gold alloys and palladium alloys. The former includes high-carat gold-platinum-palladium-type, mid- to low-carat gold-palladium-type, and gold-palladium-silver-type alloys, while the latter includes palladium-silver-type and palladium-copper-type alloys (Fig. 12.14).

Table 12.8 Composition of precious alloys for porcelain bonding

Alloy	Composition range (mass%)								Elastic modulus (GPa)
	Au	Pt	Pd	Ag	Cu	Sn	In	Other	
Au-Pt-Pd type	74–88	0–20	0–16	0–15	–	0–3	0–4	Zn < 2	90
Au-Pd type	45–68	0–1	22–45	–	–	0–5	2–10	Zn < 4	124
Au-Pd-Ag type	42–62	–	25–40	5–16	4–20	0–4	0–6	Zn < 3	110
Pd-Ag type	0–6	0–1	50–75	1–40	–	0–9	0–8	Zn < 4 Ga < 6	138
Pd-Cu type	0–2	0–1	66–81	–	4–20	0–8	0–8	Zn < 4 Ga:3-9	96

12.4.2.1   Gold Alloys for Porcelain Bonding

Table 12.8 shows the composition and elastic modulus of gold alloys for porcelain bonding. In high-carat gold-platinum-palladium alloys containing 74–88mass% of gold, the addition of platinum and palladium increases hardness and strength of the alloy, while indium and tin are also added to bring the solid phase point from 1,323 K to 1,473 K and increase fusion strength with porcelain. In gold-palladium-type and gold-palladium-silver-type alloys, which contain less gold, 22–45mass% of palladium is added, and the solid phase point is high at 1,473 K to 1,573 K. The elastic modulus is also higher than that of gold-platinum-palladium alloys. The thermal expansion coefficients ($14–15 \times 10^{-6}$ K^{-1}) of these alloys are close to those of dental porcelain ($11.5–13.5 \times 10^{-6}$ K^{-1}). Compared with other dental casting gold alloys, gold alloys for porcelain bonding contain the same amount or more of gold and platinum group metals than high-carat gold alloys, giving them high corrosion resistance. Silver and copper may cause green or yellow discoloration of porcelain. Therefore, when using gold-palladium-silver alloys, which have a lot of added silver, treatment to prevent discoloration is required.

12.4.2.2   Palladium Alloys for Porcelain Bonding

Palladium-silver and palladium-copper alloys contain at least 50mass% palladium, with a main additional element of either silver or copper, respectively (Table 12.8). As with gold alloys for porcelain bonding, indium, tin, and gallium are added to increase fusion strength. Palladium-silver alloys have a high elastic modulus even compared with precious metal alloys for porcelain bonding. Because both of these palladium alloys contain large amounts of silver or copper, treatment to prevent discoloration is necessary. Palladium alloys for porcelain bonding that contain large amounts of copper, tin, or gallium also release large amounts of palladium ions and are somewhat problematic with regard to corrosion resistance.

Brazing metal ——— Gold solder

        ⎧ **20K gold solder**
          18K gold solder
          16K gold solder
        ⎩ **14K gold solder**

      ——— Silver solder

      ⎡ **Gold-silver-palladium alloy solder**
      ⎣ **Silver solder**

Fig. 12.15 Types of dental brazing metals

Table 12.9 Compositions and melting points of brazing metals

Type		Composition (mass%)							Melting point (K)	
		Au	Ag	Pt	Pd	Cu	Zn	Other	Liquid phase point	Solid phase point
Pre-brazing for alloys for porcelain bonding		90.0	5.0	2.0	–	–	–	Sn	1,388	1,328
		79.0	17.8	1.0	1.0	–	–	In, Sn, Cu	1,343	1,288
Gold solder	18 K	75.0	5.5	–	–	10.5	7.0	In	1,078	1,003
	16 K	66.7	11.0	–	–	11.0	9.3	In	1,043	973
	14 K	58.5	14.5	–	–	14.5	10.5	In	1,038	968
Gold-silver-palladium alloy solder		20.0	31.0	–	15.0	25.0	6.0	In	1,093	1,043
Silver solder		–	56.0	–	–	22.0	17.0	Sn:5	938	–

12.4.3 Brazing Metals

Brazing metals must have a melting point of 373–473 K lower than the base metal, form an alloy with the base metal, fuse strongly, have little potential difference with the base metal to reduce galvanic corrosion, and be of a color that is similar to the base metal. Therefore, brazing metals are composed from the same type of alloy as the base metal (Fig. 12.15, Table 12.9).

12.4.3.1 Gold Solder

Gold solder is divided into that used for gold alloys for porcelain bonding and that used for gold alloys in general. JIS T6117 [8] stipulates that both must contain at least 58.33mass% gold and have a peeling strength of 350 MPa or greater. In

general, gold solder with the same amount of carats as the base metal is used, with 20–14 K being commercially available.

12.4.3.2 Silver Solder

Silver solder is divided into gold-silver-palladium alloy solder and general silver solder. JIS T6107 [9] stipulates that gold-silver-palladium alloy solder contain at least 15mass% gold, at least 30mass% total gold and palladium together, and at least 30mass% silver. JIS T6111 [10] stipulates that general silver solder contain at least 35mass% silver and have a liquid phase point of below 1,073 K. However, general silver solder may have various melting points, and low melting point silver solder, etc., can be used for joining orthodontic wires. Silver solder is a highly versatile solder metal that can not only be used with silver alloys but also welded to non-precious alloys such as cobalt-chromium alloys and nickel-chromium alloys.

12.5 Recent Progress of Research About Ag-Pd-Cu-Au Alloys

12.5.1 Unique Hardening Behavior of Ag-20Pd-12Au-14.5Cu Alloy

As mentioned above in 12.4.1.2, Ag-Pd-Cu-Au alloys are most important dental metallic materials in Japan, and it is well known that these alloys exhibit age hardening behavior [12–15]. However, it has been reported that the mechanical strength of an Ag-20Pd-12Au-14.5Cu (mass%) alloy is significantly enhanced when the alloys are subjected to solution treatments at temperatures higher than 1,073 K and subsequent water quenching without being subjected to aging treatment [16]. Figure 12.16 shows the change in the tensile properties and hardness of Ag-20Pd-12Au-14.5Cu alloys by aging treatments and solution treatments [16]. The increase in mechanical strength of Ag-20Pd-12Au-14.5Cu alloy subjected to solution treatment at high temperature is called to unique hardening behavior because solution treatment generally induces to decrease mechanical strength. This unique hardening behavior has been explained by two hardening mechanisms: one is the solid solution hardening mechanism, in which alloying elements are dissolved into the matrix (α phase) by solution treatment [16], and the other is the precipitation hardening mechanism, in which $L1_0$-type ordered β' phases are precipitated during the quenching process after solution treatment [17].

Firstly, the unique hardening behavior has been explained in terms of the solid solution hardening mechanism because the peak intensity of β phase (Cu-Pd intermetallic compound) decreases with solution treatment temperature in X-ray
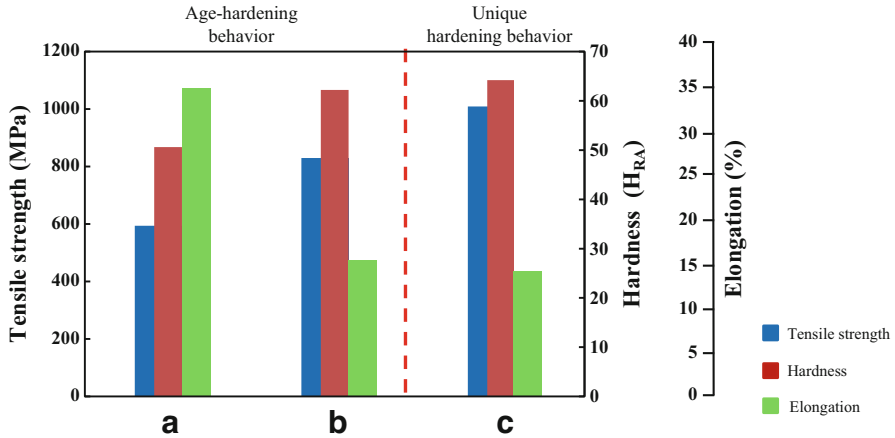
Fig. 12.16 Tensile strength and hardness of Ag-20Pd-12Au-14.5Cu alloy subjected to (**a**) solution treatment at 1,023 K for 3.6 ks, (**b**) aging treatment at 673 K for 1.8 ks after solution treatment at 1,023 K for 3.6 ks, and (**c**) solution treatment at 1,123 K for 3.6 ks

diffraction (XRD) profiles of the Ag-20Pd-14.5Cu-12Au alloy (Fig. 12.17) [16]. This implies that alloying elements of the β phase are dissolved in the matrix (α phase) by solution treatment as the solution treatment temperature increases. Thereafter, the unique hardening behavior has been explained in terms of the precipitation hardening mechanism. The precipitates of $L1_0$-type ordered β′ phases during the subsequent quenching process after solution treatment were observed by transmission electron microscopy (TEM) (Fig. 12.18) [12, 17], and the precipitated β′ phase increases the hardness [17, 18].

12.5.2 Factors for Hardening of Ag-20Pd-12Au-14.5Cu Alloy

The mechanism of this unique hardening behavior has been investigated recently using a liquid rapid solidification method in order to obtain a single α phase because commercial Ag-20Pd-12Au-14.5Cu alloy is possible to be composed of multiphase, FCC-α, FCC-$α_1$ (Cu rich), FCC-$α_2$ (Ag rich), B2-type ordered β, and $L1_0$-type ordered β′ phases (Fig. 12.19) [19], and the coarse Cu-Pd intermetallic compound (β phase) of commercial Ag-20Pd-12Au-14.5Cu alloy is difficult to be dissolved into the matrix by solution treatment. A schematic drawing of liquid rapid solidification method is shown in Fig. 12.20 [20]. A high-frequency induction coil was used for induction melting, and a commercial Ag-20Pd-12Au-14.5Cu alloy was melted inside a quartz tube in vacuum. The melted alloy was forced into a Cu die through
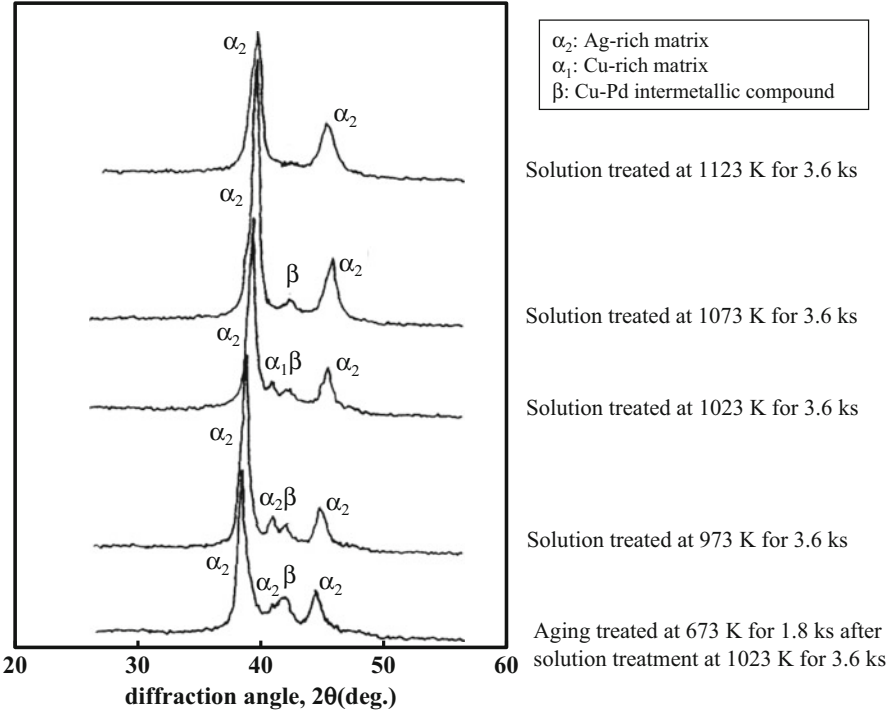
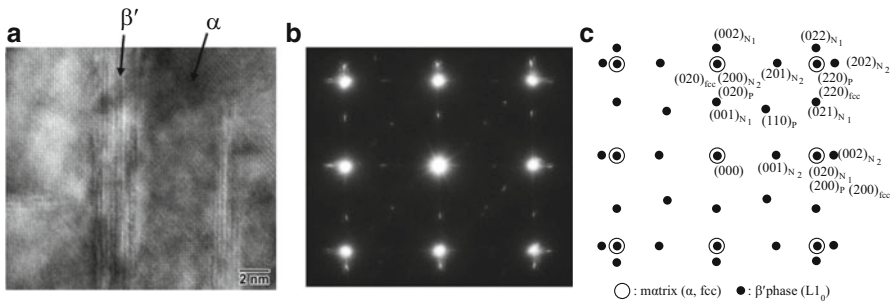Fig. 12.17 X-ray diffraction profiles of Ag-20Pd-14.5Cu-12Au alloy subjected to various heat treatments

Fig. 12.18 (a) TEM bright-field image, (b) selected area diffraction pattern, and (c) key diagram of Ag-20Pd-14.5Cu-12Au alloy subjected to solution treatment at 1,123 K for 3.6 ks subsequent water quenching

a nozzle by argon gas and then solidified rapidly (hereafter referred as to LRS specimen).

As shown in Fig. 12.21 [20], LRS specimen was subjected to solution treatment at 1,173 K for 3.6 ks in vacuum in order to obtain a single α phase (1173WQ$_{LRS}$/
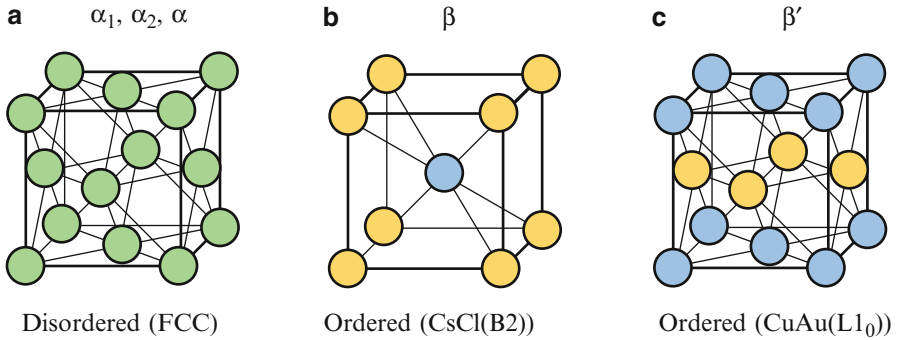
Fig. 12.19 Crystal structures of the constitutional phases in Ag-20Pd-12Au-14.5Cu alloy
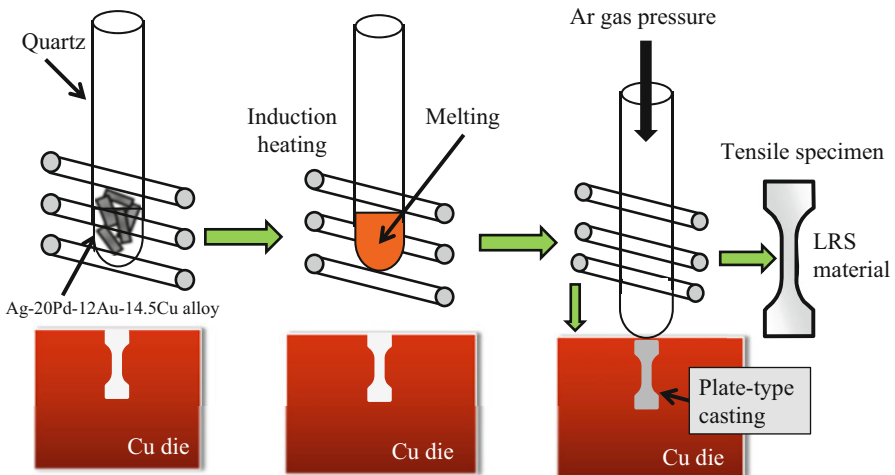
Fig. 12.20 Schematic drawing of liquid rapid solidification method (LRS) (Reprinted from Ref. [20], Copyright 2012, with permission from Elsevier)

3.6ks), and then it was subjected to solution treatment at 1,023 K for 1.8–28.8 ks (1,023WQ$_{LRS}$/1.8–28.8 ks) in vacuum in order to decompose a single α phase into α_1 and α_2 phases. Figure 12.22 shows the XRD profiles of 1173WQ$_{LRS}$/3.6ks and 1,023WQ$_{LRS}$/1.8ks–28.8ks [20]. The single α phase is identified in 1173WQLRS/ 3.6ks. The α, α_1, and α_2 phases are identified, and the β phase is not identified in 1023WQ$_{LRS}$/1.8ks–28.8ks. Figure 12.23 shows the microstructures of 1173WQ$_{LRS}$/ 3.6ks and 1023WQ$_{LRS}$/1.8ks–28.8ks by backscattered electron (BSE) analysis [20]. The microstructure of 1173WQ$_{LRS}$/3.6ks is composed of a single α phase (Fig. 12.23a). The microstructure of 1023WQ$_{LRS}$/1.8ks–28.8ks is decomposed into two (black, white) areas corresponding to α_1 and α_2 phases from the part of a single α phase (Fig. 12.23b–f). Further, the BSE image and the result of energy-dispersive X-ray spectroscopy (EDX) show that the microstructure of 1023WQ$_{LRS}$/ 28.8ks is composed of a Cu-rich α_1 phase, an Ag-rich α_2 phase, and an α phase
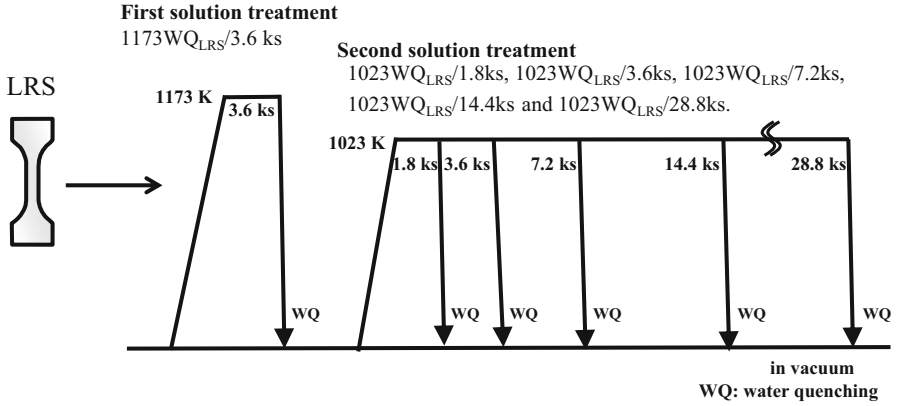
Fig. 12.21 Schematic drawing of solution treatment for Ag-20Pd-12Au-14.5Cu alloy fabricated by LRS (Reprinted from Ref. [20], Copyright 2012, with permission from Elsevier)
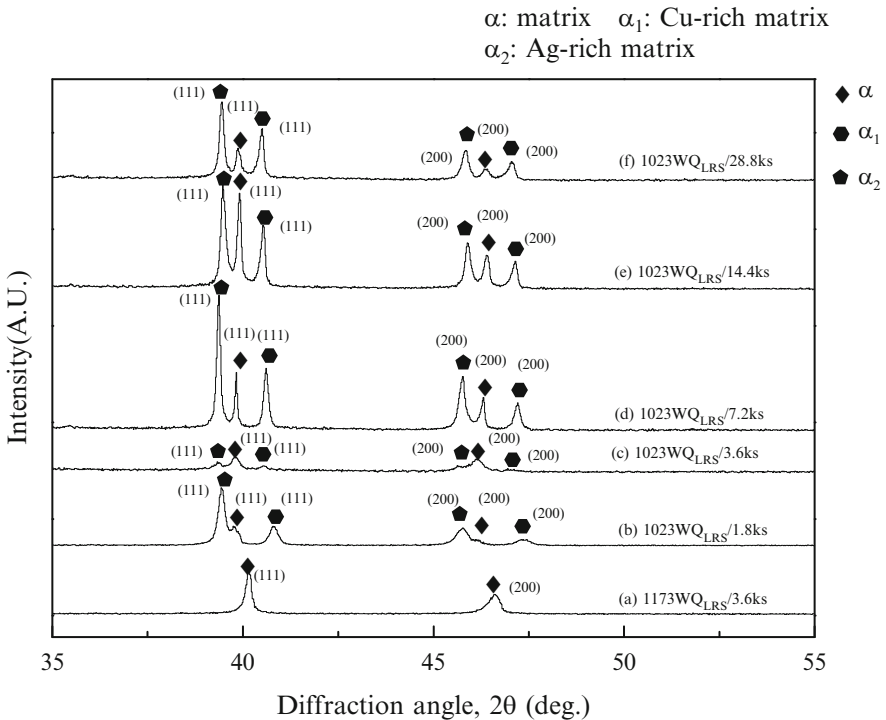

Fig. 12.22 XRD profiles of (**a**) $1173WQ_{LRS}/3.6ks$, (**b**) $1023WQ_{LRS}/1.8ks$, (**c**) $1023WQ_{LRS}/3.6ks$, (**d**) $1023WQ_{LRS}/7.2ks$, (**e**) $1023WQ_{LRS}/14.4ks$, and (**f**) $1023WQ_{LRS}/28.8ks$ (Reprinted from Ref. [20], Copyright 2012, with permission from Elsevier)
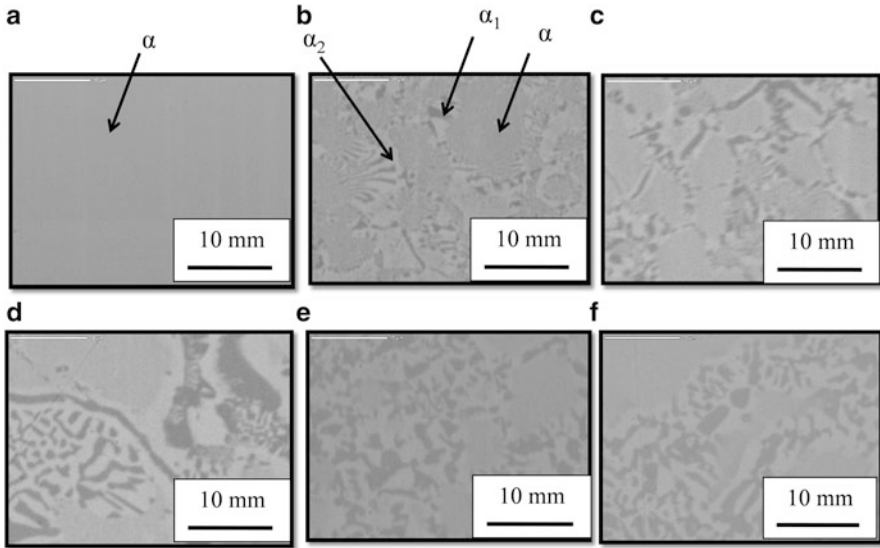
Fig. 12.23 BSE images of (**a**) 1173WQ$_{LRS}$/3.6ks, (**b**) 1023WQ$_{LRS}$/1.8ks, (**c**) 1023WQ$_{LRS}$/3.6ks, (**d**) 1023WQ$_{LRS}$/7.2ks, (**e**) 1023WQ$_{LRS}$/14.4ks, and (**f**) 1023WQ$_{LRS}$/28.8ks (Reprinted from ref. [20], Copyright 2012, with permission from Elsevier)

(Fig. 12.24) [20]. The single α phase decomposes into a Cu-rich α_1 phase and an Ag-rich α_2 phase, but the β phase does not precipitate by solution treatment at 1,023 K. Figure 12.25 shows the change in Vickers hardness of 1173WQ$_{LRS}$/3.6ks and 1023WQ$_{LRS}$/1.8ks–28.8ks [20]. The change in hardness among them is small even though the α_1 and α_2 phases are decomposed from 1173WQ$_{LRS}$/3.6ks with a single α phase by solution treatment at 1023 K. The effect of decomposition of the α_1 and α_2 phases on the increases in hardness is small.

On the other hand, as shown in Fig. 12.26, 1173WQ$_{LRS}$/3.6ks was subjected to aging treatment at 673 K for 1.8–28.8 ks (673WQ$_{LRS}$/1.8–28.8 ks) in vacuum to precipitate a β phase from a single α phase. Figure 12.27 shows the XRD profiles of 1173WQ$_{LRS}$/3.6ks and 673WQ$_{LRS}$/1.8ks–28.8ks [20]. The single α phase is identified in 1173WQ$_{LRS}$/3.6ks (Fig. 12.27a). The α, α_1, and α_2 phases are changed to α_2 and β phases during aging treatment at 673 K (Fig. 12.27b–f). Figure 12.28 shows the microstructures of 1173WQ$_{LRS}$/3.6ks and 673WQ$_{LRS}$/1.8ks–28.8ks obtained by BSE analysis [20]. The microstructure of 1173WQ$_{LRS}$/3.6ks is a single α phase. The weak contrast in the BSE images of 673WQ$_{LRS}$/1.8ks–14.4ks (Fig. 12.28b–e) appears after aging treatment. This is considered to be the result of the difference in chemical composition; the area where the β phase precipitates and the area where the β phase does not precipitate exist after aging treatment. Figure 12.29 shows the result of TEM observation of 673WQ$_{LRS}$/1.8ks [20]. The selected area diffraction pattern indicates the existence of an α phase and a β phase. The dark-field image is obtained using the (010) superlattice reflection from the B2-type ordered β phase.
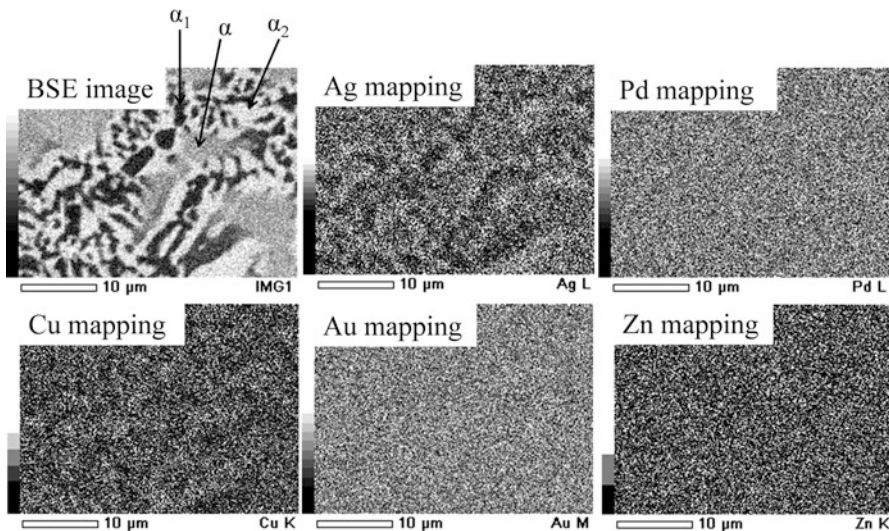
Fig. 12.24 BSE image and results of EDX analysis on specimen surface of $1023WQ_{LRS}$/28.8ks (Reprinted from Ref. [20], Copyright 2012, with permission from Elsevier)
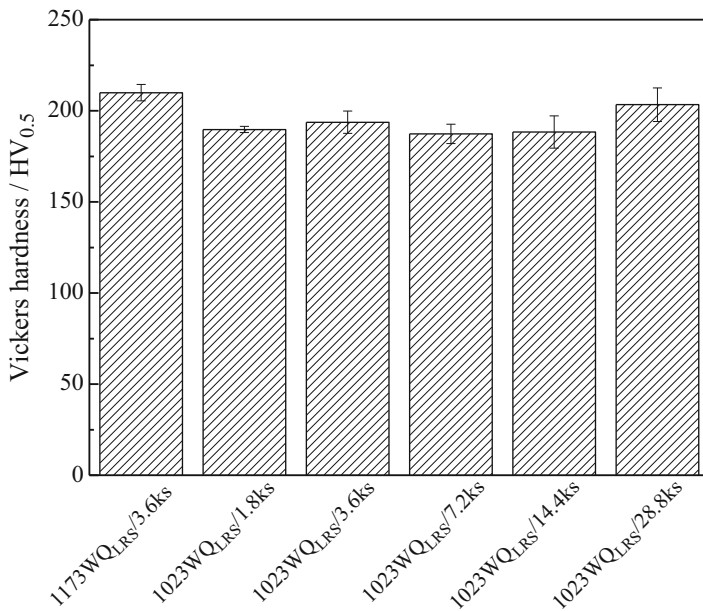

Fig. 12.25 Vickers hardness of $1173WQ_{LRS}$/3.6ks, $1023WQ_{LRS}$/1.8ks, $1023WQ_{LRS}$/3.6ks, $1023WQ_{LRS}$/7.2ks, $1023WQ_{LRS}$/14.4ks, and $1023WQ_{LRS}$/28.8ks (Reprinted from Ref. [20], Copyright 2012, with permission from Elsevier)
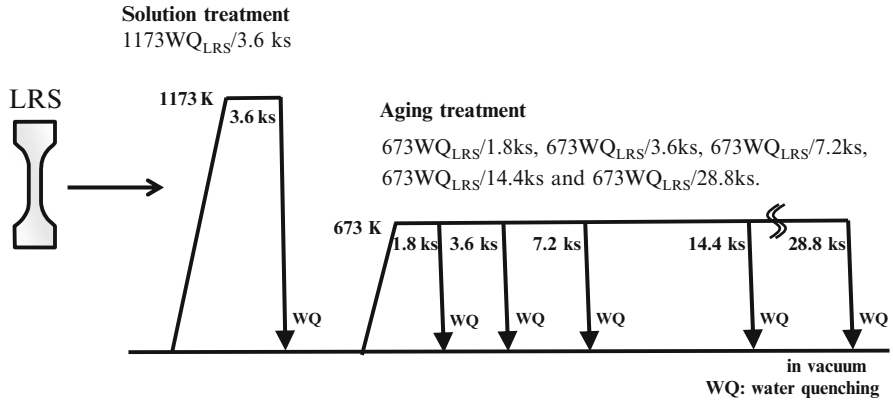
Fig. 12.26 Schematic drawing of aging treatment for Ag-20Pd-12Au-14.5Cu alloy fabricated by LRS (Reprinted from Ref. [20], Copyright 2012, with permission from Elsevier)
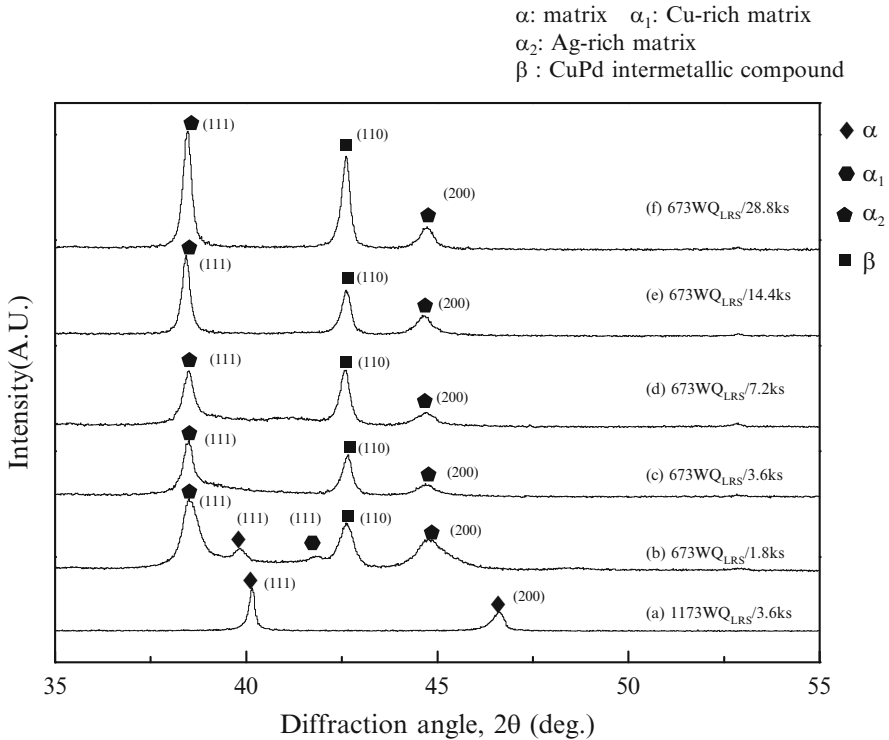

Fig. 12.27 XRD profiles of (**a**) 1173WQ$_{LRS}$/3.6ks, (**b**) 673WQ$_{LRS}$/1.8ks, (**c**) 673WQ$_{LRS}$/3.6ks, (**d**) 673WQ$_{LRS}$/7.2ks, (**e**) 673WQ$_{LRS}$/14.4ks, and (**f**) 673WQ$_{LRS}$/28.8ks (Reprinted from Ref. [20], Copyright 2012, with permission from Elsevier)
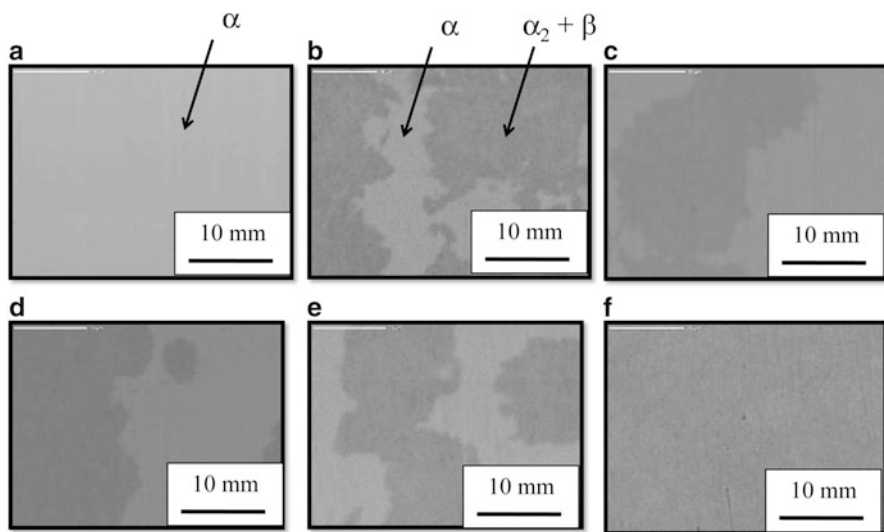
Fig. 12.28 BSE images of (**a**) 1173WQ$_{LRS}$/3.6ks, (**b**) 673WQ$_{LRS}$/1.8ks, (**c**) 673WQ$_{LRS}$/3.6ks, (**d**) 673WQ$_{LRS}$/7.2ks, (**e**) 673WQ$_{LRS}$/14.4ks, and (**f**) 673WQ$_{LRS}$/28.8ks (Reprinted from Ref. [20], Copyright 2012, with permission from Elsevier)
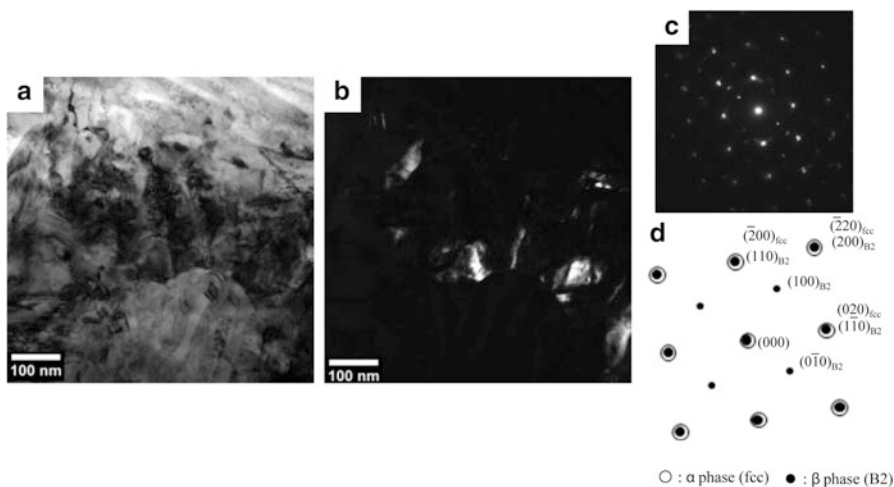

Fig. 12.29 Results of TEM observation of 673WQ$_{LRS}$/1.8ks: (**a**) bright-field image, (**b**) dark-field image by using the (010) superlattice reflection, (**c**) selected area diffraction pattern, and (**d**) key diagram. The beam direction is parallel to [001] (Reprinted from Ref. [20], Copyright 2012, with permission from Elsevier)

Fig. 12.30 Vickers hardness of 1173WQ$_{LRS}$/3.6ks, 673WQ$_{LRS}$/1.8ks, 673WQ$_{LRS}$/3.6ks, 673WQ$_{LRS}$/7.2ks, 673WQ$_{LRS}$/14.4ks, and 673WQ$_{LRS}$/28.8ks (Reprinted from Ref. [20], Copyright 2012, with permission from Elsevier)
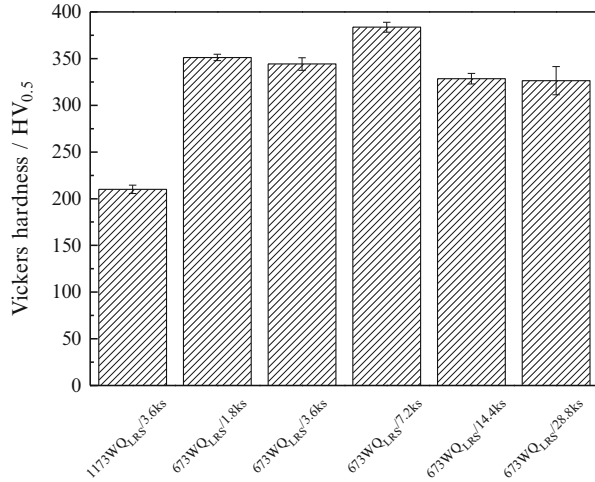
The TEM dark-field image shown in Fig. 12.29b indicates that the β phase with diameter less than 100 nm precipitates in the matrix. Figure 12.30 shows Vickers hardness in 1173WQ$_{LRS}$/3.6ks and 673WQ$_{LRS}$/1.8ks–28.8ks [20]. The hardness of 673WQ$_{LRS}$/1.8ks with the precipitated β phase increases greatly compared with that of 1173WQ$_{LRS}$/3.6ks with a single α phase. The hardness of 673WQ$_{LRS}$/7.2ks is the highest, and then the hardness tends to decrease. These results imply that the effect of precipitation of β phases on the increase in hardness is large.

Various heat treatments were carried out on the LRS specimen with a single α phase, but the β′ phase could not be obtained after the heat treatments so that the contribution of the β′ phase to the unique hardening behavior was not evaluated directly. However, it was found that the solid solution strengthening due to the decomposition of α phase to α$_1$ and α$_2$ phases is small. This fact implies that β′ phase is possible to contribute to the unique hardening behavior of the commercial Ag-20Pd-12Au-14.5Cu alloy subjected to solution treatments.

12.6 Summary

This chapter laid out the types of treatment available in clinical dentistry and outlined the types and characteristics of metallic materials used in the dental devices necessary for these treatments. The metallic materials used in dental devices must have mechanical properties that make them able to withstand occlusion, have characteristics such as corrosion resistance that allow them to withstand the severe corrosion that occurs in the intraoral environment, and be both castable and workable—important characteristics for tailor-made fabrication. Recently, esthetic properties have also come to be highly sought in addition to the properties outlined above [11]. The development of new high-performance dental metallic materials that meet these various demands is anticipated in the future.

References

1. Hanawa T (2010) Metals for medicine. The Japan Institute of Metals, Sendai
2. ISO22674 (2006) Dentistry—Metallic materials for fixed and removable restorations and appliances. International Organization for Standardization (ISO), Geneva, Switzerland
3. JIS T6113 (2011) Dental casting 14 K gold alloys. Japanese Industrial Standards Committee (JIS), Tokyo, Japan
4. JIS T6116 (2012) Dental casting gold alloys. Japanese Industrial Standards Committee (JIS), Tokyo, Japan
5. JIS T6106 (2011) Dental casting gold-silver-palladium alloys. Japanese Industrial Standards Committee (JIS), Tokyo, Japan
6. JIS T6105 (2011) Dental wrought gold-silver-palladium alloys. Japanese Industrial Standards Committee (JIS), Tokyo, Japan
7. JIS T6108 (2005) Dental casting silver alloys. Japanese Industrial Standards Committee (JIS), Tokyo, Japan
8. JIS T6117 (2011) Dental gold alloy brazing materials. Japanese Industrial Standards Committee (JIS), Tokyo, Japan
9. JIS T6107 (2011) Dental gold-silver-palladium alloy solders. Japanese Industrial Standards Committee (JIS), Tokyo, Japan
10. JIS T6111 (2011) Dental silver alloy brazing materials. Japanese Industrial Standards Committee (JIS), Tokyo, Japan
11. Takemoto S (2012) Current and Future Views of Dental Materials—Dental Implant and Resin Composite—. Materia Jpn 51:316–318
12. Ohta M, Shiraishi T, Hisatsune K, Yamane M (1980) Age-hardening of dental Ag-Pd-Cu-Au alloys. J Dent Res 59:1966–1971
13. Yu CH, Park MG, Kwon YH, Seol HJ, Kim HI (2008) Phase transformation and microstructural changes during ageing process of an Ag-Pd-Cu-Au alloy. J Alloys Compd 460:331–336
14. Seol HJ, Kim GC, Son KH, Kwon YH, Kim HI (2005) Hardening mechanism of an Ag-Pd-Cu-Au dental casting alloy. J Alloys Compd 387:139–146
15. Takahashi S, Niinomi M, Fukui H, Fukunaga K, Narita K, Hasegawa J (1998) Effect of volume fraction of β phase on tensile fracture characteristics in Ag-Pd-Cu-Au alloy. J Jpn Socr Dent Mater Devices 17:370–377
16. Fukui H, Shinoda S, Mukai M, Yasue K, Hasegawa J (1992) Effect of heat treatment on mechanical properties of type IV gold and 12 wt% Au-Pd-Ag alloys. J Jpn Socr Dent Mater Devices 11:141–148
17. Tanaka Y (2003) Microstructural change and strengthening mechanism of de tal gold-silver palladium alloy by high-temperature heat treatment. Boundary 19:14–17
18. Tanaka Y, Seol H-J, Ogata T, Miura E, Shiraishi T, Hisatsune K (2003) Hardening mechanism of dental casting gold-silver-palladium alloy by higher-temperature heat-treatment. J Jpn Socr Dent Mater Devices 22:69
19. Crystal lattice structures. http://dave.nrl.navy.mil/lattice/pearson/ctype.html
20. Kim Y-H, Niinomi M, Nakai M, Akahori T, Kanno T, Fukui H (2012) Mechanism of unique hardening of dental Ag-Pd-Au-Cu alloys in relation with constitutional phases. J Alloys Compd 519:15–24